ScuDo
Scuola di Dottorato ~ Doctoral School
WHAT YOU ARE, TAKES YOU FAR

Doctoral Dissertation
Doctoral Program in Materials Science and Technology (29th Cycle)

Study and characterisation of Ni-based superalloys produced by laser additive manufacturing

By

Giulio Marchese

******

Supervisor(s):
Prof. S. Biamino
Prof. L. Montanaro (Co-Supervisor)

Doctoral Examination Committee:
Prof. L. Fedrizzi
Prof. M. Cabrini
Prof. M. Filippini
Prof. C.F. Badini
Prof. D. Ugues

Politecnico di Torino
2017

Declaration

I hereby declare that, the contents and organization of this dissertation constitute my own original work and does not compromise in any way the rights of third parties, including those relating to the security of personal data.

Giulio Marchese

2017

* This dissertation is presented in partial fulfillment of the requirements for **Ph.D. degree** in the Graduate School of Politecnico di Torino (ScuDo).

Acknowledgment

I would like to express my sincere gratitude to my tutor Prof. Sara Biamino for her support of my Ph.D study and related research as well as for her precious advice.

I would like to thank also Prof. Paolo Fino, Prof. Mariangela Lombardi and Prof. Daniele Ugues for sharing their knowledge during these years.

I would like to thank Prof. Matteo Pavese for helping me during the first year of PhD, giving valuable advice and stimulating ideas.

I would like to express my special appreciation to the researchers of the Istituto Italiano di Tecnologia (IIT) di Torino, Dr. Flaviana Calignano, Dr. Diego Manfredi, Dr. Elisa Paola Ambrosio and Dr. Massimo Lorusso for supporting me in the research activities.

I would like to express my gratitude to all my colleagues: Alberta, Andrea, Elisa, Erica, Federico, Giorgio, Gloria, "Hamed" Abdollah, Luca, Mario and Oxana for their contribution to a positive work environment and for their help during my laboratory work.

Besides, my thanks goes also to the PhD student working in IIT: Francesco, Giulio, Simone and Jukka, who sometimes helped me with the EOS machine.

Last but not least, I would like to thank my family, my fiancé Federica, and my friends, especially Luca, Daniele and Piova for encouraging me to strive towards my goal, also when the work was very arduous.

Abstract

The laser additive manufacturing techniques (LAM) are of growing interest in different industries due to their capacity to produce near net shape components in a single step. Particularly in the case of the Ni-based superalloys, LAM processes can produce highly complex shape components more cheaply with respect to the traditional technologies.

However, nowadays, there is still a lack of knowledge on the study of the process parameters on the microstructure and densification levels and the study of tailored heat treatments to meet standard qualification as well as precise industrial requirements.

This thesis presents the research performed on two Ni-based superalloys produced by LAM processes. Inconel 625 (IN625) fabricated by laser powder bed fusion (LPBF) and directed energy deposition (DED) and Hastelloy X (HX) built by LPBF.

For LPBF IN625 alloy was studied the effect of different process parameters on the hardness and densification level, obtaining dense samples (relative density over 99.8 %). Afterward, it was studied in detail the microstructure, mechanical and thermomechanical properties of as-built IN625. The results showed that the tensile behaviours of as-built IN625 state are higher than minimum values requirements for wrought IN625 alloys, due to very fine dendritic structures (mainly less than 1.5 micron) coupled with high dislocation density. However, the characterisation of as-built IN625 samples revealed that heat treatments are necessary to decrease the residual stresses, reduce elements segregation, and produce mechanical properties suitable for industrial applications. For this reason, the microstructural evolution of LPBF IN625 under different heat treatments was investigated. According to the performed heat treatment, the mechanical properties of heat-treated IN625 were

influenced by phases precipitation (mainly γ″ phases and carbides) and/or recrystallisation, grain growth and dissolution of dendritic structures.

For DED IN625 alloy, the aim of this work was to determine the impact of different process parameters on the densification level (relative density over 99.7 %), hardness and microstructure in order to select the appropriate parameters for industrial production.

Finally, LPBF HX alloy was studied in a research collaboration with GE AVIO s.r.l. The target of this work was to investigate the microstructure of as-built and post-processed LPBF HX alloy. The as-built HX samples showed different microcracks caused by the LPBF process, so some samples were hot isostatically pressed (HIPed) to close the microcracks. The microstructure, grain size, phases and hardness of the as-built, heat-treated and HIPed HX samples were investigated. The results revealed that in case microcracks appear during production, they can be removed after specific post processing, generating LPBF HX parts with grain size similar to standard solution heat-treated (SHT) wrought HX alloy.

Contents

1. Introduction 1

  1.1 Categories of superalloys 1

    1.1.1 Solid solution strengthened superalloys 3

  1.1.2 Precipitation strengthened superalloys 4

  1.2 Phases formed 5

    1.2.1 Gamma prime (γ′) phase 5

    1.2.2 Gamma double prime (γ″) and δ phases 7

    1.2.3 Carbides 9

    1.2.4 Borides 12

    1.2.5 Sulfocarbides 12

    1.2.6 Nitrides 13

    1.2.7 Topologically Close-Packed Phases 13

  1.3 Effect of the specific elements within superalloys 15

  1.4 Heat treatments for superalloys 16

  1.5 Specific properties of IN625 and HX superalloys 21

    1.5.1 IN625 superalloy 21

    1.5.2 HX superalloy 25

  1.6 Additive manufacturing (AM) techniques 27

    1.6.1 LPBF process 28

    1.6.2 DED process 30

    1.6. 3 Difference between LPBF and DED 32

  1.7 Powders for additive manufacturing processes 33

1.8 Microstructures of LPBF and DED Ni-based superalloys 34
    1.8.1 LPBF Ni-based superalloys 34
    1.8.2 Microstructure of DED as-built Ni-based superalloys 35
1.9 Defects within LPBF and DED Ni-based alloys 36
    1.9.1 Pores..36
    1.9.2 Cracks 38
    1.9.3 Residual stresses 42
2. Materials and methods 43
2.1. LAM machines used...43
    2.1.1 LPBF process 43
    2.1.2 DED process 47
2.2 Superalloy powders used 49
    2.2.1 LPBF IN625 powder...49
    2.2.2 DED IN625 powder 50
    2.2.3 LPBF HX powder 50
2.3 Powder characterisations 52
2.4 Metallographic sample preparation 52
2.5 Orientations of the samples for microstructural analysis 53
    2.5.1 As-built IN625 specimens 53
    2.5.2 As-built HX specimens...54
2.6 Microstructural analyses and phases characterisations 55
    2.6.1 Optical microscopy (OM) 55
    2.6.2 Scanning electron microscopy (SEM) 56
    2.6.3 Transmission electron microscopy (TEM) 56
    2.6.4 XRD analysis 57
    2.6.5 Carbides extraction 57
2.7 Thermal analyses 58
    2.7.1 Thermo-mechanical analysis TMA...58

2.7.2 Laser flash analysis (LFA) 58
2.8 Mechanical tests 58
2.8.1 Hardness tests 58
2.8.2 Tensile Tests 59
2.8.3 Impulse excitation technique 59
2.9 Post process treatments: heat treatments and HIP 59
2.9.1 Post processing treatments performed on LPBF HX samples 59
2.9.2 Heat treatments performed on LPBF IN625 samples 60
3. Results and discussion of IN625 produced by LPBF 61
3.0 Powders characterisation 62
3.1 LPBF powder characterisation 62
3.2 Process parameters optimisation 65
3.3 Investigation of defects of as-built IN625 samples 68
3.4 Microstructure of as-built IN625 samples 69
3.4.1 XRD analysis on as-built IN625 samples 76
3.4.2 Thermal mechanical analyses on as-built IN625 samples 77
3.4.3 Tensile behaviour of as-built IN625 samples 78
3.4.4 Fracture surface of as-built IN625 tensile samples 80
3.5 Investigation on direct aged IN625 conditions 82
3.5.1 Hardness investigation 82
3.5.2 Microstructure of IN625 samples direct aged at 600 °C 83
3.5.3 Microstructure of IN625 samples direct aged at 700 °C 88
3.5.4 Tensile properties of direct aged samples 93
3.5.5 Tensile fracture surfaces of direct aged IN625 samples 95
3.5.6 Microstructure of IN625 samples direct aged at 800 °C 96
3.5.7 Microstructure of IN625 samples direct aged at 900 °C 102
3.6 Investigation on SHT IN625 condition 107
3.6.1 Hardness investigation 107

3.6.2 Microstructure evolution of SHT IN625 at 1000 °C 109

3.6.3 Microstructure evolution of SHT IN625 at 1150 °C 111

3.6.4 Thermomechanical analysis on SHT IN625 samples 114

3.6.5 XRD analysis on SHT IN625 samples 115

3.6.7 Tensile fracture surfaces analysis 118

3.7 Investigation on aged IN625 conditions 119

3.7.1 Hardness investigation 119

3.7.2 Microstructure evolution of IN625 sample aged at 600 °C 120

3.7.3 Microstructure evolution of IN625 sample aged at 700 °C 124

3.7.4 Tensile properties of aged IN625 samples...................................130

3.7.5 Tensile fracture surface of aged IN625 samples...........................132

3.7.6 Microstructure evolution of IN625 sample aged at 800 °C 134

3.7.7 Microstructure evolution of IN625 sample aged at 900 °C 138

3.8 Tensile behaviour of as-built and heat-treated IN625 samples 143

3.9 Conclusions 145

4. Results and discussion of IN625 produced by DED process.........................148

4.1 DED Powder characterisation 148

4.2 Process parameters optimisation 152

4.3 Investigation of defects of as-built IN625 samples 155

4.4 Microstructure of as-built IN625 samples 156

4.5 XRD analysis on as-built IN625 samples...161

4.6 Conclusions 162

5. Results and discussion of HX produced by LPBF 163

5.1 Powder characterisation..164

5.2 Characterisation of as-built HX samples 169

5.2.1 Residual Porosity and microcracks investigation 169

5.2.2 Microstructural investigation of as-built HX samples......................171

5.2.3 XRD analysis of as-built HX state 177

5.2.4 TMA of as-built HX state 178

5.2.5 Solidification and microcracks formation discussion of as-built HX samples 178

5.3 Solutionizing treatments optimisation 180

5.3.1 SHT HX samples at 1175 °C for different times 180

5.3.2 Microstructure investigation on optimised SHT condition 183

5.3.3 XRD analysis of optimised SHT HX state 188

5.3.4 TMA of optimised SHT HX state 189

5.3.5 SHT HX samples at 1066 °C for 1 hour 190

5.4 Microstructural evolution of SHT HX samples under thermal exposures 193

5.4.1 Hardness investigation of SHT HX heat-treated at 745 °C and 788 °C for different times 193

5.4.2 Microstructural investigation of SHT HX heat-treated at 745 °C for different times 194

5.4.3 XRD analysis of heat-treated SHT at 745 °C for different times . 198

5.4.4 Microstructural investigation of SHT HX heat-treated at 788 °C for different times 199

5.4.5 XRD analysis of heat-treated SHT at 788 °C for different times . 204

5.4.6 Characterisation of extracted carbides form SHT HX samples heat-treated at 745 °C and 788 °C 205

5.4.7 XRD spectra of extracted carbides of heat-treated SHT HX samples 207

5.5 Characterisation of HIPed HX samples 208

5.5.1 Microstructural characterisation of HIPed HX samples 208

5.5.2 Characterisation of extracted carbides from HIPed HX samples . 212

5.5.3 XRD spectra of HIPed HX samples and extracted carbides 214

5.5.4 TMA of HIPed HX state 215

5.6 HIPed+SHT HX samples 216

5.6.1 Solutionizing treatment optimisation on HIPed HX samples 216

5.6.2 Microstructural investigation of optimised HIPed+SHT HX samples 217
5.6.3 XRD spectrum of optimised HIPed+SHT HX state 222
5.6.4 TMA of optimised HIPed+SHT HX state 223
5.6.5 HIPed and subsequent solutionizing treatment at 1066 °C for 1 hour 224
5.7 Conclusions 227
6. Overall Conclusions and future works..228
7. Appendix A...230
8. References..236

List of Figures

Figure 1 - TEM images showing different γ′ phase shapes: (a) fine spherical γ′ phases within Inconel 718 plus alloy [11], (b) cuboidal γ′ phases along <100> direction within a Ni-8.5Al-5.4Ti alloy [12], (c) plate-like γ′ phases within Ni-12at%Al alloy [13]........7

Figure 2: (a) FESEM image of IN625 alloy showing disc-shaped γ″ phases after thermal exposure at 700 °C for 1000 hours [15]; (b) TEM image of IN625 alloys showing γ″ phases after ageing at 700 °C for 100 hours [16]; (c) FESEM image of IN625 alloys showing acicular δ phases after thermal exposures at 800 °C for 1000 hours [15]........8

Figure 3:(a,b) OM image of Inconel 738 showing MC and $M_{23}C_6$ carbides adapted from [21]; (c) FESEM image of GH984 alloy showing intergranular particle and film of $M_{23}C_6$ carbides adapted from [22]; (d) FESEM image of HX alloy showing M_6C and $M_{23}C_6$ carbides adapted from [23]; (e,f) SEM images of Ni-Cr-W alloys showing intergranular $M_{23}C_6$ carbides adapted from [24]........12

Figure 4: (a) TEM image of HX alloy showing intergranular σ phases adapted from [20]; (b) TEM images of HX ally exhibiting M_6C, $M_{23}C_6$ carbides and μ phases adapted from [20]; (c) FESEM image of IN625 plus alloy showing Laves phases with eutectic-like morphology [35]........15

Figure 5: Time-Temperature-Transformation (TTT) diagram of IN625 alloy [39]........24

Figure 6: TTT diagram of HX alloy [20].........26

Figure 7: Schematic diagram of an LPBF process [56].........29

Figure 8: Different scanning strategy for LPBF process [54].........30

Figure 9: Schematic illustration view of a DED system [45].........31

Figure 10: Different deposition strategy used in DED process: a) raster, b) zig-zag or bi-directional, c) offset-out, d) offset-in and e) fractal [80].........32

Figure 11:Characteristics of LPBF (referred as SLM) and DED (referred as LMD) [84]........33

Figure 12: 3D composite images of LPBF as-built IN718 alloy showing the melt pools along different planes [65].........34

Figure 13: EBSD images along the building direction (a) and perpendicular to the building direction (b) for LPBF IN625 alloy [55]. 35

Figure 14: OM image of gas entrapped pores within (a) the cross sectioned powder and (b) solid materials for DED Inconel 718 alloy [90]. 37

Figure 15: OM image of LPBF IN625 alloy produced with low energy density showing different pores due to lack of fusion [48]. 37

Figure 16: OM images of TiAl6V4 produced by LPBF showing the effect of the energy density: a) lack of fusion; b) optimised energy density; c) key hole produced by too high energy density [79]. 38

Figure 17: OM image of LPBF HX showing cracks along the grain boundaries [60]. 39

Figure 18: FESEM images of DED Inconel 718 showing liquation cracking due to the melting of Laves particles within the heat affected zone [94]. 40

Figure 19: FESEM images showing grain boundary crack due to the generation of voids around precipitates associated with the ductility-dip cracking for LPBF CM247LC [99]. 41

Figure 20: Effect of the residual stresses on LPBF Inconel 718 alloy [78]. ...42

Figure 21: Images of (a) EOS M270 and (b) EOS M280 devices [106,107]..43

Figure 22: Schematic illustration of the stripe scanning strategy [76]..........45

Figure 23: Schematic representation view of the adopted LPBF scanning strategy to built IN625 specimens (the red arrows depicted the laser scans) [56].45

Figure 24: Images of (a) ABB 6650 6 axis robot and (b) Sulzer Metco Twin 10 powder feeder. 47

Figure 25: Illustration view of the zig-zag deposition strategy used for DED process (the read arrows indicate the laser tracks) [56]. 48

Figure 26: Schematic representation of an IN625 cubic on the building platform showing the main orientation and the x-y plane and z direction. 53

Figure 27: Schematic views illustrating the as-built HX cylinders orientated vertically (a) and horizontally (b) to the building platform; the x-y plane is parallel to the building platform whereas the z-y plane is both perpendicular to the building platform and parallel to the building direction. 55

Figure 28: FESEM images of IN625 powder showing particles at different magnifications (a,b) in which satellite particles are indicated by the yellow arrows. 62

Figure 29: OM images of mounted IN625 powder particles cross section polished at different magnification (a, b) showing the presence of spherical pores, some of which are pointed out by red circles. 63

Figure 30: Particle size distribution determined using laser granulometry diffraction for LPBF powder with and without ultrasonic vibration. 64

Figure 31: Brinell hardness vs residual porosity for as-built IN625 samples obtained by LPBF process. 66

Figure 32: Residual porosity and Brinell hardness vs energy density for as-built IN625 samples obtained by LPBF process. 66

Figure 33: OM images of polished IN625 samples built using different process parameters (a) S7 and (b) S16 along the building direction, showing different spherical pores, where some of which are highlighted by red circles. 69

Figure 34: 3D optical image composite of as-built IN625 sample showing columnar grains (CGs) and melt pool contours (MPCs) along the building direction and equiaxed grains (EG) perpendicular to the building direction (x-y plane); Kalling’s No.2 etchant was used....................70

Figure 35: 3D optical image composite of as-built IN625 sample showing the melt pool contours (MPCs) along the building direction (z-axis) and perpendicular to the building direction (x-y) plane; Mixed acids reagent was used. 71

Figure 36: FESEM images at different magnification (a, b) exhibiting melt pools with columnar and cellular primary dendrites for as-built IN625 sample; Mixed acids reagent was used. 72

Figure 37: FESEM images of as-built IN625 sample at high magnification showing: (a) columnar dendritic structures with nanoprecipitates indicated by arrow 1 and segregation of Nb and Mo within the interdendritic zones indicated by arrow 2; (b) cellular dendritic structures with nanoprecipitates indicated by arrow 1 and segregation of Nb and Mo within the interdendritic areas indicated by arrow 2 exhibiting melt pools with columnar and cellular primary dendrites for as-built IN625 sample; Mixed acids reagent was used....................73

Figure 38: TEM bright field images exhibiting: a) columnar dendrite structures with high density of dislocation chiefly positioned in the interdendritic regions; b) precipitates along the interdendritic areas indicated by arrow 1; c) Elements segregation along the interdendritic regions indicated by arrow 2; d) Nb-rich MC carbides within the dendritic areas pointed out by arrow 3 with the inset showing the coherency with the matrix..75

Figure 39: XRD spectra of as-built IN625 samples along x-y plane and z direction. 76

Figure 40: Coefficient of thermal expansion (CTE) vs temperature of as-built IN625 samples built along x-y plane and z direction. 77

Figure 41: Tensile stress-strain curve for three as-built IN625 samples.........78

Figure 42: SEM images of as-built IN625 tensile fracture surface: a) low magnification exhibiting ductile and brittle fracture surfaces; b) higher magnification exhibiting brittle surface fractures; c) higher magnification showing fine dimples and microvoids...81

Figure 43: Brinell hardness of as-built and direct aged IN625 samples at 600 °C, 700 °C, 800 °C, 900 °C for 2 hours, 8 hours and 24 hours, respectively........82

Figure 44: OM images of direct aged IN625 samples at 600 °C for 2 h (a), 8 h (b) and 24 h (c) along the building direction; kalling's No.2 etchant was used.....84

Figure 45: OM images at high magnification of direct aged samples at 600 °C for 2 hour (a), 8 hours (b) and 24 hours (c) showing melt pools contours and fine dendritic structures. Kalling’s No.2 etchant was used..86

Figure 46: FESEM images of IN625 sample direct aged at 600 °C for 24 hours showing: a) melt pools contours (MPCs) and (GBs) of columnar grains; (b) higher magnification of a GBS and MPCs; (c) the dendritic structures and fine precipitates; (d) Dendrite structures and fine precipitates of as-built IN625 samples to compare with the aged condition. Kalling’s No.2 etchant was used..................................88

Figure 47: OM images of direct aged IN625 samples at 700 °C for 2 h (a), 8 h (b) and 24 h (c) along the building direction; kalling's No.2 etchant was used.....89

Figure 48: OM images at high magnification of direct aged samples at 700 °C for 2 hour (a), 8 hours (b) and 24 hours (c) showing melt pools contours and fine dendritic structures. Kalling’s No.2 etchant was used..90

Figure 49: FESEM images showing: (a) columnar grains and grain boundaries (GBs; (b) fine dendritic architectures and some elongated precipitates along the GBS; (c) the formation of very fine γ″ phases within the dendrite core; Kalling’s No.2 etchant was used. 92

Figure 50: TEM bright field images: c) exhibiting columnar dendrite architectures with high dislocation mainly in the interdendritic area and Nb-rich precipitates line indicated by orange oval; d) ellipsoidal γ″ phases......................93

Figure 51: Tensile stress curves of direct aged IN625 samples at 700 °C for 24 hours...94

Figure 52: SEM images of tensile fracture surfaces for the direct aged IN625 at 700 °C for 24 hours showing: a) ductile and brittle fracture surfaces; b) SEM image obtained in secondary and backscattering electrons exhibiting Cr-rich $M_{23}C_6$ carbides. 96

Figure 53 : OM images of direct aged IN625 samples at 800 °C for 2 h (a), 8 h (b) and 24 h (c) showing columnar grains along the building direction; kalling's No.2 etchant was used. 97

Figure 54: OM images at high magnification of direct aged samples at 700 °C for 2 hour (a), 8 hours (b) and 24 hours (c) showing gradually formation of inter/intragranular precipitates; Kalling’s No.2 etchant was used.........................99

Figure 55: FESEM images of IN625 sample direct aged at 800 °C for 24 hours showing: a) columnar grains with several precipitates throughout the material; b) δ phases indicated by arrow 1 and Laves phases pointed out by arrow 2; c) δ phases indicated by arrow 1 and fine spherical carbides (the same of as-built state). 100

Figure 56: EDS line of direct aged sample at 800 °C for 24 hours showing Laves phases enriched in Nb and Mo with respet to the austenitic matrix. 102

Figure 57: OM images of direct aged IN625 samples at 900 °C for 2 h (a), 8 h (b) and 24 h (c) along the building direction; Kalling's No.2 etchant was used..103

Figure 58: OM images at high magnification of direct aged IN625 samples at 800 °C for 2 h (a), 8 h (b) and 24 h (c) revealing the increment of precipitates correlate to longer thermal exposure; Kalling's No.2 etchant was used. 105

Figure 59: FESEM images of IN625 sample direct aged at 900 °C for 24 hours showing: a) columnar grains with a significant number of precipitates throughout the material, with the largest located along the grain boundaries (GBs); b) δ phases indicated by arrow 1 and Laves phases pointed out by arrow 2; c) magnificated view on δ phase and Laves phases indicated by arrow 1 and 2, respectively. Kalling’s No.2 etchant was used. 106

Figure 60 : Brinell hardness of as-built and SHT IN625 samples at 1000 °C and 1150 °C for 1 hour and 2 hours...108

Figure 61: OM images of SHT IN625 samples at 1000 °C for 1 h (a) and 2 h (b) showing a microstructure mostly consisted of equiaxed grains along the building direction; Kalling's No.2 etchant was used. 109

Figure 62: FESEM images of SHT IN625 sample at 1000 °C for 2 hours showing: a) equiaxed grains without the formation of coarse precipitates along the grain boundary (GB) and along the twin boundary (TB); (b) high magnification along a GB with presence of very fine precipitates. Kalling’s No.2 etchant was used. 110

Figure 63: OM images of SHT IN625 samples at 1150 °C for 1 hour (a) and 2 hours (b) showing equiaxed grains with twin boundaries. Kalling’s No.2 etchant was used. 111

Figure 64: FESEM images of SHT IN625 samples at 1150 °C for 2 hours showing: (a) equiaxed grains with grain boundary (GB) and twin boundary (TB) without coarse carbides; (b) (GB) areas with fine carbides. 112

Figure 65: TEM bright field images: (a) showing the austenitic matrix with low dislocation density; (b) Nb,Ti-rich MC carbides along the grain boundary (GB) indicated by arrow 1. 113

Figure 66: Coefficient of thermal expansion (CTE) vs temperature of SHT IN625 samples built along x-y plane and z direction. 114

Figure 67: XRD spectra of SHT IN625 samples along the z-axis and x-y plane. 116

Figure 68: Tensile stress curves of the SHT IN625 samples at 1150 °C for 2 h. 116

Figure 69: SEM images of SHT IN625 tensile fracture surfaces: a) low magnification showing fracture surfaces with microvoids; b) higher magnification exhibiting microvoids and fine dimples. 118

Figure 70: Brinell hardness values of solutionized (SHT at 1150 °C for 2 hours) and subsequent aged IN625 samples performed at 600 °C, 700 °C, 800 °C, 900 °C for 2 hours, 8 hours and 24 hours, respectively. 119

Figure 71: OM images of aged samples at 600 °C for 2 hour (a), 8 hours (b) and 24 hours (c) showing equiaxed grains with twin boundaries; Kalling’s No.2 etchant was used. 121

Figure 72: OM images of aged samples at 600 °C for 2 hour (a), 8 hours (b) and 24 hours (c) showing a starting precipitation along the grain boundaries; Kalling's No.2 etchant was used. 122

Figure 73: FESEM images of aged IN625 samples at 600 °C for 24 hours showing: (a) equiaxed grains without coarse carbides; (b) Grain boundary areas with fine elongated precipitates and very fine bright intergranular precipitates indicated by arrow 1; Kalling's No.2 etchant was used. 124

Figure 74: OM images of aged samples at 700 °C for 2 hour (a), 8 hours (b) and 24 hours (c) showing equiaxed grains with twin boundaries; Kalling's No.2 etchant was used. 125

Figure 75: OM images of aged samples at 600 °C for 2 hour (a), 8 hours (b) and 24 hours (c) showing a starting precipitation along the grain boundaries; Kalling's No.2 etchant was used. 126

Figure 76: FESEM images showing: (a) fine elongated precipitates along the grain boundaries; (b) fine elongated precipitates along the grain boundaries with inset showing MC carbides; (c) grain boundary with elongated precipitates and intragranular γ'' phases; Kalling's No.2 etchant was used. 128

Figure 77: TEM bright field images of aged IN625 sample at 700 °C for 24 hours showing: a) intergranular Cr-rich $M_{23}C_6$ carbide; b) intergranular Nb-rich phase; c) intragranular Nb,Ti rich-MC carbide; d) intragranular γ'' phases. 130

Figure 78: Tensile stress curves of aged IN625 samples at 700 °C for 24 hours. 131

Figure 79: SEM micrographs of aged IN625 tensile fracture surfaces: a) low magnification exhibiting mixed ductile and brittle fractures with secondary cracks; b) higher magnification exhibiting fine dimples as well as brittle fractures. 133

Figure 80: OM images of aged samples at 800 °C for 2 hour (a), 8 hours (b) and 24 hours (c) showing equiaxed grains and twin boundaries with some precipitates along and inside the grains; Kalling's No.2 etchant was used. 135

Figure 81: OM images of aged samples at 800 °C for 2 hour (a), 8 hours (b) and 24 hours (c) showing a starting precipitation within the grains and along the grain boundaries; Kalling's No.2 etchant was used. 136

Figure 82: - FESEM images showing: (a) inter/intragranular elongated precipitates; (b) intragranular acicular δ phases indicated by arrow 1 and intergranular elongated Laves phases indicated by arrow 2; (c) δ phases indicated by arrows 1 and fine Nb,Ti rich MC carbides formed during the solution treatment; Kalling's No.2 etchant was used..138

Figure 83: OM images of aged samples at 900 °C for 2 hour (a), 8 hours (b) and 24 hours (c) showing equiaxed grains and twin boundaries together with the formation of inter/intragranular phases; Kalling's No.2 etchant was used..........139

Figure 84: OM images of aged samples at 900 °C for 2 hour (a), 8 hours (b) and 24 hours (c) showing a starting precipitation within the grains and along the grain boundaries; Kalling's No.2 etchant was used...141

Figure 85: FESEM images of aged samples at 900 °c for 24 hours showing: (a) inter/intragranular elongated precipitates; (b) intragranular acicular δ phases indicated by arrow 1 and intergranular elongated Laves phases indicated by arrow 2; (c) Intergranular acicular δ phases and fine Nb,Ti-rich MC carbides; Kalling's No.2 etchant was used. 142

Figure 86: FESEM images of the IN625 powder particles at different magnifications (a,b), in which some satellite particles are pointed out by the yellow arrows...149

Figure 87: OM micrographs of mounted and polished IN625 particles at different magnification (a, b), highlighting the existence of internal spherical pores, some of which are indicated by red circles...150

Figure 88: Particle size distribution of IN625 powder obtained by means of laser granulometry diffraction with and without ultrasonic vibration [56]. 151

Figure 89: Brinell hardness vs residual porosity for as-built IN625 samples produced by DED process using different process parameters. 153

Figure 90: - OM micrographs of polished IN625 samples fabricated using different process parameters along the building direction showing: (a) R23 sample with the highest residual porosity and (b) R9 sample with the lowest residual porosity; both the micrographs exhibit different spherical pores, some of which are highlighted by red circles...156

Figure 91: Optical micrographs (a, b) of IN625 fabricated by DED process along the building direction at different showing: deposited layer boundaries (DLB), heat altered zone (HAZ), melt pools (MP), columnar dendrites (CDs), primary dendrite arm spacing (PDAS) and secondary dendrite arm spacing (SDAS); mixed acids etchant was used [56]. 157

Figure 92: FESEM images of IN625 fabricated by DED at different magnifications along the building direction showing: (a) PDAS and SDAS; (b) square voids indicated by arrows 1 in the dendritic areas; (c) square voids indicated by arrow 2 in the interdendritic areas; mixed acids etchant was used [56]. 159

Figure 93: FESEM images of IN625 fabricated by DED at different magnifications along the building direction showing: (a, b) Laves phases indicated by arrow 3, carbides indicated by arrow 4; (c) ellipsoidal precipitates indicated by arrow 5. Kalling’s No.2 etchant was used [56]. 160

Figure 94: FESEM images of IN625 fabricated by DED: a) microstructural image, b) Ni distribution map, c) Nb distribution map and d) Mo distribution map; Kalling’s No.2 etchant was used [56]. 161

Figure 95: XRD diffraction pattern of as-built IN625 sample along z-axis and x-y plane. 162

Figure 96: (a, b) FESEM images of gas atomised HX powder showing spherical, irregular particles and clusters. 165

Figure 97: OM images of mounted HX powder particles cross section polished at different magnification showing: (a, b) their morphology and size; (c, d) the dendritic structures after etching with Kalling's No.2 reagent. 166

Figure 98: Particle size distribution of frequency (a) and cumulative frequency (b) of particle size distribution obtained by laser granulometry diffraction. 167

Figure 99: OM images of polished as-built HX samples exhibiting microcracks and pores at different magnification along y-x plane (a, c) and z-y plane (b, d). 170

Figure 100: OM images of as-built HX samples showing: a) melt pool contours (MPCs) along the x-y plane, b) melt pools contours (MPCs) along the z-y plane; SEM images showing: c) randomly orientated grains pointed out by red dash line along the x-y plane; d) columnar grains indicated by red dash line along the z-y plane; e) microcracks mainly located along the grain boundaries indicated by yellow arrows along x-y plane; f) microcracks primarily located along the grain boundaries indicated by yellow arrows along the z-y plane; Kalling's No.2 etchant was used. 173

Figure 101: Graphically representation of the columnar grains along the z-y plane and the cross-sectioned columnar grain along the x-y plane. 174

Figure 102: (a) OM image of as-built HX samples showing the melt pools created by the laser beam along the x-y plane; (b, c, d, e) FESEM images of as-built HX samples along the x-y plane at different magnifications showing: (b) melt pools contours (MPCs); (c) fine primary dendritic structure; (d) primary cellular dendritic structures with nanometric precipitates; (e) primary columnar dendritic structures with nanometric precipitates; Kalling's No.2 etchant was used..........................176

Figure 103: XRD spectrum of as-built HX sample along the x-y plane.......177

Figure 104: Coefficient of thermal expansion (CTE) vs temperature of as-built HX sample. 178

Figure 105: Schematic diagram of cellular dendritic structures of as-built HX samples. The black spherical circle represents the Mo-rich M_6C carbides whereas the blue and dark blue areas represent the dendritic and interdendritic regions, respectively. Primary solidification showed a low fraction of carbides, the largest ones in the interdendritic areas. After more thermal cycle consisted of continuous remelting and resolidification coupled with continuous thermal flows dissipation the microstructure made up of a higher number of carbides with respect to the initial solidification. 179

Figure 106: Brinell hardness of as-built HX samples and SHT HX samples at 1175 °C for 15, 30 ,60 and 120 minutes. *All the SHT samples were water quenched. 181

Figure 107: OM images of SHT HX samples at 1175 °C for different times: (a) 1175 °C for 15 min; (b) 1175 °C for 30 min; (c) 1175 °C for 60 min; (d) 1175 °C for 120 min; Kalling's No.2 etchant was used. 183

Figure 108: OM images of SHT HX samples at different magnification showing the microcracks orientation along x-y plane (a) and along the z-y plane (b). 184

Figure 109: OM images of optimised SHT HX samples at 1175 °C for 1 hour showing: (a, b) equiaxed grains along x-y and z-y planes, respectively; (c, d) equiaxed grains and fine precipitates along x-y and z-y planes, respectively. Kalling's No.2 etchant was used. 186

Figure 110: FESEM images of optimised SHT HX samples along x-y plane showing: (a) the grain boundaries of equiaxed grains and M_6C carbides; (b) showing fine inter/intragranular M_6C carbides; Kalling's No.2 etchant was used. 187

Figure 111: XRD spectrum of optimised SHT HX samples showing the peaks of γ austenitic phase. 189

Figure 112: Coefficient of thermal expansion (CTE) vs temperature of SHT HX sample. 190

Figure 113: OM images of SHT HX samples at 1066 °C for 1 hour along x-y plane showing (a, b) melt pool countours (MPCs) and a starting recrystallization; FESEM images showing (c, d) Mo-rich M_6C carbides mainly located along the grain boundaries and cracks. Kalling's No.2 etchant was used. 192

Figure 114: Brinell hardness of SHT samples and heat-treated HX samples for different times at 745 °C (SHT + 745 °C represented with red colour) and 788 °C (SHT + 788 °C associated with blue colour). 193

Figure 115: Microstructure of SHT +745 °C 3 h HX sample showing:(a) OM image of equiaxed grains with $M_{23}C_6$ carbides at grain boundaries; (b, c) FESEM images exhibiting $M_{23}C_6$ carbides along the grain boundaries. 195

Figure 116: Microstructure of SHT +745 °C 6 h HX sample showing:(a) OM image of equiaxed grains with $M_{23}C_6$ carbides at grain boundaries; (b, c) FESEM images exhibiting $M_{23}C_6$ carbides along the grain boundaries. 196

Figure 117: (a) OM image of SHT + 745 °C 200 h HX sample showing equiaxed grains with a significant fraction of precipitates; (b) FESEM image of SHT + 745 °C 200 h HX sample showing the precipitates morphology. 197

Figure 118 : XRD spectra of SHT HX samples heat-treated at 745 °C for 3,6 and 200 hours showing the peaks of γ austenitic phase. 199

Figure 119: Microstructure of SHT +788 °C 3 h HX samples showing:(a) OM image of equiaxed grains with $M_{23}C_6$ carbides at grain boundaries; (b, c) FESEM images exhibiting $M_{23}C_6$ carbides along the grain boundaries. 200

Figure 120: Microstructure of SHT +788 °C 6 h HX samples showing:(a) OM image of equiaxed grains with $M_{23}C_6$ carbides at grain boundaries; (b,c) FESEM images exhibiting $M_{23}C_6$ carbides along the grain boundaries. 202

Figure 121: (a) OM image of SHT + 788 °C 200 h HX samples showing equiaxed grains with a significant fraction of precipitates; (b) FESEM image of SHT + 788 °C 200 h HX sample showing the precipitates morphology. 203

Figure 122: XRD spectra of SHT HX samples heat treated at 788 °C for 3, 6 and 200 hours showing the peaks of γ austenitic phase. 205

Figure 123: SEM images of extracted carbides from: (a) SHT + 745 °C 6 h HX samples and (b) SHT + 788 °C 6 h HX samples; the extracted carbides were deposited on a glass fiber filter. 206

Figure 124: XRD spectra of extracted carbides from SHT HX samples + 745 °C 6 h and SHT HX samples + 788 °C for 6 h. 208

Figure 125: OM images of HIPed HX samples along x-y and z-y planes showing (a, b) grain boundaries (GBs) and very small spherical pores. 209

Figure 126: OM images of HIPed HX samples showing (a, b) equiaxed grains along x-y and z-y planes respectively; (c, d) the carbides along the grain boundaries and within the grains along x-y and z-y planes, respectively. Kalling's No.2 etchant was used. 211

Figure 127: FESEM images of HIPed HX samples showing: (a) equiaxed grains with carbides along the grain boundaries and inside the grains; (b) the morphology of the Mo-rich M_6C and Cr-rich $M_{23}C_6$ carbides; Kalling's No.2 etchant was used. 212

Figure 128: SEM images showing: (a) residual of austenitic matrix; (b) Mo-rich M_6C carbides and Cr-rich $M_{23}C_6$ carbides. 213

Figure 129: XRD diffraction patterns of HIPed HX sample (along x-y plane) and extracted carbides from HIPed samples. 215

Figure 130: Coefficient of thermal expansion (CTE) vs temperature of HIPed HX sample. 216

Figure 131: Brinell hardness values of HIPed and HIPed+SHT samples at 1175 °C for 15, 30, 60 and 120 minutes. 217

Figure 132: OM images of HIPed+SHT samples (at 1175 °C for 30 minutes) at different magnifications showing (a, b) the very few pores along x-y and z-y planes, with inset of a spherical pore; (c,d) the equiaxed grains and carbides along x-y and z-y planes; (e, f) the formation of carbides inside the materials; the samples was etched with Kalling'n No.2 reagent. 220

Figure 133: FESEM images of optimised HIPed+SHT samples at (1175 °C for 30 min) showing (a, b) very fine inter/intragranular Mo-rich M_6C carbides, where a intragranular Mo-rich M_6C carbides is indicated by the yellow arrow 1; Kalling's No.2 reagent was used. 221

Figure 134: XRD spectrum of optimised HIPed+SHT HX samples. 223

Figure 135: Coefficient of thermal expansion (CTE) vs temperature of HIPed+SHT HX sample. 224

Figure 136: (a, b) OM images of HIPed+SHT samples at 1066 °C for 1 hour exhibiting equiaxed grains and carbides along x-y plane; (c, d) FESEM images of HIPed+SHT samples at 1066 °C for 1 hour showing the morphology and size of Mo-rich M_6C carbides. Kalling's No.2 etchant was used. 226

List of Tables

Table 1: Classification of some superalloys [1,2]. 2

Table 2: Characteristic of typically carbides observed in superalloys [3]. 10

Table 3: Effect of alloying elements in superalloys [3]. 16

Table 4: Common annealing treatments for wrought superalloys [3]. 17

Table 5: Common SHT treatments for wrought superalloys [3]. 18

Table 6: Common ageing treatments for wrought superalloys [3]. 20

Table 7 : Common stress relieving treatments for wrought superalloys [3]. .. 21

Table 8: Chemical requirement for IN625 alloy according to UNS N06625 specification. 22

Table 9: Minimum tensile properties of IN625 alloys according to ASTM B443 and tensile properties of wrought and cast IN625 alloys; yield strength (YS), ultimate tensile strength (UTS) and elongation (A). 23

Table 10: Chemical requirement for HX alloy according to UNS N06002. ... 25

Table 11: Minimum tensile properties of HX alloys according to ASTM B435 and tensile properties of some SHT wrought HX alloys. 26

Table 12: List of the main Ni-based superalloys produced by LPBF and DED processes. 28

Table 13: Technical available data of EOS M270 and EOS M280 devices [106–109]. 44

Table 14 : Process parameters values used for building LPBF-IN625 specimens. 46

Table 15: Different process parameters and energy density used for building DED-IN625 specimens. 49

Table 16: Nominal chemical composition of IN625 powder [110]. 50

Table 17: Nominal chemical composition declared by the company [111]. ... 50

Table 18: Chemical composition in weight percentage (wt%) of HX powder declared by the company [112]..51

Table 19: EDS results of main chemical elements in weight percentage (wt %) for LPBF IN625 powder compared to company datasheet and standard UNS N06625..64

Table 20: Average value and standard deviation of Apparent density, Flowability and Skeletal density for IN625 powder. 65

Table 21: Different process parameters and energy density used for fabricating IN625 specimens with the determined residual porosity and hardness [56]. 67

Table 22: Average CTE for as-built IN625 samples and commercially available IN625 alloy at different temperatures. 77

Table 23: Average K for as-built samples and commercially available IN625 alloy at different temperatures. 78

Table 24: Comparison of tensile properties of as-built specimens fabricated along the x-y plane, together with other LPBF-built IN625 along the x-y plane reported in other works and specifications as well as wrought IN625 alloys........80

Table 25: Brinell hardness values of direct aged IN625 samples; starting condition 285 ± 3 HBW of as-built IN625 samples. 83

Table 26: Comparison of tensile properties of as-built, direct aged at 700 °c for 24 hours, to other LPBF-built IN625 along the x-y plane reported in literature and wrought IN625 alloys. 95

Table 27: EDS results of the Laves phase and austenitic matrix for the direct aged IN625 sample at 800 °c for 24 hours...101

Table 28: EDS results of the Laves phase and austenitic matrix for direct aged sample at 900 °C for 24 hours. 107

Table 29: Brinell hardness values of SHT IN625 samples; starting condition 285 ± 3 HBW of as-built IN625 samples. 108

Table 30: Average CTE for SHT IN625 samples and commercially available IN625 alloy at different temperatures. 115

Table 31: Comparison of tensile properties of as-built and SHT IN625 samples at 1150 °C for 2 hours to SHT wrought IN625 according to ASTM B443 as well as data commercially available. 117

Table 32: Brinell hardness values of aged IN625 samples; starting condition 189 ± 3 HBW of SHT IN625 samples. 120

Table 33: Comparison of tensile properties of as-built, SHT, aged IN625 samples built along the x-y plane. 132

Table 34: EDS results of Laves phase and austenitic phase for the aged IN625 sample at 800 °C for 24 hours. 138

Table 35: EDS results of Laves phase and austenitic phase for aged IN625 samples at 900 °C for 24 hours. 143

Table 36: Strain hardening parameters as calculated on IN625 samples for as-built (AB) direct aged (700 °C for 24 hours), SHT (1150 °C for 2 hours) and aged (700 °C for 24 hours) IN625 samples. 143

Table 37: EDS results of main chemical elements reported in weight percentage (wt %) for IN625 powder compared to company datasheet and standard UNS N06625 151

Table 38: Average value and standard deviation of Apparent density, Flowability and Skeletal density for DED IN625 powder[56]. 152

Table 39: Different process parameters and energy density used for producing IN625 specimens with the correlate obtained residual porosity and hardness values [56]. 154

Table 40: EDS results in weight percentage of austenitic matrix and Laves phase for the IN625 samples produced by DED [56]. 161

Table 41: Chemical composition in weight percentage (wt%) of HX powder and solid samples determined by ICP/OES and IGF analyses compared to the supplier datasheet and the chemical composition requirements reported in the ASTM B435-16 standard. 168

Table 42: Residual porosity and cracking density of as-built HX samples along the x-y and z-y planes. 170

Table 43: The ASTM grain size number G and corresponding grain size of SHT HX samples. 181

Table 44: Residual porosity and cracking density of optimised SHT HX samples along x-y and z-y planes. 184

Table 45: EDS results of the γ austenitic matrix and Mo-rich M_6C carbide for optimised SHT HX sample. 188

Table 46: EDS results of the γ austenitic matrix and Mo-rich M_6C carbides for SHT HX samples at 1066 °C for 1 hour. 192

Table 47: EDS values of γ austenitic matrix and precipitates of prolonged heat-treated HX samples at 745 °C for 200 h. 198

Table 48: EDS results of SHT heat-treated at 788 °C for 200 h HX samples. 203

Table 49: EDS results on Cr-rich $M_{23}C_6$ carbides for extracted carbides form SHT + 745 °C 6 h and SHT + 788 °C 6 h HX samples. 206

Table 50: Residual porosity and cracking density of HIPed HX samples along x-y and z-y planes. 209

Table 51: EDS results of austenitic matrix, a Mo-rich M_6C carbide and a Cr-rich $M_{23}C_6$ carbide. 214

Table 52: Residual porosity and cracking density of HIPed+SHT HX samples along x-y and z-y planes. 220

Table 53: EDS results of γ austenitic matrix and Mo-rich M_{6C} carbide for optimised HIPed+SHT HX sample. 221

Table 54: EDS results of γ austenitic matrix and Mo-rich M_6C carbides for HIPed+SHT HX sample at 1066 °C for 1 hour. 226

Chapter 1

Introduction

This chapter gives a review of the significant literature on the basics metallurgy of superalloys, considering in detail the characteristic of Hastelloy X (HX) and Inconel 625 (IN625) alloys.

The chapter further presents the microstructures of Ni-based superalloys by two laser additive techniques, laser powder bed fusion (LPBF) and directed energy deposition (DED), also indicating the main advantages and drawbacks.

1.1 Categories of superalloys

Superalloys can be commonly divided into three primary categories:

- Fe,Ni-based alloys;
- Ni-based alloys;
- Co-based alloys;

The classification of some superalloys is provided in Table 1.

Table 1*:* Classification of some superalloys [1,2].

Ni-based	**Fe,Ni-based**	**Co-based**
Inconel (600,617,625,718)	Incoloy (800,801,802,825,903)	Haynes 188
Nimonic (75,80A,90)	A-286	L-605
Rene (41,95)	Alloy 901	MAR-M918
Astroloy	Discaloy	MP35N
Hastelloy (X,C-22,G-30)	Haynes 556	MP159
Waspaloy	H-155	Stellite 6B
Haynes 230	N-155	J-1570

All the type of superalloys share a common basic microstructure, which consists of an austenitic (γ) matrix with face-centered cubic (fcc) crystal structure, coupled with different dispersed secondary phases [1–4].

Ni-based superalloys are characterised by high strength at high-temperature, which is excellent for the production of turbine blades and disks for aircraft or industrial gas turbine parts. According to the application, they can be used as both cast and wrought conditions. Wrought processes produce materials with higher ductility and toughness than cast alloys, whereas cast alloys have larger grains than wrought alloys, resulting in enhanced creep resistance. Therefore, wrought Ni-based superalloys are frequently used for the fabrication of turbine discs and forged blades. For instance, some wrought Ni-based alloys are Udimet 700, Rene 41, Waspaloy, N-901, and Udimet 630. Differently castings Ni-based superalloys are used for high-temperature applications, as investment-cast turbine blades. Some cast Ni-based alloys are represented by Inconel 713 and 738 alloys, or MAR-M200. The Ni-based superalloys can be mainly reinforced by solid solution strengthening or by precipitation strengthening mechanisms [2,4].

Fe,Ni-based superalloys are mainly used in application such as turbine discs or forged rotors, in which high toughness and ductility are required. For these reasons, they are mainly used as wrought state, which is considered more ductile than cast materials, as mentioned before. These superalloys are cheaper than other types of superalloys, owing to the large quantity of Fe added. Also in this case, they can be solid solution strengthened or precipitation strengthened alloys [3].

Finally, Co-based superalloys are often used for components that require high hot corrosion resistance or low-stress structural applications at moderate to high temperatures, such as vanes or other components in gas turbine engines. These alloys are fabricated by both cast or wrought processes, depending on the mechanical characteristics required. For instance, some alloys are X-40, MAR-M 302, Haynes 188. These alloys are mainly solid solution strengthened alloys, and they are only reinforced by carbides, having a less strengthening effect with respect to γ′ and γ″ phases [2,4]. However, an exception is J-1570 alloy, which presents strengthening from Ni_3Ti precipitation, although it is not a valid alternative to precipitation hardened Ni-based superalloys [2].

The research presented in this thesis deals with HX and IN625 alloys, which are two solid solution strengthened Ni-based superalloys. However, the mechanical properties of these alloys can drastically change, mainly due to the formation of carbides for HX alloy and several phases such as carbides, gamma double prime (γ″) phases as well as delta (δ) phases for IN625 alloy, during service at high temperature or heat treatments. The formation of these phases can have both a positive or adverse effect on their mechanical properties depending on their size, shape, and position inside the alloys [5,6].

1.1.1 Solid solution strengthened superalloys

Solid solution strengthening mechanism derives from the addition of different soluble elements. These elements distort the lattice parameters of the matrix due to the different atomic radius, hindering the dislocation movement. Therefore, solid solution strengthening is correlated to the atomic size difference, generally up to a maximum difference of around 10 % in atomic size [2]. In order to create greater lattice distortion and reduce diffusion, high melting point elements are added.

Solid solution strengthening decreases the stacking fault energy in the crystal lattice, resulting in inhibition of dislocation cross slip, which is the primary deformation mode in imperfect crystals at high temperatures [2]. A lower stacking fault energy makes it more arduous for dislocations to alter the directions. In this way, when a dislocation hits a barrier, it is more laborious for the dislocation to be able to bypass that barrier by moving onto a new slip plane [3].

Regarding the fcc structures, the low stacking fault energy of superalloys bring to three connected effects:

- Dissociation of dislocations into partials;
- Generation of hexagonally close-packed (hcp) stacking fault ribbons;
- Improved adversity of movement of dislocations from fcc matrix to hexagonal close-packed (hcp) fault;

Finally, atomic clustering or short-range order can also reinforce the matrix. The effect is attributed to the electronic orbitals, and it is more intense for some elements such as Mo, W, Cr and Al, involving an enhanced hardening impact on the austenitic matrix, compared with Fe, Ti, Co, V [2]. Strengthening effect due to short-range order decreases rapidly above about 60 % of the absolute melting temperature ($0.6T_m$) due to the enhancement of diffusion mechanisms.

In fact, above this temperature ($0.6T_m$), creep and strength are significantly influenced by diffusion, reducing the mechanical properties. In this case, the use of heavy elements is suitable thanks to their lower diffusion rates, but they also tend to increase alloy density and provoke the formation of detrimental phases, mainly located in interdendritic or grain boundary areas [2].

1.1.2 Precipitation strengthened superalloys

By precipitation strengthening mechanism, it is possible to increase the mechanical properties and creep strength of alloys for elevated temperature applications.

In the case of Ni-based superalloys, the addition of elements such as Al, Ti and Nb promote the formation of strengthened phases. Two of the most significant coherent precipitates are intermetallic compounds γ'-$Ni_3(Ti,Al)$ or γ''-Ni_3Nb phase, which can hinder the movement of dislocations. In this case, the movement of a dislocation within the austenitic matrix can occur by cutting through or by overtaking the particles. However, the precipitates should have a precise characteristic to provide a reinforcing effect [2,7]:

- Coherency strains between the austenitic matrix (γ) and the formed phases (γ', γ'');
- Antiphase-boundary (APB) energy correlated to an ordered precipitate (γ', γ''); The APB denotes the energy necessary to the dislocation to cut through the ordered precipitate because cutting could result in disordering between the matrix and precipitate.
- Volume fraction of the precipitate (γ', γ'');
- Particle size;

The strengthening obtained using coherent strains and ordering increases with particle size since these two mechanisms require that dislocations cut through the particle.

However, the increment in strength coupled with increasing particle size is restricted by Orowan bowing, where the dislocation will bypass too large particle. The strengthening effect, in this case, is given by the extra work needed for the dislocation to alter its path [2,7].

1.2 Phases formed

The following paragraphs will describe the main precipitates present within the superalloys.

1.2.1 Gamma prime (γ′) phase

γ′ $Ni_3(Al,Ti)$ phase is considered one of the most important strengthening phase in a significant number of Ni,Fe and Ni-based superalloys [2,3,8]. γ′ is an fcc intermetallic compound, showing coherency with the γ matrix. Typically, γ′ phases are dispersed throughout the matrix, strengthening the alloys by means of Orowan mechanism. Even though, elevated thermal exposures can promote the formation of intergranular film of γ′ phase, which can play a role in avoiding the grain growth for prolonged thermal exposures [2,9]. The morphology of this phase is strongly correlated to the lattice mismatch that depends on heat treatment and chemical composition. A lattice mismatch difference from 0 % to 0.2 % involves spherical precipitate (Figure 1a); between 0.5 % and 1.0 %, a cuboidal precipitate (Figure 1b); over 1.25 %, a plate-like precipitate (Figure 1c) [8,9].

The spherical shape reduces the surface energy, but when the lattice mismatch becomes larger, the change to cuboidal morphology stemmed from the necessity to minimise elastic energy [8]. The lattice parameter of the γ matrix increases more drastically with increasing temperature than the lattice parameter of the γ′ phase, thus generating a progressively negative lattice mismatch at high temperatures where creep is an issue [10]. The higher lattice mismatch between γ/γ′ enhances creep life in single-crystal Ni-based superalloys since the γ/γ′ interface is a barrier to mobile dislocations [8].

As the lattice mismatch is further increased, the interfacial dislocations become more strictly spaced and act as a vigorous barrier to mobile dislocations shearing through the interface. Besides, the dimension of the γ′ phase is also fundamental to give remarkable precipitation hardening, because the hardening normally improves with particle size, until the particle reaches a critical size. However, it is important to avoid temperatures superior to around $0.6T_m$ and superior to the solvus temperature of γ′ phase. In the first case, the temperature involves a coarsening effect on γ′ phase, making easier the dislocation bypassing, whereas in the other case, the temperature dissolves the γ′ phases. In both cases, the thermal exposures cause a reduction of mechanical properties.

Finally, it is interesting to note that for superalloys with high Ti/Al ratios, γ′ phase tends to transform into η phase for continued service at high temperature. This last phase has a hcp structure and can form intergranular cellular shape or intragranular acicular platelets in a Widmanstätten pattern [2].

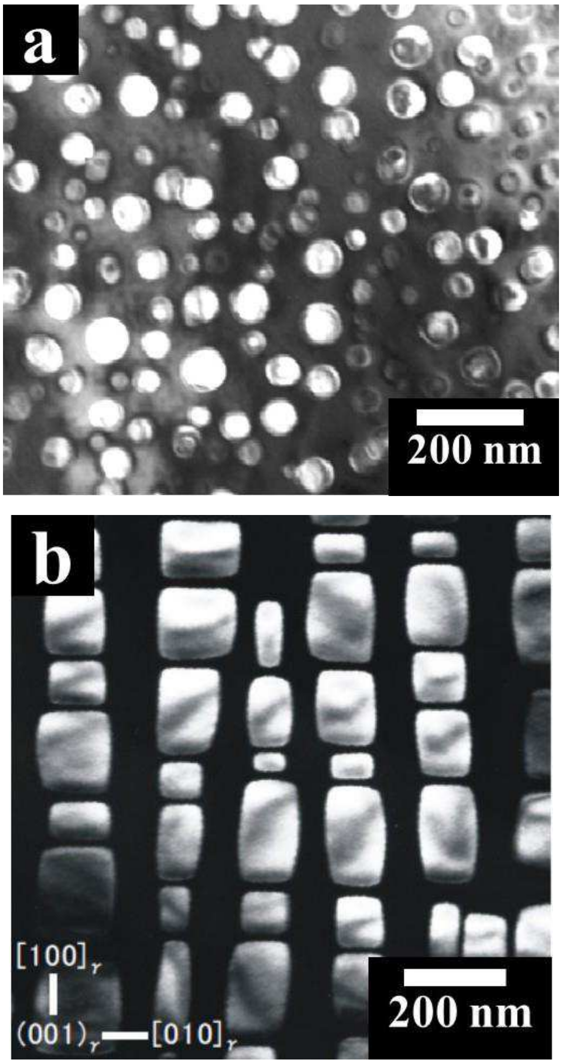

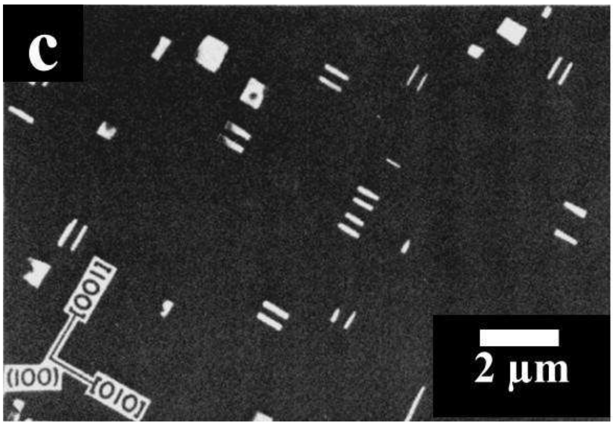

Figure 1 - TEM images showing different γ′ phase shapes: (a) fine spherical γ′ phases within Inconel 718 plus alloy [11], (b) cuboidal γ′ phases along <100> direction within a Ni-8.5Al-5.4Ti alloy [12], (c) plate-like γ′ phases within Ni-12at%Al alloy [13].

1.2.2 Gamma double prime (γ″) and δ phases

γ″ Ni_3Nb precipitate is the main strengthening phase for superalloys rich in Nb, such as Inconel 718 and 625 alloys. This phase presents a coherent body-centred tetragonal (bct) exhibiting a disc-shaped morphology (Figures 2a and 2b), generally with a thickness of 10 nm and a diameter of 50 nm [3]. This phase is usually scattered throughout the austenitic matrix with nanometric size, strengthening the alloys by means of Orowan mechanism [2,5,14].

For these alloys, the heat treatments must be correctly tailored to ensure the formation of γ″ phases instead of δ (Ni_3Nb) phases. In fact, this precipitate is metastable, and for prolonged thermal exposures, typically higher than 650 °C [2,15], γ″ phase is transformed in acicular orthorhombic δ phase (Figure 2c), leading to a severe degradation of the mechanical properties [5]. In this last case, it is necessary to perform heat treatment above the δ solvus (around 1000 °C), in order to increase the mechanical properties. However, the formation of a small amounts of δ phases can also have a positive effect to control the grain growth, and so improving tensile properties and fatigue resistance [3].

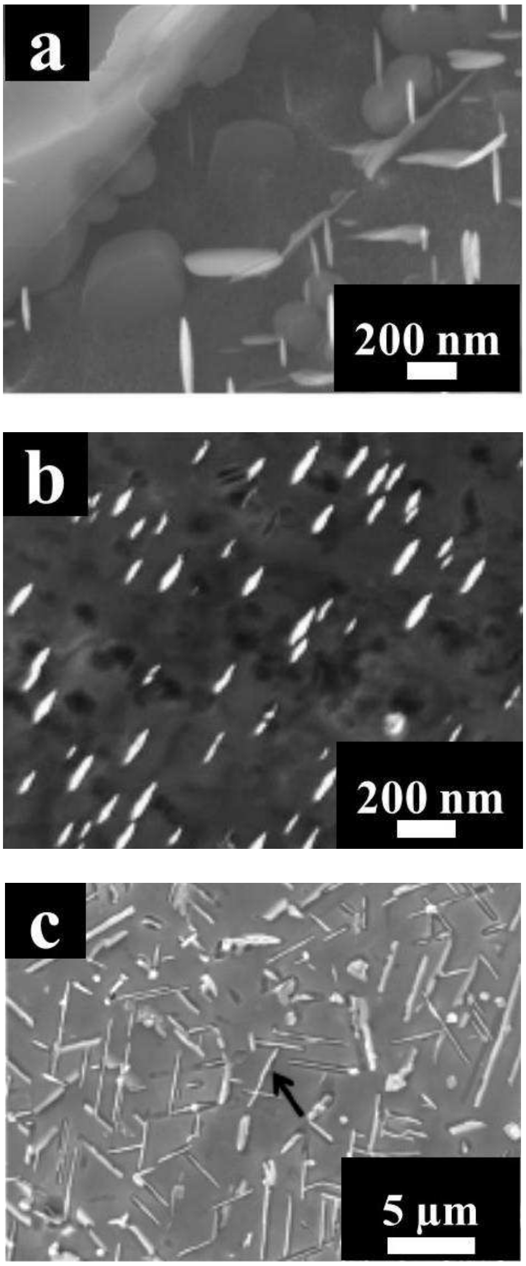

Figure 2: (a) FESEM image of IN625 alloy showing disc-shaped γ″ phases after thermal exposure at 700 °C for 1000 hours [15]; (b) TEM image of IN625 alloys showing γ″ phases after ageing at 700 °C for 100 hours [16]; (c) FESEM image of IN625 alloys showing acicular δ phases after thermal exposures at 800 °C for 1000 hours [15].

1.2.3 Carbides

The morphology, size and position of the carbides play an important factor for improving or decreasing the mechanical properties of the superalloys, especially at elevated temperatures [2]. Carbides are commonly present in all kinds of superalloys, and they tend to form mainly along the grain boundaries and twin boundaries, generating film of carbides or fine inter/intragranular disperse carbides, during thermal exposures. In the first case, this type of morphology render the alloy affected to brittle intergranular fracture. On the contrary, in the second case, they hinder the movement of dislocation hardening the alloy (Orowan mechanism), and in particular fine intergranular carbides can also obstruct the grain boundary slip during creep, and inhibit the grain growth during thermal exposures [2,17,18].

It is possible to distinguish between primary carbides, which are generated during the solidification process, and secondary carbides, which are formed during thermal exposures [3]. The primary carbides commonly assume the formula of MC and M_6C, with “M” indicating several elements, as reported in Table 2 [2,3]. Primary MC carbides mainly present fcc crystal structure, where “M” can be Nb, Ti, Ta, W, which are formed as discrete blocky particles or as eutectic phases during casting solidification. During the solidification process, these carbides form as various particles scattered throughout the material, within intragranular and intergranular regions. Besides, thermal exposures over 1038 °C can provoke the formation of secondary MC carbides, having the same shape of primary MC carbides [3]. Primary M_6C carbides having fcc crystal structure, where M is predominantly rich in refractory elements such as Mo and W, commonly form blocky particles along the grain boundaries [2,3]. Thermal exposure commonly between 816 and 982 °C can promote the formation of secondary M_6C carbides, when the concentration of Mo plus W is around 6-8 at % for Ni-based superalloys and about 4-6 at % for Co-based superalloys [2,19]. However, the decomposition of primary W-rich MC carbides can generate areas rich in W, reaching the condition to form secondary M_6C carbides, for alloys with a low level of Mo and W. Furthermore, M_6C carbides are more beneficial to control the grain size during processing of wrought alloys than other types of carbides [2,3]. During thermal exposure, the decomposition of MC carbides can result in the formation of $M_{23}C_6$ carbides, which is a Cr-rich carbide (M predominately consisted of Cr).

The $M_{23}C_6$ carbides is generally formed for thermal exposures around 790-816 °C, and they can form film of carbides along the grain boundaries, generating brittle areas that represent a favourite path for crack growth, leading to a decrease in stress-rupture strength and ductility, as mentioned before. Besides, the formation of this type of carbides cause depletion of Cr within the austenitic matrix, reducing the corrosion resistance, involving intergranular stress corrosion cracking, so their amount and size must be controlled. Differently, it is also possible to have dispersing fine intra/intergranular $M_{23}C_6$ carbides, which can reinforce the material. However, at high temperatures, $M_{23}C_6$ carbides also can form agglomerates, generating some coarse carbides on the grain boundary, promoting crack initiation sites [2,3].

Finally, among other types of carbides, it is possible to mention, the secondary Cr-rich M_7C_3 carbides, which are generally intergranular carbides having discontinuous blocky particle shape. This carbides has been observed only observed in some Co-based superalloys and in Nimonic 80A for heat treatment over 999 °C [2,3,19].

The formation of carbides during thermal exposure clearly can reduce the amount of different elements such as Nb, Mo and W within the austenitic matrix, generating areas depleted of these elements. In a similar condition, the stresses may be dissipated along these depleted areas close to the grain boundaries, instead of along the intergranular carbides [2]. It should be noted that there are other type of carbides M_xC_y in superalloys, which derive from different coefficient of “x” and “y”. For instance, the carbides from M_3C to $M_{13}C$ are typically reported as M_6C, because it is difficult to distinguish among them, due to similar characteristics [20].

The main characteristic of the different carbides reported above are listed in Table 2, while some micrographs of carbides in superalloys are shown in Figures 3.

Table 2*:* Characteristic of typically carbides observed in superalloys [3].

Phase	**Crystal structure**	**M elements**	**Temperature (°C)**
MC	Cubic	M is Ti, Nb, Ta, Hf, Th, Zr with some solubility for Ni, Zr, Mo	Over 1038
$M_{23}C_6$	Fcc	M is mainly Cr with some solubility for Ni, Co, Fe, Mo and W	790 – 816

M_6C	Fcc	M is mainly Mo and W with some solubility for Cr, Ni, Nb, Fe, Ta and Co.	816 - 982
M_7C_3	hexagonal	M is generally Cr	Over 999

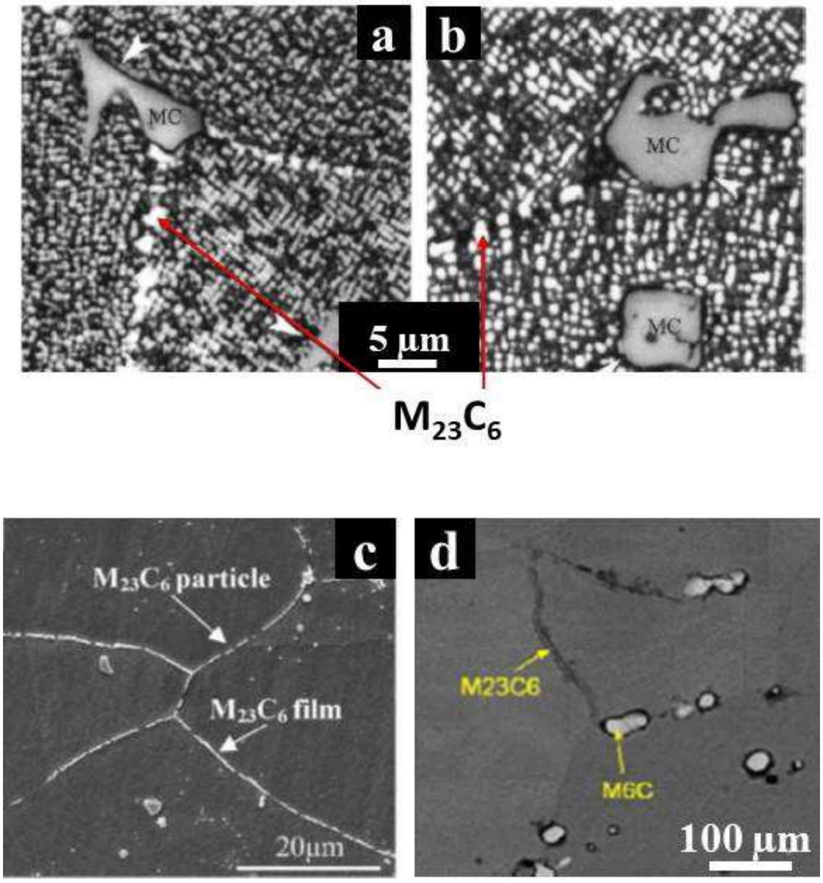
a
b
MC
MC
MC
5 µm
M₂₃C₆
c
d
M₂₃C₆ particle
M₂₃C₆ film
20µm
M23C6
M6C
100 µm

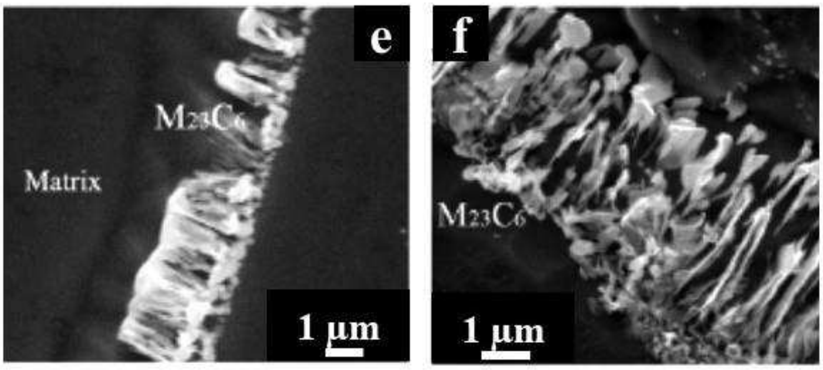

Figure 3:(a,b) OM image of Inconel 738 showing MC and $M_{23}C_6$ carbides adapted from [21]; (c) FESEM image of GH984 alloy showing intergranular particle and film of $M_{23}C_6$ carbides adapted from [22]; (d) FESEM image of HX alloy showing M_6C and $M_{23}C_6$ carbides adapted from [23]; (e,f) SEM images of Ni-Cr-W alloys showing intergranular $M_{23}C_6$ carbides adapted from [24].

1.2.4 Borides

Borides are hard refractory phases, with blocky or half-moon shapes. These particles are typically formed at grain boundaries since B has low solubility in the matrix and so tends to segregate at grain boundaries. Borides are formed in Ni-Fe, and Ni-based superalloys with a concentration of B superior to 0.03 % wt and they can reinforce the alloy similarly to carbides [2]. Boride typically revealed in superalloys are M_3B_2 borides having tetragonal crystal structures, and they can be rich in Mo, Ta, Nb, Ni, Fe or V. Even though B content is closely checked in superalloys, borides are reported in brazed joints of superalloys when low melting-point Ni-Cr-B brazing alloys are employed [2,24]. It is reported that the very low concentration of B (a few part for million) can promote the cracking of the heat affected zone in the welding of Ni-based superalloys [2,24].

1.2.5 Sulfocarbides

S has been reported to be extremely harmful to the stress-rupture life of Ni-based alloys for quantity around superior to 50 ppm [2]. This chemical element highly segregates to grain boundaries and particularly to carbide-matrix interfaces [25]. The presence of S and C can result in the generation of sulfocarbides (M_2SC), which have been noted in the interdendritic zones of cast alloys in both plate and hexagonal forms [3,26]. The M_2SC exhibits a hexagonal crystal structure, with small lattice mismatch to the fcc structure of MC carbides, and these particles can provoke cracks propagation. However, it is more detrimental the presence of S element within the grain boundaries than sulfocarbides [26].

1.2.6 Nitrides

Among the most common nitrides in superalloys, it is possible to find TiN, HfN, and NbN, with square or rectangular shapes, having cubic crystal structure [2,3]. Nitrides form in the liquid phase just before solidification, and they are nucleation sites both for primary MC carbides and for grains [27–29]. Therefore, the presence of nitride can compromise the directionally solidified alloys [27]. Nevertheless, they are usually present in small amounts, without having significant effect on mechanical properties [2]. The Nitrides are insoluble to the melting point of the alloy, and consequently, they are not influenced by heat treatment [2].

1.2.7 Topologically Close-Packed Phases

Topologically close-packed (TCP) are frequently plate-like or needle-like phases, which are harmful phases, and extensive effort has been made to avoid compositional ranges, that can provoke their significant formation during service or thermal exposures. The internal structure of these phases consisted of atoms, which are close-packed in layers that are separated by intervening layers of relatively large atoms. The TCP phases typically found in superalloys include σ-AxBy, μ-Ax′By′, and Laves-A_2B phases, where A is Fe, Ni or Co, and B is Nb, Mo, Ta, Cr.

σ phase is commonly reported in Fe-Ni and Co-based superalloys for prolonged thermal exposure from 540 °C to 980 °C, whereas it is rarely found in Ni-based superalloys, having tetragonal crystal structure. The phase has typically irregularly shaped globules, or elongated forms and it could be exchanged for $M_{23}C_6$ carbides [2,3,30].

μ phases is found in alloys enriched in Mo or W for prolonged thermal exposures, they have typically a rhombohedral crystal structure. This phase can exhibit coarse, irregular Widmanstatten platelets shapes, revealing a morphology similar to M_6C carbides [2].

Finally, Laves phases are typical in Fe-Ni base and Co-based superalloys, having hexagonal crystal structure, that appears as irregularly shaped globules, or as platelets after prolonged thermal exposures. This phase can be both formed by eutectic reaction in Nb-rich superalloys or for prolonged thermal exposures at high temperature (approximately around 727-1093 °C) [3,31,32].

These brittle phases tend to form along the grain boundaries acting as an obstacle to dislocation motion, which results in dislocation pile-ups at the precipitate interface, reducing the cohesion at the interface, thus promoting crack initiation. As a result, their formation can drastically reduce rupture strength and elongation at break as well as creep resistance [2,14,33]. Besides, these phases consume a high percentage of refractory elements such as Mo and W, which lessen the austenitic matrix of such solid-solution-hardening elements. The formation of tcp phases can be reduced by acting on the chemical compositions, tailoring the concentration of Cr, Mo, and W [2].

Some techniques have been studied to determine the susceptibility of any particular alloy to tcp-phase formation. For instance, the electron vacancy method (Nv), embodied in PHACOMP [14], has been used to determine σ, μ, and Laves phases formation in superalloys [2,34]. This method considers the correlation between tcp-phase precipitation and the number of electron vacancies in the γ matrix. Ni,Fe-based superalloys reveal a greater tendency to form tcp phases since the electronic structure of Fe has four vacant d sites and this structure tend to form intermetallic with extremely low interatomic distances, i.e., the Laves and σ phases [2]. Figures 4a, 4b and 4c show some examples of the morphology of σ, μ and Laves phases, respectively.

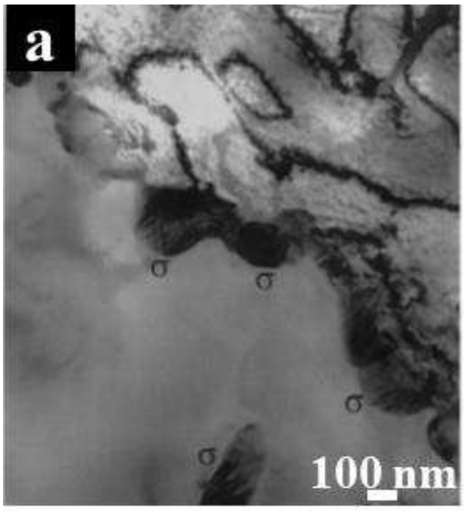

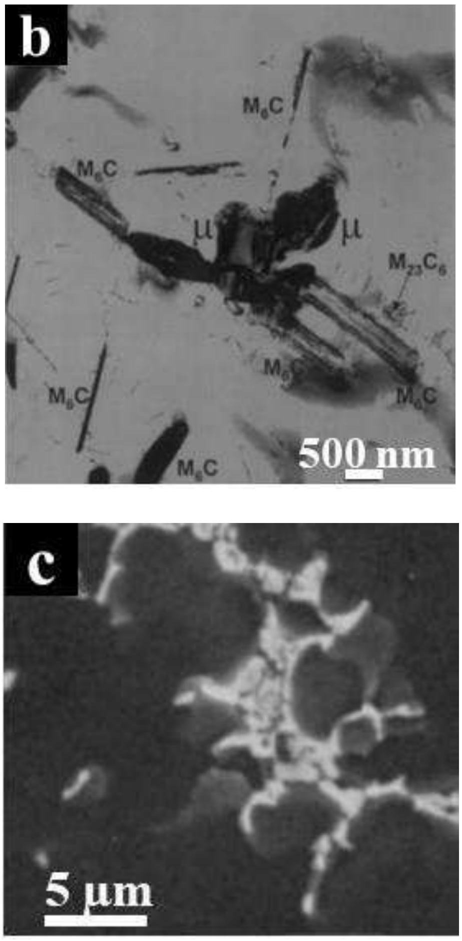

Figure 4: (a) TEM image of HX alloy showing intergranular σ phases adapted from [20]; (b) TEM images of HX ally exhibiting M_6C, $M_{23}C_6$ carbides and μ phases adapted from [20]; (c) FESEM image of IN625 plus alloy showing Laves phases with eutectic-like morphology [35].

1.3 Effect of the specific elements within superalloys

The base elements in superalloys are crucial in determining its microstructural evolution and properties, such as tensile strengths and corrosion resistance. Superalloys contain a large combination of chemical elements in order to generate the desired properties [2,3].

The austenitic matrix can be reinforced by solid solution strengthening by adding different elements like Cr, Mo. The presence of Cr and Al promote Cr_2O_3 and Al_2O_3 formation on the external surface of the superalloys, respectively. These oxides increase the oxidation resistance. Elements such as Ti, Al, Nb can lead to the formation of secondary phases involving a further strengthening effect. There are also some useful minor elements, which can improve determined properties in superalloys. C and B are added to promote the carbides and borides formation, which can be helpful in precise condition. Instead, B, Zr and Hf are added to give grain boundary effects other than precipitation or carbide formation.

Finally, detrimental tramp elements, such as Si, P, S, P, Ag often in amounts of parts-per-million level, have been correlated to mechanical properties reduction, since they tend to segregate in grain boundaries and reduce the cohesive energy between grains generating crack propagation sites. In this case, Mg can be added for tramp elements control since it tends to tie up and eliminate some harmful elements such as S in the solid solution state, whereas Ti tends to form TiN using N within the matrix austenitic.

Table 3 provides a summary of the main effects of the chemical elements within the three categories of superalloys [2,3].

Table 3: Effect of alloying elements in superalloys [3].

Effects	**Fe,Ni-base**	**Ni-base**	**Co-base**
Solid-solution strengtheners	Cr,Mo	Nb, Cr, Mo, Ni, W, Ta	Co, Cr ,Fe, Mo, W, Ta ,Re
Form MC	Ti, C	Ti, C	W, Ta, Ti, Mo, Nb, Hf, C
Form M_7C_3	-	Cr, C	Cr, C
Form $M_{23}C_6$	Cr, C	Cr, C	Cr, Mo, W, C
Form M_6C	Mo	Mo, W	Mo, W, Nb
Form Carbonitrides	C,N	C,N	C, N
Form γ' phase	Al, Ni, Ti	-	Al, Ti
Form γ'' phase	Ni, Nb	Nb	-
Retardant for η	Al, Zr	-	-
Oxidation resistance	Cr	Al, Cr	Al, Cr, La, Ce
Grain boundary refiners	-	-	B, C, Zr, Hf

1.4 Heat treatments for superalloys

Heat treatments are a fundamental process in order to obtain the desired microstructure and mechanical features for superalloy components [2,3,36]. The heat treatment can be classified into 4 types:

1) Annealing treatment is performed to trigger recrystallisation and grain growth, reducing hardness of the materials.

The annealing treatment, therefore, is used at least for one of the following objectives:

A. Increase the ductility and so reduce the hardness, to make easier the forming or machining;
B. Relieve residual stresses (e.g. after welding process);
C. Produce specific microstructure features, or soften age hardened structures by resolution of second phases.
D. To homogenise a cast ingot.

Temperatures vary widely, depending on alloy and working service. Occasionally, when final application components are being shaped (e.g., forging of a gas turbine disk), reheating for hot working is limited to temperatures that do not solubilise all secondary phases since these phases at grain boundaries limit the grain growth. The temperature and time of some typical annealing treatments for wrought superalloys are listed in Table 4.

Table 4: Common annealing treatments for wrought superalloys [3].

Fe,Ni-based alloys	**Temperature (°C)**	**Holding time for inch of section (hours)**
19-9 DL	980	1
A-286	980	1
Discaloy	1035	1
Ni-based alloys		
Hastelloy X	1175	1
Inconel 625	980	1
Inconel 718	955	1
Nimonic 80A	1080	2
Waspaloy	1010	4
Co-based alloys		
L-605	1230	1
S-816	1205	1

2) Solution heat treatment is typically performed between 1040 °C and 1230 °C, just under below the incipient melting temperature.

The temperature of the solutioning treatments is higher than the annealing ones, because it is mainly applied to dissolve secondary phases dispersed within the alloys. Although, solutioning treatments may not fully dissolve all second phases as MC carbides.

Another function of this heat treatment is to homogenise the microstructure by means of solid state diffusion, and to eliminate microsegregations, generating a more uniform distribution of the elements.

Finally, it can also induce recrystallisation and grain growth, obtaining maximum ductility. For the same alloy, the solutioning generates larger grains than the annealing treatments. Table 5 provides some common solution heat-treated (SHT) conditions for wrought superalloys.

Table 5: Common SHT treatments for wrought superalloys [3].

Fe,Ni based alloys	**Temperature (°C)**	**Time (hours)**	**Cooling**
A-286	980	1	Oil quench
Discaloy	1010	2	Oil quench
Ni-based alloys			
Hastelloy X	1175	1	Rapid quench*
Inconel 625	1150	2	Rapid quench*
Inconel 718	980	1	Air cool
Nimonic 80A	1080	8	Air cool
Waspaloy	1080	4	Air cool
Co-based alloys			
L-605	1230	1	Rapid cool

**It is necessary to cool down rapidly at 540 °C to avoid the formation of precipitates.*

3) Ageing treatments promote the formation of strengthened phases, such as γ' and γ'' phases or secondary carbides, also controlling the formation of detrimental phases.

It is interesting to note that some alloys present a double ageing treatment. For instance, U- 500 is double aged for the stabilization of grain boundary carbides, in order to obtain a compromise between tensile strength and stress-rupture life.

The heat treatments are the following:

- SHT at 982 °C for 4 h (air cooled);
- Stabilised at 843 °C for 24 h (air cooled);
- Aged at 760 °C for 16 h (air cooled);

The solution treatment dissolves all phases exclude MC carbides. Afterwards, the cooling promotes the formation of γ' precipitate nucleates. The stabilization at 843 °C provokes the formation of fine intergranular $M_{23}C_6$ carbides as well as more γ' phases. Finally, the second ageing treatment increases the volume fraction, and possibly the number, of γ' precipitates.

These heat treatments modify the original microstructure allowing the improvement of stress-rupture life and reinforcing the alloys by the formation of fine intergranular $M_{23}C_6$ carbides and γ' phases within the alloys. However, overageing can have detrimental effects producing undesirable or too large precipitates.

For example, overageing of A-286 at 650 °C results in $\gamma' \rightarrow \eta$ transformation, and overageing of Inconel 718 leads to in $\gamma'' \rightarrow \delta$ transformation.

Some typical ageing treatment conditions for wrought superalloys are given in Table 6.

Table 6: Common ageing treatments for wrought superalloys [3].

Fe,Ni based alloys	**Temperature (°C)**	**Time (hours)**	**Cooling**
A-286	720	16	Air cool
Discaloy	730	20	Air cool
Ni-based alloys			
Inconel 718*	1° step720 2° step 620	1° step 8 2° step 8	Air cool
Nimonic 80A	705	16	Air cool
Waspaloy*	1° step 845 2° step 760	1° step 24 2° step 16	Air cool
Co-based alloys			
S-816	760	12	Air cool

**double ageing (divided into 2 steps)*

4) Stress relieving of superalloys is carried out to reduce the stress within the materials, and it must be carefully designed to avoid possible undesired effects such as an excessive grain growth or the formation of secondary phases.
For these reasons, stress relieving is generally performed below the annealing or recrystallisation temperatures.

Regarding the wrought alloys, stress relieving is typically performed on solution strengthened superalloys, whereas on age-hardenable alloys an annealing or solution treatment is commonly applied, that guarantees the reduction of the internal stresses and also prepares the alloys for the subsequent ageing treatment.

A large number of casting superalloys are Ni-based superalloys and most of them are age hardenable alloys, and elevated temperature exposures involve microstructural changes. Therefore, stress relief treatments are not usual practiced with cast Ni-based superalloys. However, this heat treatment can be used to prevent dimensional changing for stringent geometrical tolerances, or after welding processes.

For many alloys, stress relief has been designed by empirical studies of stress decay with time and temperature, assessed by nondestructive means such as X-ray diffraction. However, this is not an entirely useful technique for superalloys, where the effect of the stress relieving on the microstructure should also evaluate the impact on other properties such as low-cycle fatigue, crack growth, and creep rupture [2,3,36].

The stress relieving conditions for some wrought superalloys are reported in Table 7.

Table 7 : Common stress relieving treatments for wrought superalloys [3].

Fe,Ni based alloys	**Temperature (°C)**	**Holding time for inch of section (hours)**
19-9 DL	675	4
Ni-based alloys		
Inconel 625	870	1
Inconel 600	900	1

To sum up the heat treatments applied to superalloys are used for these functions:

- To promote grain growth or recrystallization;
- To homogenise the alloy or solubilise the precipitate in precipitation-hardened alloys;
- To promote the formation of secondary phases;
- To reduce residual stresses within the superalloys.

1.5 Specific properties of IN625 and HX superalloys

1.5.1 IN625 superalloy

IN625 is a solid solution strengthened Ni-based superalloy, which is used for its high temperature strength, excellent fabricability, weldability as well as outstanding corrosion resistance [5,37,38]. The chemical composition is under the UNS N06625 specification, and it is reported in Table 8.

Table 8: Chemical requirement for IN625 alloy according to UNS N06625 specification.

Element	Weight percent (wt %)
Ni	58.0 min
Cr	20.0-23.0
Mo	8.0 -10.0
Fe	5.0 max
Nb+Ta	3.15-4.15
Co	1.0 max
Mn	0.50 max
Si	0.50 max
Al	0.40 max
Ti	0.40 max
C	0.10 max
P	0.015 max
S	0.015 max

According to ASTM B443, this material is generally available in two different conditions:

- Grade 1 described as annealed state;
- Grade 2 described as solution annealed or solution heat-treated (SHT) state;

Grade 1 IN625 parts are annealed over 871 °C, commonly between 871 °C and 982 °C, and this material is used for service up to medium high temperature (around 593 °C). Grade 2 IN625 components are SHT at least at 1093 °C, and they are used for service over 593 °C. The main difference between the two conditions is the grain size, which enhances specific properties of the alloy.

Grade 1 IN625 alloys present smaller grains and so higher corrosion resistance than Grade 2 alloy. On the other hand, the large grains of grade 2 IN625 alloys provide higher creep resistance and also higher ductility than grade 1 IN625 alloys [39]. Grade 1 IN625 alloys having high corrosion-fatigue strength, high tensile strength, and resistance to chloride-ion stress-corrosion cracking are widely used for the production of seawater applications. It is also used for wire rope for mooring cables, propeller blades for motor patrol gunboats, submarine auxiliary propulsion motors, exhaust ducts for Navy utility boats, submarine transducer controls, and steam-line bellows.

Differently IN625 grade 2 alloys are desirable to the aerospace field. It is widely used in applications as aircraft ducting systems, engine exhaust systems, combustion system, turbine seals, fuel and hydraulic line tubing, spray bars, heat-exchanger, turbine shrouds, spray bars, hydraulic tubing and turbine blades [15,37,39,40].

Table 9 summarises the minimum mechanical properties of IN625 alloys according to the ASTM B443 together with the values of wrought and cast IN625 alloys presented in the literature.

Table 9: Minimum tensile properties of IN625 alloys according to ASTM B443 and tensile properties of wrought and cast IN625 alloys; yield strength (YS), ultimate tensile strength (UTS) and elongation (A).

IN625 State	YS (MPa)	UTS (MPa)	A (%)
Annealed cold-rolled sheet and strip [37]	414	827	30
SHT cold/hot-rolled sheet and strip [37]	276	690	30
Annealed hot-rolled [40]	479	965	54
Cast [3]	350	710	48

**1038 °C for 1 hour*

As mentioned before, IN625 is a solid solution strengthened alloys, although its mechanical properties can highly change for the precipitation of different phases during service in temperature or heat treatments. Figure 5 shows a Time-Temperature-Transformation (TTT) diagram of IN625 alloy, revealing the formation of different phases as carbides (MC, M_6C and $M_{23}C_6$), γ″ phase, δ phase as well as Laves phases. Typically, the formation of γ″ phases increase the tensile strengths, whereas δ and Laves phases are detrimental leading to a ductility reduction. Differently, the carbides can give both positive and negative effect based on position, morphology and size.

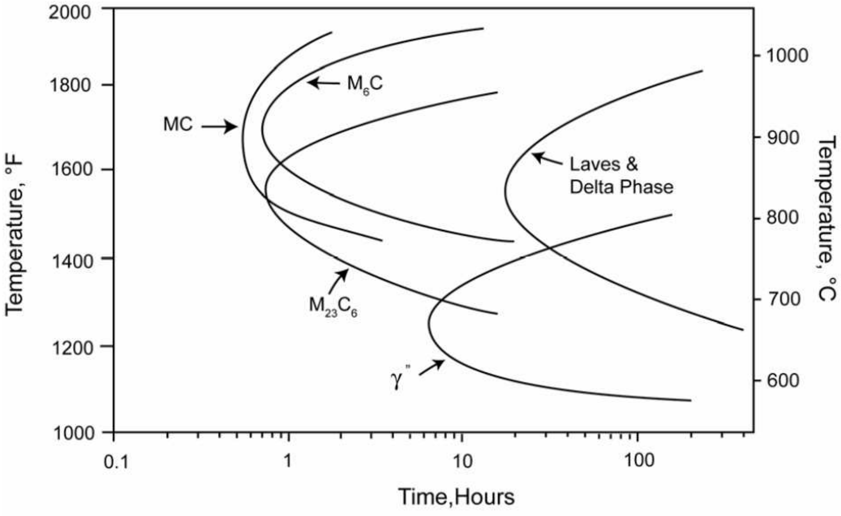

Figure 5: Time-Temperature-Transformation (TTT) diagram of IN625 alloy [39].

Cast IN625 alloys present the formation of NbC carbides (T around 1250 °C) and Laves phases (T around 1200 °C) due to eutectic reactions [29,31]:

$$L \rightarrow \gamma + NbC$$

$$L \rightarrow \gamma + Laves\ phases$$

Due to the Laves phases are very detrimental to the ductility, it is therefore crucial to perform a solution treatment over 1093 °C to dissolve Laves phases. On the other hand, also by solution treatment is difficult to eliminate NbC carbides, because they start di dissolve around 1190 °C. However, they do not give any particular problem when they are scattered inside the matrix [5,38].

1.5.2 HX superalloy

HX is another solid-solution strengthened Ni-based superalloys with very high temperature strength and oxidation resistance. Table 10 reports the chemical composition of HX alloy, which is under the UNS N06002 specification [41–43].

Table 10: Chemical requirement for HX alloy according to UNS N06002.

Element	Weight percent (wt%)
Ni	Bal.
Cr	20.5-23.0
Fe	17.0-20.0
Mo	8.0-10.0
Co	0.5-2.5
W	0.2-1.0
Mn	1.0 max
Si	1.0 max
P	0.04 max
S	0.03 max

This alloy is generally SHT at 1175 °C for 1 hour, and it presents grain size ASTM number between 4 and 5 (around 90 µm and 63 µm, respectively) [36,43,44]. In this state, the microstructure of SHT HX alloys typically consisted of a γ matrix and primary Mo-rich M_6C carbides, generated during solidification [6,43,44].

HX is widely used for the fabrication of the cross ducts in the high-temperature gas-cooled reactor (HTGR), operating between 618 °C and 816 °C as well as combustor cans and spray bars. Besides, it can also be used in industrial furnace applications thanks to its high oxidation resistance up to around 1177 °C. Finally, HX is broadly employed in the chemical process industry for retorts, muffles, catalyst support grids, tubing for pyrolysis operations [41–43].

The minimum tensile properties reported in the ASTM B435 standard and the tensile properties of some available data on wrought HX alloys are given in Table 11.

Table 11: Minimum tensile properties of HX alloys according to ASTM B435 and tensile properties of some SHT wrought HX alloys.

HX State	YS (MPa)	UTS (MPa)	A (%)
Wrought*	240 min	655 min	35 min
Wrought (sheet) [41]	381	788	57
Wrought (sheet) [3]	360	785	43

**according to ASTM B435.*

However, also in this case, during service at high temperatures, HX alloy is subjected to the formation of different phases, which can remarkable change its mechanical properties.

Figure 6 illustrates a TTT diagram of HX alloy, revealing the formation of different phases, mainly carbides (M_6C and $M_{23}C_6$), μ and σ phases. Primarily, the formation of film of carbides can result in premature components failures, as discussed in paragraph 2.4.3.

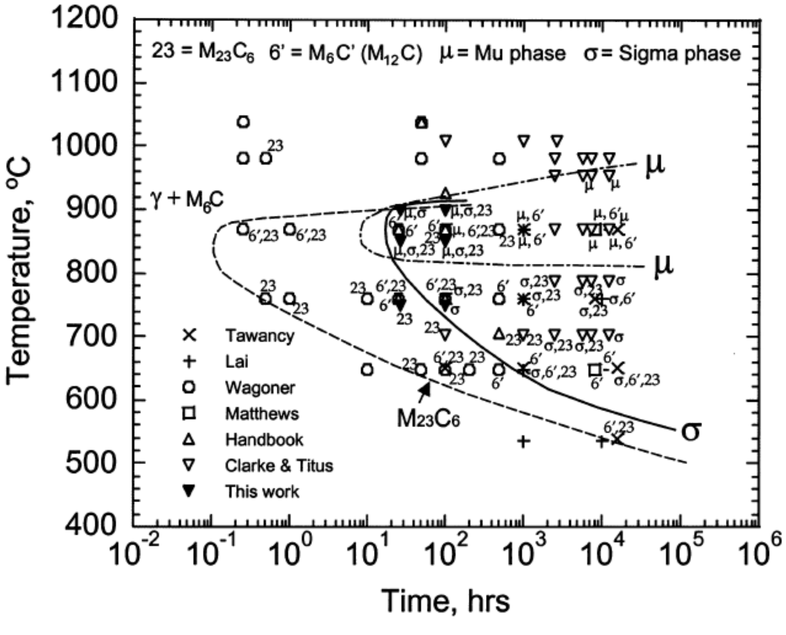

Figure 6: TTT diagram of HX alloy [20].

In the past, the main research on HX alloy had studied its evolution of the microstructure under different thermal exposures, in order to evaluate the mechanical properties development for application at high temperature [6,20,42–44].

1.6 Additive manufacturing (AM) techniques

Additive manufacturing (AM) represents a class of layer by layer manufacturing techniques that enable the production of highly complex components from a 3D CAD model [45–47]. This model is then divided and approximated to a sequence of 2-D slices of with a determined thickness, and subsequently, each layer is built up by adding material.

Among AM process, the LPBF and DED are two of the most widely used processes to fabricate Ni-based superalloys [47–49]. These AM processes can overcome the problems related to the traditional subtractive manufacturing of Ni-based superalloys, which is significantly arduous and expensive, due to these materials are characterised by high hardness, temperature strength and low thermal diffusivity [1,50,51]. Furthermore, the AM technologies present other different advantages: [45,52–54]

- Raw material efficiency. AM, consume less material than subtractive manufacturing processes.
- Production flexibility. AM processes do not require mould or other expensive manufacturing set up, and so they result to be cheaper for the small batches.

However, these new technologies also present some drawback: [45,52–54]

- Size limitation: the dimensions of the components depends on the dimensions of the building chamber.
- Support design and removal: Due to the presence of high residual stresses the AM components require support structures to avoid distortion. Afterward, these support structures have to be removed, thus increasing the post-processing time.
- Defects: the surface roughness could be not suitable for the industrial application, so post processing treatments are required.
- Anisotropy: These processes create anisotropic materials.

- Cost: The high cost of the machines and powder make these processes available for the fabrication of components with complex shapes and not for simple shapes.

Some of the Ni-based superalloys produced by LPBF and DED processes are listed in Table 12.

Table 12: List of the main Ni-based superalloys produced by LPBF and DED processes.

Ni-based superalloys	**LPBF**	**DED**
Inconel 625	[55–57]	[51,58]
Hastelloy X	[8,59–61]	-
Inconel 718	[62–66]	[67,68]
Inconel 939	[69]	-
Inconel 738	[70]	[71]
CM247LC	[72,73]	-

1.6.1 LPBF process

One of the main laser additive manufacturing (LAM) technologies applied to the fabrication of Ni-based superalloy parts is laser powder bed fusion (LPBF) process, which is considered a powder bed fusion (PBF) process [48,74].

The LPBF machines are known with different names, selective laser melting (SLM), direct metal laser remelting, direct metal laser sintering (DMLS) or Lasercusing according to the producer [45]. The LPBF process melts consecutive layers of loose powder according to precise 3D CAD data, to build dense components [45,47,75].

Figure 7 illustrates a schematic representation of an LPBF system.

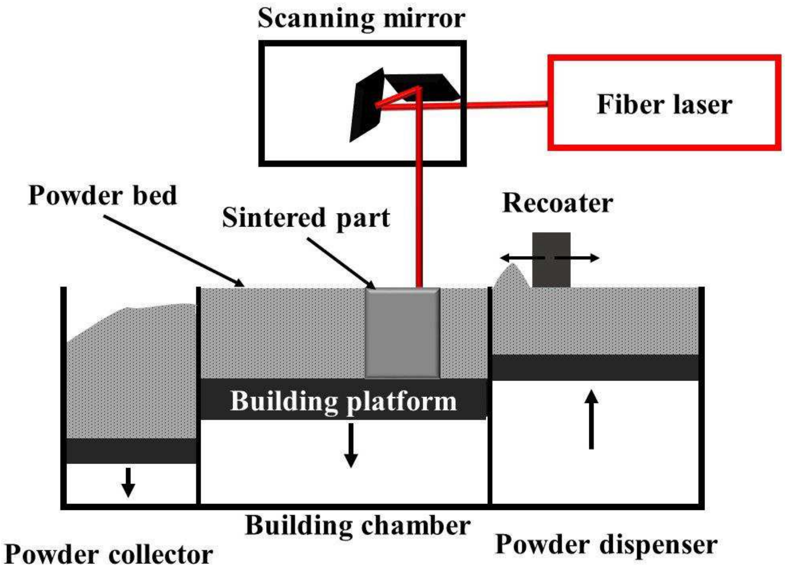

Figure 7: Schematic diagram of an LPBF process [56].

The main steps of the operation are:

1) The recoater blade moves from the powder dispenser to building platform, spreading a determined thin layer of loose powder across the building platform or previously solidified layers;

2) After the powder is laid, the laser beam selectively melts some areas of the layer of loose powder according to the processed data;

3) The building platform is lowered by the thickness of a single layer, meanwhile the recoater blade comes back to the original position (powder dispenser side);

4) The powder dispenser moves up in order to allow the deposition of a new layer of loose powder;

5) The process is replicated layer by layer until completion of the component.

During the LPBF process, the components are built under inert gas protection, typically Ar or N_2, to prevent oxidation. The main process parameters are the laser power P (in W), the hatching distance h_d (mm), which is the offset between two adjacent scan tracks, the scan speed of the laser v (in mm/s) and the layer thickness. Using all the parameters excepted the layer thickness is possible to assess the energy delivered per unit area of material, known as Energy density (E_D - J/mm^2) using the following formula [56,76]:

$$E_D = \frac{P}{v * h_D} \tag{1}$$

Different scanning strategy can be applied to build components by LPBF process. Typically, the scanning areas is divided into stripe or square areas [54]. The stripe can be orientated along x or y direction or alternate (Figure 8a, 8c and 8d).

An alternative is the EOS scanning strategy, in which the stripes are rotated to 67 ° between subsequent layers (Figure 8e) [56,77]. For the square areas (Figure 8c), these squares can be scanned and melted according to a precise configuration called chess strategy or in a randomly way known as island strategy [72,78].

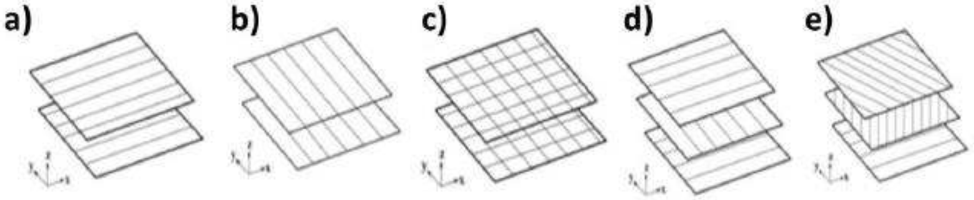

Figure 8: Different scanning strategy for LPBF process [54].

Using different process parameters and scanning strategy the thermal history of the components change, generating different microstructures and residual stresses. In the literature, it is possible to find a lot of works on this topic [48,56,72,79].

1.6.2 DED process

DED is another of the main LAM technologies used to fabricate Ni-based superalloy components (Figure 9) [45,47,80]. This type of process is also known with different names: laser metal deposition (LMD), laser engineering net shaping (LENS), direct metal deposition (DMD), etc., based on the producers and different modification about the material deposition strategy [47,80].

DED process employs a high-power laser beam to produce a melt pool on a metallic substrate, into which metallic powder is directly deposited using a carrier gas. The powder melts to form a deposited material onto the substrate. Typically, the substrate is moved along the x-y plane to deposit consecutive layers by a computer controlled system, in order to form the desired geometry. In this system, the z-direction is controlled by moving up the lens and powder nozzles. The inert gas is used to deliver the powder onto the support and shield the deposited material from oxidation, during the process [45,47,51,58].

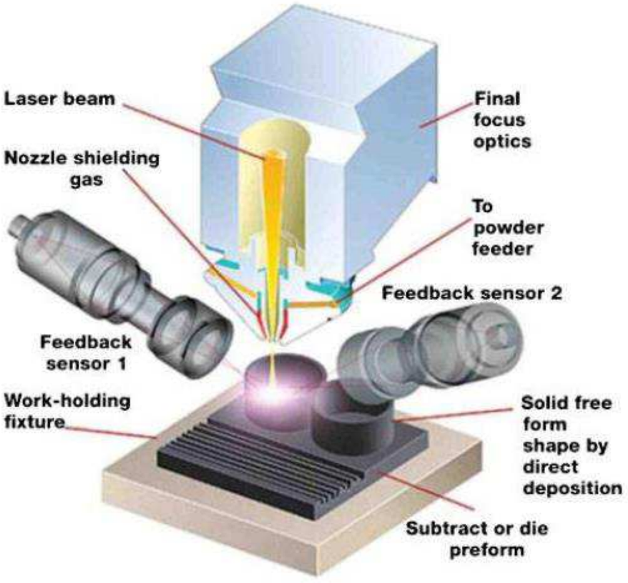
Laser beam
Nozzle shielding gas
Final focus optics
To powder feeder
Feedback sensor 2
Feedback sensor 1
Work-holding fixture
Solid free form shape by direct deposition
Subtract or die preform

Figure 9: Schematic illustration view of a DED system [45].

The main controllable process parameters, common to all DED processes, are laser power P (Watt), the scan speed v (in mm/s), the average diameter of the laser track d (in mm) and the powder flow rate P_f (g/min). In the literature, the energy density, also known as specific energy, Ed (J/mm^2) is a combined parameter, obtained using the following formula [80,81]:

$$E_D = P/(d \times v) \tag{2}$$

It allows the quantification of the energy delivery for unit area of material. Other process parameters are considered material-dependent and diverge with DLD machines (e.g. number of nozzles, nozzle design) as well as the type and flux of inert gas used.

Finally, also the scanning strategy plays a crucial role to produce dense components [80]. The five most common deposition strategies for DED process are illustrated in Figure 10. These various deposition patterns remarkable influence the geometric, residual stresses and mechanical properties of the components [80].

Among all the deposition strategies, the raster pattern is the most used in DED process due to its ease of implementation [80]. In fact, this deposition strategy of the raster pattern does not base on the geometry of the fabricated component, and consequently can be implemented to fabricate a variety of parts [82]. Nickel et al.[83] demonstrated that a deposition strategy with lines oriented 90◦ from the substrate's longer axis diminish the deflection of parts.

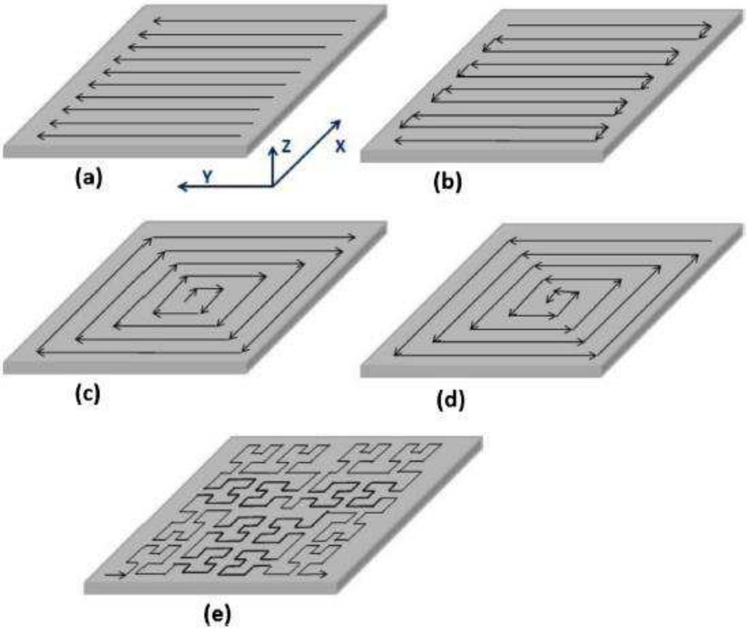

Figure 10: Different deposition strategy used in DED process: a) raster, b) zig-zag or bi-directional, c) offset-out, d) offset-in and e) fractal [80].

1.6. 3 Difference between LPBF and DED

A comparison of the main features between the LPBF (referred as SLM) and DED (referred as LMD) is reported in Figure 11.

The LPBF process produces samples with higher dimensional accuracy and lower roughness than DED process. On the other hand, the DED has a higher build-up rate and can create larger components than LPBF. In fact, the maximum dimensions of the LPBF components are limited by the building chamber [84]. However, the two processes can be complementary each other depending on the components characteristics.

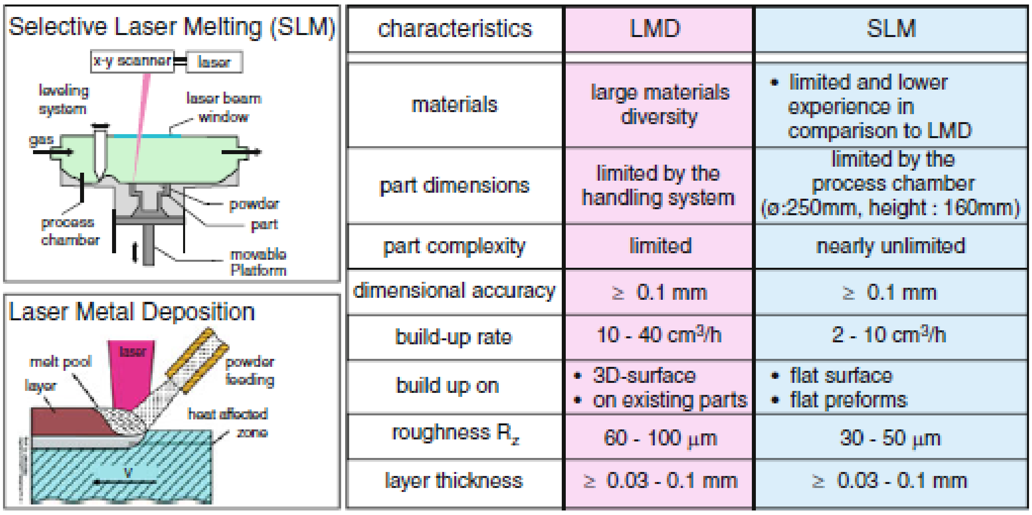
Selective Laser Melting (SLM)
x-y scanner
laser
leveling system
laser beam window
gas
powder
part
process chamber
movable Platform
Laser Metal Deposition
melt pool
layer
laser
powder feeding
heat affected zone
v

characteristics	LMD	SLM
materials	large materials diversity	• limited and lower experience in comparison to LMD
part dimensions	limited by the handling system	limited by the process chamber (ø:250mm, height : 160mm)
part complexity	limited	nearly unlimited
dimensional accuracy	≥ 0.1 mm	≥ 0.1 mm
build-up rate	10 - 40 cm³/h	2 - 10 cm³/h
build up on	• 3D-surface • on existing parts	• flat surface • flat preforms
roughness R_z	60 - 100 µm	30 - 50 µm
layer thickness	≥ 0.03 - 0.1 mm	≥ 0.03 - 0.1 mm

Figure 11:Characteristics of LPBF (referred as SLM) and DED (referred as LMD) [84].

1.7 Powders for additive manufacturing processes

The powder used for AM processes are typically gas atomised powder obtained using an inert gas (such as Ar or N_2), reducing the risk of oxidation. Besides, gas atomisation is characterised by lower cooling rate than water atomisation, generating more regular and spherical particles [53,85,86].

In order to obtain dense samples, AM processes primarily need powders with excellent flow properties to guarantee a smooth spreading of the powder bed for LPBF and powder feeding for DED. However, the humidity content, the particles size distribution and size can significantly influence the powder flowability [45,85,86].

Furthermore, other characteristics of the powder can have an impact on the densification of the components. For instance, the determination of the skeletal density of the powder is crucial to assess the presence of internal pores. In fact, during the gas atomisation process, the inert gas can be entrapped within the particles powders, thus generating pores in the solid samples during the LAM processes [53,56,85].

Another factor is to determine the presence of surface oxides, which can also reduce the solidification due to the balling effect, leading to the formation of irregular porosities [85]. Finally, it is possible to note that LPBF powders have size around 10 - 63 µm while DED powders have size around 45 - 150 µm [53,56,68,85].

1.8 Microstructures of LPBF and DED Ni-based superalloys

1.8.1 LPBF Ni-based superalloys

In LPBF process, the laser beam melts layers of powder generating a microstructure consisted of melt pools, as visible in Figure 12. The shape and position of the melt pools are correlated to the scanning strategy used.

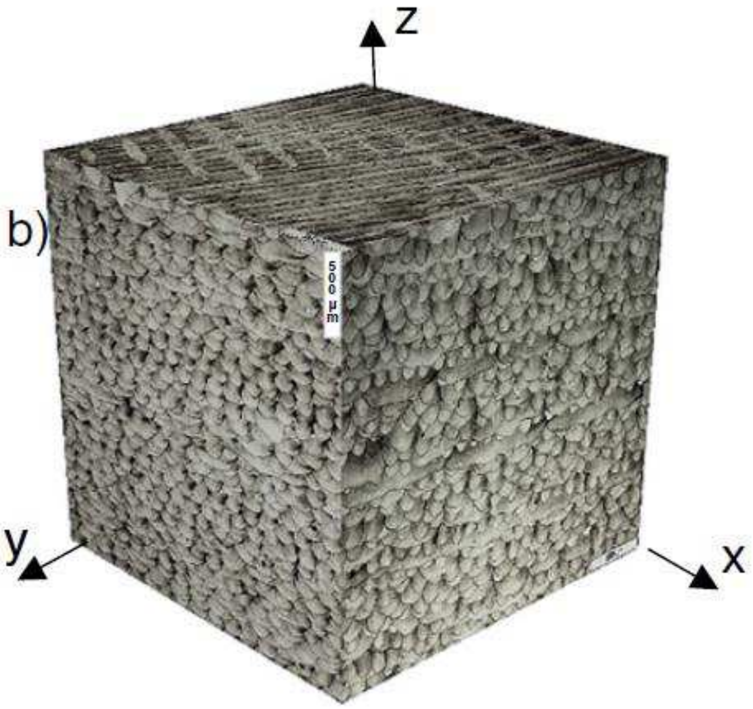

Figure 12: 3D composite images of LPBF as-built IN718 alloy showing the melt pools along different planes [65].

During the process, the heat fluxes are dissipated along the z-axis from the top of the samples to the building platform, generating strong anisotropy due to the formation of columnar grains along the building direction. Differently, perpendicular to the building direction the microstructure is characterised by random orientated equiaxed grains as can be seen in EBSD images of IN625 alloy in Figure 13 [61,72,87].

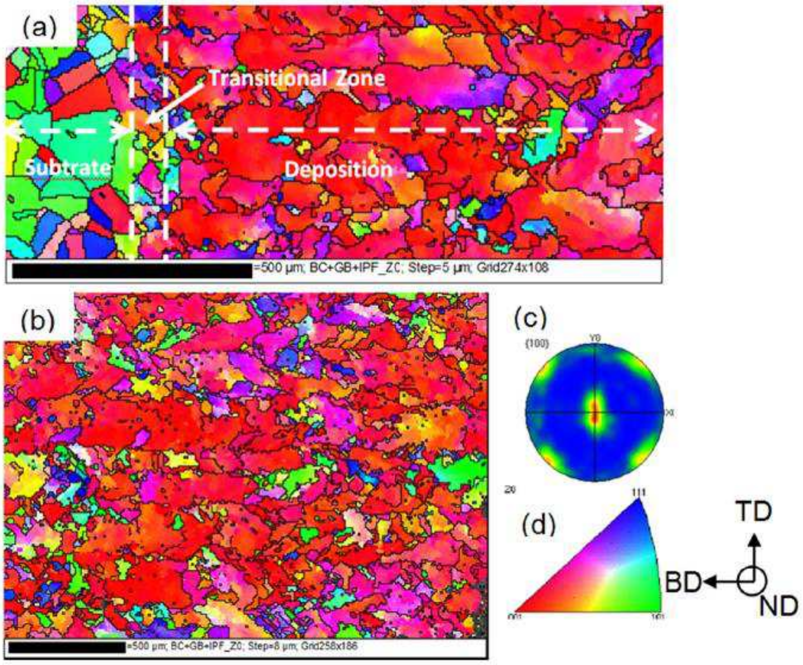
(a)
Transitional Zone
Subtrate
Deposition
=500 µm; BC+GB+IPF_Z0; Step=5 µm; Grid274x108
(b)
=500 µm; BC+GB+IPF_Z0; Step=8 µm; Grid258x186
(c)
{100}
Y0
X0
Z0
(d)
111
001
101
TD
BD
ND

Figure 13: EBSD images along the building direction (a) and perpendicular to the building direction (b) for LPBF IN625 alloy [55].

It was demonstrated that the texture is influenced by the laser scanning strategy and process parameters, becoming stronger with the increment of the energy density (energy delivered on the layer of powder) [65].

The grains and melt pools consisted of extremely fine columnar and cellular dendritic architectures, having typically size less than 1 µm [55,60,88]. These dendrites are created due to the high heating/melting and cooling/solidification in narrow areas result in high cooling rates around (10^3 to 10^8 K/s) [55,88,89].

It is well known that the high mechanical properties of the Ni-based superalloys produced by LPBF mainly derive from these very fine dendritic architectures coupled with high dislocation density) [55,88,89].

1.8.2 Microstructure of DED as-built Ni-based superalloys

The microstructure of DED Ni-based superalloys is similar to LPBF ones, revealing the presence of columnar grains along the building direction (z-axis) and dendrite architectures.

In this case, the DED materials are characterised by larger precipitates and dendrite architectures than LPBF ones, showing primary and secondary dendrite with micrometric size [51,56,58]. These differences are attributed to the cooling rates around 10^2 and 10^3 K/s that is lower with respect to the LPBF samples [45,80].

1.9 Defects within LPBF and DED Ni-based alloys

The main defects present within LPBF and DED Ni-based superalloys will be discussed in the following paragraphs (1.9.1 and 1.9.2).

1.9.1 Pores

LPBF Ni-based superalloys can present spherical or irregular pores [46,74,78,89,90]. The spherical pores can derive from entrapped gas within the gas atomised powder. In this case, when the laser beam melts the powder, the gas within the powders has no time to overflow from the molten pool.

Figure 14 shows this kind of porosity that affect the formation of an Inconel 718 alloy for DED process.

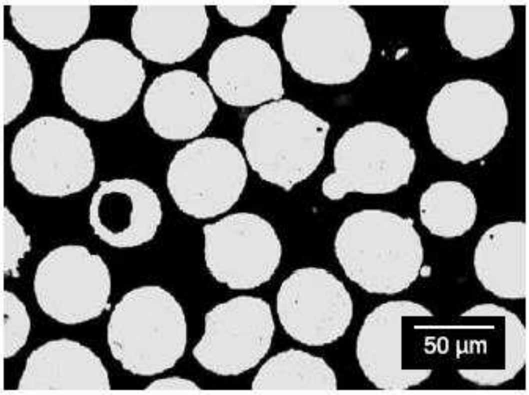

(a)

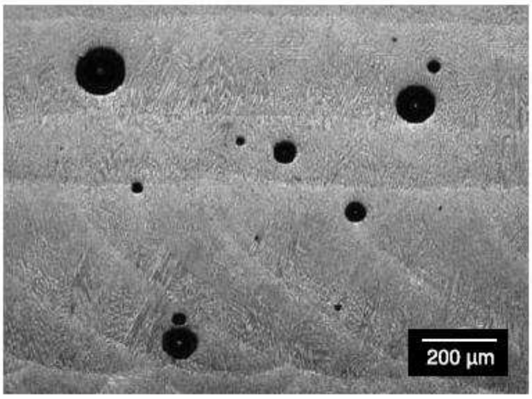

(b)

Figure 14: OM image of gas entrapped pores within (a) the cross sectioned powder and (b) solid materials for DED Inconel 718 alloy [90].

Besides, the spherical pores can also be caused by gas (in the chamber process) entrapped within the melt pools or/and gas evolution during melting owing too much moisture in the powder [46,89]. Differently, the irregular pores are caused by the unstable molten pool shape.

During the solidification, in fact, the liquid contraction can result in the balling phenomenon, which block the formation of dense components [75,89]. The balling phenomenon is correlated to poor wetting between the liquid material and the substrate, due to low energy density. Rombouts et al. [91] and Yadroitsev et al. [92] demonstrated that the Marangoni convection causes the instability within the molten pool. Figure 15 shows an example of the porosity caused by low energy density on LPBF IN625 alloy.

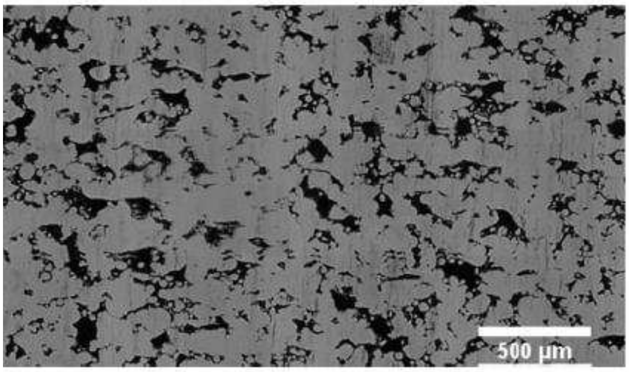

Figure 15: OM image of LPBF IN625 alloy produced with low energy density showing different pores due to lack of fusion [48].

In order to eliminate the balling effect it is possible to modify the process parameters using higher energy density [62]. Furthermore, it was reported that the formation of oxide surfaces during the process tend to improve the balling effect, so a better control of the inert gas within the building chamber can contrast this phenomenon [74,93].

However, too high energy density can provoke the material evaporation creating deep keyhole pores with irregular shapes [74,78]. The effect of different energy density applied to build TiAl6V4 alloy generating different keyhole pores is displayed in Figure 16.

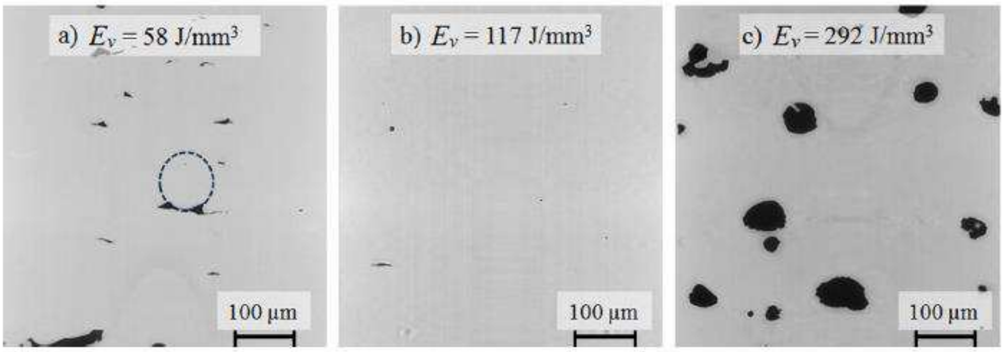

Figure 16: OM images of TiAl6V4 produced by LPBF showing the effect of the energy density: a) lack of fusion; b) optimised energy density; c) key hole produced by too high energy density [79].

1.9.2 Cracks

The cracks present within Ni-based superalloys produced by LPBF and DED process can be correlated to cracks produced during welding or post-welding treatments, considering that these AM processes are multilayer/repeated welding process [49,74]. Primarily the cracks derived from welding of Ni-based superalloys can be caused by four different mechanisms:

1) Solidification cracking knows also as hot tearing or hot cracking;
2) Liquation cracking;
3) Ductility-dip cracking;
4) Strain-Age Cracking (SAC) or Post-Weld Heat Treatment (PWHT) Cracking.

1) Solidification cracking also known as hot tearing and hot cracking is strongly associated with the chemical composition of the alloy [49] .

This phenomenon occurs during the last period of solidification when the fraction solid is around 0.7-0.98, when the increment of the viscosity of the liquid reduce it flow ability. During this point, the interdendritic liquid flow is not able to backfill into the contracting regions, promoting the formation of cracks. The thermal residual stresses localised into the liquid areas can induce the formation of cracks, typically crossing along dendritic or grain boundaries. The solidification cracking susceptibility is enhanced by increasing solidification range (difference between solidus and liquidus of material) or by the presence of segregated element into the interdendritic areas or grain boundaries [8,31,49,60,94].

Nevertheless little literature studied this phenomenon associated with the LPBF and DED processes [8,60]. Specifically for LPBF process, the cooling and solidification of the molten pool involve a shrinkage, hindered by the previously solidified layer. This mechanism produces tensile stress in the top layer and compressive stress in the inferior ones. Therefore, the cracks are formed when the residual stress surpass the ultimate tensile stress (UTS) of the alloy [60]. Typically, these cracks formed along the grain boundaries since they are the weakest areas due to the impurity segregation, as visible in Figure 17.

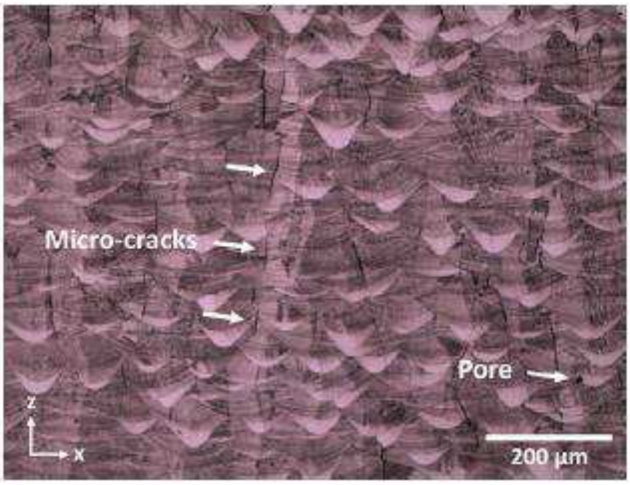

Figure 17: OM image of LPBF HX showing cracks along the grain boundaries [60].

For LPBF HX alloy, Harrison et al [60] suggested that increase the thermal shock resistance of the alloy by improving the UTS is possible to reduce the presence of hot cracking. The UTS can be conceivable enhanced by the increment of solid solution strengthening elements and the decrement of tramp elements within the alloy.

2) The liquation cracking occurs when a material is quickly subjected to high temperature exposures, although under the overall melting point of the bulk material. In a similar condition, intergranular low-melting point phases (e.g. eutectic compounds) can melt, and thus the liquid infiltrates the grain boundaries, weakening them and provoking the cracking formation under residual or thermal stresses.

In solid solution strengthened alloys this kind of cracking is typically associated with the liquation of carbides [95,96], whereas for γ′ strengthened alloys is caused by the formation of low melting compounds, γ/γ″ eutectic or Laves/γ compound in the heat affected zone [71,94]. For instance, Figure 18 displays two liquation cracking within DED Inconel 718 alloys. In this case, Chen et al. [94] indicated that the cracks derives from the liquation of Laves phases within the heat affected zone.

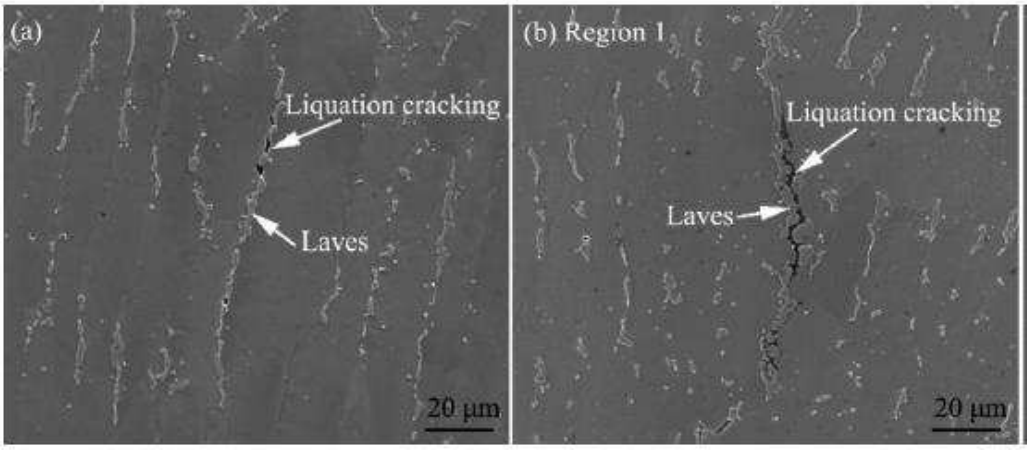

Figure 18: FESEM images of DED Inconel 718 showing liquation cracking due to the melting of Laves particles within the heat affected zone [94].

3) In the literature, the ductility-dip cracking is often approximated as hot cracking, although different mechanisms generate it. The formation of intergranular precipitates in high-angle grain boundaries coupled with the high residual stresses promote the cracks formation.

Two different mechanisms have been indicated for the ductility-dip cracking.

Collings et al. [97] suggested ductility-dip cracking is a a ‘creep-like’ mechanism, which at a certain temperature provoke grain boundary sliding. In this way, the strain is concentrated along the intergranular precipitates, that hinder the grain boundaries movement, causing the formation of voids around the precipitates.

Young et al.[98] suggested another possible mechanism, in which the carbides at grain boundaries under intermediate temperatures produce stresses forming the voids which act for initial cracking formation.

For the LPBF and DED processes the continuous heating flux may promote the formation of intergranular precipitates, generating the above mentioned mechanisms [74].

For LPBF-CM247LC Carter et al.[72] and Xiang et al. [99] reported the formation of cracks caused by ductility dip cracking in high-angle grain boundaries, as shown in FESEM images of CM247LC in Figure 19.

In the specific case of LPBF CM247LC, by TEM analysis, Xiang et al. [99] proposed that the ductility-dip cracking is caused by the interaction between intergranular carbides and dislocations that involve the formation of voids around the precipitates. The presence of voids coupled to high thermal residual stress of this process result in the crack formation.

Besides, Tomus et al.[8] indicated the formation of cracks within LPBF HX alloy could be attributed to the formation of intergranular carbides coupled with the thermal stresses. They used the more general term hot cracking to define this type of cracks, although it may be correlated to ductility-dip cracking mechanism.

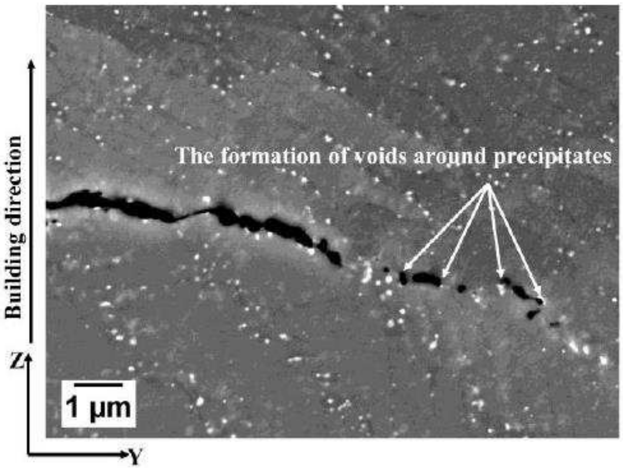

Figure 19: FESEM images showing grain boundary crack due to the generation of voids around precipitates associated with the ductility-dip cracking for LPBF CM247LC [99].

4) Strain-Age Cracking is correlated to the welding process and derives from the precipitation of phases such as γ' phases or carbides along the grain boundaries

after subsequent thermal exposures. An excessive formation of these precipitates combined with high residual stresses of the LPBF and DED processes can creates weak patch for the crack propagation. Henderson et al. [98] reported that these cracks typically open at grain boundaries where there are a significant amount of carbides acting as initiation points.

1.9.3 Residual stresses

The LPBF and DED processes are characterised by high residual stresses, which can have an adverse effect on the geometrical accuracy as well as the mechanical properties. In order to avoid the bending of the parts are commonly adopted support structures, although the residual stresses can deform it (Figure 20).

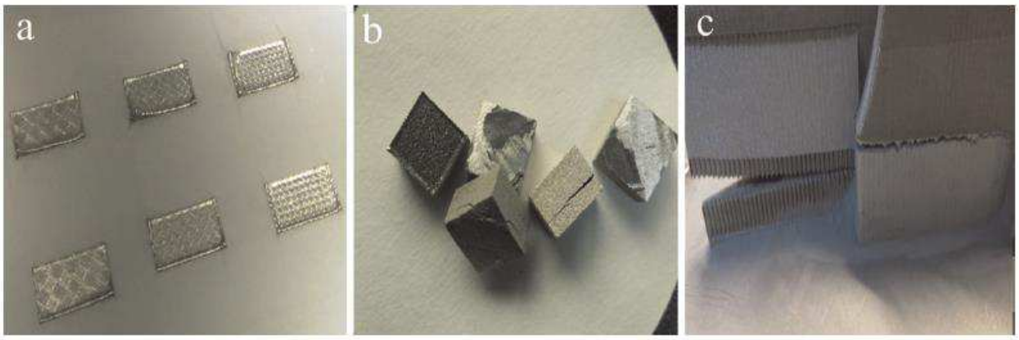

Figure 20: Effect of the residual stresses on LPBF Inconel 718 alloy [78].

The study of these residual stresses based on different factors such as the shape of the component, the support structure, the materials properties as well as the processing parameters.

For the DED process, different works have measured or modelled these stresses [100–103], even though this is generally for simple thin walls and a simple scan path.

For LPBF process, Kruth et al. [104] reported that the residual stresses are strongly associated with the laser scan strategy. A simple raster scanning strategy seems to involve high stresses in one direction (transverse to the path), while longitudinally to the path the residual stress are almost zero; differently an island strategy shows a greater, but much more distributed residual stress level. Abe et al.[105] studied the steels produced by LPBF, showing that a second laser following the first can reduce the residual stress and also increase the ductility.

Chapter 2

Materials and methods

This chapter presents the materials and experimental methods used in the processing, sample preparation as well as characterisation of materials investigated within this thesis.

2.1. LAM machines used

2.1.1 LPBF process

In this work, IN625 samples were fabricated using an EOS M270 Dual Mode system, whereas HX samples were built by means of an EOSINT M280 by GE AVIO s.r.l. The two LPBF machines are illustrated in Figure 21.

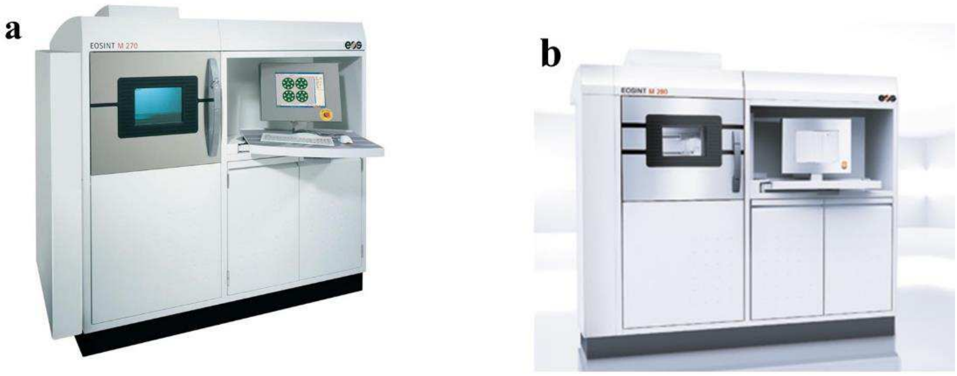

Figure 21: Images of (a) EOS M270 and (b) EOS M280 devices [106,107].

The main characteristics of the two machine are given in Table 13.

Table 13: Technical available data of EOS M270 and EOS M280 devices [106–109].

	EOS M270	**EOS M280**
Building volume (including building platform)	250x250x250 mm^3	250x250x325 mm^3
Layer thickness (material-dependent)	20-100 µm	Typically 20-60 µm
Laser type	Yb-fiber laser, 200 W	Yb-fiber laser, 200 or 400 W
Precision optics	F-theta-lens	F-theta-lens
Scan speed	Up to 7 m/s	Up to 7 m/s
Variable focus diameter	100-500 µm	100-500 µm
Power supply	32 A	32 A
Powder consumption	5.5 KW max	8.5 KW max
Building platform temperature	40-80 °C*	100 °C

**M270 Dual Mode version can reach a building platform temperature up to 200 °C.*

The two devices employ the EOS stripe scanning strategy characterised by the scan vector width (e.g. stripe width), the hatching distance (h_d) between adjacent tracks and the overlap with the neighbouring stripes. Figure 22 provides a simplified representation of this strategy.

During the process, the laser advances due to mirrors that have to be accelerated to a precise speed, and considering the inertia of the mirror the speed might not be constant. To solve this problem, it is therefore employed the skywriting option which allows the movement of the mirrors when the laser is not active, involving a carefully controlled scan speed during the exposure.

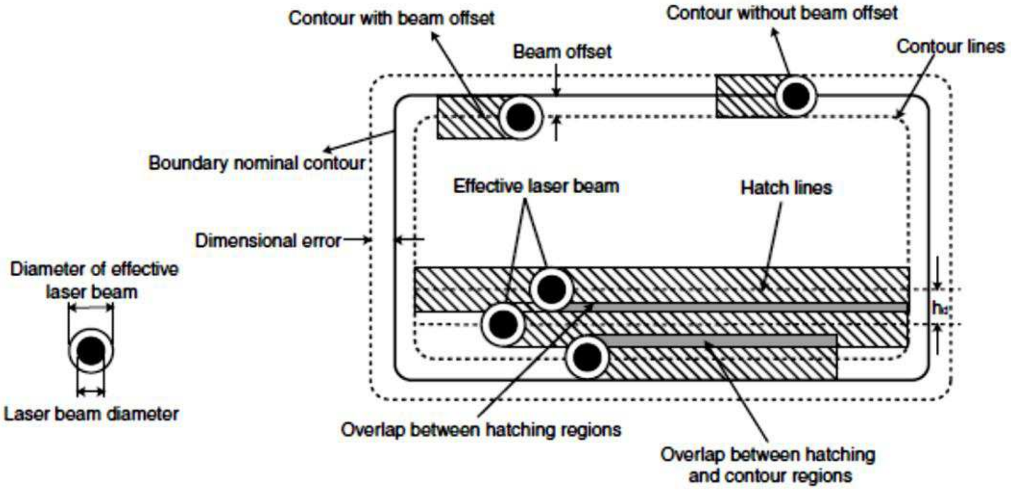
Contour with beam offset
Contour without beam offset
Beam offset
Contour lines
Boundary nominal contour
Effective laser beam
Hatch lines
Dimensional error
Diameter of effective laser beam
h_s
Laser beam diameter
Overlap between hatching regions
Overlap between hatching and contour regions

Figure 22: Schematic illustration of the stripe scanning strategy [76].

For the production of IN625 specimens, the building platform was kept at 80°C. Each layer was subdivided into 5 mm stripes with an overlap of 0.12 mm, between adjacent ones. The stripes are melted with subsequent scan tracks produced by the laser. Afterward, the laser beam is rotated by 67° in comparison to the previous layer. A schematic illustration view of LPBF scanning strategy adopted to built IN625 samples is provided in Figure 23.

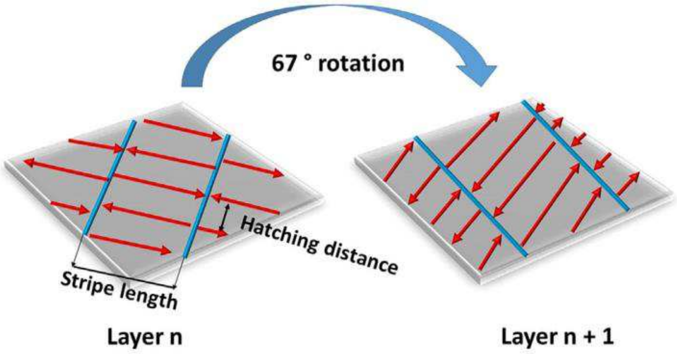
67 ° rotation
Hatching distance
Stripe length
Layer n
Layer n + 1

Figure 23: Schematic representation view of the adopted LPBF scanning strategy to built IN625 specimens (the red arrows depicted the laser scans) [56].

During the work, different combination of laser power P (in W), hatching distance h_d (mm), and scan speed of the laser v (in mm/s) were used, while the layer thickness was kept at 20 µm. The energy density (E_D- J/mm^2) approach was used to assess the energy delivered per unit area of material.

For the process parameter optimisation, three cubic IN625 samples (15x15x15 mm^3) was built using each set of process parameters (from S1 to S27) reported in Table 14.

Table 14 : Process parameters values used for building LPBF-IN625 specimens.

Sample	**P [W]**	**v [mm/s]**	**h_d [mm]**	**E_D [J/mm^2]**
S1	185	1200	0.07	2.20
S2	185	600	0.11	2.80
S3	175	900	0.11	1.77
S4	185	600	0.09	3.43
S5	185	900	0.09	2.28
S6	185	1200	0.11	1.40
S7	185	900	0.07	2.94
S8	175	1200	0.11	1.33
S9	195	600	0.11	2.95
S10	175	600	0.07	4.17
S11	175	1200	0.09	1.62
S12	175	1200	0.07	2.08
S13	185	1200	0.09	1.71
S14	175	900	0.09	2.16
S15	185	600	0.07	4.40
S16	195	1200	0.11	1.48
S17	195	900	0.11	1.97
S18	195	600	0.09	3.61
S19	195	900	0.07	3.10
S20	185	900	0.11	1.87
S21	195	900	0.09	2.41
S22	175	600	0.11	2.65
S23	195	1200	0.07	2.32
S24	175	600	0.09	3.24
S25	175	900	0.07	2.78
S26	195	600	0.07	4.64
S27	195	1200	0.09	1.81

Differently, the process parameters used to build the LPBF-HX specimens are omitted to protect the proprietary information.

2.1.2 DED process

The DED IN625 specimens were fabricated by Grupo Nicolas Correa Laser (GNC Laser) in Spain. The machine was equipped with a Laserline 3200 high power diode laser (with an output fibre of 600 µm) and a cladding nozzle mounted onto an ABB 6650 6 axis robot (Figure 24a). The machine also consisted of a company designed coaxial cladding head with three powder inputs, using Ar as the carrier gas, as well as a Sulzer Metco Twin 10 powder feeder (Figure 24b).

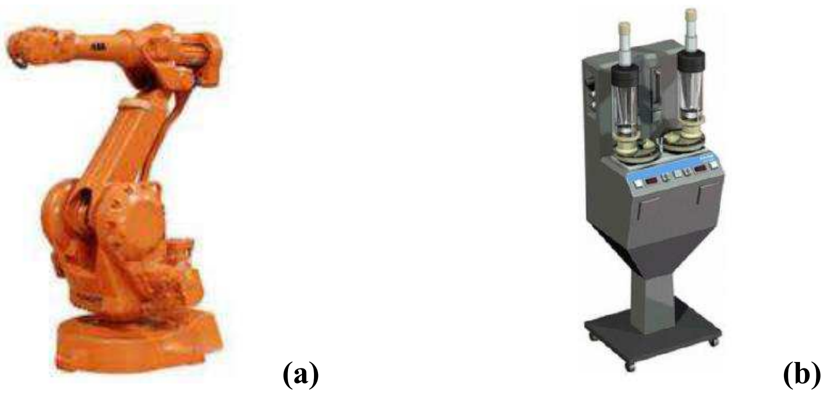
(a) **(b)**

Figure 24: Images of (a) ABB 6650 6 axis robot and (b) Sulzer Metco Twin 10 powder feeder.

During the process, the laser beam was defocused with a spot of 3 mm, using a 60% overlapping ratio between contiguous laser tracks. A zig-zag deposition strategy was employed to build the components, which means that the laser beam is rotated 90° after each deposited layer as depicted in Figure 25.

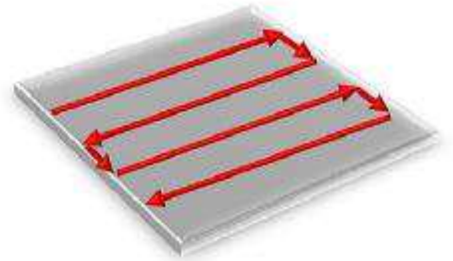

Figure 25: Illustration view of the zig-zag deposition strategy used for DED process (the read arrows indicate the laser tracks) [56].

During the experiment, different combination of process parameters, modifying the laser power P (in W), the scan speed v (in mm/s), the mean diameter of the laser track d (in mm) and the powder flow rate P_f (g min^{-1}) were employed. The energy density E_D (J /mm^2) approach was used to evaluate the energy delivered per unit area of material.

For the process parameter optimisation, three cubic IN625 samples (15x15x15 mm^3) was fabricated using each set of process parameters from R1 to R27 reported in Table 15.

Table 15: Different process parameters and energy density used for building DED-IN625 specimens.

Sample	P [W]	v [mm/s]	P_f [g/min]	E_D [J/mm^2]
R1	2100	10.0	9	70.0
R2	1800	13.3	13	45.1
R3	2100	13.3	9	52.6
R4	2100	10.0	5	70.0
R5	2100	13.3	5	52.6
R6	1800	16.7	13	35.9
R7	1800	10.0	13	60.0
R8	2400	16.7	13	47.9
R9	1800	13.3	5	45.1
R10	1800	16.7	9	35.9
R11	2400	16.7	9	47.9
R12	2100	13.3	13	52.6
R13	2400	13.3	9	60.2
R14	2400	13.3	5	60.2
R15	1800	10.0	9	60.0
R16	1800	10.0	5	60.0
R17	2400	16.7	5	47.9
R18	2400	10.0	13	80.0
R19	2400	13.3	13	60.2
R20	2100	16.7	5	41.9
R21	1800	13.3	9	45.1
R22	2100	16.7	13	41.9
R23	1800	16.7	5	35.9
R24	2400	10.0	9	80.0
R25	2100	16.7	9	41.9
R26	2400	10.0	5	80.0
R27	2100	10.0	13	70.0

2.2 Superalloy powders used

2.2.1 LPBF IN625 powder

A gas atomised IN625 powder, provided by EOS GmbH, with a nominal composition reported in Table 16, was used. The declared particles size distribution is mainly between 40 μm and 60 μm [110].

Table 16: Nominal chemical composition of IN625 powder [110].

Element	Company data sheet (wt %)
Ni	Balance (>58.0)
Cr	20.0-23.0
Mo	8.0-10.0
Fe	≤ 5.0
Nb	3.15-4.15.
Co	≤1.0
Si	≤0.5
Mn	≤0.5
Ti	≤0.4
Al	≤0.4
C	≤0.1
Ta	≤0.05
P	≤0.015
S	≤0.015

2.2.2 DED IN625 powder

A gas atomised IN625 powder supplied by Höganäs (Sweden) was used. According to the company, the powder had particle size distribution between 53 μm and 150 μm and the nominal chemical composition is reported in Table 17 [111].

Table 17: Nominal chemical composition declared by the company [111].

Element	Company data sheet (wt %)
Ni	Bal.
Cr	21.5
Mo	9.0
Nb + Ta	3.8
Fe	1.4.
Si	0.4.
Ti	-.
Al	-
Mn	-.
C	<0.03

2.2.3 LPBF HX powder

In the present study, gas atomised HX powders supplied by LPW Technology Ltd was used. The nominal chemical composition declared by the company is listed in Table 18.

Table 18: Chemical composition in weight percentage (wt%) of HX powder declared by the company [112].

Element	Datasheet by company (wt%)
Ni	Balance
Cr	20.50-23.00
Fe	17.00-20.00
Mo	8.00-10.00
Co	1.50-2.50
W	0.60-1.00
Si	1.00 max
V	0.25
Hf	0.25 max
Nb	0.25 max
Cu	0.20 max
C	0.05-0.07
P	0.015 max
S	0.015 max
O	0.015
B	0.100 max

2.3 Powder characterisations

The gas atomised HX and IN625 powders were analysed using a field emission scanning electron microscope (FESEM - Zeiss Supra TM40) and scanning electron microscopy (SEM) Phenom XL, in order to study their morphology. The powder was mounted, ground and polished down to 0.05 µm using Al_2O_3 suspension, in order to analyse the cross section by means of an optical microscope (OM – Leica DMI 5000 M). The average value and standard deviation of residual porosity were determined using 200 particles at a magnification of 500x. The mounted and polished particles were etched with Kalling's No.2 reagent (5 g $CuCl_2$ in 100 ml HCl and 100 ml CH_3CH_2OH) to study their microstructure.

The laser granulometry (Fritsch model Analysette 22 Compact) was used to determine the powder size distribution. The Hall flowmeter was used to evaluate both the apparent density and the flow rate according to the ASTM B 212 and ASTM B213, respectively for HX and DED powders. Differently, the flow rate of the LPBF-IN625 powder was assed using Carney flowmeter funnel according to ASTM B964, due to the powder did not flow in the Hall flowmeter. The skeletal density was determined by means of a pycnometer analysis using He (Quantachrome Ultrapyc 1200e).

The chemical composition of the IN625 powders were analysed by FESEM equipped with energy dispersive X-ray spectrometry (EDS), in order to compare the results with the data sheets declared by the company. Finally, the chemical composition of the HX powder was assessed through an inductively coupled plasma-optical emission spectroscopy (ICP-OES) analysis, expected for C, S, and O determined by inert gas fusion (IGF) analysis.

2.4 Metallographic sample preparation

The HX and IN625 samples were sectioned using a precision cutting machine with aluminium oxide cutting wheels. The samples were sectioned both parallel the building direction (z) and perpendicular to the building direction (x-z) plane (see paragraphs 2.5.1 and 2.5.2).

The samples were ground using different silicon carbides grinding papers down to grit 2400 and then polished down to 1 µm using diamond suspensions. The polished as-built and post-processed HX samples were etched with Kalling's No.2 reagent (5 g $CuCl_2$ in 100 ml HCl and 100 ml CH_3CH_2OH), which is a typical etchant used for superalloys [113–115].

Differently, for polished as-built and heat-treated IN625 samples were used two different etchants, in order to point out different microstructural features:

To better reveal the grain boundaries and phases, samples were etched using Kalling's No.2 reagent [113–115].

To better reveal the melt pools and dendritic architectures, samples were etched using a specific mixed acids for IN625 alloy (15 ml HCl, 10 ml CH_3COOH and 10 ml HNO_3) [113,115].

For both HX and IN625 alloys, the etching time for Kalling's No.2 solution ranges between 30 sec and 3 minutes, based on the condition of the materials (as-built or heat-treated). Likewise, for IN625 alloy the etching time for mixed acids range between 15 sec and 30 sec, for the same reason.

2.5 Orientations of the samples for microstructural analysis

2.5.1 As-built IN625 specimens

The microstructures of DED as-built IN625 samples as well as LPBF as-built and heat-treated IN625 samples were studied using cubic samples (15x15x15 mm^3).

The samples were sectioned along x-y plane parallel to the building platform and z direction parallel to the building direction, as shown in Figure 26.

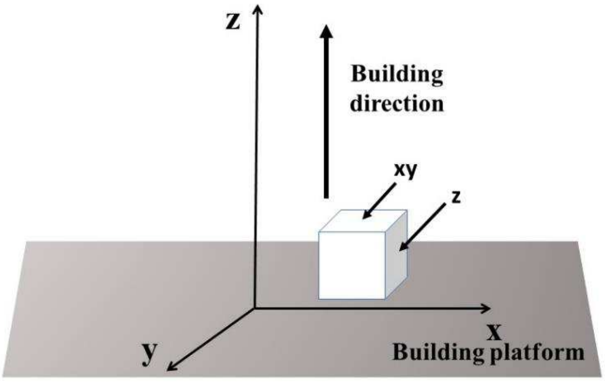

Figure 26: Schematic representation of an IN625 cubic on the building platform showing the main orientation and the x-y plane and z direction.

2.5.2 As-built HX specimens

The as-built HX cylinders with a length of 77 mm and a diameter of 14 mm were built orientated vertically and horizontally to the building platform. A schematic representation of the cylindrical samples built vertically and horizontally to the building platform together with their z-y and x-y planes is displayed in Figure 27a and 27b, respectively.

At the beginning, it was studied the microstructure of both orientated specimens, revealing a very similar level of porosity and microcracks between the x-y and z-y planes of the two orientated specimens. Besides, the microstructure features such as the shape of melt pools and grains along the x-y plane and z-y plane are the same for the two orientated conditions.

Therefore, it was chosen to characterise and perform subsequent heat treatments only on the specimens built vertically to the building platform. In fact, this configuration allows the production of a greater number of components with respect to the other configuration, using the same building platform.

The cylinders were cut along two different planes. The parallel plane to the building platform will be indicated as the x-y plane, whereas the perpendicular plane to the building platform (so parallel to the building direction) will be designated as the z-y plane. The as-built HX cylinders specimens were cut in samples with a thickness of 5 mm to have samples for performing subsequent heat treatments.

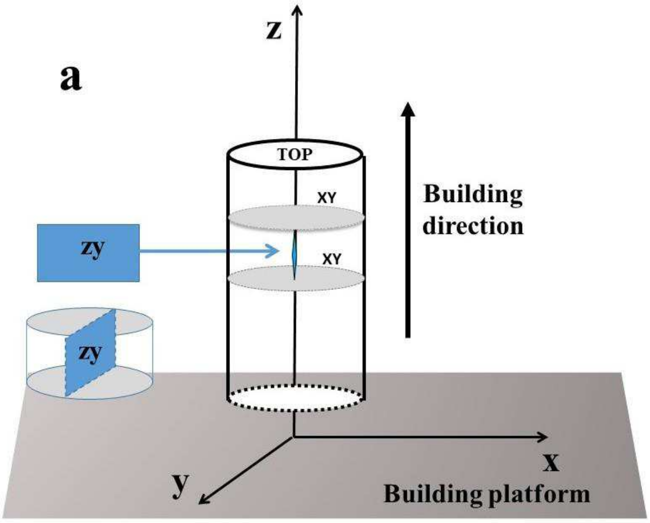

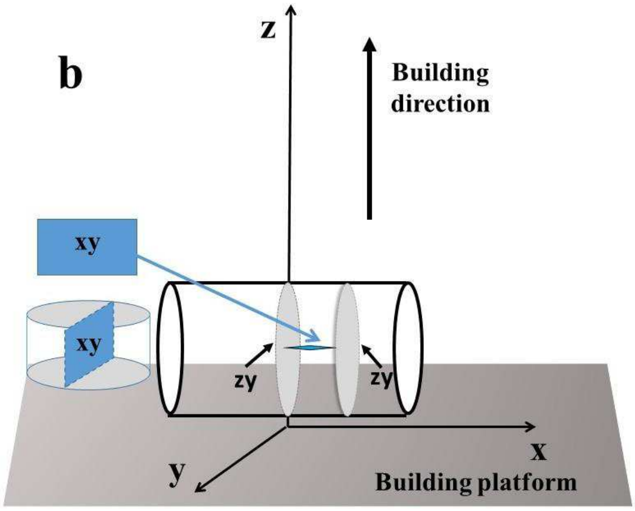

Figure 27: Schematic views illustrating the as-built HX cylinders orientated vertically (a) and horizontally (b) to the building platform; the x-y plane is parallel to the building platform whereas the z-y plane is both perpendicular to the building platform and parallel to the building direction.

2.6 Microstructural analyses and phases characterisations

2.6.1 Optical microscopy (OM)

Optical microscopy (Leica DMI 5000 M) was employed to observe mounted particles powders, polished and etched solid samples.

For HX samples, the residual porosity and cracking density were examined by taking 20 OM micrographs of polished samples and through image analysis using Image J software. A magnification of 100x using a resolution of 0.80 μm (equal to 2 pixels) was selected. In such manner, an average porosity value was determined for each HX sample covering a total surface area of 13.2 mm^2. The residual porosity was determined as a percentage with respect to the OM image area.

For the measurement of cracking density was used the ferret length and the values were reported in the unit “mm of microcracks per mm^2 of OM image” as performed in other studies on Ni-based superalloys with microcracks [48,49].

Differently, for IN625 samples, the residual porosity was determined by taking 10 OM micrographs of polished samples at 100x with a resolution of 0.80 µm, analysing a areas of 6.6 mm^2. In this case no microcraking were detected.

For all the samples, the percentage of carbides and/or different phases was also evaluated by taking 10 OM images (of etched samples) at a magnification of 500x analysing a total surface area of 0.25 mm^2 with a resolution of 0.20 µm (equal to 2 pixels).

Finally, using the OM images of etched samples for HX conditions the grain size was assessed by means of the planimetric method according to the standard ASTM E112-12.

Differently, the grain dimensions of IN625 samples were determined using Image J software, analysing different images.

2.6.2 Scanning electron microscopy (SEM)

The gas atomised powder dimensions, shape and morphology as well as microstructures of as-built and post-processed HX and IN625 samples were investigated by means of different FESEM equipped with energy-dispersive X-ray spectrometry (EDS) detector and scanning electron microscope (SEM – EDS).

Furthermore, also the extracted carbides of HX samples were analysed by FESEM/SEM in order to study the morphology and chemical composition to support their indentification by XRD analysis.

The following FESEM and SEM were used in this thesis:

- FESEM + EDS SEM-FEG Assing SUPRA 25, Zeiss
- FESEM + EDS Zeiss SupraTM40;
- SEM Hitachi S4000
- SEM + EDS Phenom XL;

2.6.3 Transmission electron microscopy (TEM)

Transmission electron microscopy (TEM) was used to visualise very fine precipitates within LPBF as-built and heat-treated IN625 samples.

Thin foils were prepared by fine grinding to a thickness of 0.08 mm, cut to obtain 3 mm diameter discs, and subsequently electropolished to perforation with a 90 % CH_3COOH and 10 % $HClO_4$ electrolyte. Electropolishing was performed at approximately -20°C and 130 mA using a double-jet electropolisher (Struers TenuPol-5).

TEM imaging was carried out by means of a JEOL JEM-2100F TEM (operating at 200 keV) equipped with energy dispersive spectroscopy (EDS).

2.6.4 XRD analysis

XRD analyses were carried out using an X-Pert Philips diffractometer (CuKα radiation) in a Bragg Brentano configuration operated at 40 kV and 40 mA with a step size of 0.013° and a counting at each step for a duration of 25 s. The lattice parameter of the γ austenitic matrix and different phases were calculated using the peaks determined by XRD spectra recorded within the 2θ range from 30° to 95°.

The XRD spectra can be analysed using the 2theta and the wavelength of the X-ray (λ) to determine the interplanar spacing (d) following the Bragg's Law [116]:

$$n\lambda = 2\, d_{h,k,l} sin\theta \tag{3}$$

$$d_{h,k,l} = \frac{n\,\lambda}{2\sin\theta} \tag{4}$$

Where n is an integer, d is the interplanar spacing, λ is the wavelength of the X-ray and θ is the incident angle.

Afterward, it is possible to use the following equation to determine the lattice parameters:

$$\frac{1}{d_{h,k,l}^2} = \frac{h^2}{a^2} + \frac{k^2}{b^2} + \frac{l^2}{c^2} \tag{5}$$

Where *a, b, c* are the lattice parameters and h, k, l are the Miller indices. For cubic structures determined *d* and knowing that *a=b=c* it is possible to rewrite the equation to find the lattice parameter:

$$a = d_{h,k,l} * \sqrt{h^2 + k^2 + l^2} \tag{6}$$

2.6.5 Carbides extraction

An adequate amount of carbides for some HX conditions were anodically extracted at 2V with a stainless steel cathode using a solution of 25% HCl – 75% CH_3OH at room temperature [117]. The extracted carbides were subsequently analysed by means of XRD analysis and FESEM +EDS analysis to identified the type of carbides.

2.7 Thermal analyses

2.7.1 Thermo-mechanical analysis TMA

Thermo-mechanical analysis (TMA-SETSYS Evolution Setaram instrument) was used to determine the coefficient of thermal expansion (CTE) in the range of 150-1200 °C with a heating rate of 5 °C/min under an argon atmosphere.

The samples used are parallelepipeds having a length of 10 mm and side 6x6 mm^2, built along x-y plane (parallel to the building platform) and z direction (parallel to the building direction).

2.7.2 Laser flash analysis (LFA)

The thermal conductivity (k) was calculated using the thermal diffusivity (a) and specific heat (Cp) determined by means of a laser flash FlashLine 4010 system, using the following equation [118,119]:

$$k = \alpha * \rho * C_p \tag{7}$$

Where ρ is the material density approximated constant with the temperature.

The experiments were performed in Ar atmosphere from 600 to 1000 °C with steps of 200 °C, using three IN625 disk samples (diameter of 12.7 mm and a thickness of 3 mm) were built along x-y plane and z direction.

2.8 Mechanical tests

2.8.1 Hardness tests

The Brinell hardness was evaluated on two different samples for each condition of HX samples and for three different samples for each state of IN625 samples, performing at least five indentations on each sample using an EMCO TEST M4U test machine. It was applied a load of 62.5 kg_f for 15 seconds (HBW2.5/62.5) based on the ASTM E10-14 standard.

The hardness Rockwell B (HRB) was performed according to the ASTM B18-16, using two different samples for selected HX conditions.

2.8.2 Tensile Tests

Using the optimised parameters, oversized cylindrical IN625 samples (length of 110 mm and diameter of 15 mm) for the tensile tests were fabricated parallel to the building platform along the x-y plane. Afterward, the specimens were machined to have a gauge length and a diameter of 40 mm and 8 mm, respectively. All tensile specimens were tested using a Zwick Z100 tensile machine applying a strain rate of 8x10^{-3} s^{-1}, following the ASTM E8M standard. The tensile specimens were tested for as-built IN625 and three selected heat-treated conditions. To ensure representative behaviour, three specimens were performed for each conditions.

The tensile data were used to determine the flow curve parameters by fitting the curve following the Ludwik-Hollomon equation:

$$\sigma = \sigma_0 + K \cdot \varepsilon^n \qquad \textbf{(8)}$$

where σ_0 is the yield stress, K is the strength coefficient, ε is the plastic strain and n is the strain hardening coefficient.

2.8.3 Impulse excitation technique

An Impulse excitation technique was used to evaluate Young's modulus on IN625 samples with a length of 50 mm, a width of 10 mm and thickness of 4 mm, built along x-y plane. The test and the dimensions of the samples follow the ASTM E1876-15. The test were carried out on three samples for selected state.

2.9 Post process treatments: heat treatments and HIP

All the heat treatments were carried out using a muffle furnace (Bicasa mod B.E. 35, Milano, Italy) with a maximum operative temperature of 1450 °C. The temperature of the furnace was controlled by means of K-type thermocouple positioned close to the samples. Differently, HIP treatments on HX specimens were carried out at at Aubert & Duval facility.

2.9.1 Post processing treatments performed on LPBF HX samples

Solution treatments were performed at 1175 °C for different times using the recommended temperature for the solution treatment followed by water quenching [36]. Furthermore, another solution treatment was carried out at 1066 °C. Hardness measurements and microstructural analyses were used to select the optimised SHT condition for improving the creep resistance. Heat treatments were performed on the SHT HX samples at 745 °C and 788 °C for short and prolonged times, simulating possible thermal exposures which could undergo components made of HX alloy, as the cross ducts in the high-temperature gas-cooled reactor (HTGR)[42,43].

A group of as-built HX samples was HIPed at 1160 °C for 4 hours at 103 MPa, that result to be standard parameters for HX alloy [120]. In the current commercial HIP equipment cooling rates used for large parts cannot be faster than 10 °C/min, promoting the formation and growth of carbides. Hence, subsequent solution treatments were carried out at 1175 °C and 1066 °C. It should be noted that after each heat treatment, the samples were water quenched to avoid the formation of carbides during the cooling.

2.9.2 Heat treatments performed on LPBF IN625 samples

The microstructural and hardness evolution of the LPBF as-built IN625 samples under different heat treatments was studied. Several direct ageing (without previous solutioning treatment), solution treatments as well as solutioning followed by ageing treatments were performed.

Direct ageing treatments were carried out at 600, 700, 800 and 900 °C for 2, 8, and 24 hours, investigating 12 different conditions. Solution treatments were carried out at 1000 and 1150 °C for 1 and 2 hours, observing four distinct states. On SHT samples at 1150 °C for 2 hours subsequently, ageing treatments were carried out at 600, 700, 800 and 900 °C, for 2, 8 and 24 hours studying 12 conditions. It should be noted that all the heat-treated IN625 samples were water quenched (WQ) to avoid any phases precipitation during cooling, as recommended in the literature for large sections [36].

Chapter 3

Results and discussion of IN625 produced by LPBF

The purpose of this chapter is to present the study on IN625 alloy produced by LPBF process using an EOSINT M270 Dual Mode. The work started with the powder characterisation to determine the particles size distribution, as well as their morphology, size and residual porosity. Afterward, it was performed a process parameters optimisation to define a good compromise between densification level and build-up rate. Besides, it was studied the effect of different process parameter on the microstructure, densification level, and hardness.

The above results were already published in an international scientific journal [56]. Afterward, the work was focused on studying the microstructure and phases of the as-built state. However, post heat treatments are fundamental to generate specific microstructure and mechanical properties to match industrial requirements. For this reason, different heat treatments were carried out on IN625 samples. More specifically, direct ageing treatments (without soluton-treatment), solution treatments, and ageing treatments were performed. The microstructure and hardness evolution of the heat-treated IN625 samples were studied and using hardness measurements, three different heat treatments were selected for further analyses.

On these three conditions was performed an in deep characterisation through TEM analysis and tensile test. Finally, the development of the tensile properties was correlated to microstructure and tensile fracture surfaces.

The main target of this work can be drawn:

1) Study and characterisation of the starting IN625 powder.
2) Process parameters optimisation of as-built IN625 samples.
3) Microstructural study of as-built IN625 samples.
4) Study of the microstructure evolution under specific heat treatments.
5) Study of the tensile properties of three selected heat-treated IN625 conditions compared to as-built one.

3.0 Powders characterisation

3.1 LPBF powder characterisation

FESEM Micrographs for gas atomised IN625 particles powder are displayed in Figure 28a, showing fairly regular spherical particles, with the presence of some elongated particles. The magnified view in Figure 28b reveals some satellite particles, highlighted by yellow arrows, caused by the gas atomised process.

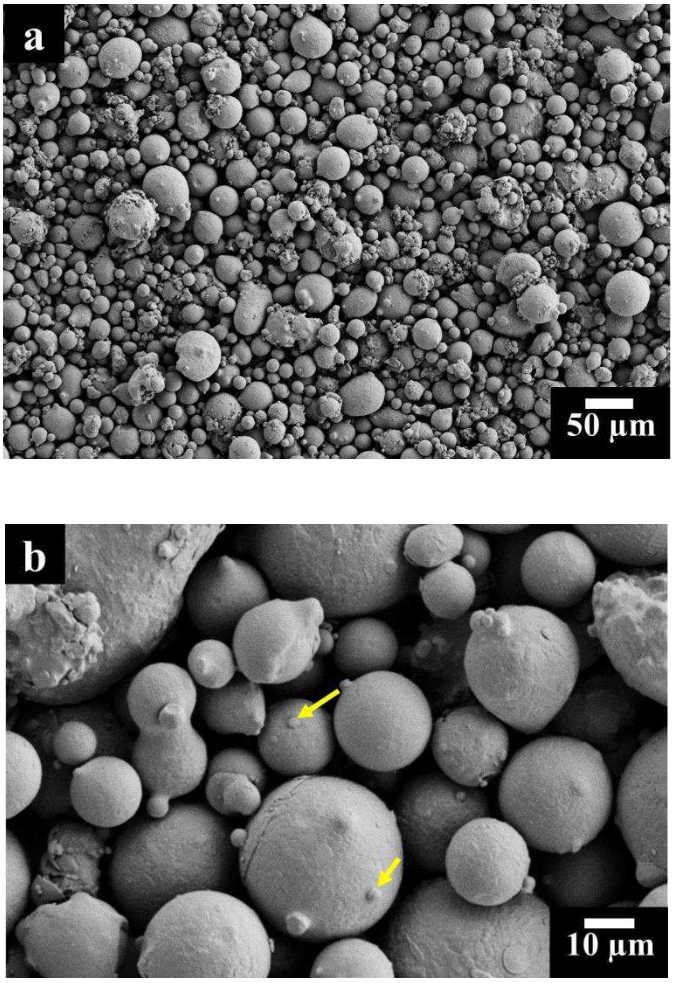

Figure 28: FESEM images of IN625 powder showing particles at different magnifications (a,b) in which satellite particles are indicated by the yellow arrows.

The powder particles were also mounted and polished to determine the residual porosity inside the particles. The particle cross-section, showing fine spherical pores with a size of 2 µm and 8 µm pointed out by red circles in Figure 29a and 29b. For the particles was estimated a residual porosity of about 0.040 %. This kind of pores can be ascribed to the entrapped gas during the LPBF process [53,90,121,122].

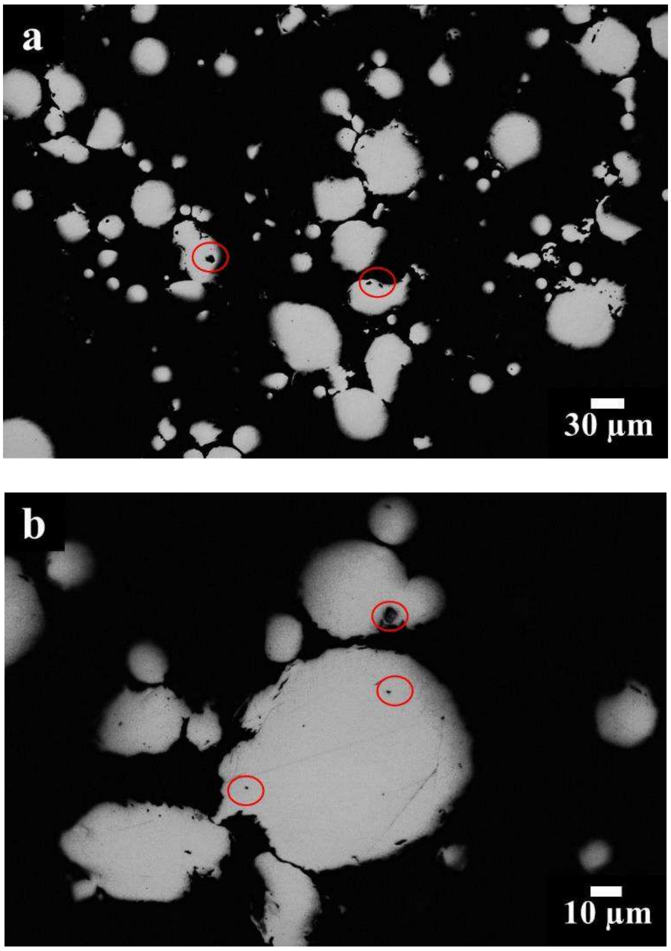

Figure 29: OM images of mounted IN625 powder particles cross section polished at different magnification (a, b) showing the presence of spherical pores, some of which are pointed out by red circles.

The EDS analysis of the LPBF powder presented a chemical composition in the range of the declared company data sheet and standard UNS N06625, as reported in Table 19. Ta was not determined by EDS analysis due to the very low quantity (less than 0.1 % wt), whereas C was not determined to avoid overestimation.

Table 19: EDS results of main chemical elements in weight percentage (wt %) for LPBF IN625 powder compared to company datasheet and standard UNS N06625.

Element	Company data sheet (wt %)	EDS powder (wt %)	UNS N06625 (wt %)
Ni	58.0 min.	64.2	58.0 min
Cr	20.0-23.0	21.6	20.0-23.0
Mo	8.0-10.0	8.5	8.0-10.0
Nb	3.15-4.15	3.6	3.15-4.15**
Ta	0.05 max	-	-
Fe	5.0max	0.6	5.0 max
Co	1.0 max	0.3	1.0 max
Si	0.5 max	0.3	0.5 max
Mn	0.4 max	0.3	0.5 max
Ti	0.4 max	0.3	0.4 max
Al	0.4 max	0.3	0.4 max
C	0.1 max	-*	0.10 max

not detected by EDS analysis due to overestimation; reported as Nb + Ta*

From Figure 30, the particle size distribution of the SLM powder can be observed. The particle size had a d(0.1), d(0.5) and d(0.9) of 16 µm, 27 µm, and 48 µm respectively. Besides, using an ultrasonic during the experiment, some agglomerate particles tend to disaggregate leading to higher detection of smaller particles, with subsequent modifications of d(0.5) and d(0.9) to a lower size of 25 µm and 34 µm, respectively. The tendency of LPBF powder particles to form aggregates is caused by its small diameters.

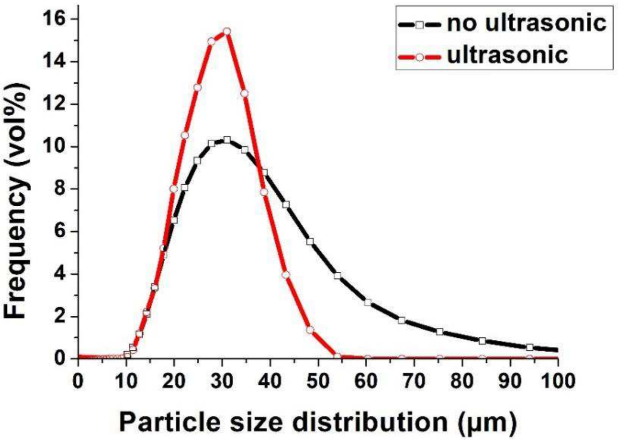

Figure 30: Particle size distribution determined using laser granulometry diffraction for LPBF powder with and without ultrasonic vibration.

The average values and standard deviations of apparent density, flowability and skeletal density are listed in Table 20. The results revealed that LPBF powder had a skeletal density of 8.47 ± 0.02 g/cm^3, which is compatible with the IN625 alloy theoretical density of 8.44 g/cm^3 [3].

The high skeletal density indicated that the particles had low residual porosity in agreement with the values of residual porosity determined during the particle cross-section analysis (see Figure 29). The apparent density was 4.09 ± 0.12 g/cm^3, whereas the flowability was 13.0 ± 0.4 s/ 200g.

It should be noted that the flowability was determined using the Carney flowmeter, since the powder did not flow in the Hall flowmeter due to a wide particle size distribution, as reported in the specification ASTM B964-09 and literature [86].

Table 20: Average value and standard deviation of Apparent density, Flowability and Skeletal density for IN625 powder.

IN625 powder	**Apparent density [g/cm^3]**	**Flowability [s/ 200g]**	**Skeletal density [g/cm^3]**
LPBF powder	4.09 ± 0.12	13.0 ± 0.4	8.47 ± 0.02

3.2 Process parameters optimisation

Figure 31 displays the Brinell hardness values versus residual porosity of the as-built IN625 samples produced adopting various process parameters (reported in paragraph 2.1.1).

The graph shows a hardness increment correlated to residual porosity reduction, with hardness mainly from 265 to 290 HBW and residual porosity around 0.04-0.20 %. However, the very high hardness increase of 25 HBW associated with a residual porosity reduction of around 0.16%, seem to indicate that the different process parameters had an impact on the microstructure features of the samples, giving a hardness increment. In fact, modifying the scan speed, hatching distance, as well as the laser power, lead to different thermal profile during the process, thus involving different melting and consequent cooling as well as solidification rates, generating different microstructures.

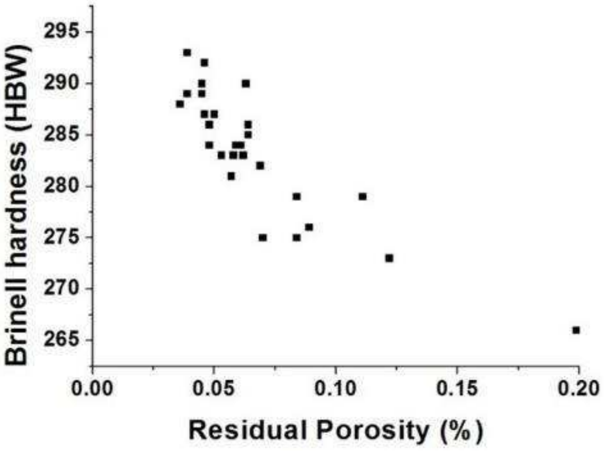

Figure 31: Brinell hardness vs residual porosity for as-built IN625 samples obtained by LPBF process.

Figure 32 displays the correlation between residual porosity and hardness to the energy density, clearly showing the effect of different energy density on the microstructure. From the graph, it is possible to observe how using high energy density around 3.0 – 4.5 J/mm^2 is possible to improve the hardness and densification of the IN625 samples.

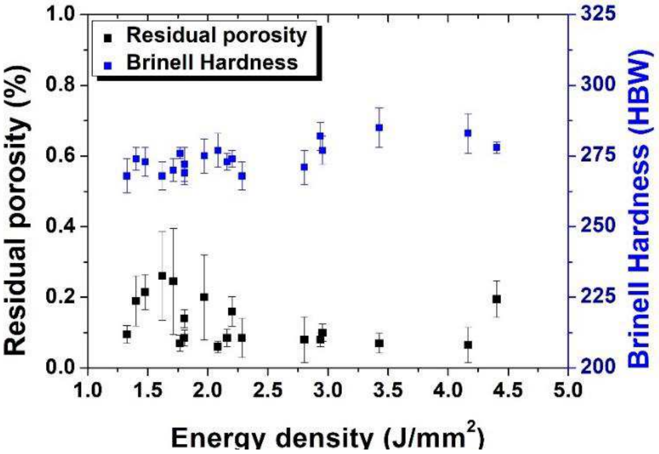

Figure 32: Residual porosity and Brinell hardness vs energy density for as-built IN625 samples obtained by LPBF process.

Table 21 summaries the process parameters, energy density correlated to the residual porosity and hardness determined during the experiment, in order to evaluate the effect of the single parameter.

The samples with the lowest porosity (0.0036 %) and highest hardness (293 HBW) were fabricated using the same scan speed of 900 mm/s and hatching distance of 0.07 mm.

By contrast, a laser power of 185 W and 175 W was employed to fabricate the samples with the lowest porosity and the highest hardness, respectively, although the difference is almost neglectable.

The reduction of hatching distance causes a greater number of laser scanning and melt pools that may improve the densification levels and also allow the formation of more precipitates or segregate elements. Furthermore, the results highlight that slower scan speed of 1200 mm/s seems to improve the densification levels slightly, although the residual porosity was below 0.2 %. However, regarding the high densification levels obtained a scan speed of 1200 mm/s can be suitable for the industrial production, in order to improve the build-up rate.

Table 21: Different process parameters and energy density used for fabricating IN625 specimens with the determined residual porosity and hardness [56].

Sample	P [W]	V [mm/s]	h_d [mm]	E_D [J/mm^2]	Residual porosity [%]	Brinell hardness [HBW]
S1	185	1200	0.07	2.20	0.050 ± 0.014	287 ± 3
S2	185	600	0.11	2.80	0.069 ± 0.024	282 ± 3
S3	175	900	0.11	1.77	0.063 ± 0.011	290 ± 4
S4	185	600	0.09	3.43	0.046 ± 0.008	287 ± 3
S5	185	900	0.09	2.28	0.039 ± 0.007	289 ± 4
S6	185	1200	0.11	1.40	0.084 ± 0.021	275 ± 2
S7	185	900	0.07	2.94	0.036 ± 0.009	288 ± 4
S8	175	1200	0.11	1.33	0.122 ± 0.038	273 ± 2
S9	195	600	0.11	2.95	0.058 ± 0.009	283 ± 2
S10	175	600	0.07	4.17	0.048 ± 0.011	284 ± 4
S11	175	1200	0.09	1.62	0.084 ± 0.018	279 ± 2
S12	175	1200	0.07	2.08	0.045 ± 0.013	289 ± 3

S13	185	1200	0.09	1.71	0.062 ± 0.008	283 ± 3
S14	175	900	0.09	2.16	0.053 ± 0.011	283 ± 4
S15	185	600	0.07	4.40	0.061 ± 0.025	284 ± 4
S16	195	1200	0.11	1.48	0.199 ± 0.025	266 ± 4
S17	195	900	0.11	1.97	0.089 ± 0.016	276 ± 4
S18	195	600	0.09	3.61	0.057 ± 0.015	281 ± 6
S19	195	900	0.07	3.10	0.048 ± 0.012	286 ± 5
S20	185	900	0.11	1.87	0.059 ± 0.017	284 ± 6
S21	195	900	0.09	2.41	0.045 ± 0.013	290 ± 2
S22	175	600	0.11	2.65	0.111 ± 0.023	279 ± 2
S23	195	1200	0.07	2.32	0.046 ± 0.012	292 ± 5
S24	175	600	0.09	3.24	0.070 ± 0.025	275 ± 3
S25	175	900	0.07	2.78	0.039 ± 0.015	293 ± 4
S26	195	600	0.07	4.64	0.064 ± 0.020	286 ± 4
S27	195	1200	0.09	1.81	0.064 ± 0.014	285 ± 3

3.3 Investigation of defects of as-built IN625 samples

Figure 33 reveals the optical images of polished IN625 samples S7 and S16, which are the sample with the lowest porosity and the samples with the highest porosity, respectively.

For the S7 samples, the micrograph (Figure 33a) mainly revealed occasional fine isolated spherical pores with the largest ones detected around 4-5 µm, whereas for the S16 samples the micrograph (Figure 33b) chiefly showed homogeneous distributed spherical pores, the largest ones around 5-7 µm.

These spherical pores, some of which highlighted by red circles in Figure 33a and 33b, can derive from the entrapped gas in the starting powders that is released when the laser beam melts the powder, causing small pores in the molten melt pool [56].

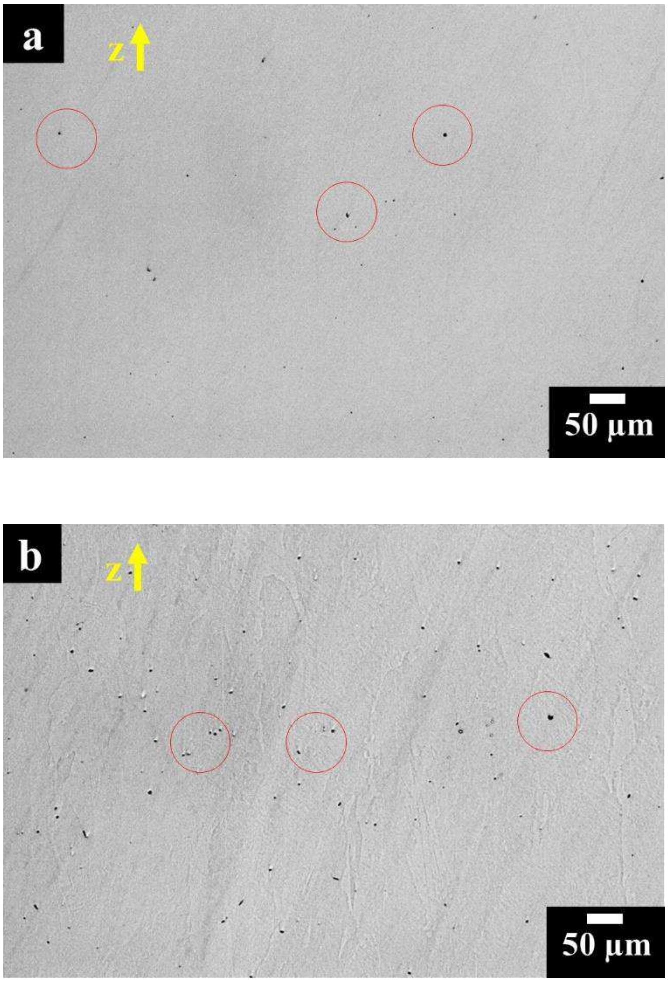

Figure 33: OM images of polished IN625 samples built using different process parameters (a) S7 and (b) S16 along the building direction, showing different spherical pores, where some of which are highlighted by red circles.

3.4 Microstructure of as-built IN625 samples

The following characterisation was performed on IN625 samples processed using a laser power of 195 W, a scan speed of 1200 mm/s and a hatching distance of 0.09 mm, in order to guarantee a compromise between the build-up rate and densification level (porosity 0.064 ± 0.014 %).

Figure 34 shows a 3D composite OM image of an as-built IN625 sample along different planes. As can be observed from the micrograph, the microstructure of as-built IN625 samples are made up of columnar grains (CGs) developing epitaxially, thus crossing several melt pools along the building direction (z-axis), with a length generally from 400 to 5 µm. On the contrary, the microstructure mostly consists of equiaxed grains (EGs) with size from 5 to 100 µm, perpendicular to the building direction (x-y plane). Krietcber et al. [123] reported for the as-built IN625 samples mostly equiaxed grains with similar size to those determined during our investigation.

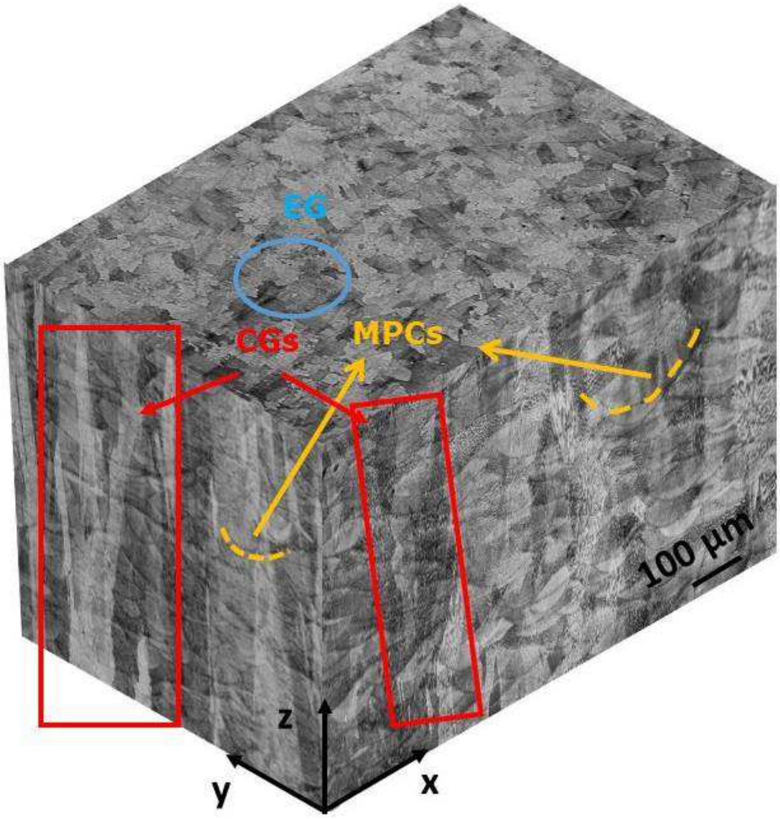

Figure 34: 3D optical image composite of as-built IN625 sample showing columnar grains (CGs) and melt pool contours (MPCs) along the building direction and equiaxed grains (EG) perpendicular to the building direction (x-y plane); Kalling's No.2 etchant was used.

Figure 35 displays another 3D composite OM image of an as-built IN625 sample along different plane, etched with another reagent. In this case, it is possible to observe the difference melt pool contours (MPCs) along the building direction (z-axis) and perpendicular to the building (x-y plane) both highlights by orange lines. The melt pools are not alienated along the building direction caused by the EOS scanning strategy involving a scanning laser beam rotation of 67° between two consecutive layers [56,77,87].

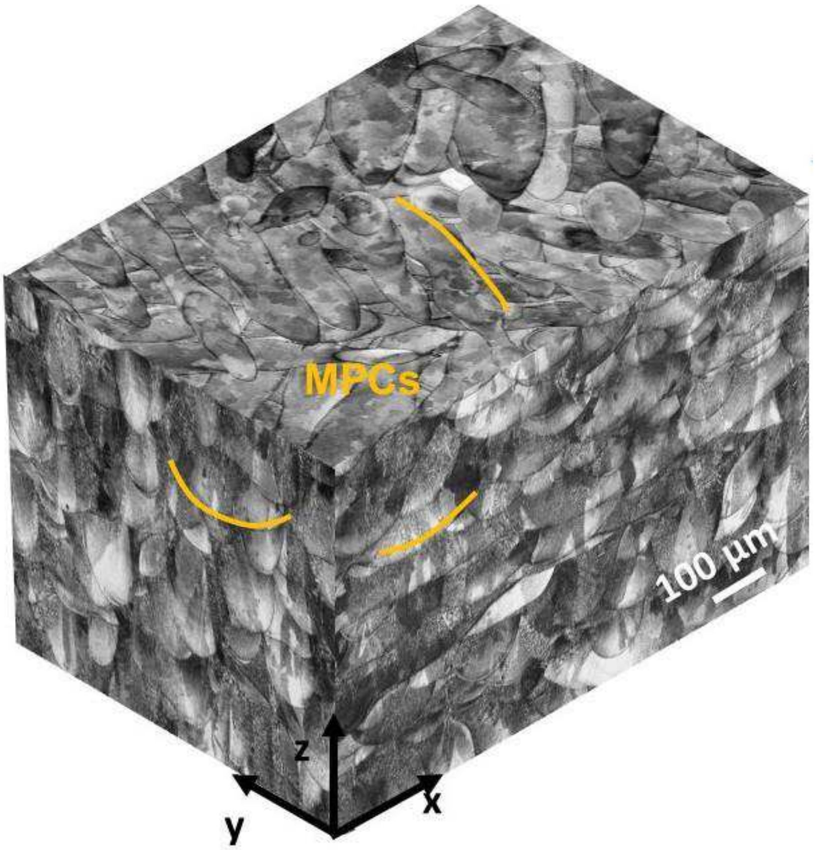

Figure 35: 3D optical image composite of as-built IN625 sample showing the melt pool contours (MPCs) along the building direction (z-axis) and perpendicular to the building direction (x-y) plane; Mixed acids reagent was used.

Figure 36a reveals the FESEM image of as-built IN625 samples along the building direction, showing that the melt pools are made up of very fine primary dendritic structures.

These primary dendrites had both cellular and columnar shapes as can be observed in Figure 36b. The cellular dendrites structures are believed to be associated with alteration of columnar dendrite structures caused by very high cooling rates, as reported in literature [124].

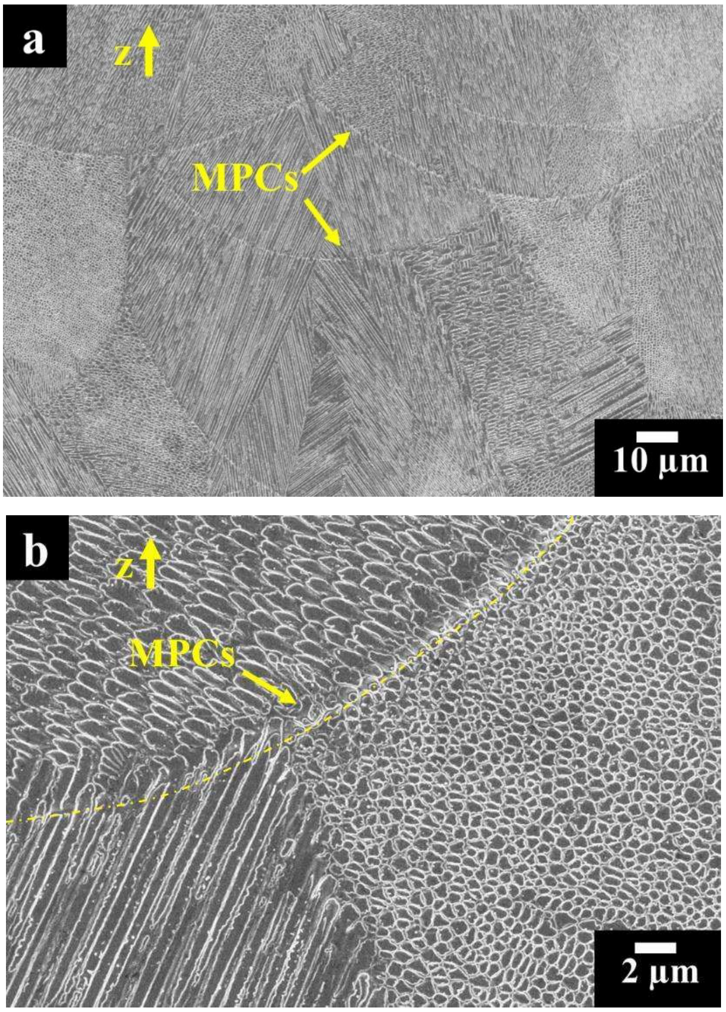

Figure 36: FESEM images at different magnification (a, b) exhibiting melt pools with columnar and cellular primary dendrites for as-built IN625 sample; Mixed acids reagent was used.

Furthermore, it is interesting to note that the high heating and cooling rates of the process do not allow the full formation of secondary dendritic structures.

The cellular dendritic structures have a size between 300 nm to 1 µm, whereas the primary dendritic arms spacing (PDAS) of columnar dendrites were determined 0.7 ± 0.3 µm. The determined values of PDAS are compatible with other research activities on IN625 and nickel based superalloys produced by the LPBF process [55,60,66].

At higher magnification (Figure 37a and 37b) very fine bright precipitates along the dendritic areas indicated by arrows 1 and bright elongated phases along the interdendritic regions pointed out by arrows 2 can be observed.

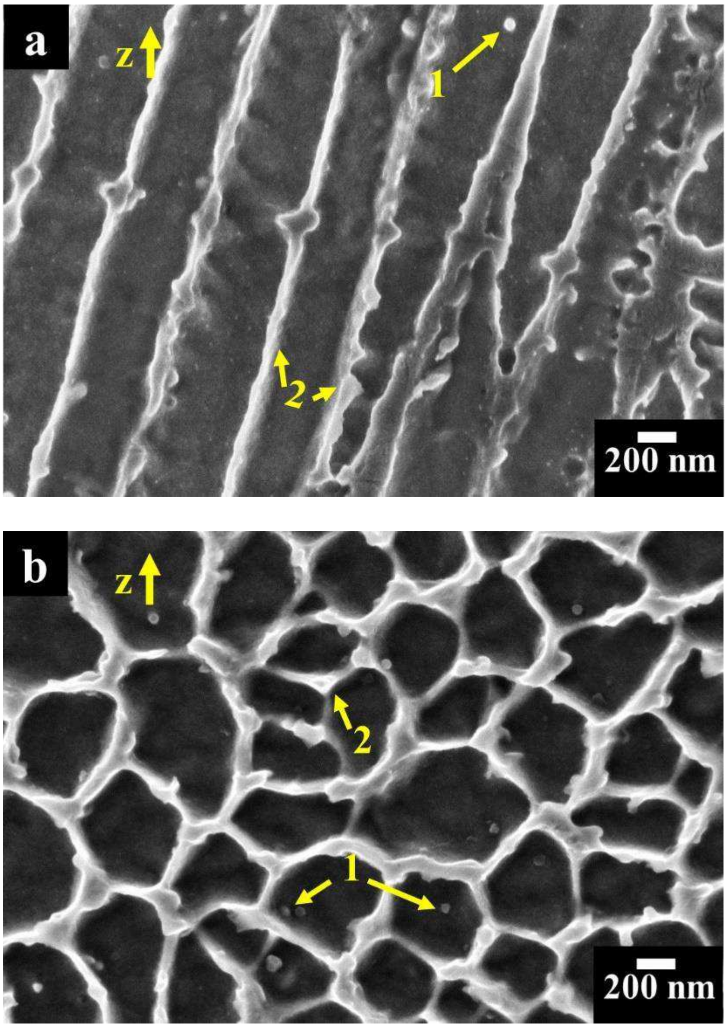

Figure 37: FESEM images of as-built IN625 sample at high magnification showing: (a) columnar dendritic structures with nanoprecipitates indicated by arrow 1 and segregation of Nb and Mo within the interdendritic zones indicated by arrow 2; (b) cellular dendritic structures with nanoprecipitates indicated by arrow 1 and segregation of Nb and Mo within the interdendritic areas indicated by arrow 2 exhibiting melt pools with columnar and cellular primary dendrites for as-built IN625 sample; Mixed acids reagent was used.

The very high cooling rates generate high density of tangled dislocations mainly located in the interdendritic regions, as can be seen in TEM image in Figure 38a. Indefinite precipitate-like features can be noted in the interdendritic regions as pointed out by arrow 1 in Figure 38b. EDS analysis reported a relatively high concentration of Nb and C for these precipitates, suggesting the early stage formation of fine MC carbides.

Besides, EDS results revealed enrichment in Nb and Mo within the interdendritic areas, as highlighted by arrow 2 in Figure 38c. These areas indicated possible segregation of Nb and Mo due to their elevated tendency to segregate with interdendritic and grain boundary areas, as confirmed by the literature [32,125,126].

Furthermore, TEM image (Figure 38d) showed in detail the hexagonal morphology of these precipitates within the dendritic core that have a size around 10-50 nm. These phases are enriched in Nb, C and coherent with the austenitic matrix, as detailed in the inset in Figure 38d, indicating the formation of Nb-rich MC carbides due to eutectic reaction [5,32,125].

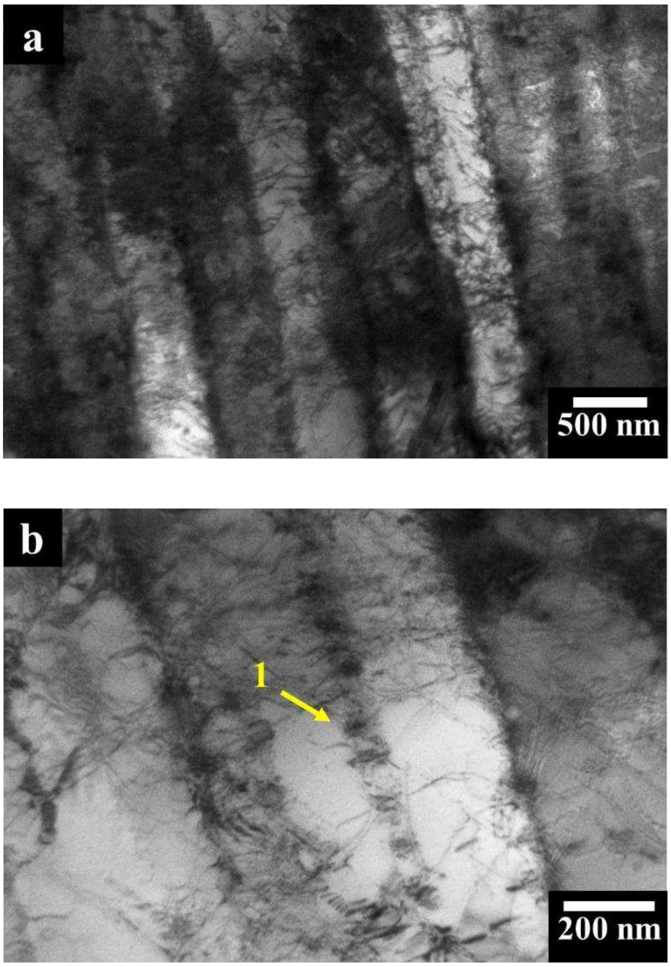

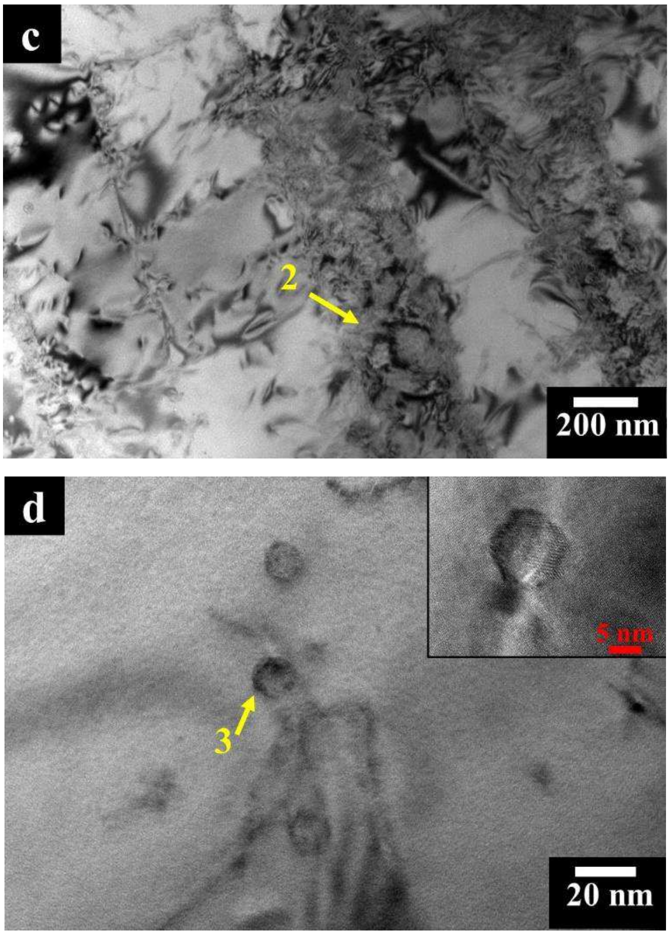

Figure 38: TEM bright field images exhibiting: a) columnar dendrite structures with high density of dislocation chiefly positioned in the interdendritic regions; b) precipitates along the interdendritic areas indicated by arrow 1; c) Elements segregation along the interdendritic regions indicated by arrow 2; d) Nb-rich MC carbides within the dendritic areas pointed out by arrow 3 with the inset showing the coherency with the matrix.

The presence of nanometric Nb-rich MC carbides is originated from eutectic reaction during solidification ($L \rightarrow \gamma + MC$) T~1250 °C [31,125]. They should be mostly formed along the interdendritic areas which are enriched in Nb, C and other segregated elements.

However, the very high cooling rates generate a supersaturated solution in which a part of the highly segregated elements (e.g. Nb, C) remain entrapped in the dendritic core, as reported in literature for the LPBF process [55,60]. The supersaturated state is also denoted by the presence of very fine Nb-rich MC carbides within the dendritic core.

The eutectic reaction during the solidification can promote the Laves phases formation (L → γ + Laves phases) T~1200 °C, which can have elongated irregular shapes and appear as bright phases during FESEM investigation [31,125]. However, during the TEM investigation, no Laves phases were found, and these bright areas seem to be elements segregation.

The presence or absence of Laves phases is mainly correlated to the chemical composition of the starting powder. In fact, it was reported that a high C/Nb ratio promotes the precipitation of Nb-rich MC carbides without formation of Laves phases, as well as a low concentration of Si and Fe can decrease their formation [5].

3.4.1 XRD analysis on as-built IN625 samples

Figure 39 compares the XRD spectra of as-built IN625 samples along the building direction (z-axis) and perpendicular to the building direction (x-y plane). The XRD spectra only revealed the presence of solid solution γ-fcc austenitic phase with a lattice parameter of around 3.59 Å for both the planes.

It is interesting to note a very strong (200) orientation along the x-y plane, as well as a strong (111) orientation along the z direction. It is stated that Inconel alloys produced by LPBF or electron beam melting (EBM) processes can involve particular crystallographic texture [64,87,123].

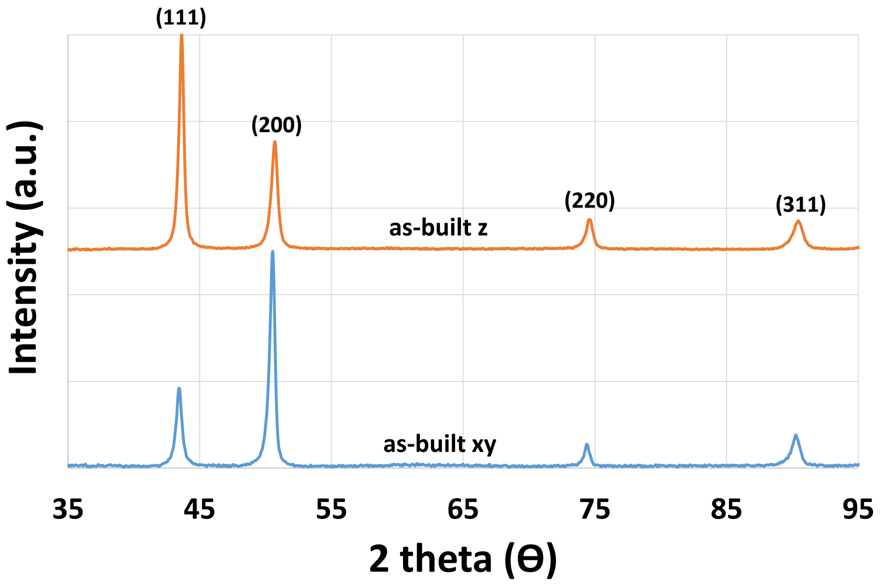

Figure 39: XRD spectra of as-built IN625 samples along x-y plane and z direction.

3.4.2 Thermal mechanical analyses on as-built IN625 samples

The CTE of as-built samples built both along x-y plane and z direction are reported in Figure 40, showing very similar curves for both the samples.

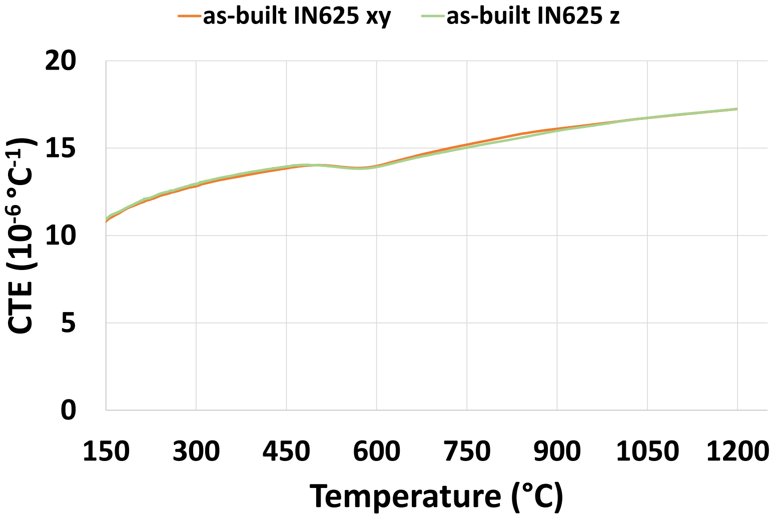

Figure 40: Coefficient of thermal expansion (CTE) vs temperature of as-built IN625 samples built along x-y plane and z direction.

The TMA curves revealed a deflection around 550-650 °C that may be caused by phases precipitation. The average values of the obtained CTE values were compared with available data on IN625 alloy at different temperatures, showing a good agreement, as reported in Table 22.

Table 22: Average CTE for as-built IN625 samples and commercially available IN625 alloy at different temperatures.

T (°C)	538	649	760
CTE (10^{-6} °C^{-1}) [37]	14.0	14.8	15.3
CTE (10^{-6} °C^{-1}) as-built xy	14.1	14.5	15.3
CTE (10^{-6} °C^{-1}) as-built z	14.1	14.5	15.2

The thermal conductivity (K) of as-built samples built along the two different orientaton are reported in Table 23, showing K slighly higher than values commercially available.

Table 23: Average K for as-built samples and commercially available IN625 alloy at different temperatures.

T (°C)	600	800	1000
K (W/ m °C) as-built z	20.8 ± 0.4	22.7 ± 0.4	25.0 ± 0.9
K (W/ m °C) as-built xy	22.8 ± 2.0	24.2 ± 1.4	26.4 ± 1.0
K (W/ m °C) [37]	19.0 (649 °C)	20.8 (760 °C)	25.2 (982 °C)

3.4.3 Tensile behaviour of as-built IN625 samples

The tensile engineering stress-strain curves of three as-built IN625 specimens are illustrated in Figure 41.

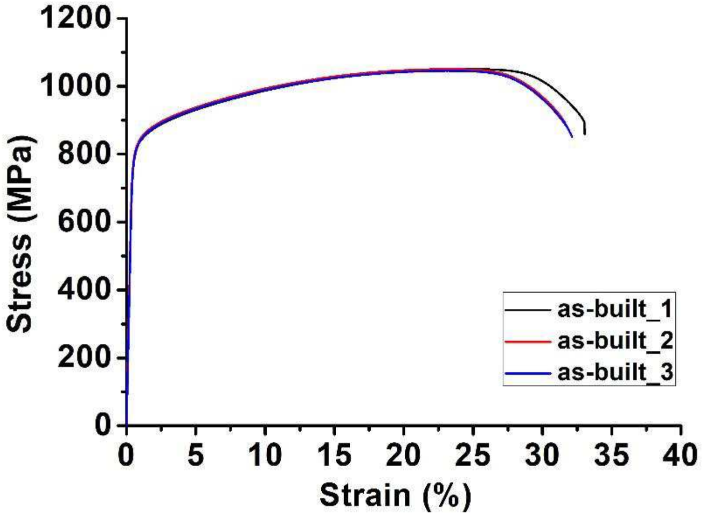

Figure 41: Tensile stress-strain curve for three as-built IN625 samples.

The tensile properties of as-built specimens compared to the yield strength (YS), ultimate tensile strength (UTS) and ductility (A) of other LPBF as-built IN625 and wrought IN625 alloy are listed in Table 24.

The as-built IN625 samples exceed the minimum requirements for LPBF IN625 alloy presented in the ASTM F3056-14 standard.

Besides, the as-built IN625 samples revealed tensile properties compatible with the IN625 samples produced by EOS company, although the studied IN625 samples had lower standard deviation than company IN625 ones. This difference can be caused by different process parameters used to fabricate the samples.

The tensile properties of LPBF-built IN625 samples compared with other investigations, showed the tensile properties of as-built samples had YS and UTS similar to as-built LPBF IN625 processed by Yadroitsev et al. [127]. However, they determined a porosity lower than 1%, whereas a porosity of 0.064 ± 0.014% was determined during this investigation, so the divergence in ductility can be attributed to different densification levels.

On the contrary, the elongation at break of IN625 processed by Wang et al.[128] showed similar values to the present as-built IN625 samples, but remarkable lower YS and UTS were reported in their study.

In this case, the variation of tensile strengths can be associated with the use of different process parameters and scanning strategy, as pointed out in the literature [129]. Regarding the minimum tensile properties of commercially available wrought IN625 alloy, it is possible to note that as-built samples revealed higher strength and similar ductility with respect to as-rolled IN625 alloys [37].

The high tensile properties of these materials derived from the very fine dendritic architectures together with high dislocation density owing to the fast solidification and cooling rates of the LPBF process.

Finally, Young's modulus (E) of as-built IN625 determined by tensile test showed a value of 182 ± 13 GPa, whereas using a IMCE test was determined a value of 186 ± 2 GPa (using samples built along xy).

Table 24: Comparison of tensile properties of as-built specimens fabricated along the x-y plane, together with other LPBF-built IN625 along the x-y plane reported in other works and specifications as well as wrought IN625 alloys.

IN625 sample	E (GPa)	YS (MPa)	UTS (MPa)	A (%)
This study				
As-built	182 ± 13	783 ± 23	1041 ± 36	33 ± 1
Other works and specifications				
LPBF ASTM F3056-14	-	275 (min)	485 (min)	30 (min)
LPBF*[110]	170 ± 20	725 ± 50	990 ± 50	35 ± 5
LPBF [127]	-	800 ± 20	1030 ± 50	8-10
LPBF [128]	196 ± 12	641.5 ± 23.5	878.5 ± 1.5	30 ± 2
As-rolled [37]	-	414 (min)	827 (min)	30 (min)

**As-built state according to EOS data sheet;*

3.4.4 Fracture surface of as-built IN625 tensile samples

The fracture surfaces of as-built IN625 tensile specimens were examined under SEM. The fracture surface showed a ductile fracture mode correlate to microvoids coalescence, some of which could be generated by gas porosity (Figure 42a).

However, also some brittle fractures transgranular cleave like facets can be observed as indicated by the arrows in Figure 42b, as already observed for IN625 samples [129]. It is possible to presume that the brittle fractures can be promoted by the segregation of Nb and Mo in the interdendritic regions. The very fine dimples are illustrated in Figure 42c.

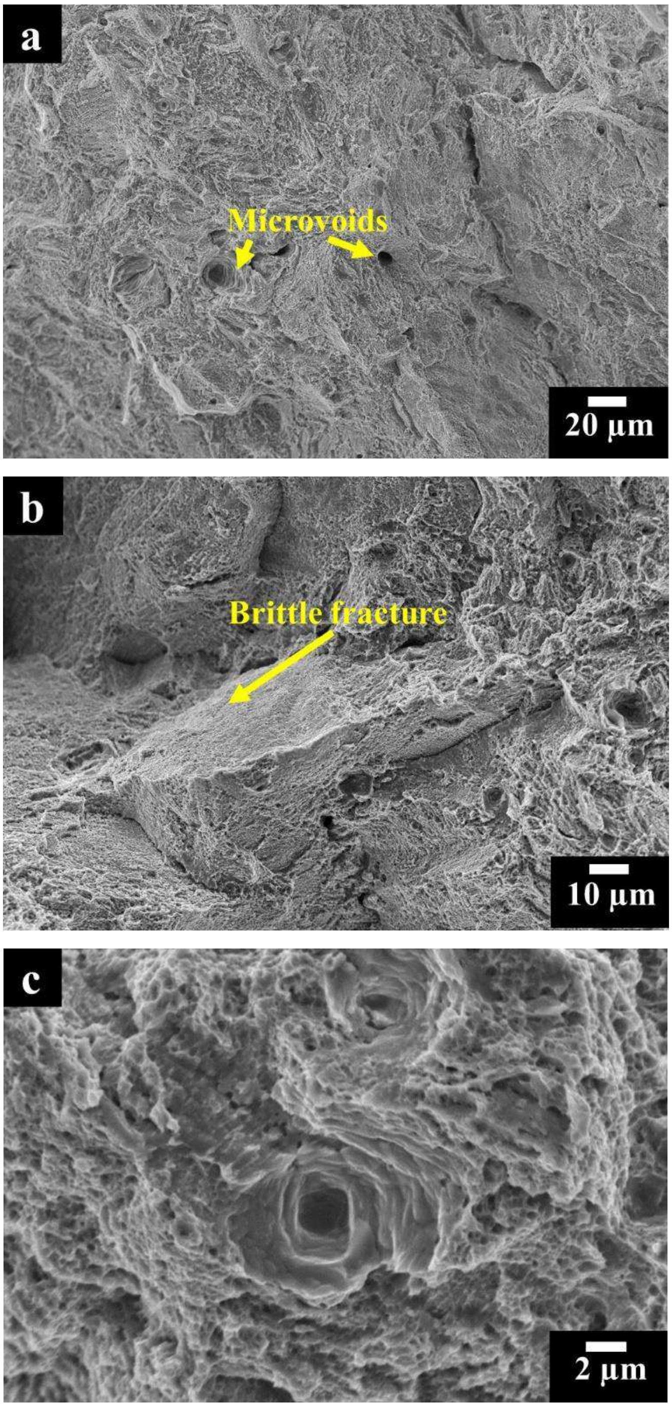
a
Microvoids
20 µm
b
Brittle fracture
10 µm
c
2 µm

Figure 42: SEM images of as-built IN625 tensile fracture surface: a) low magnification exhibiting ductile and brittle fracture surfaces; b) higher magnification exhibiting brittle surface fractures; c) higher magnification showing fine dimples and microvoids.

3.5 Investigation on direct aged IN625 conditions

3.5.1 Hardness investigation

The hardness of as-built and direct aged IN625 samples at different temperatures and times are reported in Figure 43 and Table 25.

As can be noted, the greatest hardness values were obtained with heat treatments performed at 700 °C and 800 °C for 24 hours. By contrast, heat treatments performed at 600 °C and 900 °C did not lead to significantly hardness improvement.

It is interesting to observe that heat-treated IN625 samples at 700 °C for 2 hours revealed a hardness increase of around 10%, whereas a thermal exposure at 600 °C and 900 °C for 2 hours did not significantly change the hardness with respect to the as-built state.

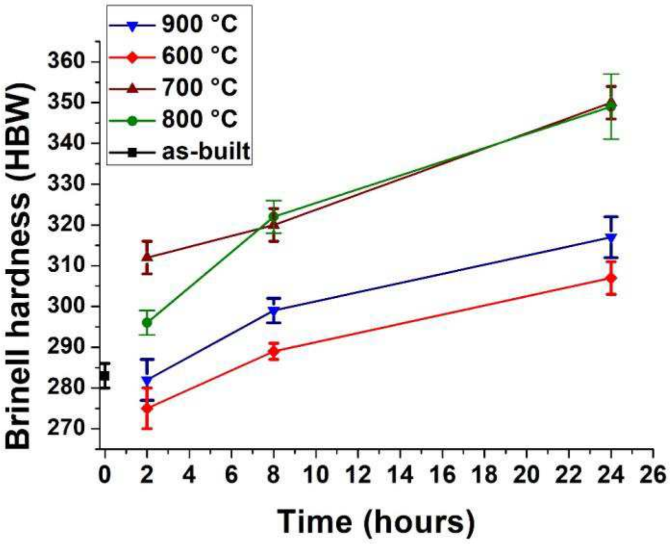

Figure 43: Brinell hardness of as-built and direct aged IN625 samples at 600 °C, 700 °C, 800 °C, 900 °C for 2 hours, 8 hours and 24 hours, respectively.

Table 25: Brinell hardness values of direct aged IN625 samples; starting condition 285 ± 3 HBW of as-built IN625 samples.

/	Temperature (°C)			
Time (h)	600	700	800	900
2	275 ± 5	312 ± 4	296 ± 3	282 ± 5
8	289 ± 3	320 ± 4	322 ± 4	299 ± 3
24	307 ± 4	350 ± 4	349 ± 6	317 ± 5

The microstructure of the direct aged IN625 samples will be discussed in the following sections. For the aged condition that revealed the highest hardness (700 °C for 24 hours) will be studied more in deep its microstructure and its tensile properties. In this case, it was not selected the direct aged at 800 °C for 24 hours, since a similar thermal exposure promote the formation of δ phases that is detrimental to the mechanical properties[5,15,39]. On the contrary, the thermal exposure at 700 °C should promote the formation of fine γ″ phases which is the main strengthening precipitate in IN625 alloy [5,15].

3.5.2 Microstructure of IN625 samples direct aged at 600 °C

The OM images of the direct aged IN625 samples at 600 °C for 2 h, 8 h as well as 24 h are shown in Figure 44a, 44b and 44c, respectively.

The three direct aged samples revealed a very similar microstructure to each other, showing the MPCs and CGs having size analogous to as-built IN625 state.

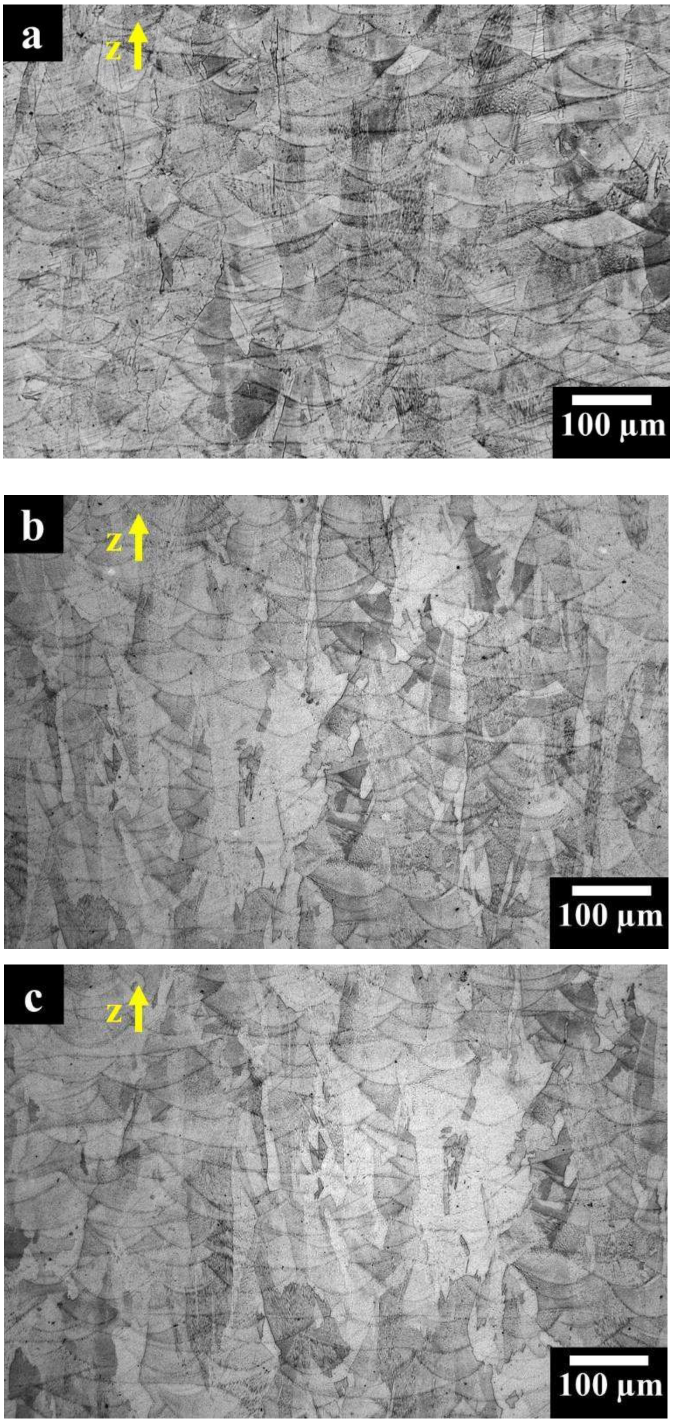
a
z
100 µm
b
z
100 µm
c
z
100 µm

Figure 44: OM images of direct aged IN625 samples at 600 °C for 2 h (a), 8 h (b) and 24 h (c) along the building direction; kalling's No.2 etchant was used.

At higher magnification, OM images of direct aged samples at 600 °C for 2 hours (Figure 45a), 8 hours (Figure 45b), and 24 hours (Figure 45c) did not reveal significant modification with respect to the as-built state.

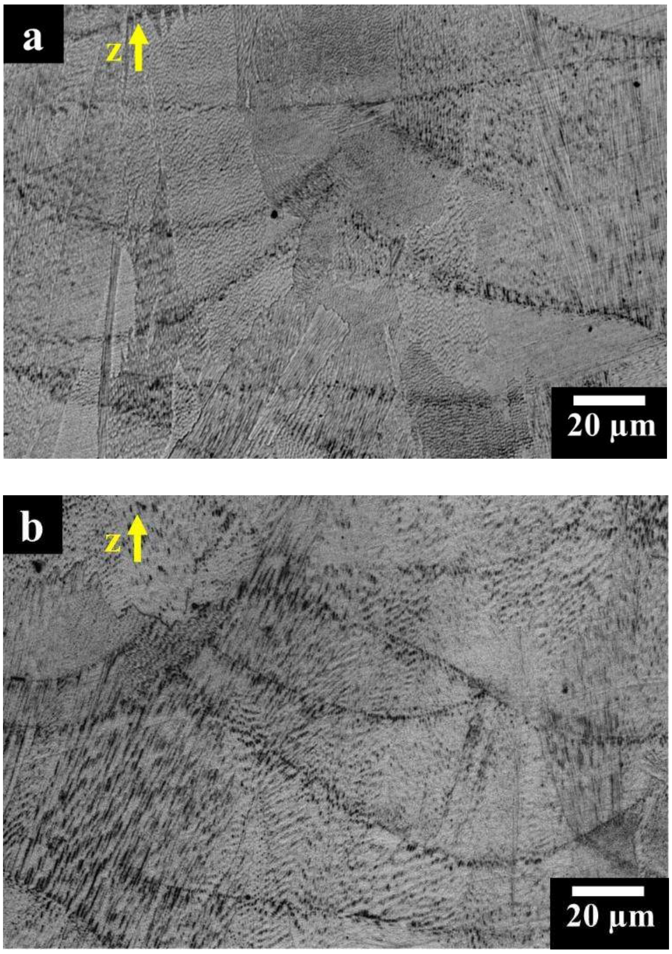

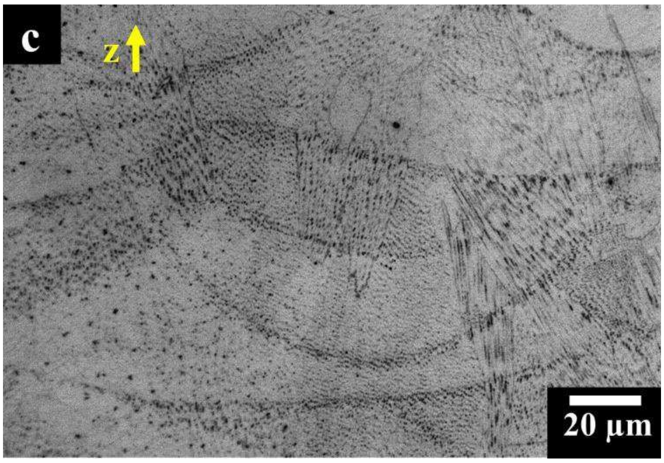

Figure 45: OM images at high magnification of direct aged samples at 600 °C for 2 hour (a), 8 hours (b) and 24 hours (c) showing melt pools contours and fine dendritic structures. Kalling’s No.2 etchant was used.

FESEM images of the direct aged sample at 600 °C for 200 hours (Figure 46a and 46b) display the grain boundaries (GBs) as well as MPCs.

Comparing the FESEM images at a higher magnification of direct aged (Figure 46c) and as-built IN625 state (Figure 46d) is possible to note a very similar dendritic structure consisted of fine precipitates, identified as Nb-rich MC carbides for the as-built state. Besides, Nb and Mo segregations in the interdendritic areas can be observed.

According to the literature, a similar heat treatment should start promoting the formation of very fine γ″ phases that can explain the hardness increase of around 8 % with respect to the as-built condition [5,39].

However, the very fine dimensions of γ″ phases make difficult to discern them from carbides by means of FESEM analysis.

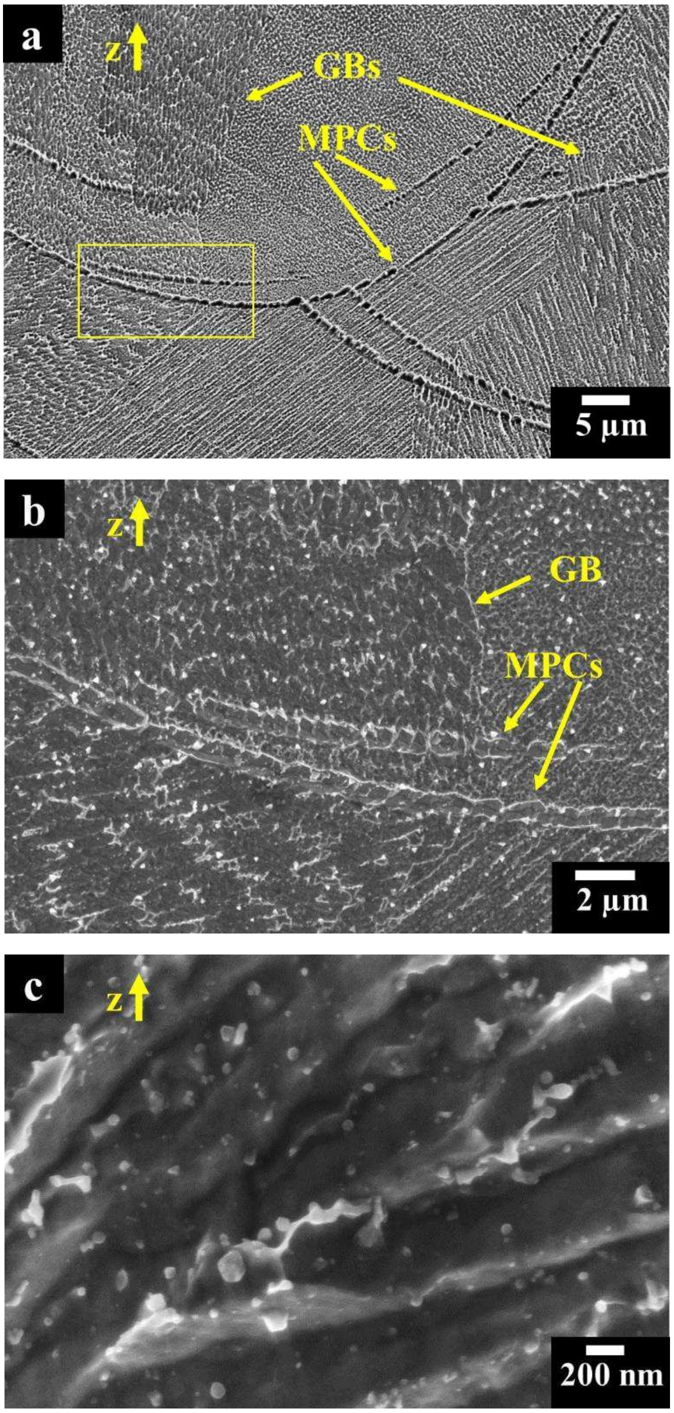
a
z
GBs
MPCs
5 µm
b
z
GB
MPCs
2 µm
c
z
200 nm

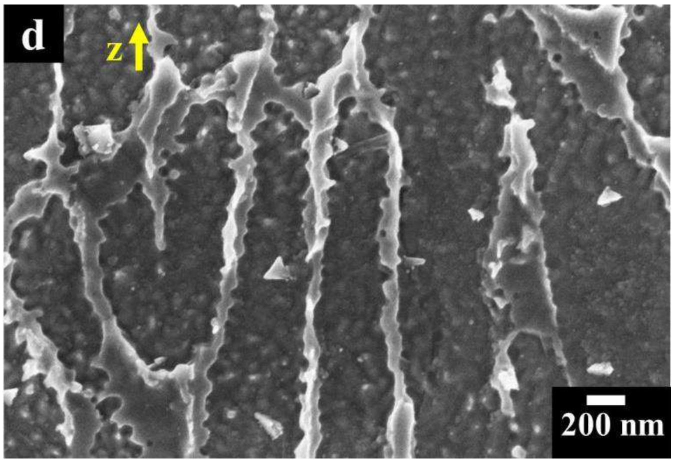

Figure 46: FESEM images of IN625 sample direct aged at 600 °C for 24 hours showing: a) melt pools contours (MPCs) and (GBs) of columnar grains; (b) higher magnification of a GBS and MPCs; (c) the dendritic structures and fine precipitates; (d) Dendrite structures and fine precipitates of as-built IN625 samples to compare with the aged condition. Kalling's No.2 etchant was used.

3.5.3 Microstructure of IN625 samples direct aged at 700 °C

The OM images of the direct aged IN625 samples at 700 °C for 2 h, 8 h as well as 24 h are shown in Figure 47a, 47b and 47c, respectively. The microstructure at low magnification resulted to be very similar to as-built materials, showing the MPCs and CGs.

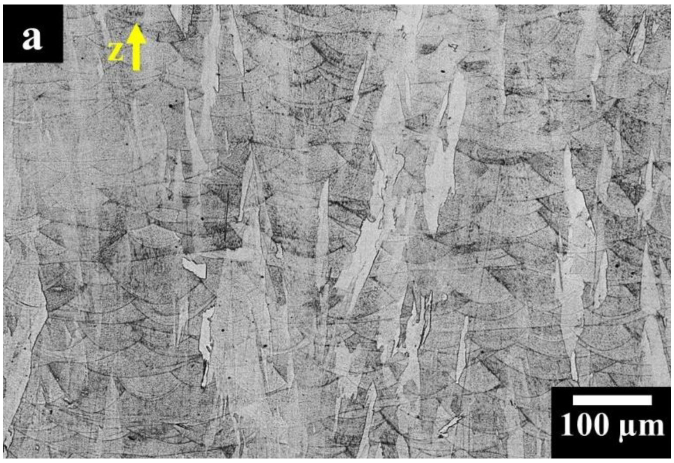

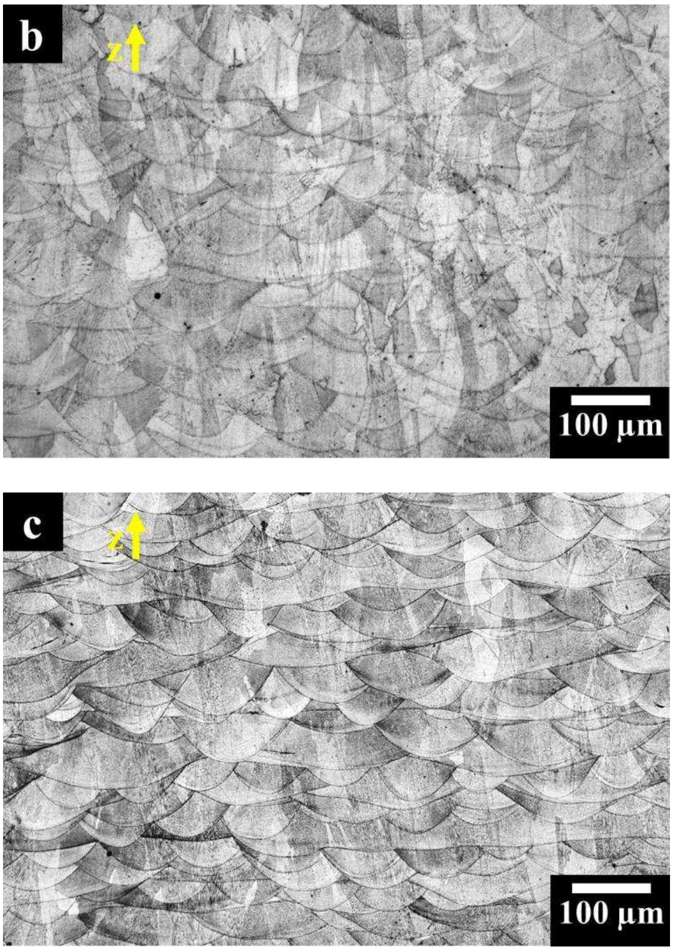

Figure 47: OM images of direct aged IN625 samples at 700 °C for 2 h (a), 8 h (b) and 24 h (c) along the building direction; kalling's No.2 etchant was used.

At higher magnified view, OM images of direct aged samples at 700 °C for 2 hours (Figure 48a) 8 hours (Figure 48b) and 24 hours (Figure 48c) did not denote the formation of coarse precipitates.

Therefore, the high hardness improvement must derive from the formation of nanometric phases, not visible by OM investigation.

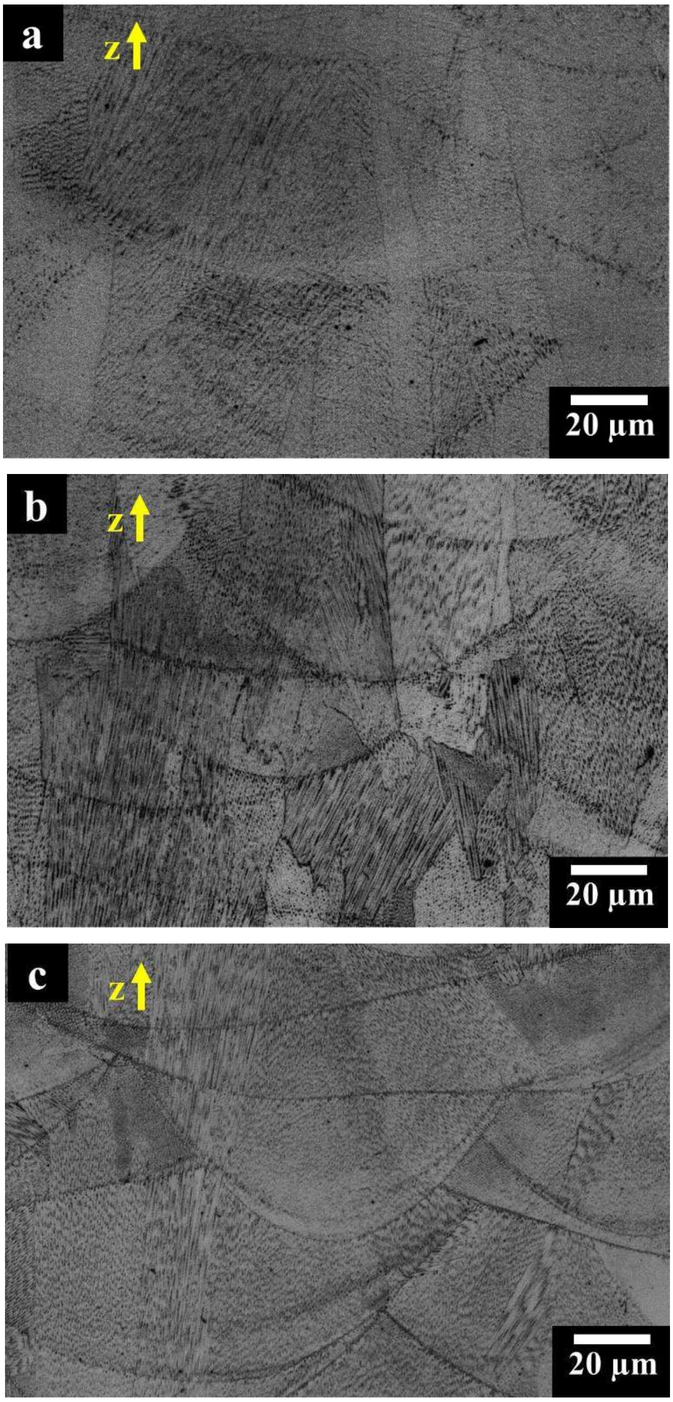

Figure 48: OM images at high magnification of direct aged samples at 700 °C for 2 hour (a), 8 hours (b) and 24 hours (c) showing melt pools contours and fine dendritic structures. Kalling’s No.2 etchant was used.

FESEM images (Figure 49a, 49b and 49c) of the direct aged sample at 700 °C for 24 h revealed dendritic architectures with shape and size similar to the as-built state.

From Figure 49b, can be observed some sub-micrometric elongated phases (one of them pointed out by a yellow circle) along the grain boundaries. Besides, at higher magnification (Figure 49c), it is evident the presence of very fine nanometric precipitates attributed to the formation of γ″ phases.

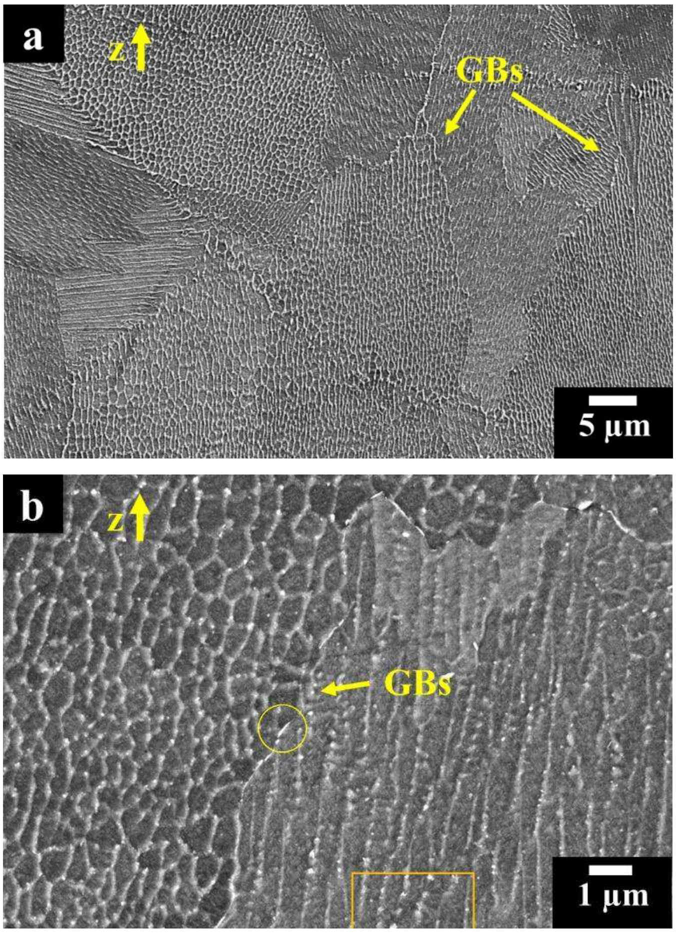

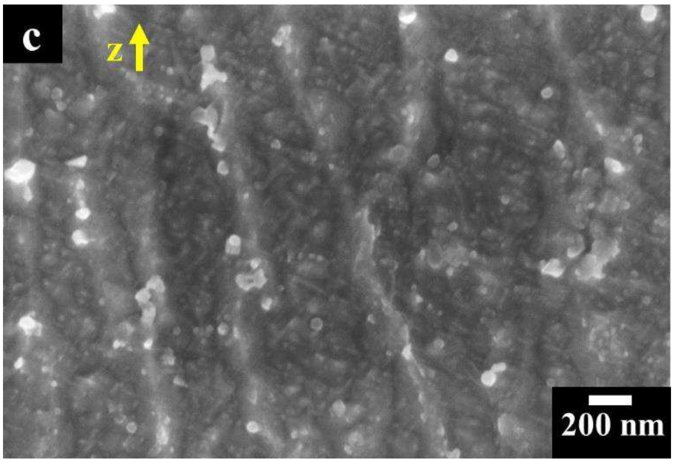

Figure 49: FESEM images showing: (a) columnar grains and grain boundaries (GBs; (b) fine dendritic architectures and some elongated precipitates along the GBS; (c) the formation of very fine γ″ phases within the dendrite core; Kalling's No.2 etchant was used.

The TEM image (Figure 50a) shows slightly less definited high density of tangled dislocations in the interdendritic zones similar to the as-built materials, together with Nb-rich precipitate-like lines.

However, the thermal exposure involved the formation of fine elongated precipitates and fine γ″ phases with a size around 10-30 nm. According to the literature, these elongated precipitates should be Cr-rich $M_{23}C_6$ carbides, although the very low quantity of carbon may indicate that a part of the elongated precipitates may be Nb-rich precipitates such as δ phases or Laves phases. In fact, the grain boundaries could have an enrichment in segregated element, promoting their formation for shorter time with respect to the TTT diagram of IN625 alloy.

The γ″ phases were inhomogeneous scattered, observing some clusters of γ″ precipitates together with γ″-depleted zones (Figure 50b).A similar phenomenon may derive from inhomogeneous solute concentration (especially Nb) due to the very fast solidification, generating Nb-rich and Nb-depleted region in the dendrites core.

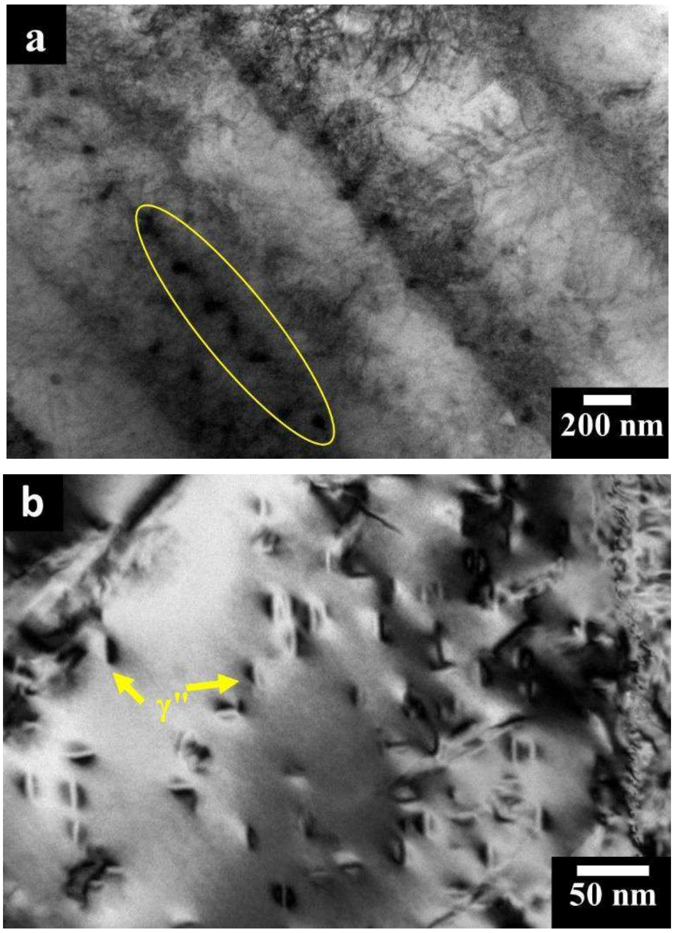

Figure 50: TEM bright field images: c) exhibiting columnar dendrite architectures with high dislocation mainly in the interdendritic area and Nb-rich precipitates line indicated by orange oval; d) ellipsoidal γ'' phases.

3.5.4 Tensile properties of direct aged samples

The tensile engineering stress-strain curves of three direct aged IN625 specimens at 700 °C for 24 hours are illustrated in Figure 51, whereas the tensile properties of the LPBF aged samples compared to wrought IN625 are reported in Table 26.

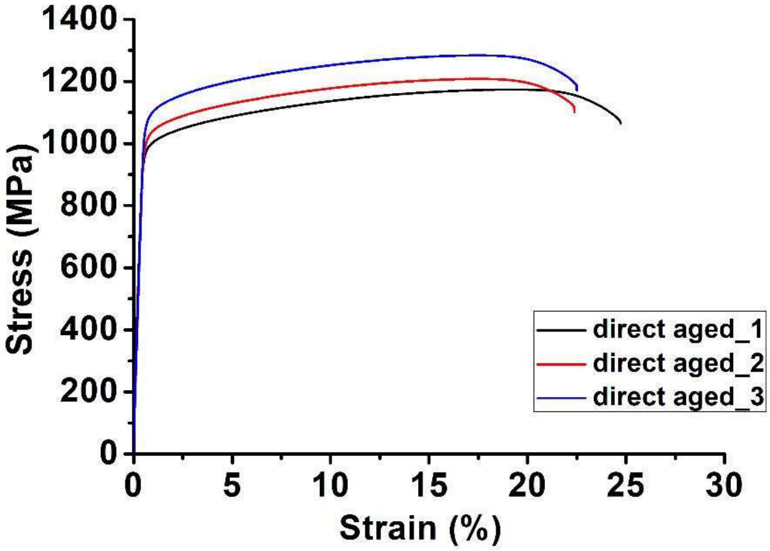

Figure 51: Tensile stress curves of direct aged IN625 samples at 700 °C for 24 hours.

The direct aged IN625 samples reveald higher YS and UTS but lower A than as-built state. There is chiefly associated with the strengthening effect of the γ'' phases. Besides, the direct aged samples revealed higher YS and UTS and lower A than LPBF-built IN625 produced by EOS, minimum requirements for LPBF-built and as-rolled IN625 alloys, as reported in Table 26.

In fact, a direct ageing at 700 °C for 24 hours did not dissolve the dendrite structures, so it was not possible to improve the ductility.

Table 26: Comparison of tensile properties of as-built, direct aged at 700 °c for 24 hours, to other LPBF-built IN625 along the x-y plane reported in literature and wrought IN625 alloys.

Inconel 625 sample	E (GPa)	YS (MPa)	UTS (MPa)	A (%)
This study				
AB	182 ± 13	783 ± 23	1041 ± 36	33 ± 1
DA	204 ± 3	1012 ± 54	1222 ± 56	23 ± 1
Other works and specifications				
LPBF ASTM F3056-14	-	275 (min)	485 (min)	30 (min)
LPBF* [32]	170 ± 20	725 ± 50	990 ± 50	35 ± 5
As-rolled [33]	-	414 (min)	827 (min)	30 (min)

*As-built state according to EOS data sheet;

3.5.5 Tensile fracture surfaces of direct aged IN625 samples

Figure 52a reveals the tensile fracture surface of direct aged sample, showing the presence of both ductile and brittle fractures. The fracture surface seem to start from highly segregated areas along the grain boundaries or interdendritic areas, but can also start in areas with Cr-rich $M_{23}C_6$ carbides and γ″ phases, which promote the brittle fractures.

During the investigation, a higher number of brittle fractures was observed with respect to the as-built state, showing intergranular Cr-rich $M_{23}C_6$ carbides, as shown in Figure 52b.

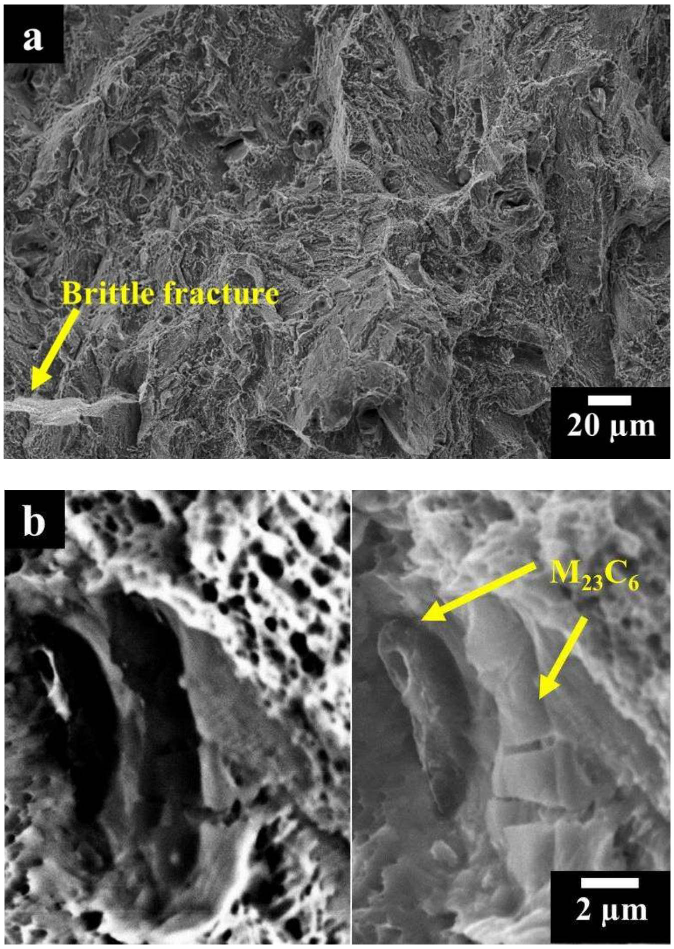

Figure 52: SEM images of tensile fracture surfaces for the direct aged IN625 at 700 °C for 24 hours showing: a) ductile and brittle fracture surfaces; b) SEM image obtained in secondary and backscattering electrons exhibiting Cr-rich $M_{23}C_6$ carbides.

3.5.6 Microstructure of IN625 samples direct aged at 800 °C

The microstructural evolution of as-built IN625 samples heat-treated at 800 °C for 2, 8 and 24 hours is illustrated in Figure 53a, 53b and 53c, respectively. For this heat treatment, the MPCs were less definite whereas it is still possible to observe the CGs. The grain boundaries resulted in being more definite due to the phase precipitation.

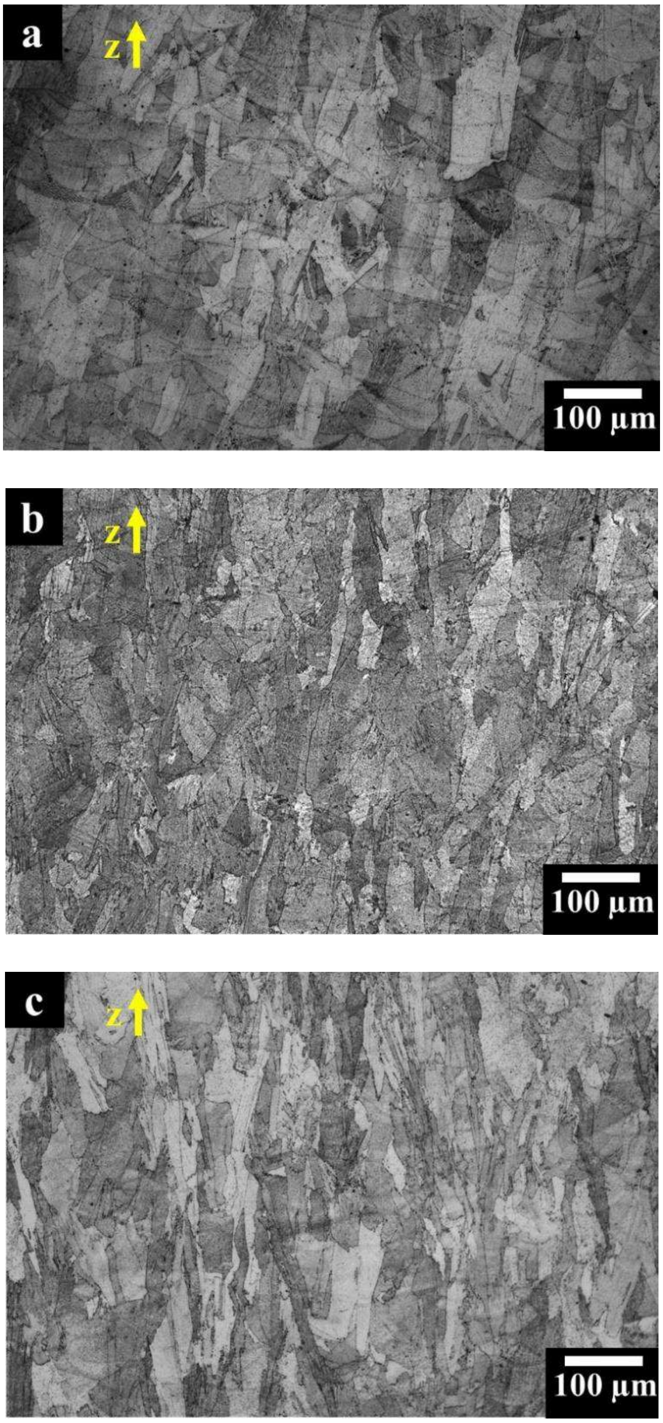
a
z
100 µm
b
z
100 µm
c
z
100 µm

Figure 53 : OM images of direct aged IN625 samples at 800 °C for 2 h (a), 8 h (b) and 24 h (c) showing columnar grains along the building direction; kalling's No.2 etchant was used.

At higher magnified OM view, the direct aged samples at 800 °C for 2 hours (Figure 54a), 8 hours (Figure 54b) and 24 hours (Figure 54c) showed a progressive formation of inter/intragranular phases.

The formation of phases along the grain boundaries was estimated by means of image analysis, obtaining 1.65 ± 0.39 %, 2.44 ± 0.34 % and 3.01 ± 0.31 % after heat treatment for 2 hours, 8 hours and 24 hours, respectively.

It should be noted that the fraction of intragranular precipitates was not determined since it is arduous to distinguish them from interdendritic areas due to their very fine dimensions.

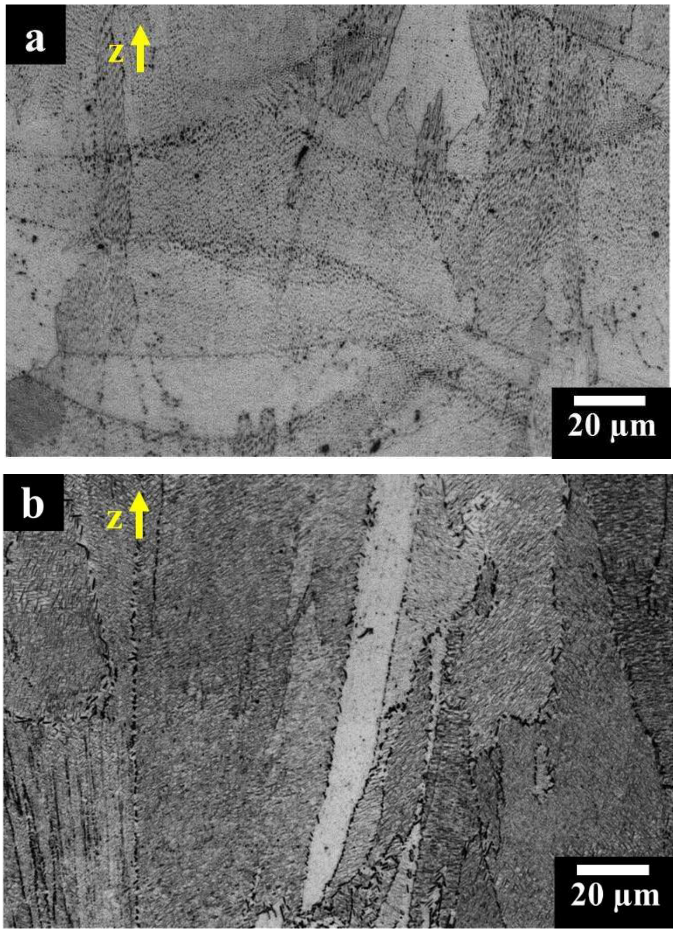

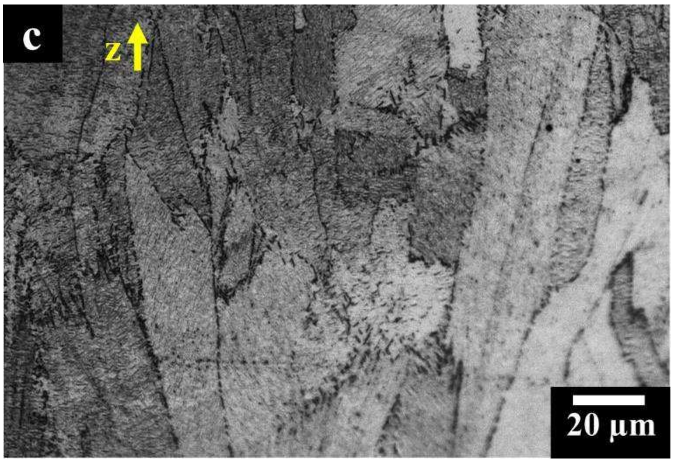

Figure 54: OM images at high magnification of direct aged samples at 700 °C for 2 hour (a), 8 hours (b) and 24 hours (c) showing gradually formation of inter/intragranular precipitates; Kalling's No.2 etchant was used.

The FESEM view of direct aged sample at 800 °C for 24 hours in Figure 55a reveals the precipitation of acicular δ phases, with sub-micrometric size up to 1 µm within the grains and 1-2 µm along the grain boundaries. Furthermore, other precipitates with block shape around 1-2 µm were detected (Figure 55b). According to the TTT diagram of IN625, these precipitates could be carbides or Laves phases[5,39].

However, regarding the very low quantity of C it seems unlike the presence of a significant number of carbides with similar size. In fact, the EDS results (Table 27) revealed the precipitates were enriched in Nb, suggesting the precipitation of Laves phases.

Finally, it is still possible to observe fine spherical precipitates (Figure 55c), the same of the as-built state indicated as Nb-rich MC carbides. The hardness increment of these heat-treated IN625 samples is clearly attributed to formation of δ phases and Laves phases.

According to the T-T-T diagram of IN625 other carbides such as M_6C and $M_{23}C_6$ could be presence after a similar thermal exposure, although the very low level of carbon seems to inhibit their formation.

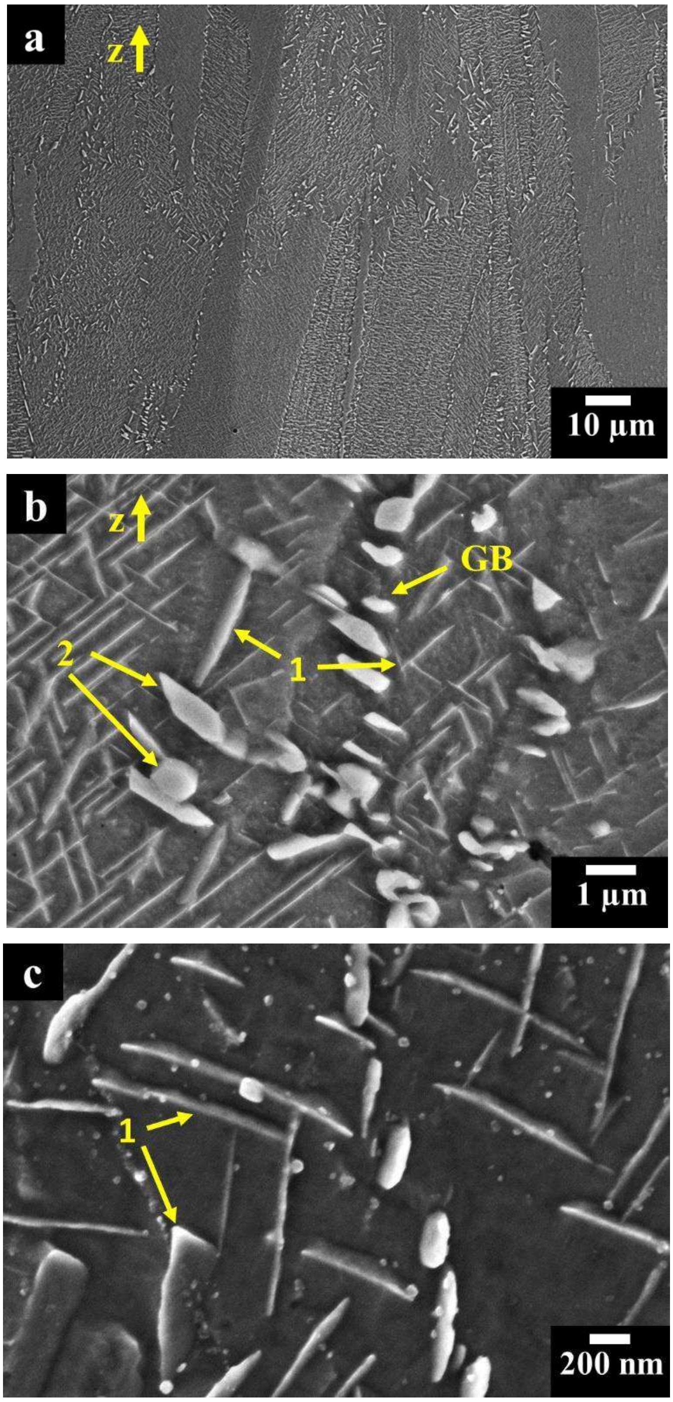

Figure 55: FESEM images of IN625 sample direct aged at 800 °C for 24 hours showing: a) columnar grains with several precipitates throughout the material; b) δ phases indicated by arrow 1 and Laves phases pointed out by arrow 2; c) δ phases indicated by arrow 1 and fine spherical carbides (the same of as-built state).

Table 27: EDS results of the Laves phase and austenitic matrix for the direct aged IN625 sample at 800 °c for 24 hours.

	Laves phase (arrow 2)		Austenitic matrix	
	Wt %	At %	Wt %	At %
Ni	62.1	64.8	62.8	64.3
Cr	18.0	21.2	21.1	24.4
Mo	10.0	6.3	10.1	6.3
Nb	8.1	5.3	4.4	2.8
Fe	0.5	0.5	0.6	0.7
Co	0.4	0.4	0.3	0.3
Ti	0.5	0.6	0.4	0.5
Al	0.4	0.9	0.3	0.7

The EDS line reports in Figure 56 shows both elongated and almost globular Laves phases. The EDS clearly revealed an enrichment of Nb and Mo together with a depletion of Cr. A fraction of the elongated precipitates could be confused with δ phases (Ni_3Nb), but the enrichment in Mo, exclude their formation.

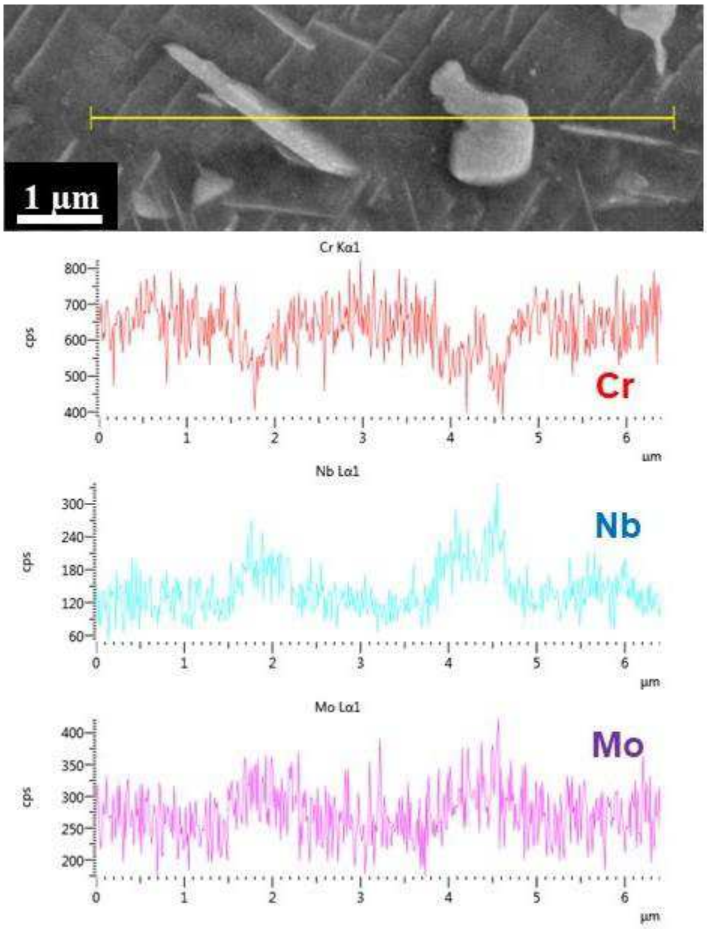

Figure 56: EDS line of direct aged sample at 800 °C for 24 hours showing Laves phases enriched in Nb and Mo with respet to the austenitic matrix.

3.5.7 Microstructure of IN625 samples direct aged at 900 °C

During the OM investigation, the direct aged samples at 900 °C for 2 (Figure 57a), 8 (Figure 57b) and 24 hours (Figure 57c) exhibited a microstructure similar at samples heat treatment at 800 °C for the same times.

In fact, the microstructure was dominated of CGs (with size similar to as-built state) along the building direction, coupled with a significant precipitation inside the grains as well as along the grain boundaries.

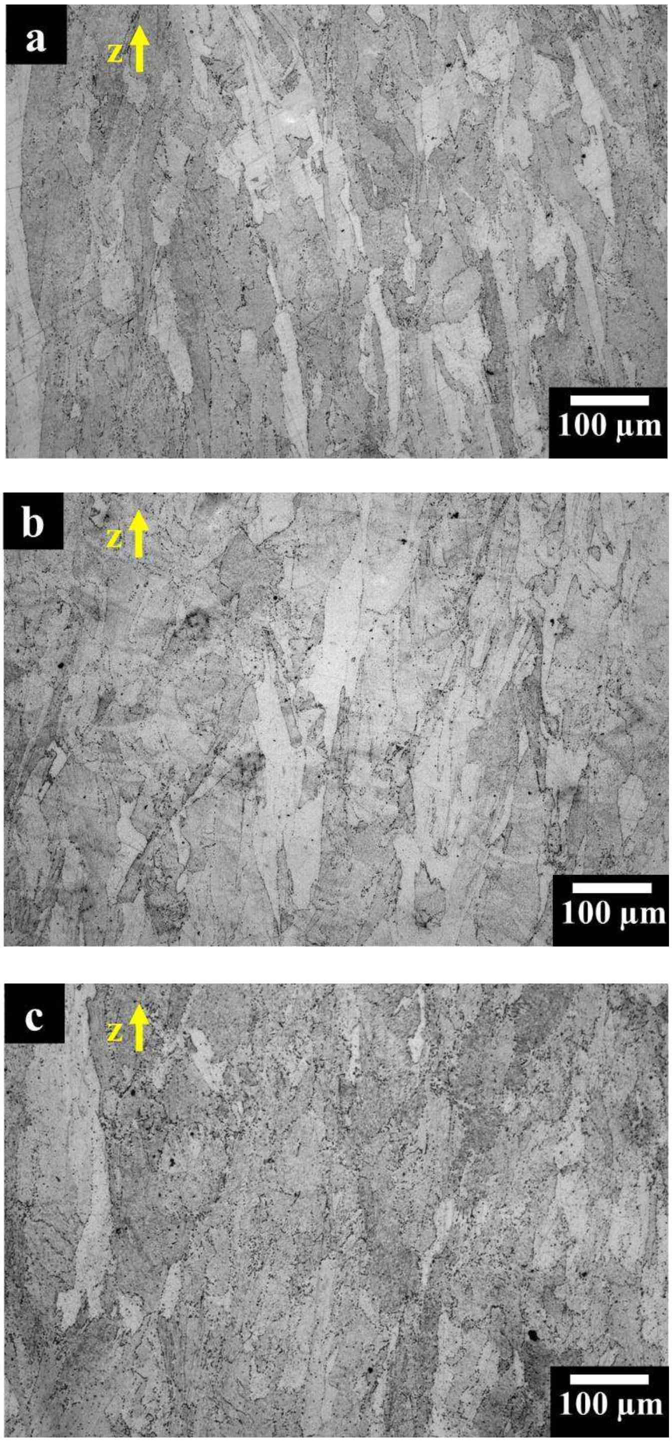
a
z
100 µm
b
z
100 µm
c
z
100 µm

Figure 57: OM images of direct aged IN625 samples at 900 °C for 2 h (a), 8 h (b) and 24 h (c) along the building direction; Kalling's No.2 etchant was used.

At higher magnification (Figure 58a, 58b and 58c), it is evident as increasing the thermal exposure leaded to larger formation of inter/intragranular phases.

By analysis the fraction precipitates along the grain boundaries, it was determined a fraction of 0.73 ± 0.14 %, 2.29 ± 0.36 % and 3.95 ± 0.72 % after thermal exposure at 900 °C for 2, 8 and 24 hours, respectively.

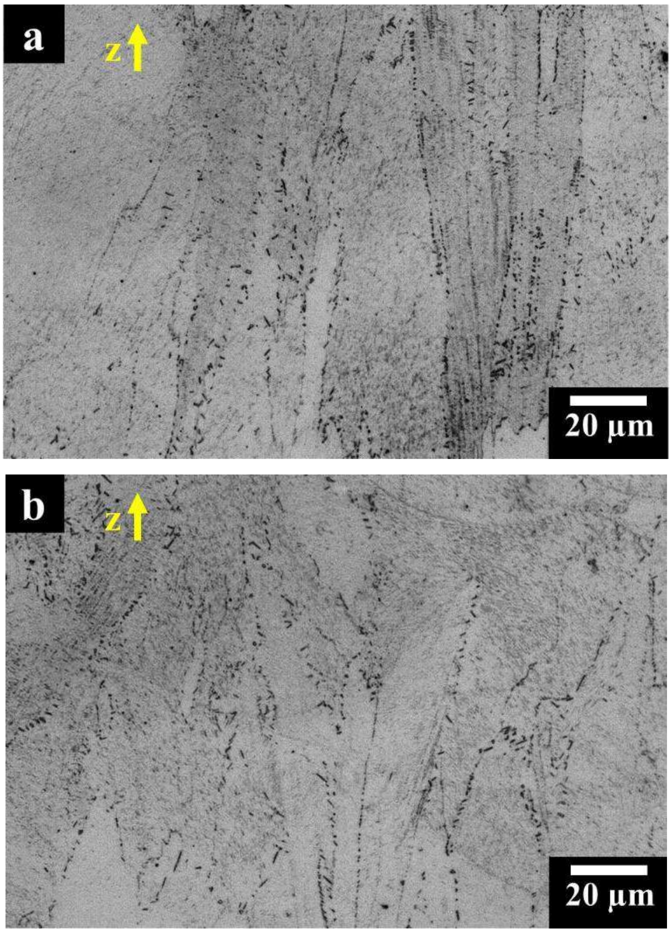

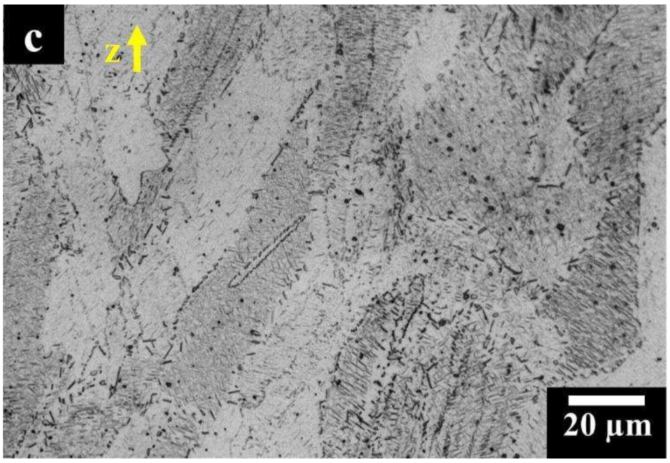

Figure 58: OM images at high magnification of direct aged IN625 samples at 800 °C for 2 h (a), 8 h (b) and 24 h (c) revealing the increment of precipitates correlate to longer thermal exposure; Kalling's No.2 etchant was used.

FESEM images revealed the presence of the largest precipitates along the grain boundaries (Figure 59a).

At higher magnification in Figure 59b, δ phases indicated by arrow 1 and block of precipitates, identified as Laves phases, indicated by arrow 2 can be observed. The δ phase had a length from 200 nm up to 3 µm, whereas the Laves phases had a size up to 3 µm. The δ phases were homogeneously distributed within the materials whereas the Laves phases were mainly located along the grain boundaries. Furthermore, very nanometric spherical carbides (the same of the as-built state) were still presence (Figure 59c).

The presence of Laves phases was also supported by EDS analysis (Table 28), revealed a Nb enrichment correlated to a depletion of Cr with respect to the matrix.Furthermore, it should be noted that the meager quantity of C cannot generate the formation of such a high number of micrometric carbides located along the grain boundaries.

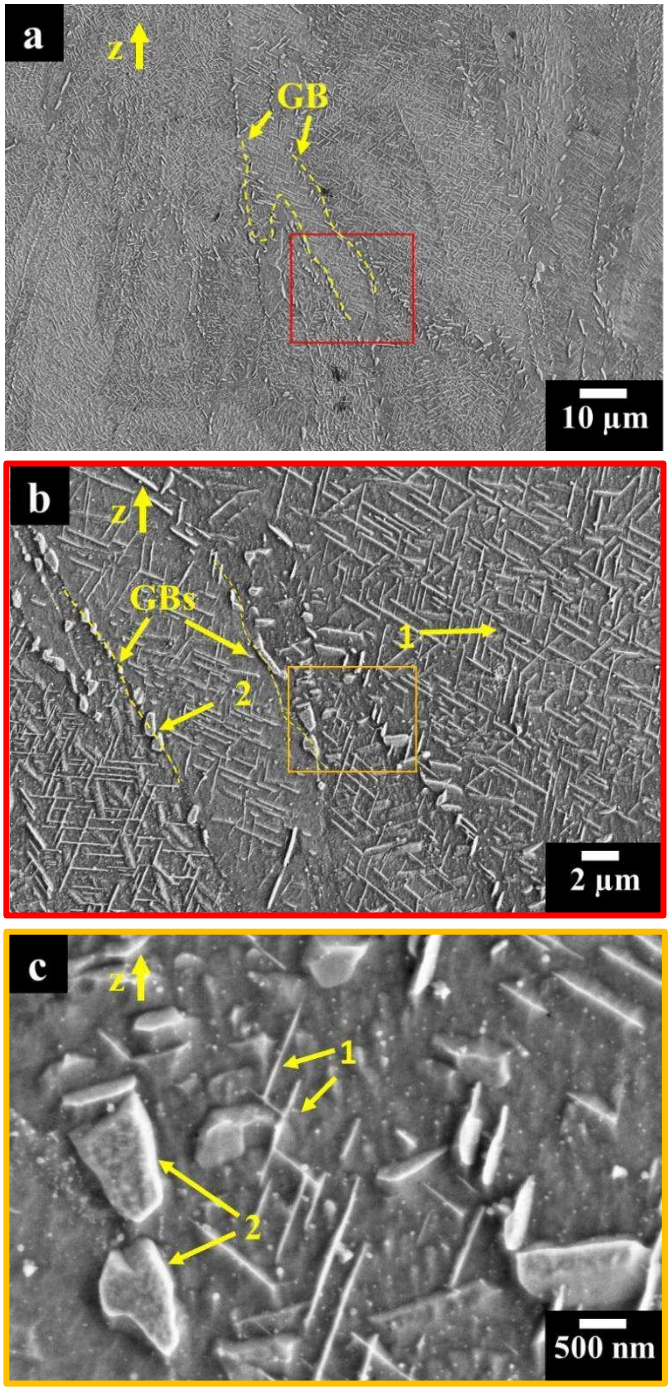

Figure 59: FESEM images of IN625 sample direct aged at 900 °C for 24 hours showing: a) columnar grains with a significant number of precipitates throughout the material, with the largest located along the grain boundaries (GBs); b) δ phases indicated by arrow 1 and Laves phases pointed out by arrow 2; c) magnificated view on δ phase and Laves phases indicated by arrow 1 and 2, respectively. Kalling's No.2 etchant was used.

Table 28: EDS results of the Laves phase and austenitic matrix for direct aged sample at 900 °C for 24 hours.

	Laves phase (arrow 2)		Austenitic matrix	
	Wt %	At %	Wt %	At %
Ni	62.5	65.1	64.0	65.3
Cr	17.0	20.0	21.3	24.5
Mo	10.0	6.4	9.5	5.9
Nb	8.6	5.7	3.9	2.5
Fe	0.6	0.7	0.5	0.5
Co	0.1	0.1	0.2	0.2
Ti	0.6	0.8	0.3	0.4
Al	0.6	1.4	0.3	0.7

3.6 Investigation on SHT IN625 condition

3.6.1 Hardness investigation

Figure 60 displays the Brinell hardness values of as-built and SHT IN625 samples at 1000 °C and 1150 °C for 1 hour and 2 hours, respectively. The solution treatments drastically reduced the hardness, and the SHT samples at 1150 °C revealed lower hardness than SHT ones at 1000 °C.

It is worthwhile to note that solution treatments at 1150 °C generated hardness values similar to as-rolled IN625 after solution treatments (116-194 HBW)[37]. The Brinell hardness values of the SHT IN625 samples are listed in Table 29.

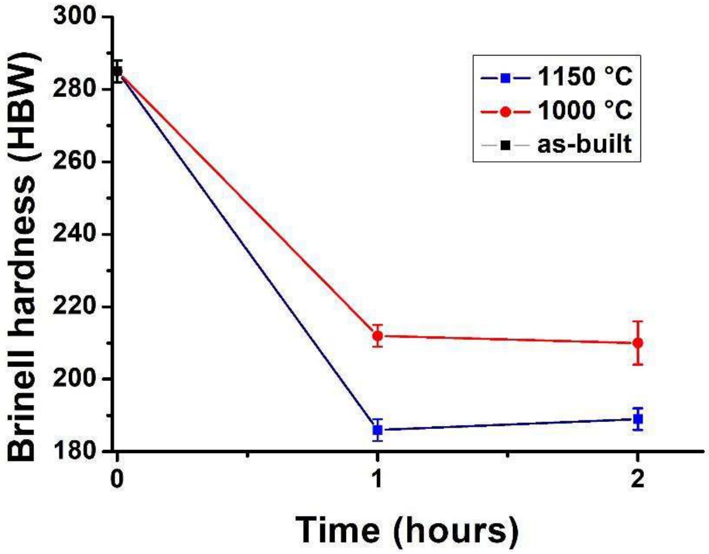

Figure 60 : Brinell hardness of as-built and SHT IN625 samples at 1000 °C and 1150 °C for 1 hour and 2 hours.

Table 29: Brinell hardness values of SHT IN625 samples; starting condition 285 ± 3 HBW of as-built IN625 samples.

/	Temperature (°C)	
Time (hours)	1000	1150
1	212 ± 3	186 ± 3
2	210 ± 5	189 ± 3

The microstructure of the SHT IN625 samples will be investigated in the following paragraphs. In particular, for the conditions showed the lowest hardness (SHT at 1150 °C 2 hours) will be studied more in detail the microstructure and the tensile properties.

It should be noted that it was not selected the solution treatment performed at 1150 °C for 1 hour, in order to guarantee a major homogenisation reducing the chemical segregation of the as-built state.

3.6.2 Microstructure evolution of SHT IN625 at 1000 °C

The solution treatment triggered the recrystallization and grain growth leading to the formation of equiaxed grains. In this case, the recrystallization chiefly stemmed from the high dislocation density of the as-built state.

The microstructures of samples SHT for 1 hour (Figure 61a) were equal to samples SHT for 2 hours (Figure 61b), which seems to indicate that at this temperature the grain growth was limited. The equiaxed grains had a large size distribution mainly from 5 µm to 80 µm, and both the micrographs showed many twin boundaries throughout the grains.

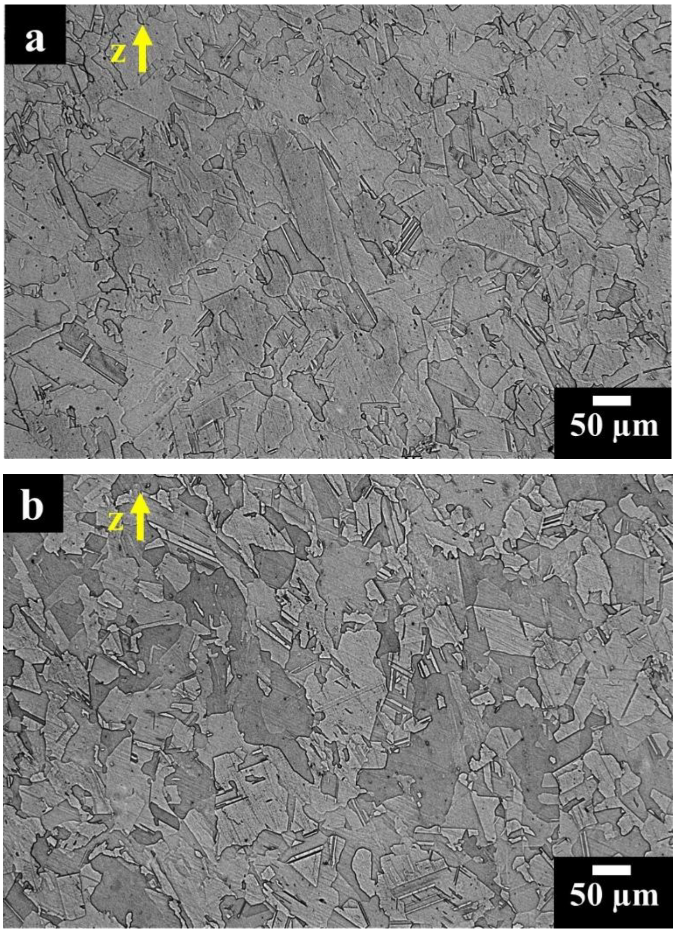

Figure 61: OM images of SHT IN625 samples at 1000 °C for 1 h (a) and 2 h (b) showing a microstructure mostly consisted of equiaxed grains along the building direction; Kalling's No.2 etchant was used.

The FESEM image (Figure 62a) of SHT samples at 1000 °C for 2 hours revealed equiaxed grains without the presence of coarse precipitates along the grain boundaries, as well as along the twin boundaries. At higher magnification (Figure 62b), it is evident how the heat treatment dissolved the very fine dendritic architectures, and it is also possible to observe fine precipitates (around 20-250 nm) homogeneously distributed throughout the material.

According to the TTT diagram of IN625 alloys, a similar heat treatment (1000 °C for 2 hours) can promote the carbide formation [5,39,130]. Therefore, these precipitates could be secondary carbides or grown primary carbides.

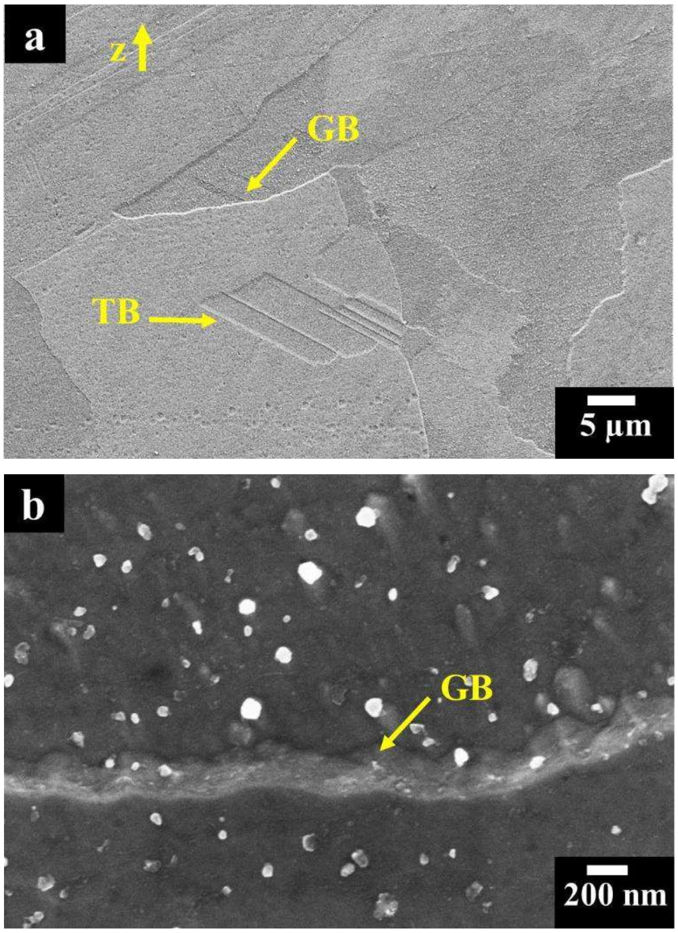

Figure 62: FESEM images of SHT IN625 sample at 1000 °C for 2 hours showing: a) equiaxed grains without the formation of coarse precipitates along the grain boundary (GB) and along the twin boundary (TB); (b) high magnification along a GB with presence of very fine precipitates. Kalling’s No.2 etchant was used.

3.6.3 Microstructure evolution of SHT IN625 at 1150 °C

Figure 63a and 63b reveal the microstructure of SHT IN625 samples at 1150 °C for 1 hour and 2 hours, respectively. The SHT IN625 samples mostly exhibited equiaxed grains with a large grain size distribution, mainly from 10 to 90 μm, together with copious numbers of twin boundaries. This microstructure derived from the recrystallisation and grain growth due to the high density dislocation of as-built state.

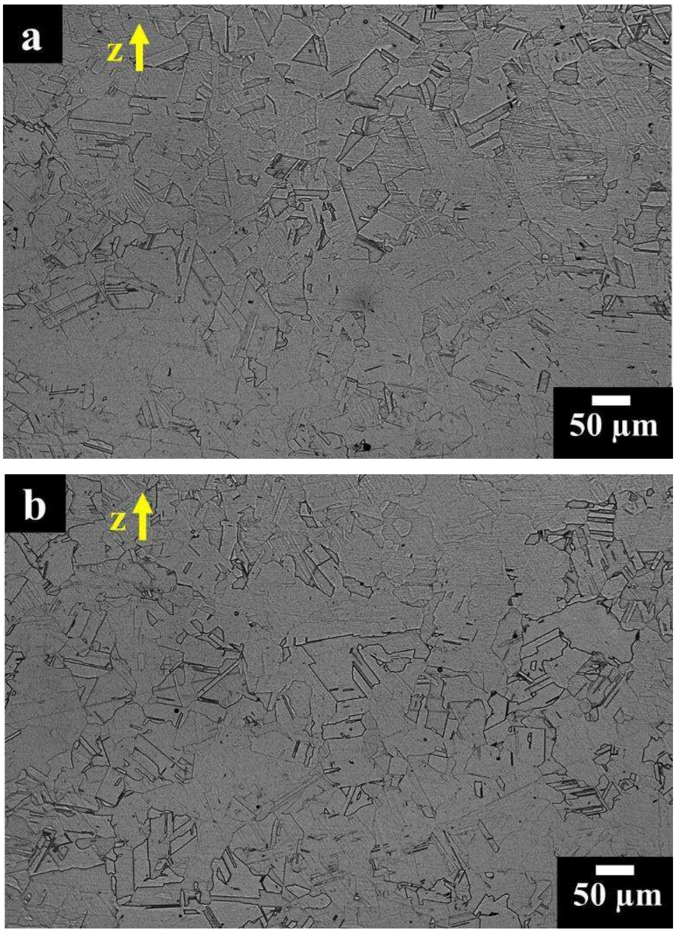

Figure 63: OM images of SHT IN625 samples at 1150 °C for 1 hour (a) and 2 hours (b) showing equiaxed grains with twin boundaries. Kalling's No.2 etchant was used.

As can be seen in FESEM image (Figure 64a), the microstructure did not reveal coarse carbides along the grain boundaries or the twin boundaries. Besides, the dendritic architectures disappeared as an effect of the heat treatment. At higher magnification (Figure 64b), it is possible to observe very fine carbides (generally around 20-400 nm) with the largest one mainly located along the grain boundaries.

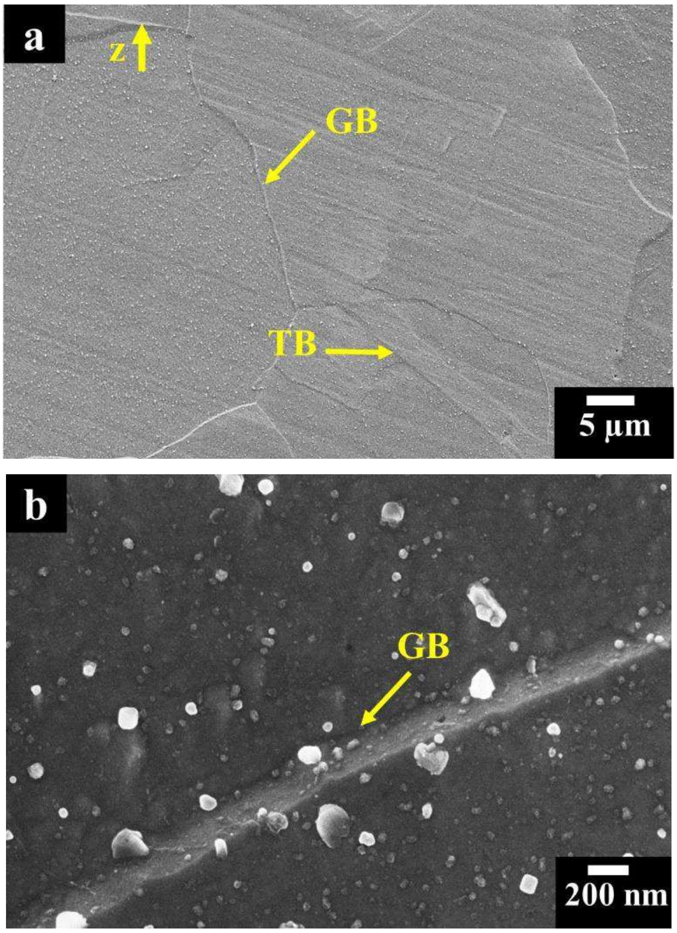

Figure 64: FESEM images of SHT IN625 samples at 1150 °C for 2 hours showing: (a) equiaxed grains with grain boundary (GB) and twin boundary (TB) without coarse carbides; (b) (GB) areas with fine carbides.

TEM image in Figure 65a reveals very low dislocation density of the SHT condition caused by the recrystallisation. Besides, Figure 65b displays a carbide along the grain boundary. The EDS analysis revealed enrichment in Nb and Ti, indicating the formation of Nb,Ti rich MC carbides, in accordance with the TTT diagram of IN625 and literature on IN625 alloys [5,39,131,132].

Therefore, the solution treatment generates new Nb,Ti-rich MC carbides, which can be correlated to the growth of primary carbides as well as the formation of secondary carbides. To dissolve this type of carbide is necessary to reach a temperature around 1200 °C [5].

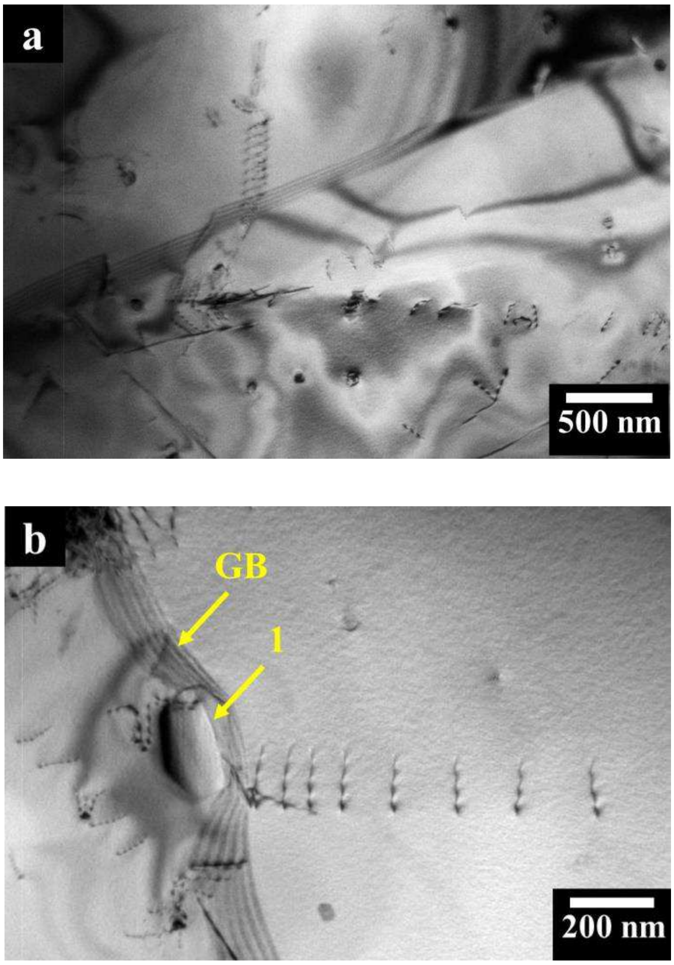

Figure 65: TEM bright field images: (a) showing the austenitic matrix with low dislocation density; (b) Nb,Ti-rich MC carbides along the grain boundary (GB) indicated by arrow 1.

3.6.4 Thermomechanical analysis on SHT IN625 samples

The CTE of SHT IN625 samples fabricated along x-y plane and z direction are illustrated in Figure 66, revealing very similar trends for both the samples.

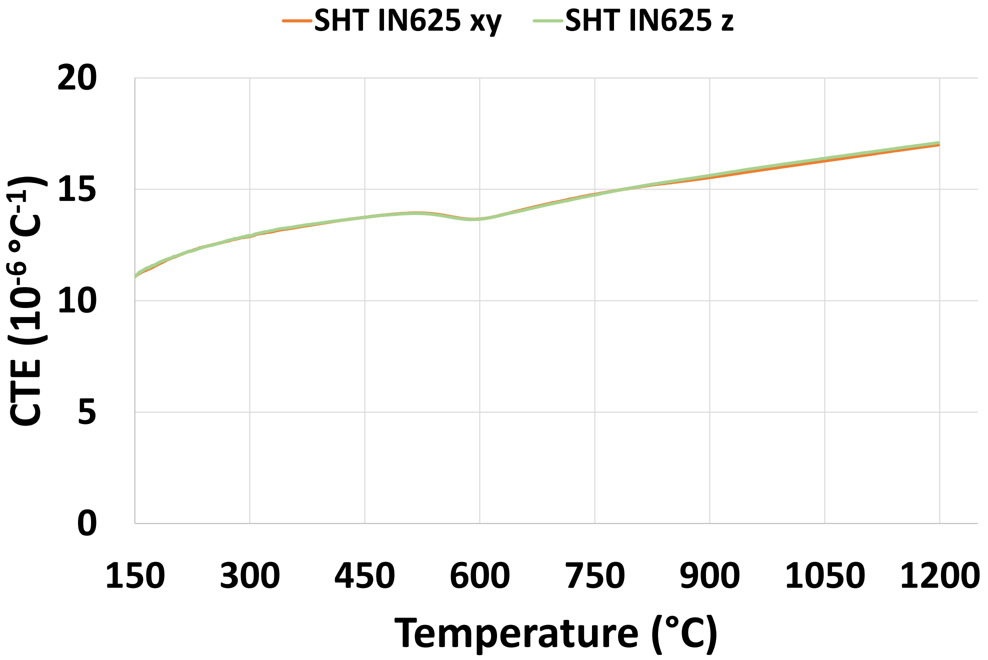

Figure 66: Coefficient of thermal expansion (CTE) vs temperature of SHT IN625 samples built along x-y plane and z direction.

The obtained TMA curves presented a deflection around 500-700 °C, probably due to the formation of phases inside the material. The average values of the CTE revealed a good correlation with the available data on IN625 alloy at different temperatures, as reported in Table 30.

Table 30: Average CTE for SHT IN625 samples and commercially available IN625 alloy at different temperatures.

T (°C)	538	649	760
CTE (10^{-6} °C^{-1}) [37]	14.0	14.8	15.3
CTE (10^{-6}°C^{-1}) SHT xy	13.9	14.0	14.8
CTE (10^{-6} °C^{-1}) SHT z	13.9	14.0	14.8

3.6.5 XRD analysis on SHT IN625 samples

Figure 67 compares the XRD patterns of SHT IN625 samples along the building direction (z-axis) and perpendicular to the building direction (x-y plane). The patterns showed the γ austenitic phase with a lattice parameter of around 3.59 Å for both the states.

For the SHT IN625 state can be observed a signification reduction of the texture with respect to the as-built state (see Figure 39), due to recrystallisation and grain growth leading to the formation of equiaxed grains both along z-axis and x-y plane. Besides, for the SHT IN625 state, the peaks were narrower than as-built IN625 state, indicating a increment of the crystal size [55].

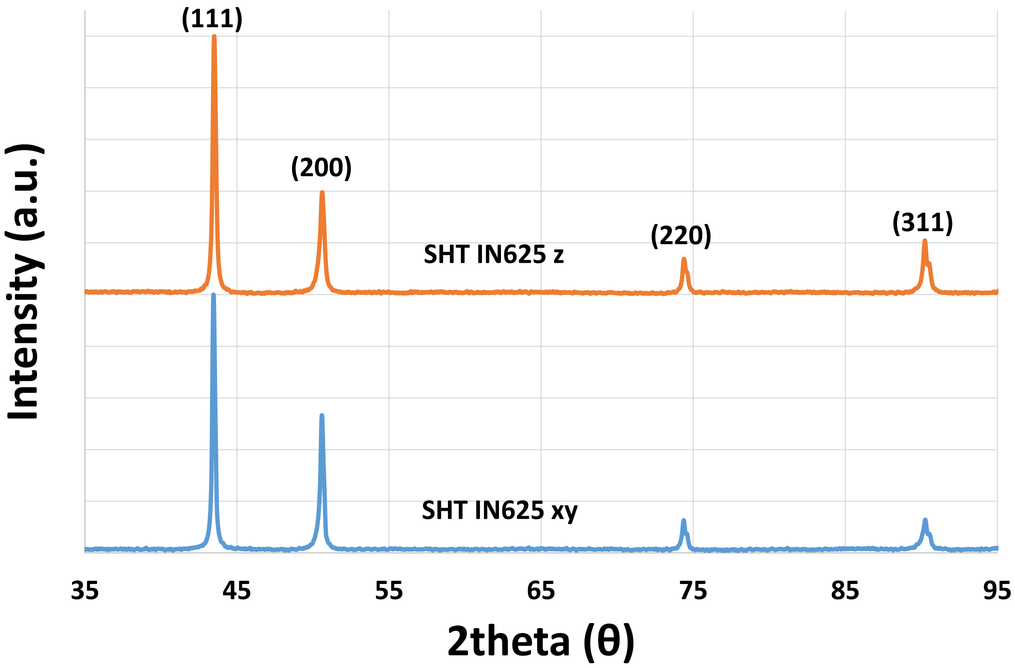

Figure 67: XRD spectra of SHT IN625 samples along the z-axis and x-y plane.

3.6.6 Tensile properties of SHT IN625 samples

The tensile engineering stress-strain curves of three SHT IN625 specimens at 1150 °C for 2 hours are displayed in Figure 68, whereas the tensile properties of LPBF-built and solution-treated IN625 samples compared to wrought IN625 are reported in Table 31.

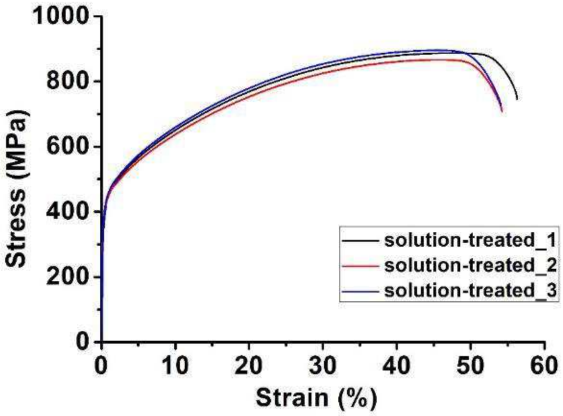

Figure 68: Tensile stress curves of the SHT IN625 samples at 1150 °C for 2 h.

The SHT IN625 samples showed lower tensile strengths and higher elongation at failure than as-built state. There is mainly attributed to the elimination of the very fine dendritic architectures. Besides, it is interesting to note that the SHT IN625 samples revealed higher tensile properties than minimum requirements for the traditional wrought grade 2 IN625 alloy based on ASTM B443.

Comparing the tensile properties of the LPBF SHT IN625 samples to commercially available SHT wrought IN625, it is possible to note that the tensile properties are still superior to the minimum values, while the maximum values slightly exceed the tensile properties of LPBF SHT IN625 samples.

Finally, the tensile test determined an E of 182 ± 13 GPa, whereas the IMCE test assessed a value of 206 ± 3 GPa for the SHT IN625 state. According to the IMCE test, the SHT state had a higher E than as-built state. The solution treatments dissolved Nb and Mo segregations involving a E reduction. However, the SHT samples revealed larger carbides than as-built state, so the reduction of Nb Ti ect. from the austenitic matrix could explain the increment of E, as reported in the literature [133].

Table 31: Comparison of tensile properties of as-built and SHT IN625 samples at 1150 °C for 2 hours to SHT wrought IN625 according to ASTM B443 as well as data commercially available.

Inconel 625 sample	Young's modulus (GPa)	YS (MPa)	UTS (MPa)	Elongation (%)
This study				
As-built	182 ± 13	783 ± 23	1041 ± 36	33 ± 1
SHT	181 ± 16	396 ± 9	883 ± 15	55 ± 1
Specifications				
Wrought SHT*	-	276 (min)	690in)	30 (min)
Wrought SHT [37]	-	290-414	724-896	40-65

**Wrought grade 2 solution annealed at least at 1093 °C according to ASTM B443*

3.6.7 Tensile fracture surfaces analysis

The SHT IN625 sample chiefly showed a ductile fracture mode resulting in a coalescence of microvoids, as can be seen in Figure 69a and 69b. The larger size of microvoids with respect to the as-built samples can reasonably derive from its greater ductility. Finally, for the solution-treated fracture surfaces, the dimples seem to be slightly deeper than as-built ones.

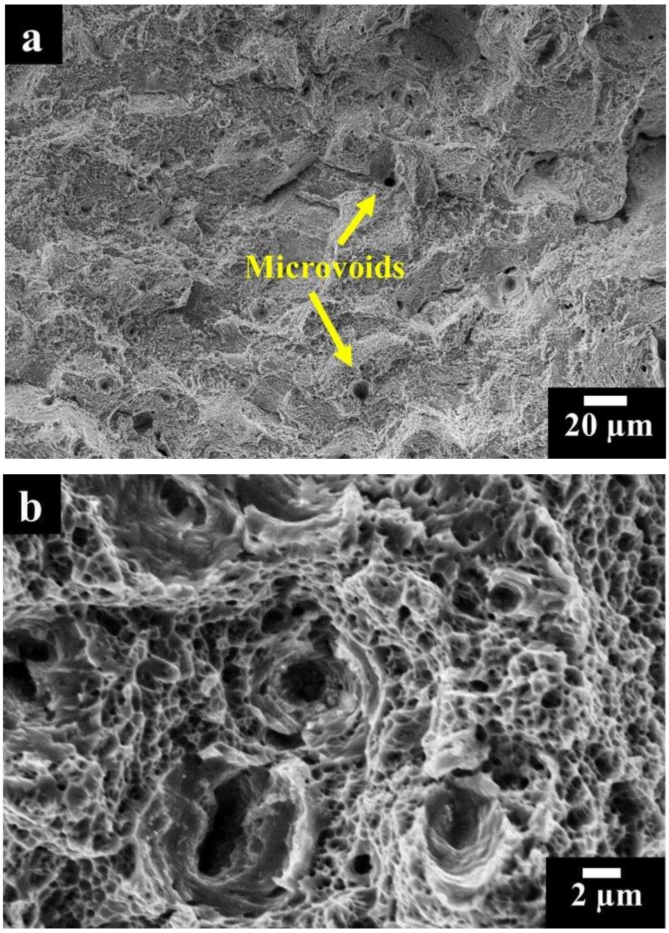

Figure 69: SEM images of SHT IN625 tensile fracture surfaces: a) low magnification showing fracture surfaces with microvoids; b) higher magnification exhibiting microvoids and fine dimples.

3.7 Investigation on aged IN625 conditions

3.7.1 Hardness investigation

The Brinell hardness values of the SHT samples at 1150 °C for 2 hours and subsequently aged at 600 °C, 700 °C, 800 °C and 900 °C for different times are reported in Figure 70 and Table 32.

The ageing treatments at 700 °C led to the highest hardness values, whereas thermal exposure at 900 °C resulted in the lowest hardness improvement, showing values compatible with the as-built state.

Finally, ageing treatments performed at 600 °C and 800 °C revealed similar hardness improvement.

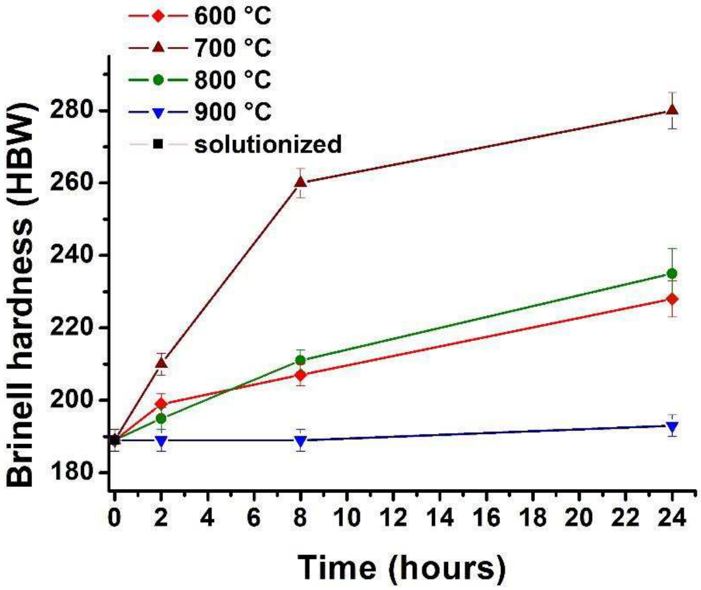

Figure 70: Brinell hardness values of solutionized (SHT at 1150 °C for 2 hours) and subsequent aged IN625 samples performed at 600 °C, 700 °C, 800 °C, 900 °C for 2 hours, 8 hours and 24 hours, respectively.

Table 32: Brinell hardness values of aged IN625 samples; starting condition 189 ± 3 HBW of SHT IN625 samples.

/	Temperature (°C)			
Time (h)	600	700	800	900
2	199 ± 3	210 ± 3	195 ± 3	189 ± 3
8	207 ± 3	260 ± 4	211 ± 3	189 ± 3
24	228 ± 5	280 ± 5	235 ± 7	193 ± 3

The microstructure of the SHT IN625 samples at 1150 °C for 2 hours followed by ageing treatments at different temperatures and times will be discussed in the following sections. In particular, for the aged IN625 state revealed the highest hardness values (700 °C 24 hours) will be considered in deep its microstructure and its tensile properties.

3.7.2 Microstructure evolution of IN625 sample aged at 600 °C

The OM images of aged samples at 600 °C for 2 hours (Figure 71a), 8 hours (Figure 71b) and 24 hours (Figure 71c), did not represent substantial modification with respect to the SHT IN625 state. In fact, the microstructure was made up of equiaxed grains with the same size of SHT IN625 samples as well as a high number of twin boundaries.

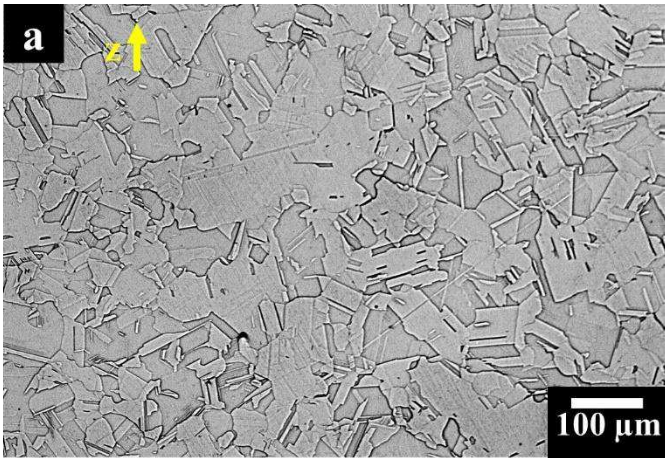

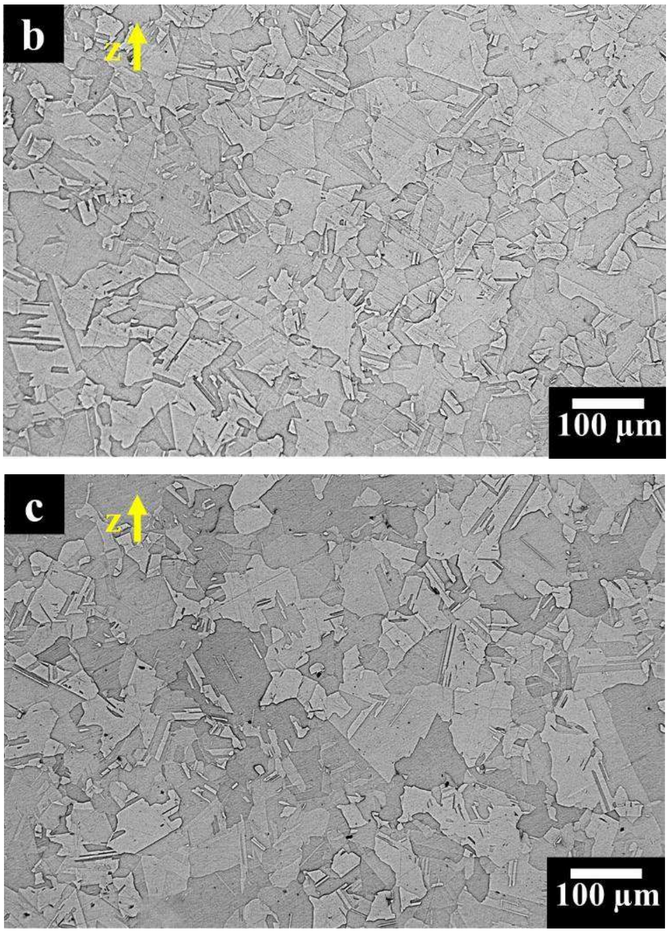

Figure 71: OM images of aged samples at 600 °C for 2 hour (a), 8 hours (b) and 24 hours (c) showing equiaxed grains with twin boundaries; Kalling’s No.2 etchant was used.

At higher magnification, OM images of aged samples at 600 °C for 2 hours (Figure 72a) 8 hours (Figure 72b) and 24 hours (Figure 72c) showed an slightly improvement of phases along the grain boundaries correlated to the time of heat treatment.

By image analysis was calculated a precipitation fraction of 0.60 ± 0.12 % (aged at 600 °C 2 hours), 0.76 ± 0.16 % (aged at 600 °C 8 hours) and 1.03 ± 0.24 % (aged at 600 °C 24 hours).

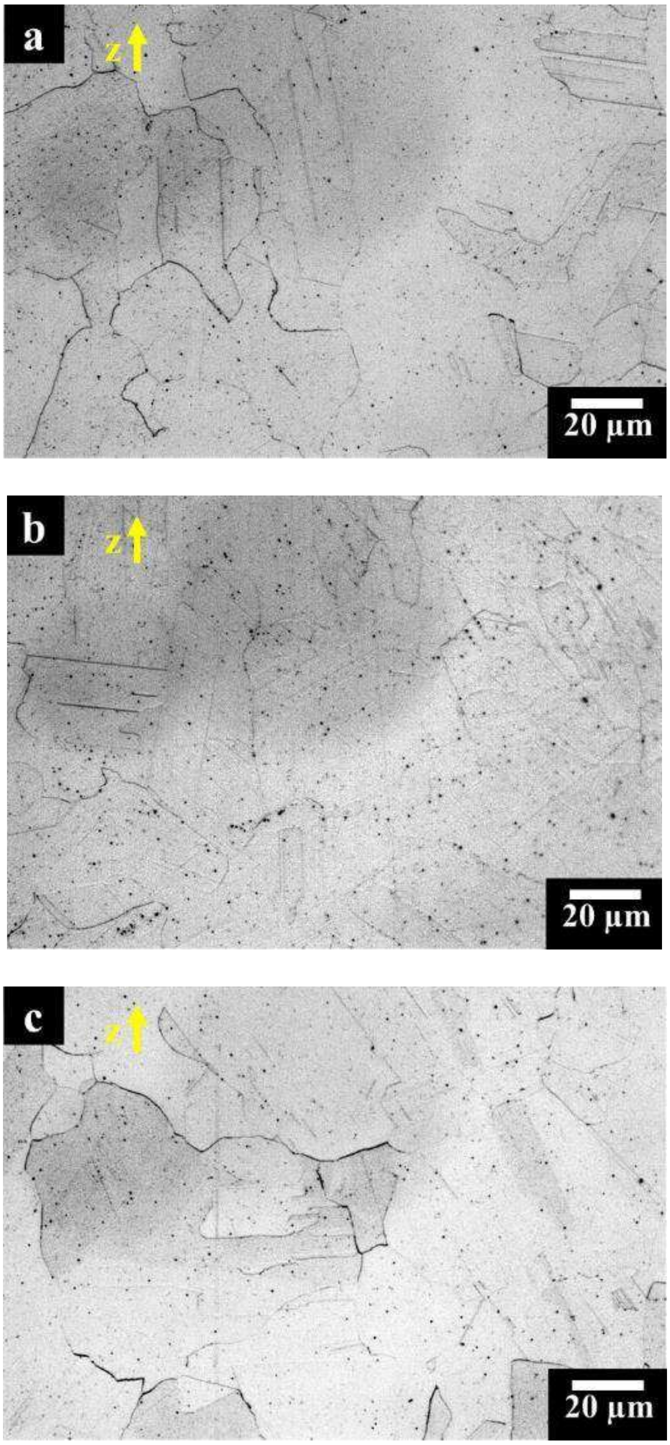

Figure 72: OM images of aged samples at 600 °C for 2 hour (a), 8 hours (b) and 24 hours (c) showing a starting precipitation along the grain boundaries; Kalling’s No.2 etchant was used.

FESEM images (Figure 73a) of the aged samples at 600 °C for 24 hours shows some equiaxed grains without the presence of coarse precipitates. As evident from Figure 73b, the thermal exposure generated fine precipitates (200-600 nm) along the grain boundaries, whereas nanometric white spots (around 10-25 nm) were detected throughout the materials (one of which indicated by arrow 1).

According to the literature, this temperature and time could promote the precipitation of γ″ phases, which could be the white spots detected during the analysis (Figure 73b) [5,15,39]. The presence of fine γ″ phases can explain the hardness improvement of the aged IN625 samples (around 20 %) with respect to the SHT state.

On the contrary, no Laves phases or δ phases should form for a similar thermal exposure up to 24 hours, although the FESEM analisys found some sub-micrometric precipitates along the grain boundaries. However, it is well known the formation of phases is strong correlate to the chemical composition, so some chemical variation could alter the phases formation [5].

Another possible speculation is that grain boundary areas enriched in Nb, Mo and other segregated elements accelerated the formation of phases such as δ phases or Laves phases. However, future studies will be performed to confirm this theory.

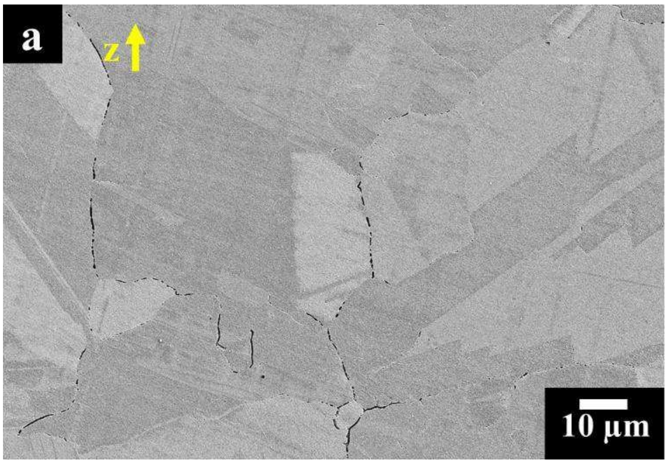

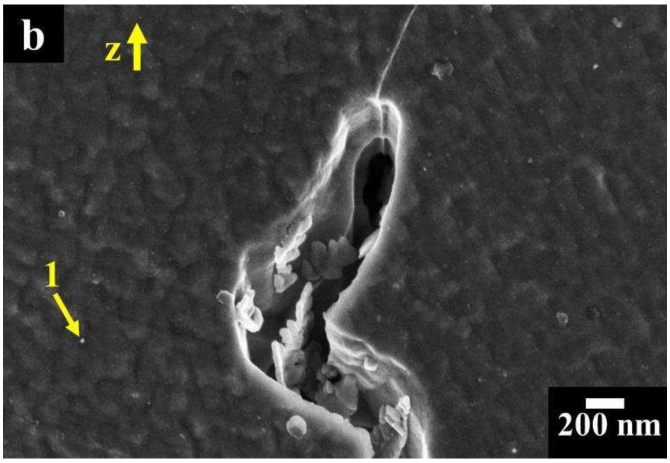

Figure 73: FESEM images of aged IN625 samples at 600 °C for 24 hours showing: (a) equiaxed grains without coarse carbides; (b) Grain boundary areas with fine elongated precipitates and very fine bright intergranular precipitates indicated by arrow 1; Kalling's No.2 etchant was used.

3.7.3 Microstructure evolution of IN625 sample aged at 700 °C

The samples aged at 700 °C for 2 hours (Figure 74a), 8 hours (Figure 74b) and 24 hours (Figure 74c) showed equiaxed grains with dimensions similar to the SHT condition, pointing out that a similar thermal exposure did not alter the grain size.

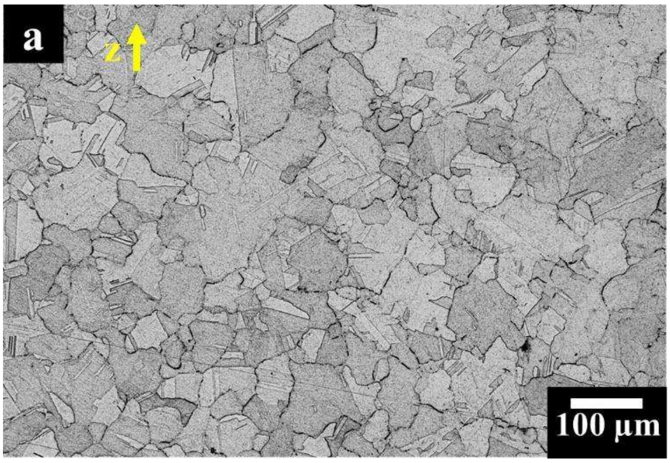

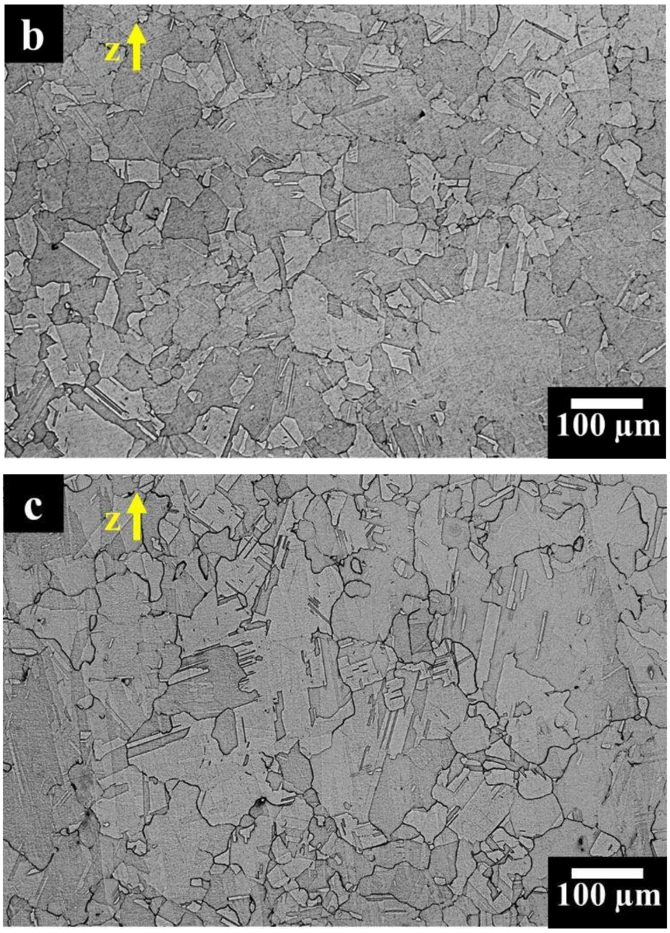

Figure 74: OM images of aged samples at 700 °C for 2 hour (a), 8 hours (b) and 24 hours (c) showing equiaxed grains with twin boundaries; Kalling’s No.2 etchant was used.

At higher magnification, OM images of aged samples aged at 700 °C for 2 hours (Figure 75a), 8 hours (Figure 75b) and 24 hours (Figure 75c) revealed an increment of phases.

By image analysis was calculated a precipitate fraction of 1.28 ± 0.19 %, 1.52 ± 0.43 % and 2.54 ± 0.39 % after heat treatment for 2 hours, 8 hours and 24 hours, respectively.

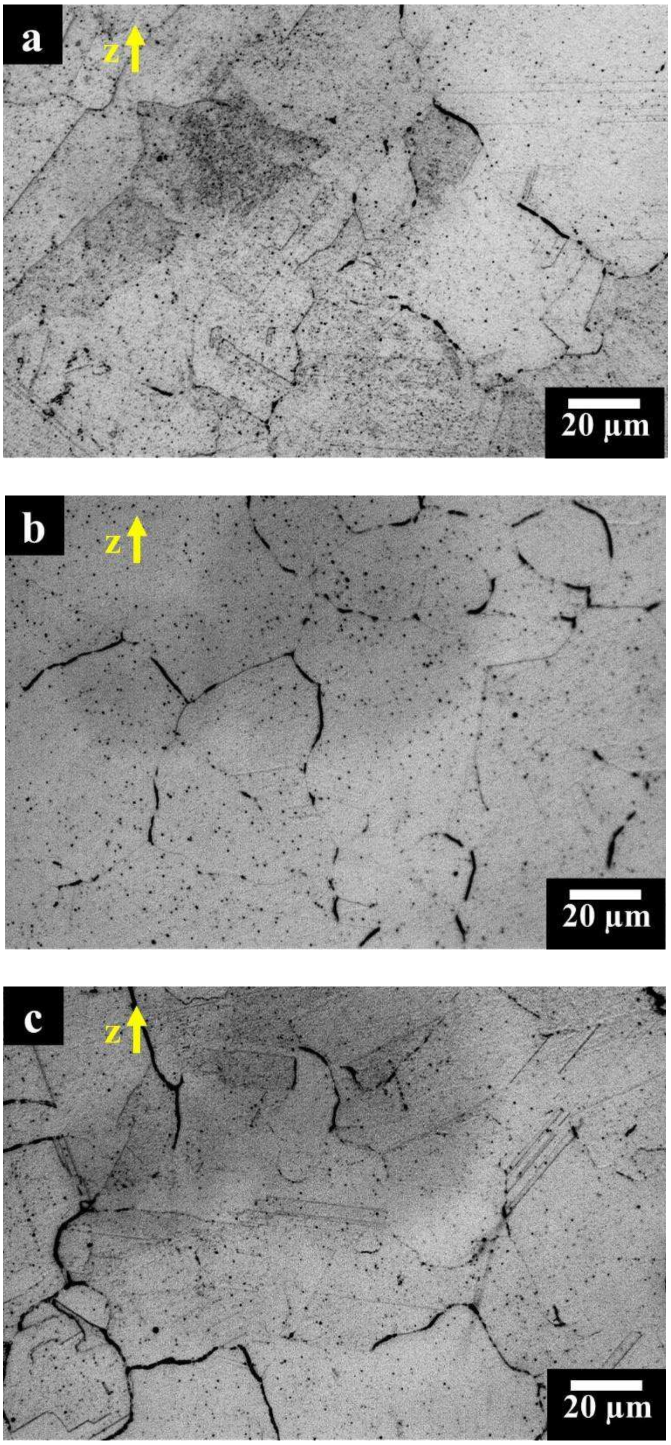

Figure 75: OM images of aged samples at 600 °C for 2 hour (a), 8 hours (b) and 24 hours (c) showing a starting precipitation along the grain boundaries; Kalling’s No.2 etchant was used.

At higher magnification, FESEM image (Figure 76a) of aged sample at 700 °C for 24 hours revealed grain boundaries covered by elongated phases.

Figure 76b displays both fine carbides (see inset in Figure 76b) and the elongated phases with size from nanometric up to 2 µm along the grain boundaries.

At higher magnification (Figure 76c), fine γ″ phases (less than 30 nm) can be observed as slightly bright spots.

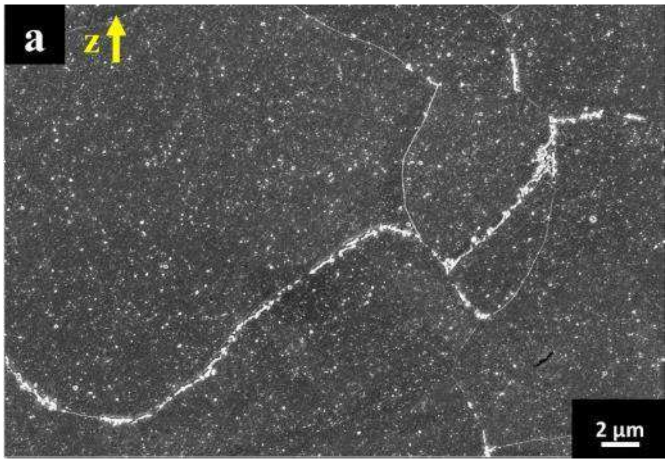

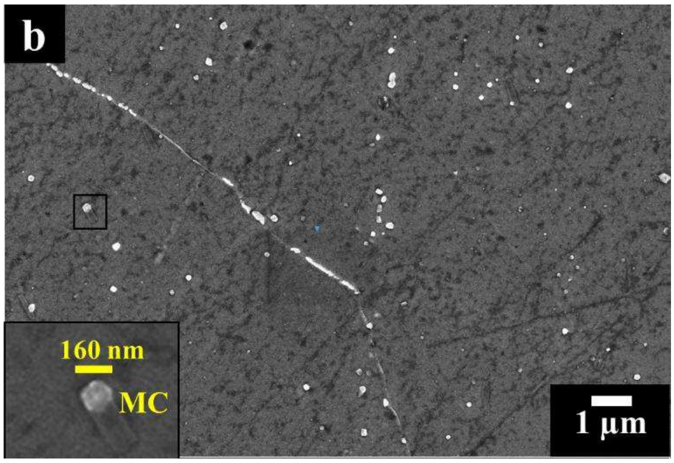

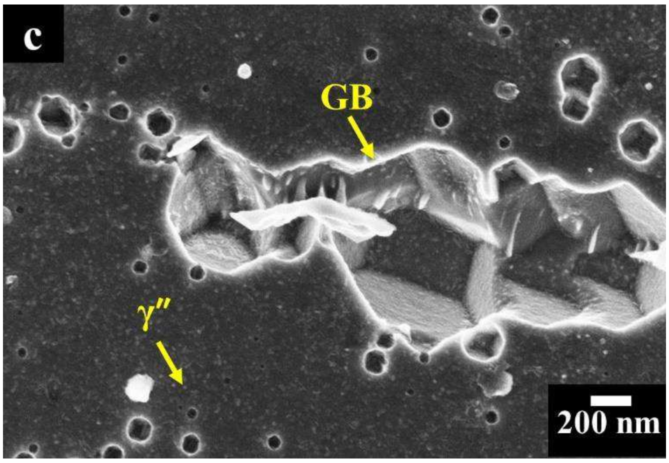

Figure 76: FESEM images showing: (a) fine elongated precipitates along the grain boundaries; (b) fine elongated precipitates along the grain boundaries with inset showing MC carbides; (c) grain boundary with elongated precipitates and intragranular γ″ phases; Kalling's No.2 etchant was used.

TEM image (Figure 77a and 77b) reveal the presence of a phase enriched in Cr (length 400 nm) and another one (length 300 nm) enriched in Nb, respectively, determined by EDS analysis. The first result denoted the formation of Cr-rich $M_{23}C_6$ carbides whereas the other phases could be δ phases or Laves phases.

As observed before, the very low quantity of carbon does not allow the precipitation of a very high number of carbides, so a part of the elongated precipitates may be δ phases or Laves phases.

TEM images (Figure 77c and 77d), inside the grains revealed the presence of Nb,Ti-rich MC carbides (generated during the solution treatment) as well as the formation of ellipsoidal γ″ phases with dimension from 10 to 30 nm homogeneously scattered within the grains. The very high number of nanometric γ″ phases explain why the samples revealed a hardness improvement of around 50 % with respect to the SHT state, reaching values similar to the as-built state.

Regarding the thermal exposure at 700 °C for 24 hours, the presence of Cr-rich $M_{23}C_6$ carbides and γ″ phases are in agreement with the T-T-T diagrams of IN625 alloy mentioned in the literature. By contrast, it reported the presence of δ phases or Laves phases for thermal exposure at 700 °C longer than 24 hours [5,39].

However, the phases' formation can be subject to variation based on the chemical composition. Besides, as mentioned before, another possible theory is that segregated elements such as Nb, Mo etc. play a crucial role to accelerate the formation of these phases along the grain boundaries.

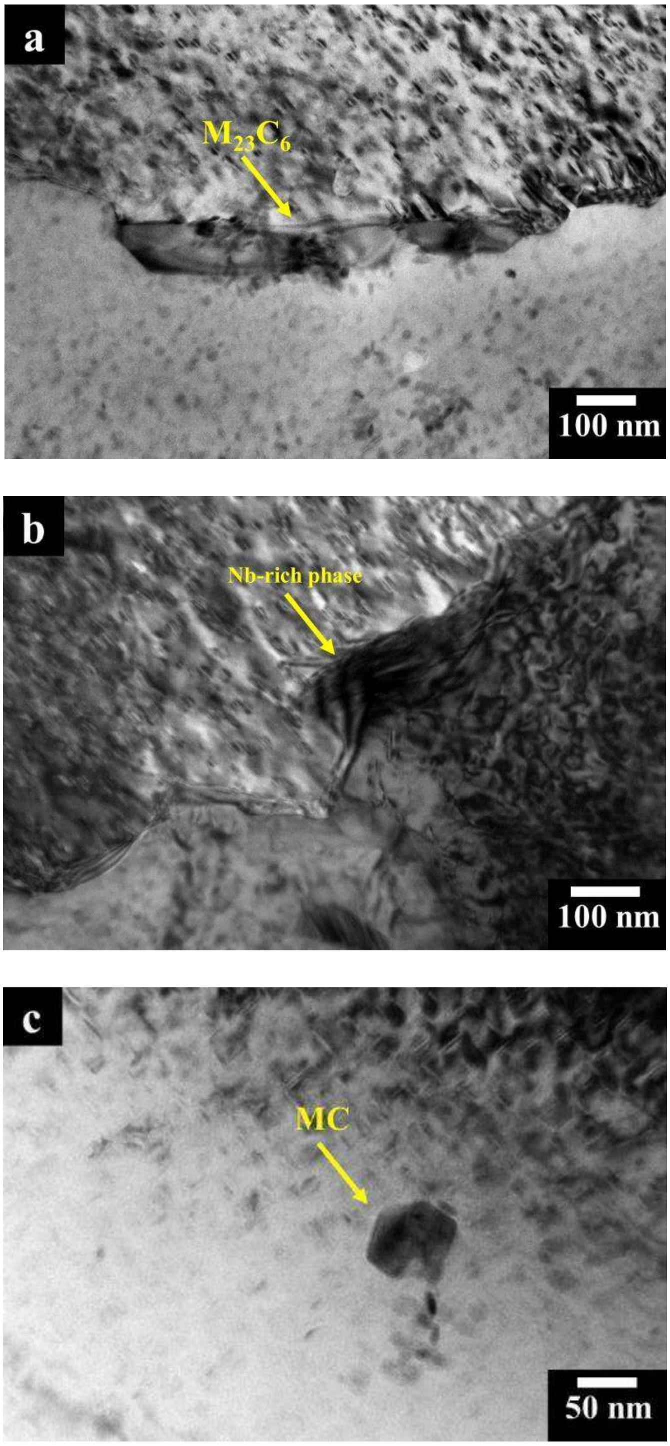
a
$M_{23}C_6$
100 nm
b
Nb-rich phase
100 nm
c
MC
50 nm

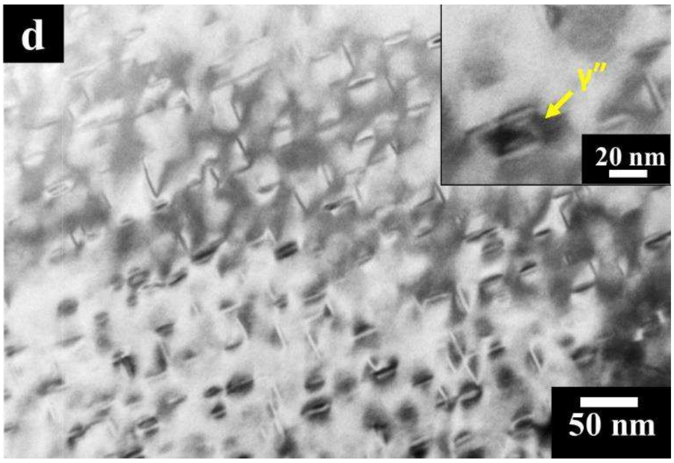

Figure 77: TEM bright field images of aged IN625 sample at 700 °C for 24 hours showing: a) intergranular Cr-rich $M_{23}C_6$ carbide; b) intergranular Nb-rich phase; c) intragranular Nb,Ti rich-MC carbide; d) intragranular γ'' phases.

3.7.4 Tensile properties of aged IN625 samples

The tensile engineering stress-strain curves of three aged IN625 specimens at 700 °C for 24 hours are illustrated in Figure 78, whereas the tensile properties of the LPBF aged samples compared to wrought IN625 are reported in Table 33.

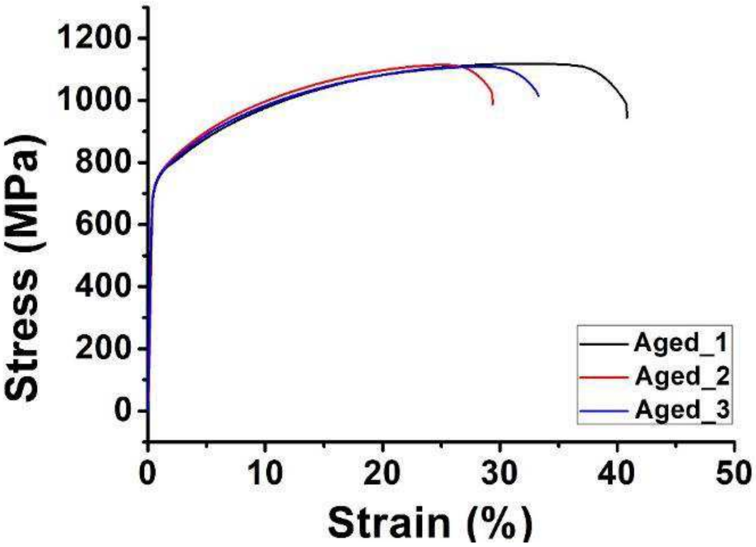

Figure 78: Tensile stress curves of aged IN625 samples at 700 °C for 24 hours.

The aged IN625 samples exhibited lower A, and higher YS and UTS than SHT IN625 samples. The difference can be mainly attributed to the precipitation of fine γ″ phases, as observed during TEM investigation. The tensile properties of aged samples showed lower YS and greater UTS than as-built state, whereas the two condition revealed similar A.

Comparing the tensile properties of the LPBF aged IN625 samples to commercially available SHT wrought IN625, it is possible to note that the tensile properties are still superior to the minimum values, while the maximum values slightly exceed the tensile properties of LPBF SHT IN625 samples.

Finally, the tensile test revealed a E of 200 ± 7 GPa, whereas the IMCE test estimated a value of 213 ± 6 GPa for the SHT IN625 state.

In this case, the higher E of aged samples with respect to the SHT and as-built state derive from the precipiation of γ″ phases, as reported in the literature [133]. In fact, the formation of γ″ phases reduce the quantity of Ni, Nb, Al and Ti, involving a E variation.

Table 33: Comparison of tensile properties of as-built, SHT, aged IN625 samples built along the x-y plane.

Inconel 625 sample	E (GPa)	YS (MPa)	UTS(MPa)	A (%)
This study				
As-built	182 ± 13	783 ± 23	1041 ± 36	33 ± 1
Solution-treated	181 ± 16	396 ± 9	883 ± 15	55 ± 1
Aged	200 ± 7	722 ± 7	1116 ± 6	35 ± 5

3.7.5 Tensile fracture surface of aged IN625 samples

The tensile fracture surfaces of aged IN625 samples showed both brittle fractures showing secondary cracks (Figure 79a) and ductile fractures with fine dimples (Figure 79b).

The presence of the brittle fractures can be associated with the presence of Cr-rich $M_{23}C_6$ carbides along the grain boundaries as well as the formation of Nb-rich phases (probably Laves phases or δ phases) along the grain boundaries. Besides, the cracks formation could be caused by the presence of γ″ phases, as reported in the literature [132,134].

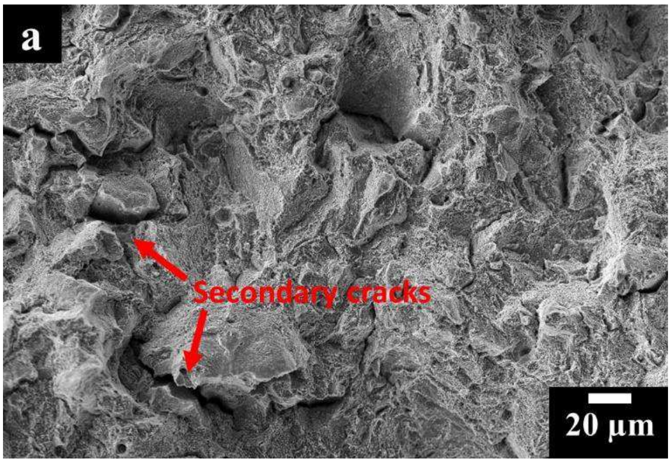

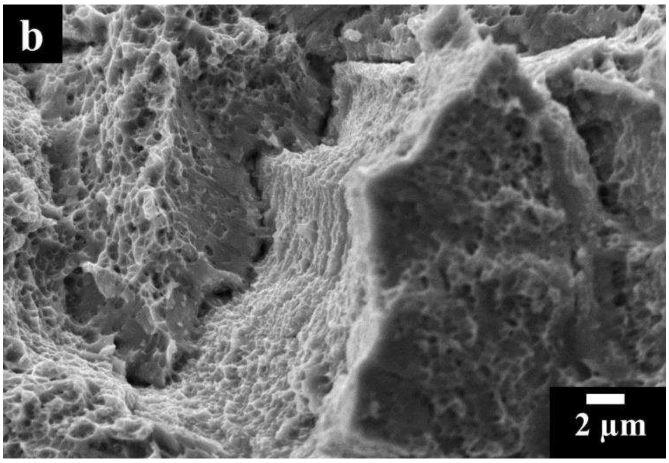

Figure 79: SEM micrographs of aged IN625 tensile fracture surfaces: a) low magnification exhibiting mixed ductile and brittle fractures with secondary cracks; b) higher magnification exhibiting fine dimples as well as brittle fractures.

3.7.6 Microstructure evolution of IN625 sample aged at 800 °C

The OM micrographs of aged samples at 800 °C for 2 hours (Figure 80a), 8 hours (Figure 80b) and 24 hours (Figure 80c) exhibited grain shape and size similar to SHT condition. Differently, it is possible to note the formation of intergranular and intragranular precipitates.

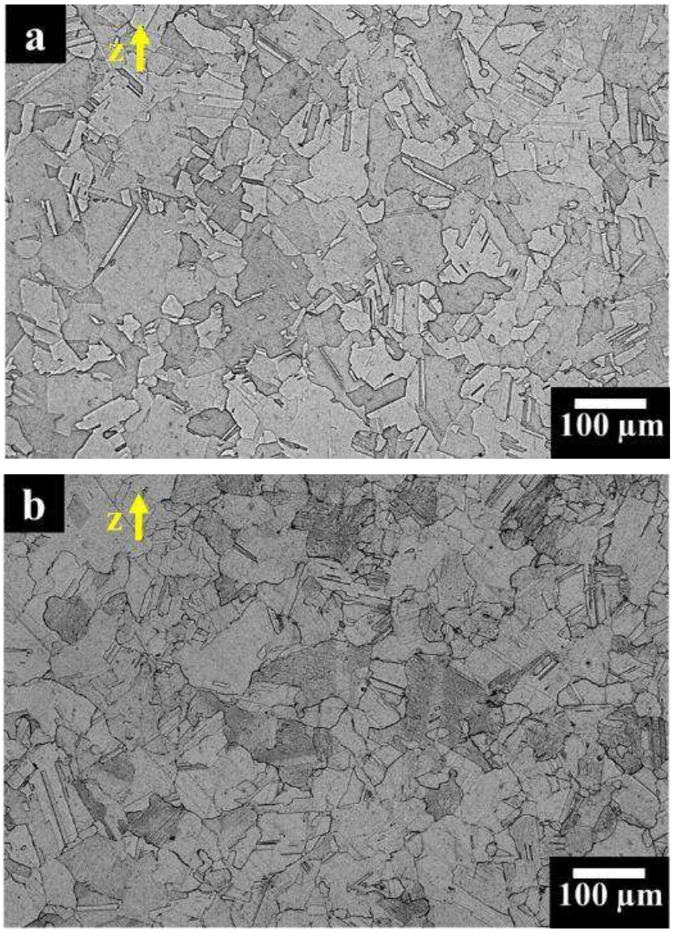

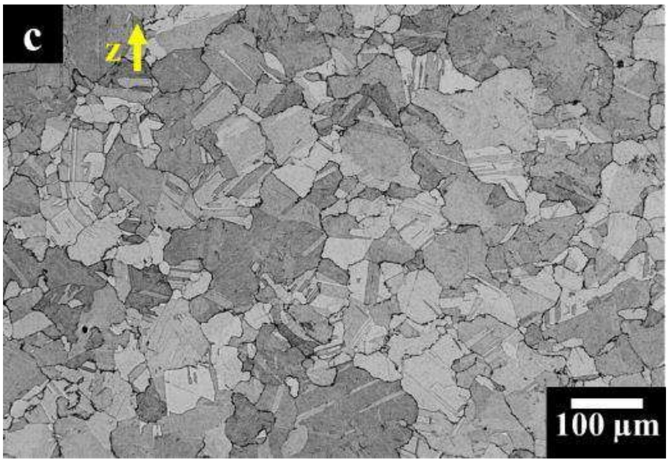

Figure 80: OM images of aged samples at 800 °C for 2 hour (a), 8 hours (b) and 24 hours (c) showing equiaxed grains and twin boundaries with some precipitates along and inside the grains; Kalling's No.2 etchant was used.

At higher magnified OM view, aged samples at 800 °C for 2 hours (Figure 81a) 8 hours (Figure 81b) and 24 hours (Figure 81c) exhibited a gradual formation of inter/intragranular phases. The formation of phases was estimated by means of image analysis, obtaining 2.72 ± 0.59 %, 2.75 ± 0.24 %, 4.08 ± 0.51 % after heat treatment for 2 hours, 8 hours and 24 hours, respectively.

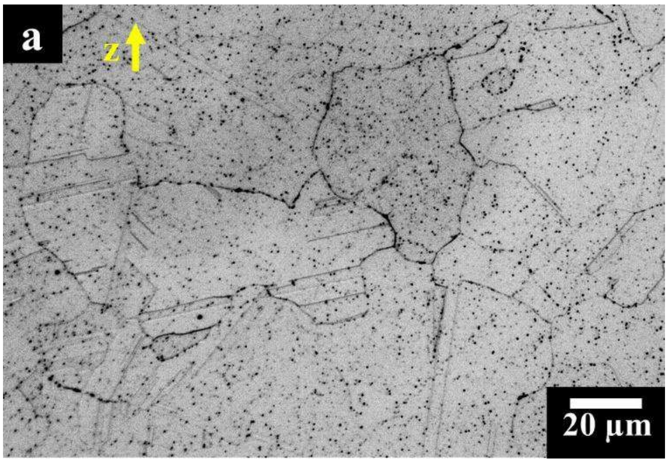

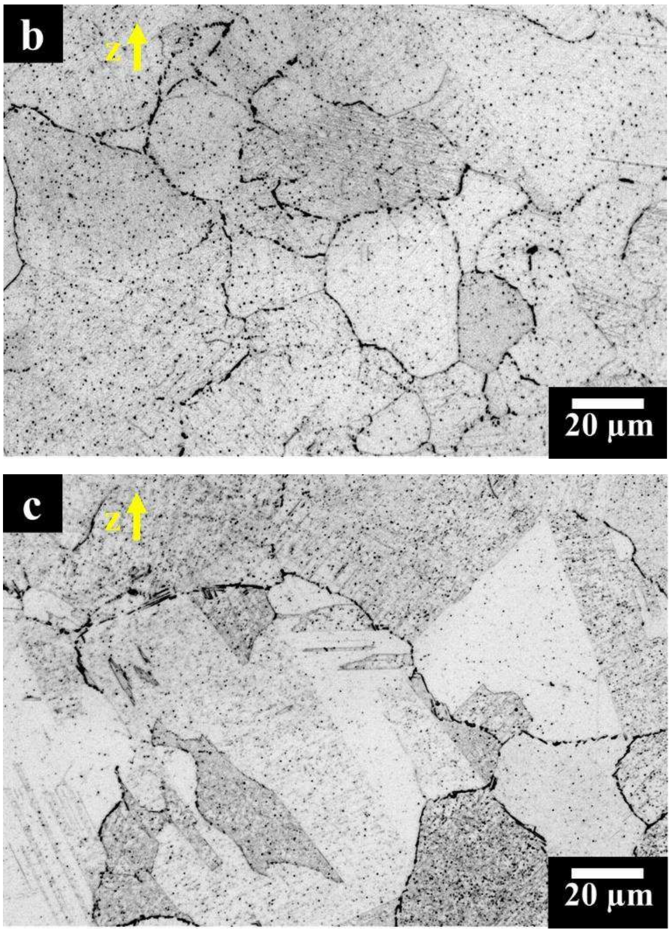

Figure 81: OM images of aged samples at 800 °C for 2 hour (a), 8 hours (b) and 24 hours (c) showing a starting precipitation within the grains and along the grain boundaries; Kalling's No.2 etchant was used.

FESEM image of aged sample at 800 °C for 24 hours (Figure 82a) revealed a massive presence of inter/intragranular precipitates, the largest ones located along the grain boundaries.

The intragranular areas showed acicular precipitates associated with δ phases indicated by arrow 1 in Figure 82b. Other elongated intergranular precipitates around 1-2 µm pointed out by arrow 2, revealed an enrichment in Nb and Mo coupled to a depletion of Cr with respect to the austenitic matrix, as highlighted by EDS results in Table 34, compatible with the formation of Laves phases.

The δ phases was generally longer along the intergranular areas (up to 3 µm) than intragranular ones (from nanometric up to 1 µm) as pointed out by arrows 1 in Figure xc. Besides, the very fine Nb,Ti-rich carbides of the SHT state can be still observed. The presence of δ phases and Laves phases are compatible to the TTT diagram of IN625 alloys [5,15,39].

These microstructural features can explain why the hardness of aged samples at 800 °C for 24 hours had a hardness improvement around 24 % with respect to the SHT state.

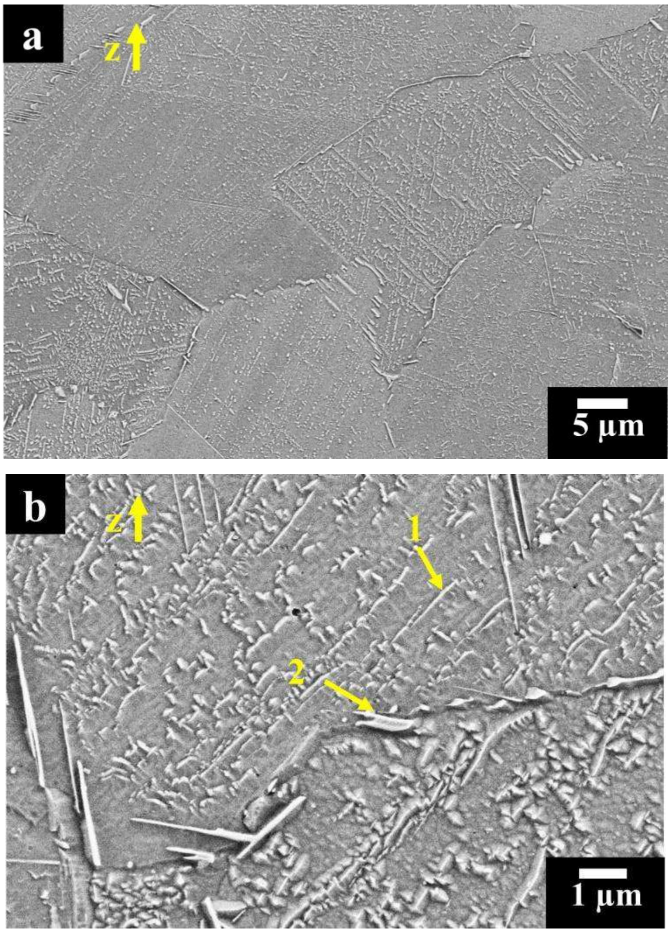

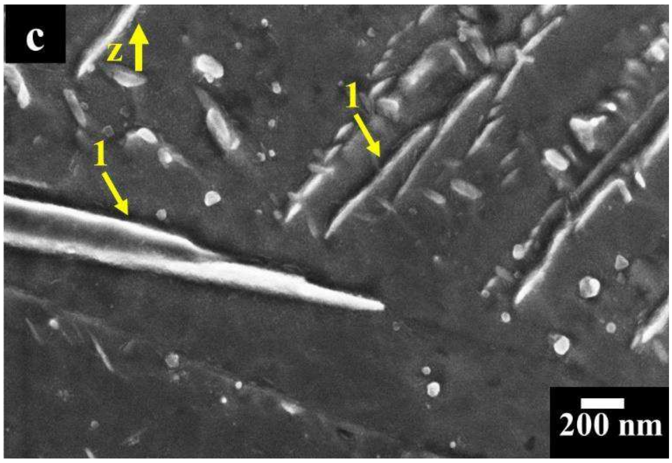

Figure 82: - FESEM images showing: (a) inter/intragranular elongated precipitates; (b) intragranular acicular δ phases indicated by arrow 1 and intergranular elongated Laves phases indicated by arrow 2; (c) δ phases indicated by arrows 1 and fine Nb,Ti rich MC carbides formed during the solution treatment; Kalling's No.2 etchant was used.

Table 34: EDS results of Laves phase and austenitic phase for the aged IN625 sample at 800 °C for 24 hours.

	Laves phase (arrow 2)		Austenitic matrix	
	Wt %	At %	Wt %	At %
Ni	61.7	64.3	63.4	64.6
Cr	17.6	20.8	21.4	24.6
Mo	10.3	6.6	9.2	5.7
Nb	8.2	5.4	4.2	2.7
Fe	0.8	0.8	0.7	0.7
Co	0.2	0.2	0.3	0.3
Ti	0.7	0.9	0.4	0.5
Al	0.5	1.0	0.4	0.9

3.7.7 Microstructure evolution of IN625 sample aged at 900 °C

The SHT IN625 samples after ageing at 900 °C for 2 hours (Figure 83a), 8 hours (Figure 83b) and 24 hours (Figure 83c) revealed equiaxed grains and twin boundaries, as previously observed for the SHT state. However, it is possible to note a progressive precipitation inside the grains and along the grain boundaries.

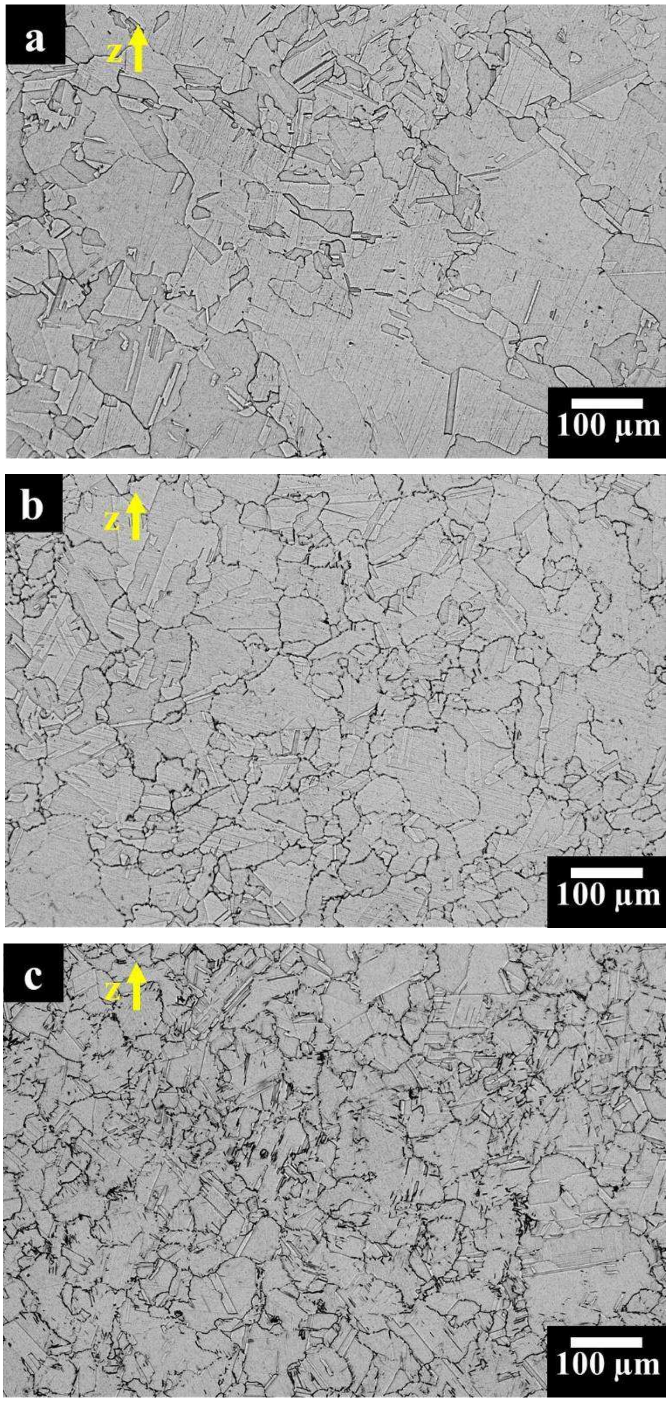

Figure 83: OM images of aged samples at 900 °C for 2 hour (a), 8 hours (b) and 24 hours (c) showing equiaxed grains and twin boundaries together with the formation of inter/intragranular phases; Kalling's No.2 etchant was used.

In fact, thermal exposure at 900 °C gradually promoted the formation of inter/intragranular precipitates, as can be seen in Figure 84a (after 2 hours), Figure 84b (after 8 hours), Figure 84c (after 24 hours). The fraction of phases was calculated 4.16 ± 0.11 %, 4.59 ± 0.36 %, 5.65 ± 0.39 % after heat treatment for 2 hours, 8 hours and 24 hours, respectively.

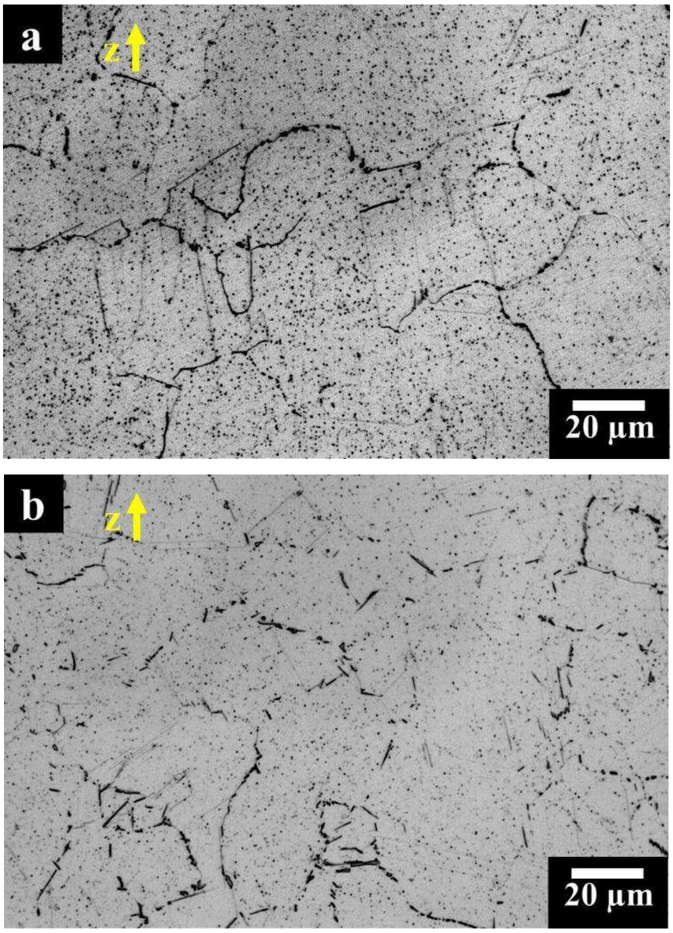

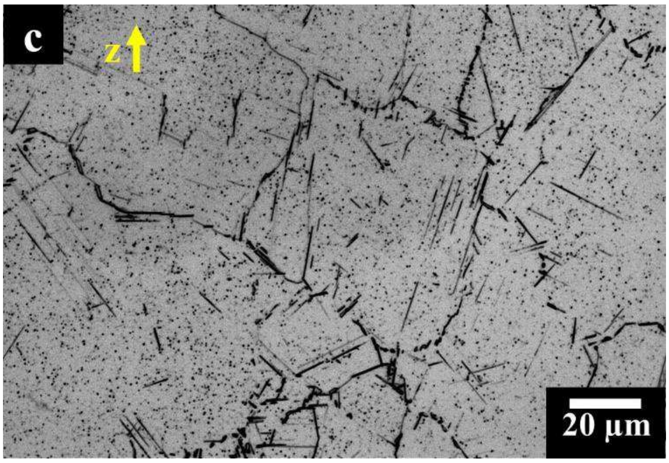

Figure 84: OM images of aged samples at 900 °C for 2 hour (a), 8 hours (b) and 24 hours (c) showing a starting precipitation within the grains and along the grain boundaries; Kalling’s No.2 etchant was used.

FESEM image of aged sample at 900 °C for 24 hours (Figure 85a) revealed a massive presence of acicular δ phases, mainly located along the grains boundaries. Differently, from the previous case (aged at 800 °C for 24 hours), the δ phases had length up to 12 µm. Figure 85b reveals one of the intergranular acicular δ phases with size around 10 µm, indicated by arrow 1 in Figure 85b, whereas Figure 85c shows a small δ phase around 1.5 µm.

Besides, intergranular precipitates around 2 µm, indicated by arrow 2 in Figure 85b, can be also observed in Figure 85b. The EDS analysis (Table 35) revealed enrichment in Nb and depletion of Cr, compatible with the formation of Laves phases. Also at this temperature, the Nb,Ti rich MC carbides (formed during the solution treatment) were still visible. The presence of δ phases and Laves phases are compatible to the TTT diagram of IN625 alloys [5,15,39]. The coarse microstructure of this aged IN625 samples apparently explains why they underwent a hardness increment of only around 2 % with respect to the SHT state.

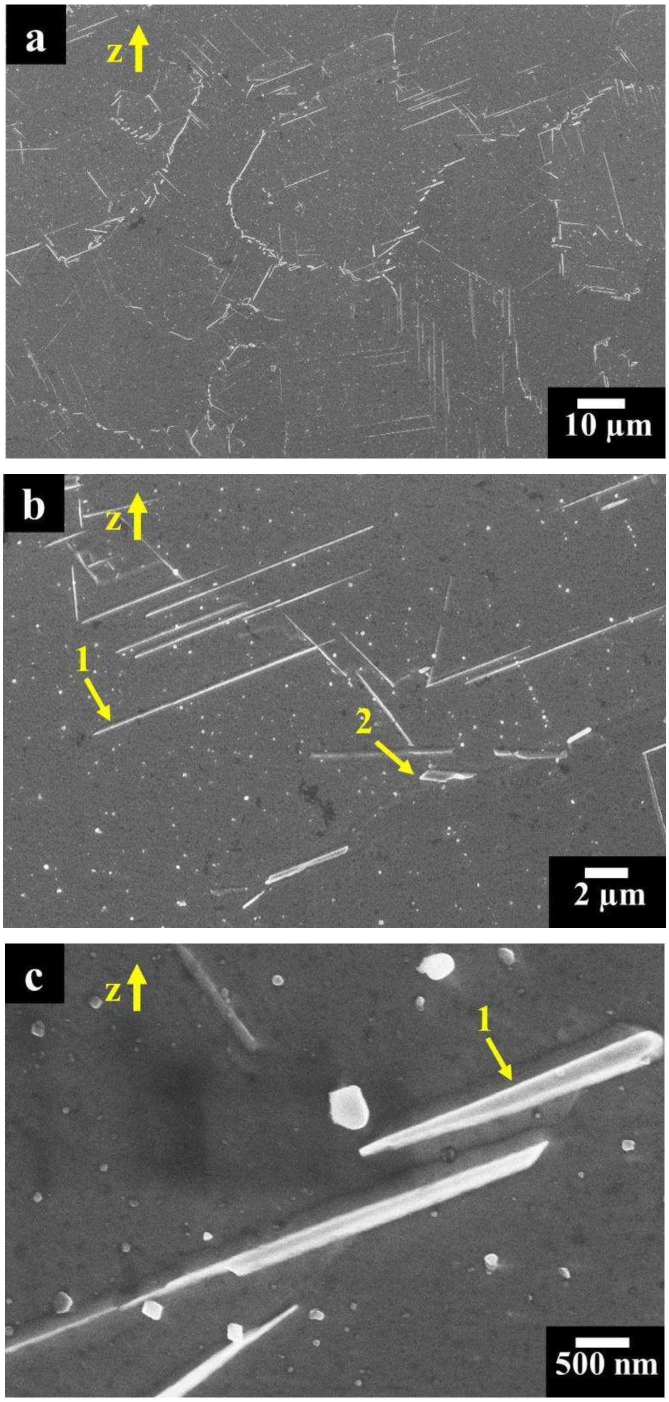

Figure 85: FESEM images of aged samples at 900 °c for 24 hours showing: (a) inter/intragranular elongated precipitates; (b) intragranular acicular δ phases indicated by arrow 1 and intergranular elongated Laves phases indicated by arrow 2; (c) Intergranular acicular δ phases and fine Nb,Ti-rich MC carbides; Kalling's No.2 etchant was used.

Table 35: EDS results of Laves phase and austenitic phase for aged IN625 samples at 900 °C for 24 hours.

	Laves phase (arrow 2)		Austenitic matrix	
	Wt %	At %	Wt %	At %
Ni	62.9	68.1	64.0	65.2
Cr	9.6	11.7	20.8	23.9
Mo	8.8	5.8	9.2	5.7
Nb	16.5	11.3	4.1	2.6
Fe	0.6	0.6	0.8	0.9
Co	0.3	0.3	0.2	0.2
Ti	0.9	1.3	0.5	0.6
Al	0.4	0.9	0.4	0.9

3.8 Tensile behaviour of as-built and heat-treated IN625 samples

The Ludwik-Hollomon equation has been used to study the flow curve in the uniform elongation stage, thus obtaining the strain hardening parameters for the as-built, direct aged at 700 °C for 24 hours, SHT at 1150 °C for 2 hours, as well as aged at 700 °C 24 hours IN625 samples. The strain hardening stage, the K and n parameters together with the ratio between YS and UTS are given in Table 36.

Table 36: Strain hardening parameters as calculated on IN625 samples for as-built (AB) direct aged (700 °C for 24 hours), SHT (1150 °C for 2 hours) and aged (700 °C for 24 hours) IN625 samples.

IN625 Samples	YS/UTS	K (MPa)	n
As-built	0.75	1408 ± 6	0.595 ± 0.004
Direct aged	0.82	1285 ± 6	0.504 ± 0.005
SHT	0.45	1861 ± 2	0.711 ± 0.001
Aged	0.65	1853 ± 5	0.601 ± 0.002

The direct ageing of the as-built material provides a reduction of the strain hardening region with respect to the as-built state. This can be assumed by the increment of the YS/UTS ratio, by the slight reduction of the n-exponent and by the considerable reduction of the uniform elongation at break. The increase of YS/UTS ratio is caused by the marked improvement of the YS (~30%) and by the more limited increase in UTS (~17%) with respect to the as-built state. Regarding the microstructural investigation reported above, such marked increase in the YS can come from the precipitation of the intergranular Cr-rich $M_{23}C_6$ carbides, Nb-rich phases along the grain boundaries and γ'' phases.

All these phases generate obstacles to dislocation motion, thus resulting in higher resistance for plasticity to occur. At the same time when the energy state for plasticity is obtained, these phases limited the capability of the material to deform in the plastic region, reducing the strain hardening region and elongation at break. This is also supported by the higher number of brittle features in the fracture surface of direct aged samples. Furthermore, it is interesting to note that the direct aged state revealed similar dendritic architectures and high dislocation density to as-built condition. As a result, these features do not take part to the modification of the tensile properties of the LPBF IN625. This is pointed out by the shape of the flow curve and the values of the n-exponent which resulted to be similar for both conditions.

Differently, in the SHT condition the recrystallization, dissolution of the dendritic architectures and segregated elements, as well as the recovery of tangled dislocation lead to an evident alteration of the flow curve shape and of the n-exponent with respect to the as-built and direct aged states. Regarding the plasticity, the SHT state reveals an expansion of the strain hardening region. This can be ascribed to the diversity between YS and UTS levels and by the striking increase in the n-exponent value and uniform elongation. These aspects are evident by confronting the SHT and as-built condition.

Specifically, in this case, the YS level is remarkably reduced due to recrystalization and by the almost complete suppression of the tangled dislocations structure. Besides, both strength levels dropped off, with a~ 50% and a~ 15% reduction for YS and UTS, respectively.Furthermore, the solution treatment also increases the n-exponent, involving a total variation of the flow curve shape with respect to the as-built state. In fact, the microstructural modification triggered by solution treatment generates a more homogeneous material with a greater ability for plastic deformation, as indicated by the increase in maximal elongation at break. The enhancement of plastic behaviour is also evident by the higher amount of micrometric and sub-micrometric dimples revealed by the fracture surface observation, when compared to on the as-built samples.

Finally, ageing treatment after solutioning provides a YS level similar to the as-built state and a UTS greater than those of the as-built condition, resulting in a YS/UTS ratio slightly lower than those of the as-built state. Also, in this case, the enhancement of the YS and UTS derived from the precipitation of grain boundary Cr-rich $M_{23}C_6$ carbides, Nb-rich phases and the homogeneous formation of the γ'' phases. By contrast to the direct aged state, the elimination of dendritic structures and tangled dislocation structures promotes the capability of the materials to deform plastically. The carbides and γ'' phases precipitation do not modify the shape of the flow curve and provide a limited decrease of the n-exponent and elongation.

When confronting the direct aged and SHT and aged conditions, the significant microstructural difference that can be observed is the existence of the latter state of fine secondary carbides and homogenous γ″ phases precipitation. In fact, the solution treatment eliminate the segregation homogeneously the material, thus making available the elements for the phases formation. The formed phases give an actual strengthening effect without remarkable decrease the elongation. On the other hand, as for direct aged samples, brittle fractures of aged samples can be correlated to intergranular carbides or Nb-rich phases. It was therefore discussed that the modulation of microstructural features performing heat treatment of as-built LPBF IN625 involves a broad spectrum of possible mechanical behaviour influencing chiefly the YS, YS/UTS ratio, the strain hardening parameters and the ductility of the material.

3.9 Conclusions

This work started with the process parameters optimisation of LPBF IN625 samples, investigating the effect of different laser power, scan speed and hatching distance on the densification and hardness levels, reaching relative density superior to 99.8 %.

The microstructure of as-built LPBF IN625 (built using optimised parameters) revealed microstructure consisted of columnar grains and randomly equiaxed grains along the building direction (z-axis) and perpendicular to the building direction (x-y plane), respectively. TEM images revealed very fine dendritic architectures (generally less than 1.5 μm) with a high density of dislocations due to the rapid cooling rates involved during the process.

FESEM and TEM analyses seem to point out the existence of fine Nb-rich MC carbides (10-50 nm) within the dendritic cores. The as-built IN625 samples exhibited higher mechanical properties than minimum values for as-rolled IN625 alloy, showing mixed brittle and ductile fractures. Finally, also CTE and K were determined.

Afterwards, the work was especially focused on studying the microstructural evolution of the LPBF IN625 alloy under different heat treatments, performing direct ageing treatments on as-built IN625 samples as well as ageing treatments on SHT IN625 samples at 1150 °C for 2 hours. Direct ageing and ageing at 600 °C up to 24 hours mainly revealed the presence of γ″ phases. Direct ageing and ageing at 700 °C up to 24 hours chiefly promoted the formation of γ″ phases and $M_{23}C_6$ carbides. Direct ageing or ageing at 800 °C and 900 °C up to 24 hours led to the formation of δ phases and Laves phases. All these heat treatments applied to as-built or SHT IN625 samples did not alter the grains size. Differently, solutioning performed at 1000 °C and 1150 °C for different times resulted in dendritic architectures dissolution, recrystallisation and grain growth, exhibiting the presence of sub-micrometric carbides (20-400 nm). The different heat-treated IN625 conditions were characterised by hardness test, OM and FESEM analyses.

By these analyses, a direct ageing, a solutioning and an ageing condition were selected, in order to characterise in detail their microstructure by means of TEM analysis as well as their tensile properties. The direct aged IN625 at 700 °C for 24 h showed a microstructure similar to as-built IN625 state. However, the heat treatment led to the generation of discoidal γ″ phases with size around 10-30 nm as well as the formation of elongated intergranular Cr-rich $M_{23}C_6$ carbides. These phases remarkable improved the tensile strengths and hardness of IN625 alloy, while the ductility decreased. Besides, by analysing the fracture surfaces was possible to note more brittle areas than as-built state. The SHT IN625 samples at 1150 °C for 2 h revealed a microstructure made up of equiaxed grains (from 10 to 90 micron) due to recrystallisation and grain growth. TEM analysis revealed a significant reduction of the dislocation density and the formation of inter/intragranular Nb,Ti-rich MC carbides around 20-400 nm.

The dissolution of dendritic architectures together with the formation of equiaxed grains led to lower tensile strengths and greater ductility than as-built and direct aged states, showing both brittle and ductile fracture surfaces. Besides, SHT LPBF IN625 exhibited higher mechanical properties than minimum values of SHT wrought IN625 according to ASTM B443.

The SHT IN625 samples were aged at 700 °C for 24 hours, promoted the formation of γ″ phases homogeneously scattered within the alloys and intergranular

Cr-rich $M_{23}C_6$ carbides. The presence of these precipitates involved higher tensile strengths and lower ductility than SHT state, while the fracture mechanism showed mixed brittle and ductile fractures.

To sum up the tensile properties of the LPBF as-built and heat-treated IN625 samples surpassed the minimum values reported in ASTM standard for Inconel 625. The only exception is for the directed aged condition that showed remarkable tensile strengths but slightly lower ductility than minimum values recorded in the ASTM standard.

These results highlighted how it is possible to drastically modify the microstructure of LPBF IN625 alloy to create tailored microstructure and so determined mechanical properties for industrial application, exceeding the minimum requirements for traditional IN625 alloy reported in the ASTM standards.

Chapter 4

Results and discussion of IN625 produced by DED process

This chapter is concerned with the study and development of IN625 alloy by means of directed energy deposition (DED) process. Firstly, it was characterised the starting powder, focusing on the powder particles in term of particle size distribution, morphology, chemical composition as well as residual porosity.

Secondly, it was carried out a process parameter optimisation using different parameters for fabricating IN625 samples, in order to determine their impact on the densification level and hardness.

Finally, it was studied the microstructure of the samples with the highest densification level.

The main finding of this investigation was published in an international scientific journal [56].

4.1 DED Powder characterisation

The gas atomised IN625 powder presented a significant number of almost spherical particles, including a few elongated and irregular particles, as illustrated in Figure 86a and 86b. Besides, observing the surface of some particles was also possible to distinguish satellite particles, as pointed out by arrows in Figure 86b.

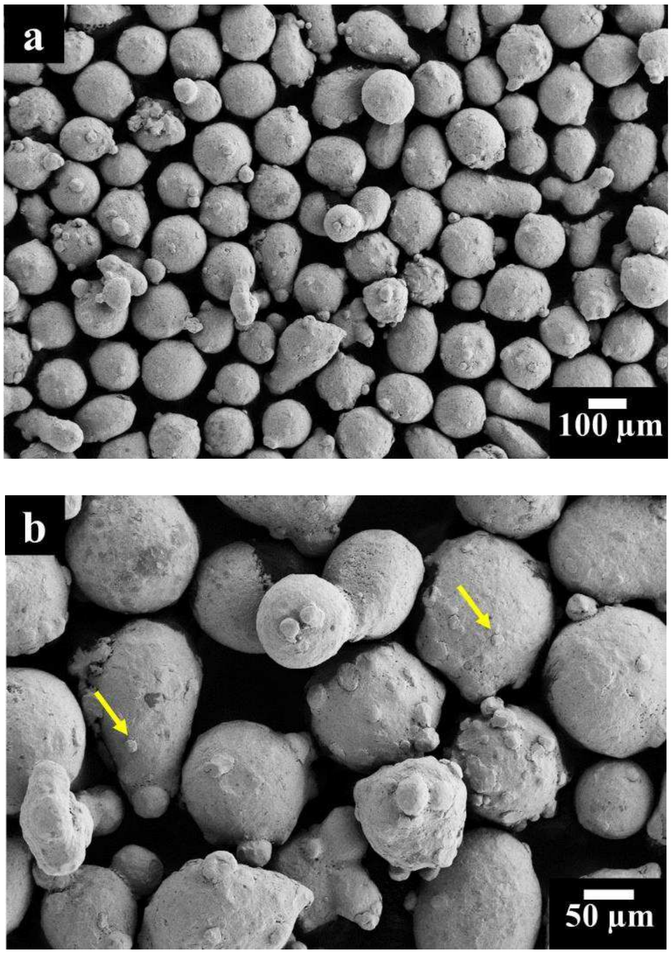

Figure 86: FESEM images of the IN625 powder particles at different magnifications (a,b), in which some satellite particles are pointed out by the yellow arrows.

The cross-section of powder particles (Figure 87a and 87b) mainly displayed spherical pores from 1 µm to 30 µm, some of which are indicated by red circles, obtaining a residual porosity of about 0.213 %. These spherical pores are commonly generated during the gas atomisation process, containing entrapped inert gas [46,80,90,135].

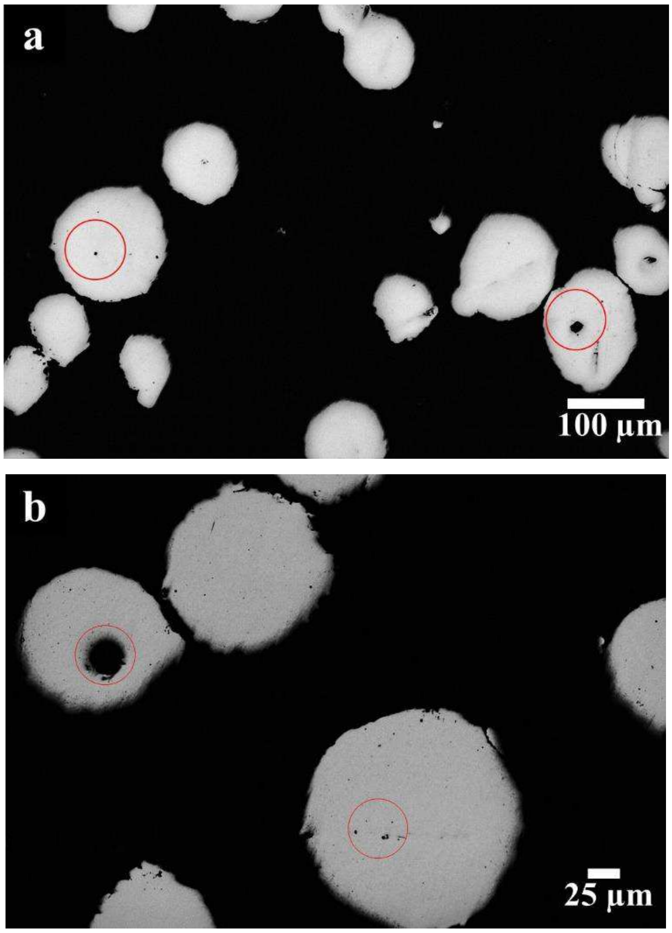

Figure 87: OM micrographs of mounted and polished IN625 particles at different magnification (a, b), highlighting the existence of internal spherical pores, some of which are indicated by red circles.

The EDS analysis of the powder revealed a chemical composition similar to the declared company data sheet and standard UNS N06625, also showing the presence of elements not determined in the data sheet, such as Al, Si, Mn, as reported in Table 37. The values of Ti and Nb obtained by EDS are marginally outside the requirements of the standard UNS N06625. However, it should be considered that EDS analysis does not allow a precise chemical composition quantification.

Table 37: EDS results of main chemical elements reported in weight percentage (wt %) for IN625 powder compared to company datasheet and standard UNS N06625.

Element	Company data sheet (wt %)	EDS powder (wt %)	UNS N06625 (wt %)
Ni	Bal.	66.1	58.0 min
Cr	21.5	22.1	20.0-23.0
Mo	9.0	8.6	8.0-10.0
Nb + Ta	3.8	2.9	3.15-4.15
Fe	1.4.	0.8	5.0 (max)
Si	0.4.	0.4	0.5 (max)
Ti	-.	0.5	0.4 (max)
Al	-	0.3	0.4 (max)
Mn	-.	0.3	0.5 (max)
C	<0.03	-*	0.10 (max)

**not detected by EDS analysis due to overestimation*

The particle size distribution of the DED powder revealed particle size with d(0.1), d(0.5) and d(0.9) of 81 µm, 110 µm, and 150 µm, as illustrated in Figure 88. After the application of ultrasonic vibration, the DED powder had essentially the same particle size distribution, thus indicating their low tendency to form aggregates.

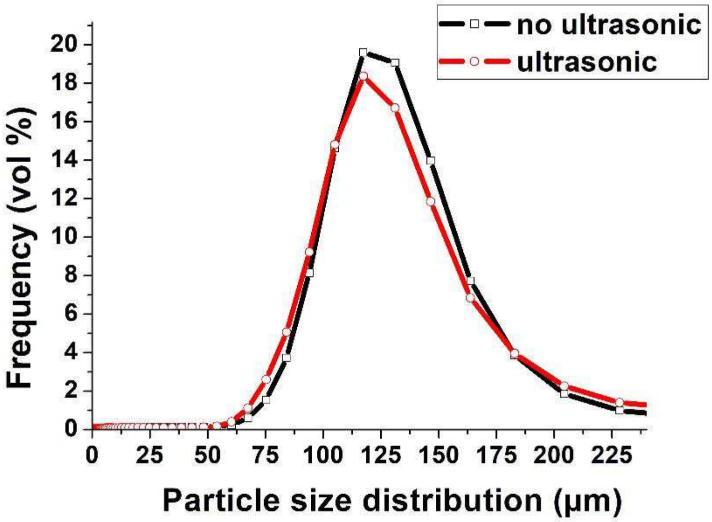

Figure 88: Particle size distribution of IN625 powder obtained by means of laser granulometry diffraction with and without ultrasonic vibration [56].

Table 38 provides the values of the apparent density, flowability as well as skeletal density, and they can be compared to the determined values of LPBF IN625 powder reported in paragraph 3.1.

The apparent density revealed higher values than LPBF IN625 powder, which can be associated with its wider powder size distribution. In this case, it was possible to perform both Hall and Carney flowmeters, obtaining a Carney flow rate lower than LPBF IN625 powder, indicating a greater flowability.Finally, the skeletal density revealed values similar to the theoretical IN625 density, although the value was less than those of LPBF IN625 powder [3]. This slight difference is caused by a higher level of residual pores within the powder, as determined during the particle cross-section analysis, thus reducing the skeletal density.

Table 38: Average value and standard deviation of Apparent density, Flowability and Skeletal density for DED IN625 powder[56].

IN625 powder	Apparent density [g/cm^3]	Hall flow rate [s/ 50g]	Carney flow rate [s/ 200g]	Skeletal density [g/cm^3]
	4.63 ± 0.04	17.4 ± 1.4	12.3 ± 0.1	8.43 ± 0.02

4.2 Process parameters optimisation

Figure 89 reveals the hardness trend versus residual porosity of the samples built using different process parameters by DED process (reported in paragraph 2.1.2). The graph shows a linear trend confirming the negative correlation between porosity and hardness, the lower the porosity the higher hardness, is obtained.

For the employed parameters, the hardness had values between 200 and 225 HBW, whereas the residual porosity modified from 0.11 % to 0.25 %. The determined hardness values of DED as-built samples are similar to the commercially available data of as-rolled IN625, with Brinell hardness between 175 HBW and 240 HBW [37].

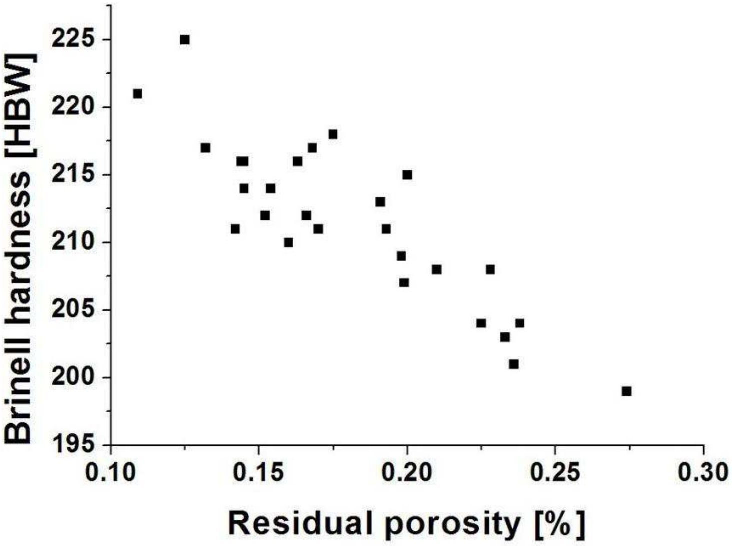

Figure 89: Brinell hardness vs residual porosity for as-built IN625 samples produced by DED process using different process parameters.

Differently, from the LPBF process, it was not possible to note some trends in residual porosity and hardness values vs. energy density. However, according to the data determined for the DED process (Table 39), the R9 samples produced with a laser power of 1800W, a scan speed of 13.3 mm/s and a powder flow rate of 5 g/min had the lowest porosity, 0.109 %. On the other hand, the sample R4 produced with a laser power of 2100W, a scan speed of 10.0 mm/s and a powder flow rate of 5 g/min had the highest hardness, 225 HBW.

Regarding all the samples built using different parameters, the variation in hardness can be associated with different residual porosity. However, the difference may also be correlated to different heating and cooling rates, which create a microstructure with larger dendritic structures or promoting the formation of a different concentration of phases inside the materials.

Table 39: Different process parameters and energy density used for producing IN625 specimens with the correlate obtained residual porosity and hardness values [56].

Sample	P [W]	v [mm/s]	P_f [g/min]	E_D [J/mm^2]	Residual Porosity [%]	Brinell hardness [HBW]
R1	2100	10.0	9	70.0	0.145 ± 0.015	214 ± 3
R2	1800	13.3	13	45.1	0.160 ± 0.043	210 ± 2
R3	2100	13.3	9	52.6	0.166 ± 0.032	212 ± 4
R4	2100	10.0	5	70.0	0.125 ± 0.029	225 ± 3
R5	2100	13.3	5	52.6	0.200 ± 0.037	215 ± 2
R6	1800	16.7	13	35.9	0.168 ± 0.034	217 ± 3
R7	1800	10.0	13	60.0	0.163 ± 0.033	216 ± 4
R8	2400	16.7	13	47.9	0.175 ± 0.043	218 ± 4
R9	1800	13.3	5	45.1	0.109 ± 0.012	221 ± 3
R10	1800	16.7	9	35.9	0.199 ± 0.030	207 ± 5
R11	2400	16.7	9	47.9	0.236 ± 0.051	201 ± 3
R12	2100	13.3	13	52.6	0.233 ± 0.050	203 ± 3
R13	2400	13.3	9	60.2	0.238 ± 0.440	204 ± 5
R14	2400	13.3	5	60.2	0.154 ± 0.034	214 ± 4
R15	1800	10.0	9	60.0	0.132 ± 0.018	217 ± 5
R16	1800	10.0	5	60.0	0.152 ± 0.030	212 ± 4
R17	2400	16.7	5	47.9	0.198 ± 0.027	209 ± 3
R18	2400	10.0	13	80.0	0.145 ± 0.011	216 ± 3
R19	2400	13.3	13	60.2	0.228 ± 0.071	208 ± 4
R20	2100	16.7	5	41.9	0.144 ± 0.018	216 ± 3
R21	1800	13.3	9	45.1	0.170 ± 0.041	211 ± 3
R22	2100	16.7	13	41.9	0.142 ± 0.042	211 ± 5
R23	1800	16.7	5	35.9	0.274 ± 0.072	199 ± 2
R24	2400	10.0	9	80.0	0.225 ± 0.021	204 ± 3
R25	2100	16.7	9	41.9	0.210 ± 0.012	208 ± 7
R26	2400	10.0	5	80.0	0.193 ± 0.035	211 ± 3
R27	2100	10.0	13	70.0	0.191 ± 0.055	213 ± 3

4.3 Investigation of defects of as-built IN625 samples

Figure 90 reveals the optical micrographs of polished R9 and R23 IN625 samples, which are the samples with the highest densification level and the samples with the highest residual porosity, respectively.

For the R9 samples (Figure 90a) can be mainly detected spherical pores around 3 μm, with the largest ones around 15 μm, whereas for the R23 samples (Figure 90b) can be mainly observed spherical pores around 3 μm with the biggest ones around 30 μm.

This kind of pores are indicated by red circles in Figure 90a and 90b, and their shape and size seem to indicate that they derive from the entrapped gas in the powders.

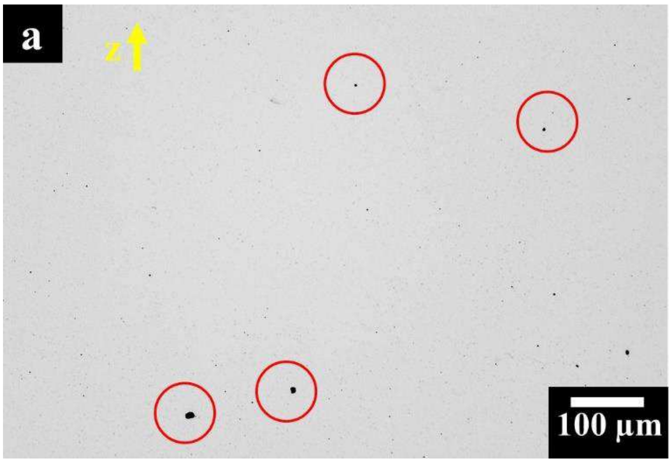

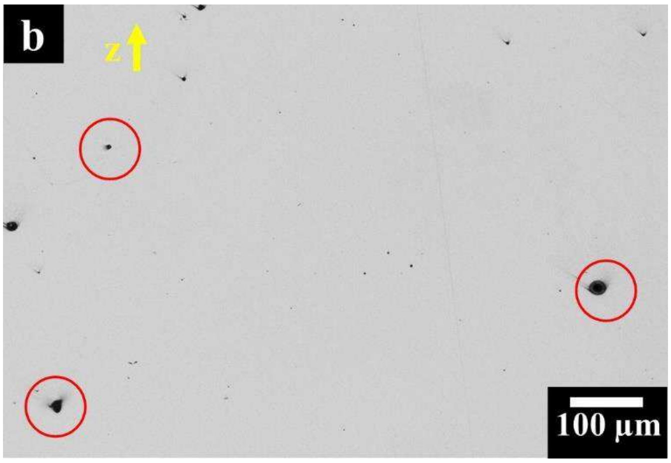

Figure 90: - OM micrographs of polished IN625 samples fabricated using different process parameters along the building direction showing: (a) R23 sample with the highest residual porosity and (b) R9 sample with the lowest residual porosity; both the micrographs exhibit different spherical pores, some of which are highlighted by red circles.

4.4 Microstructure of as-built IN625 samples

The following microstructure analyses were performed on R9 samples, which revealed the highest densification level. From Figure 91a, it is possible to distinguish the deposited layer boundaries (DLB), heat altered zone (HAZ), melt pool (MP) and areas with columnar dendrites (CDs).

The DLB is positioned between two MPs along the building direction (z-axis), as highlighted by the dotted lines, while the heat altered zone exhibited slightly coarse microstructure. The directions of CDs stem from the orientation of the heat fluxes, which are closely associated with the building strategy, thus generating various orientated columnar grains.

As evident in Figure 91b, the microstructure displayed the presence of PDAS and SDAS, and by means of OM investigation was determined PDAS values of around 10 ± 2 µm together with SDAS value of around 3.5 ± 0.8 µm. The dimensions of the dendrite architecture dimensions are similar to those determined by other research on IN625 and IN718 produced by DED processes [135,136].

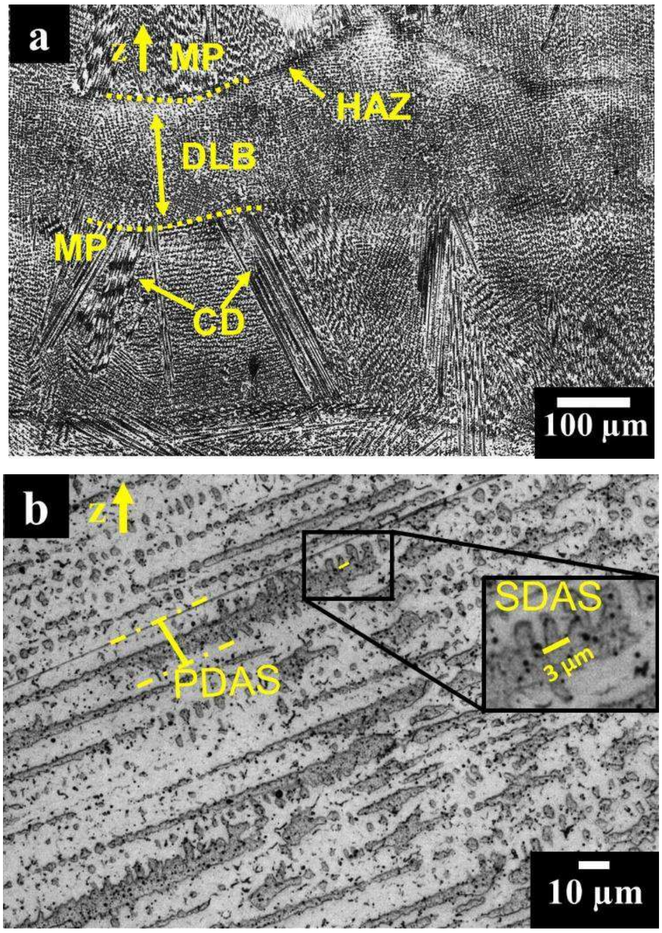
a
z
MP
HAZ
DLB
MP
CD
100 µm
b
z
SDAS
3 µm
PDAS
10 µm

Figure 91: Optical micrographs (a, b) of IN625 fabricated by DED process along the building direction at different showing: deposited layer boundaries (DLB), heat altered zone (HAZ), melt pools (MP), columnar dendrites (CDs), primary dendrite arm spacing (PDAS) and secondary dendrite arm spacing (SDAS); mixed acids etchant was used [56].

After mixed acids etching, FESEM image (Figure 92a) shows the dendritic architectures with PDAS and SDAS. At higher magnifications (Figure 92b and 92c), small square voids along the dendritic and interdendritic regions, as pointed out by arrows 1 and 2, can be observed. These voids may be caused by the dissolution of small precipitates due to the used etchant.

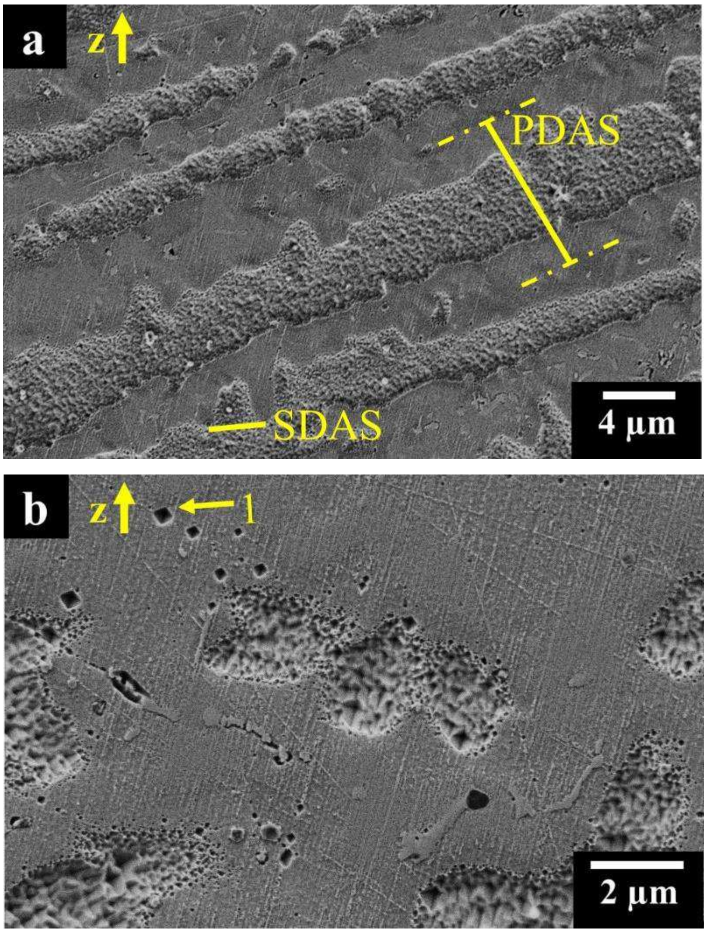

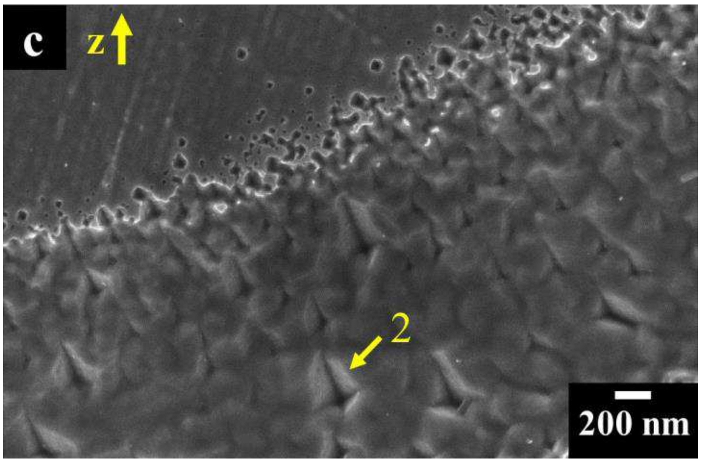

Figure 92: FESEM images of IN625 fabricated by DED at different magnifications along the building direction showing: (a) PDAS and SDAS; (b) square voids indicated by arrows 1 in the dendritic areas; (c) square voids indicated by arrow 2 in the interdendritic areas; mixed acids etchant was used [56].

After Kalling’s No.2 etching, Figure 93a and 93b reveal the presence of elongated and globular precipitates indicated by arrows 3 and 4, respectively. The EDS analysis (Table 40 and Figure 94) showed the elongated precipitates phases had an enrichment in Nb, Mo, Si together with Cr depletion, suggesting the formation of Laves phases due to eutectic reaction [5,29,137]. Likewise, the fine globular precipitates may be associated with the formation of Nb-rich MC carbides due to eutectic reaction [5,31,138].

According to the literature, these two phases are commonly formed by eutectic reaction during the solidification of IN625 alloys [5,31]. The elongated Laves phases had length up to 10 µm, whereas the square carbides had sizes between 0.1 µm and 1.0 µm. At higher magnification in Figure 93c, it is also possible to note some very fine (around 100 nm) ellipsoidal particles. The ellipsoidal precipitates could be identified as gamma double prime (γ'') phases, although prolonged thermal exposure commonly forms them [5]. However, a possible theory is that the continuous heating flux of the DED process promotes the formation of γ'' phases.

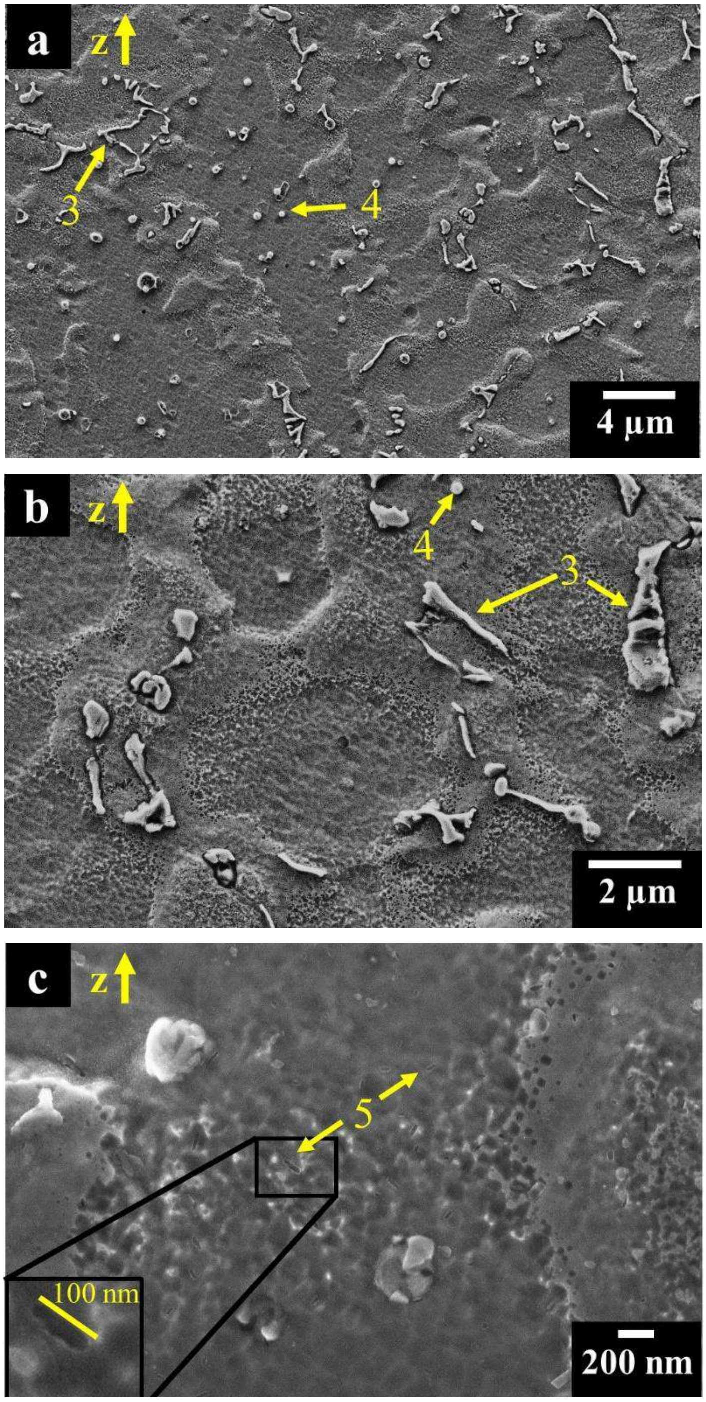

Figure 93: FESEM images of IN625 fabricated by DED at different magnifications along the building direction showing: (a, b) Laves phases indicated by arrow 3, carbides indicated by arrow 4; (c) ellipsoidal precipitates indicated by arrow 5. Kalling's No.2 etchant was used [56].

Table 40: EDS results in weight percentage of austenitic matrix and Laves phase for the IN625 samples produced by DED [56].

Chemical composition [wt %]	Ni	Cr	Nb	Mo	Fe	Si	Ti
Austenitic matrix (1)	65.9	22.4	2.8	8.7	0.6	0.5	-
Laves phases (2)	52.9	19.4	13.0	12.7	0.3	1.7	-

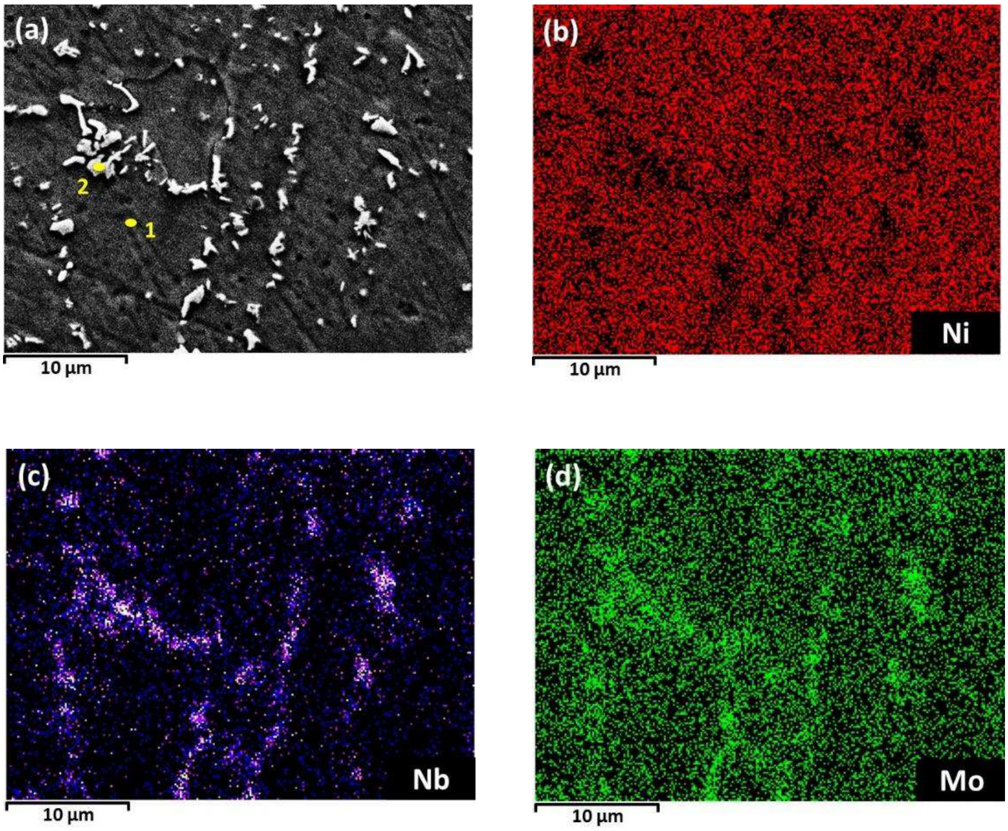

Figure 94: FESEM images of IN625 fabricated by DED: a) microstructural image, b) Ni distribution map, c) Nb distribution map and d) Mo distribution map; Kalling’s No.2 etchant was used [56].

4.5 XRD analysis on as-built IN625 samples

The XRD diffraction patterns of as-built IN625 samples along the building direction (z-axis) and perpendicular to the building direction (x-y plane) are given in Figure 95. The XRD spectra revealed the presence of γ phase having a lattice parameter of around 3.59 Å. However, the Laves phases and Nb-rich carbides were not detected, probably their quantity is lower the threshold of the instrument.

The diffraction pattern interesting revealed a strong (111) orientation along the z direction, and a strong (200) orientation along the x-y plane, that can indicate a particular crystallographic texture as observed for Inconel alloys produced by LPBF or electron beam melting (EBM) processes [64,87].

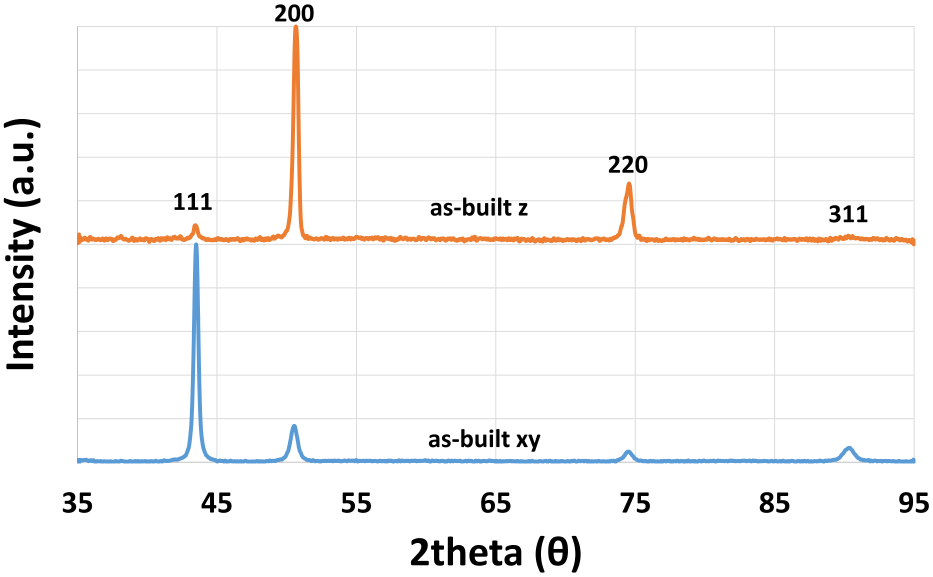

Figure 95: XRD diffraction pattern of as-built IN625 sample along z-axis and x-y plane.

4.6 Conclusions

At the beginning of this work, it was studied the DED IN625 powder, and then it was performed a process parameter optimization in order to choose the correct process parameter to create dense samples. Finally, it was carried out a microstructural investigation on the optimised IN625 samples.

The employed process parameters generated IN625 samples with a residual porosity from 0.11 to 0.25 %, with a hardness between 200 and 225 HBW. The obtained hardness values are compatible with the commercially available values of the as-rolled IN625 alloy. The OM and FESEM investigations proved that these high hardness values can be attributed to the fine microstructure attainable by DED process. The microstructure consisted of PDAS of 10 ± 2 μm and SDAS with a size of 3.5 ± 0.8 μm, together with the presence of Laves phases and carbides formed by eutectic reaction during the solidification process.

Chapter 5

Results and discussion of HX produced by LPBF

This chapter focuses on the microstructural and hardness investigation on Hastelloy X (HX) alloy processed by laser powder bed fusion (LPBF) using an EOSINT-M280 by GE AVIO s.r.l.

At the beginning, it was studied morphology, size, particle size distribution, chemical composition as well as the microstructure of the starting gas atomised HX powder. Afterward, it was investigated the microstructure and hardness of as-built and SHT (abbreviated as SHT) HX samples in order to meet the industrial requirements for components that require high creep resistance. In this part of the work an optimised solution treatment was determined.

The successive target of the current investigation was to study the microstructural evolution of SHT HX samples simulating possible thermal exposure for parts that work at relatively high temperature. Preliminary results of the previous studies were already published [139]. The as-built and SHT HX specimens exhibited large microcracks formed during the LPBF process owing to the low thermal shock resistance of the alloy. A similar microstructure with a high number of microcracks can reduce the mechanical properties and the fatigue life of the as-built HX components.

In the light of the above, some as-built HX samples were hot isostatically pressed (HIPed) at Aubert & Duval facility in order to eliminate the microcracks inside the material. Afterward, GE AVIO s.r.l has performed low-cycle fatigue tests on some as-built and HIPed HX specimens to determine the detrimental effect of the microcracks inside the as-built material. Furthermore, the company has also conducted a study to eliminate the microcracks inside the as-built HX samples in order to reduce post-processing costs avoiding the HIP treatment.

The microstructure of HIPed HX samples was studied and compared to as-built and SHT HX samples, showing a significant precipitation of carbides due to the slow furnace cooling. In order to reduce the carbides formation, different solution treatments were performed on HIPed HX samples, resulting in a microstructure similar to traditional SHT HX alloy, indicating that it was possible to generate HX components suitable for industrial applications by means of LPBF process followed by subsequent tailored post-processing.

To sum up, the work can be divided into four parts:

1) Study and characterisation of the starting HX powder.
2) Microstructure and hardness characterisation of the as-built and different SHT HX samples.
3) Study of the microstructure and hardness development of SHT HX alloy under specific thermal exposure.
4) Study of the microstructure and hardness evolution of HIPed HX samples SHT at different temperatures and times.

5.1 Powder characterisation

The HX powder obtained by gas atomisation exhibited fairly spherical and regular particles together with some irregular particles and clusters as illustrated in Figure 96a and 96b.

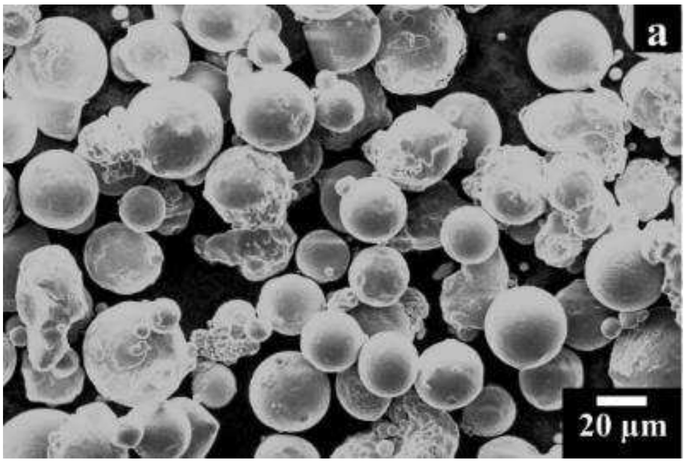

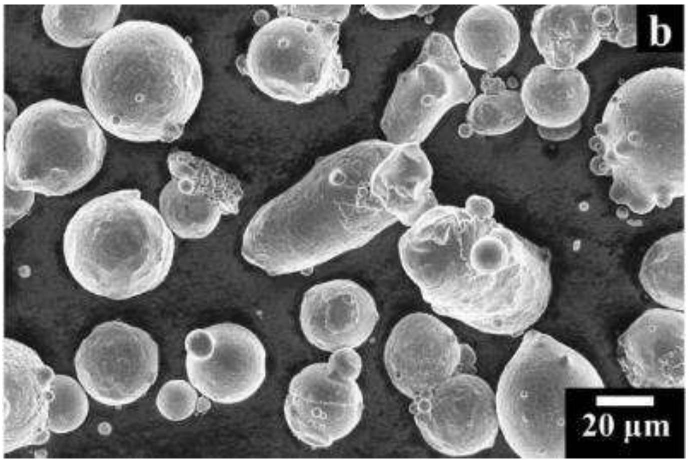

Figure 96: (a, b) FESEM images of gas atomised HX powder showing spherical, irregular particles and clusters.

The mounted and polished particles cross-section exhibited spherical and irregular particle sections (Figure 97a). At higher magnification (Figure 97b), it was possible to observe spherical pores inside the particles, the largest ones with a diameter of 2.5 µm, quantifying a residual porosity of 1.50 ± 0.30 % (using 200 particles).

These spherical pores may be attributed to the entrapped gas during the atomisation process [135]. The mounted and polished particles cross-section was etched with Kalling's No.2 reagent revealing the very fine dendritic structures of the powder (Figure 97c and 97d).

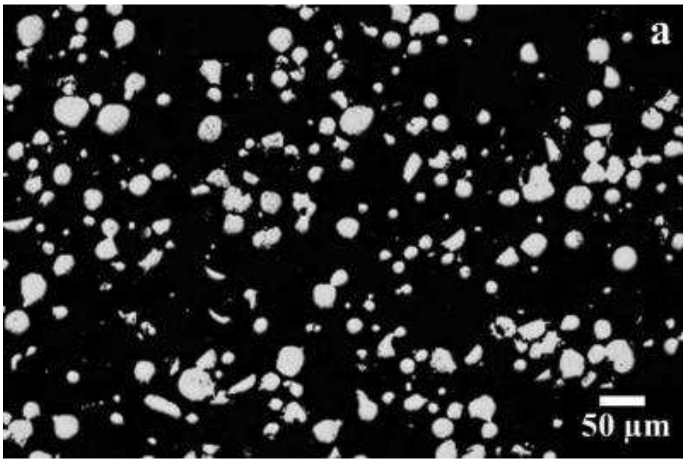

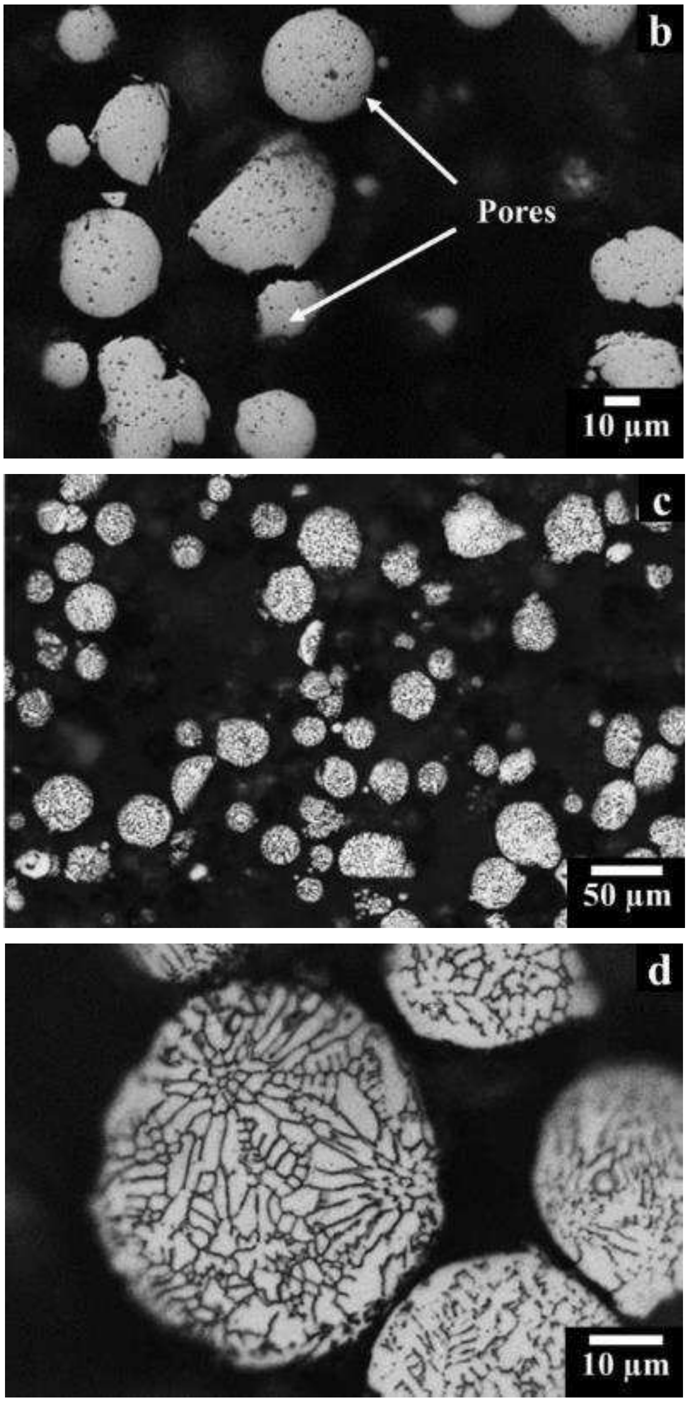

Figure 97: OM images of mounted HX powder particles cross section polished at different magnification showing: (a, b) their morphology and size; (c, d) the dendritic structures after etching with Kalling's No.2 reagent.

The HX powder exhibited a particle size with d(0.1), d(0.5), and d(0.9) of 23.9 µm, 34.8 µm and 52.2 µm, respectively and the curve of frequency (vol %) and cumulative frequency (vol %) are illustrated in Figure 98a and 98b.

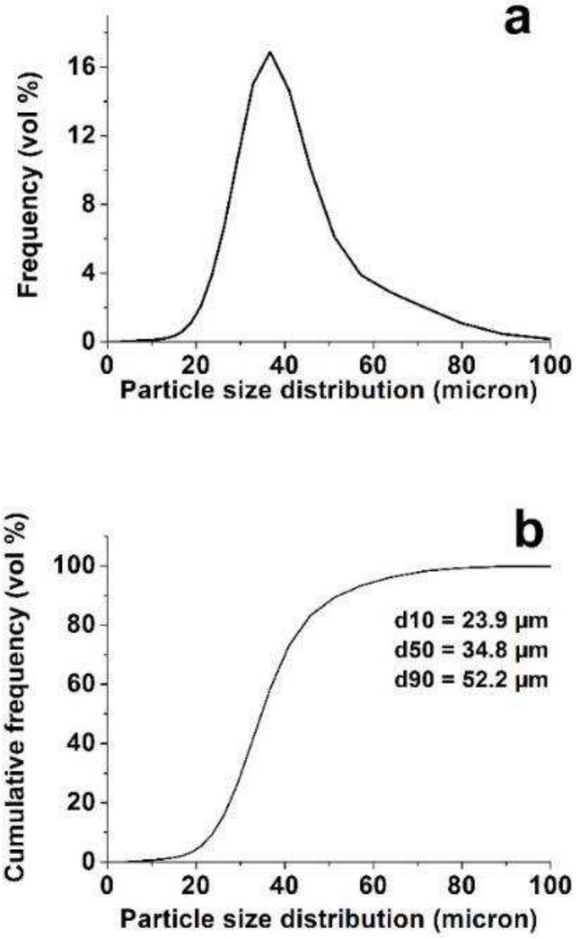

Figure 98: Particle size distribution of frequency (a) and cumulative frequency (b) of particle size distribution obtained by laser granulometry diffraction.

The average apparent density for the SLM powder was 3.98 ± 0.02 g/cm^3, whereas the flow rate obtained by Hall flowmeter was of 13.6 ± 0.4 s 50/g.

The chemical composition was determined by ICP/OES and IGF analyses showing a good correlation with the chemical composition declared by the supplier and the chemical composition requirements according to the ASTM B435, as reported in Table 41. However, it is possible to see that the currently used HX powder had other elements in trace such as V, Hf, Nb, Cu, etc. did not present in the ASTM B435 standard.

Table 41: Chemical composition in weight percentage (wt%) of HX powder and solid samples determined by ICP/OES and IGF analyses compared to the supplier datasheet and the chemical composition requirements reported in the ASTM B435-06 standard.

Element	Determined HX alloy (wt%)	Determined HX Powder (wt%)	Supplier datasheet (wt%)	ASTM B435-06
Ni	Balance	Balance	Balance	Balance
Cr	21.40	21.70	20.50-23.00	20.50-23.00
Fe	18.70	18.60	17.00-20.00	17.00-20.00
Mo	9.35	9.20	8.00-10.00	8.00-10.00
Co	1.85	1.82	1.50-2.50	0.50-2.50
W	0.92	0.90	0.60-1.00	0.20-1.00
Si	0.37	0.36	1.00 max	1.00 max
V	0.01	<0.01	0.25	-
Hf	<0.01	<0.01	0.25 max	-
Nb	<0.01	<0.01	0.25 max	-
Cu	<0.01	<0.01	0.20 max	-
C	0.051	0.056	0.05-0.07	0.05-0.15
P	0.008	0.008	0.015 max	0.04 max
S	0.003	0.002	0.015 max	0.03 max
O	0.008	0.017	0.015	-
B	0.0016	0.0012	0.001 max	-

5.2 Characterisation of as-built HX samples

5.2.1 Residual Porosity and microcracks investigation

The OM images of polished HX samples showed different microcracks and very fine isolated spherical pores for the x-y and z-y planes, derived from the LPBF process. The microcracks with a length up to 100 µm were randomly positioned along the x-y plane (Figure 99a), whereas they were mainly located along the building direction (z-y plane) as visible in Figure 99b.

On the other hand, there were a few spherical pores with a diameter from sub-micrometric size up to around 4 µm, as can be observed in Figure 99c and 99d. These spherical pores could be caused by the entrapped gas within the starting powder as observed previously in Figure 3b [53,90].

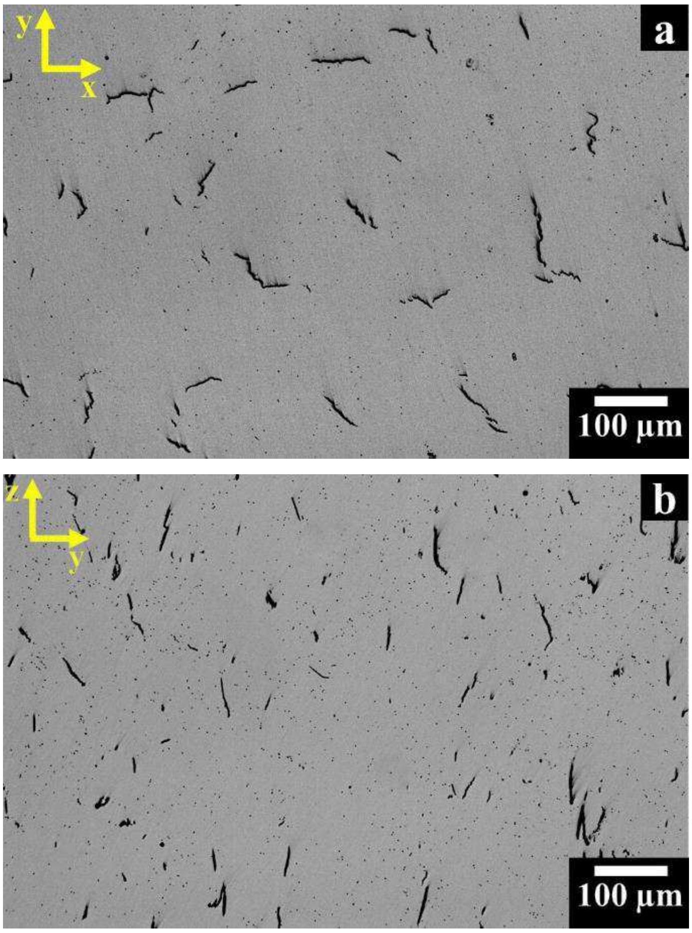

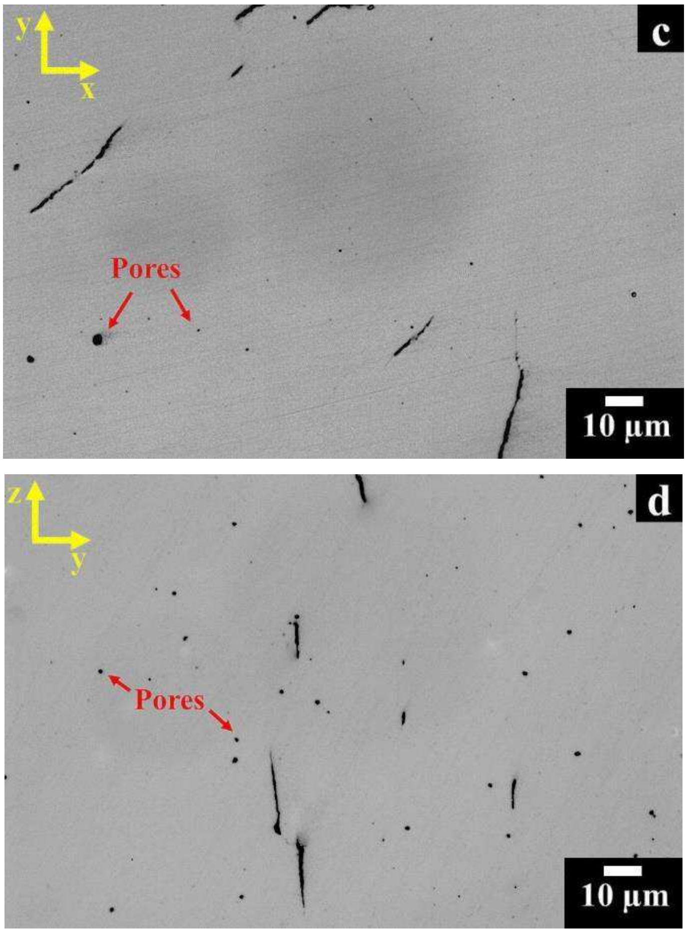

Figure 99: OM images of polished as-built HX samples exhibiting microcracks and pores at different magnification along y-x plane (a, c) and z-y plane (b, d).

The average value and standard deviation of residual porosity and cracking density of as-built HX samples determined by image analysis method are given in Table 42. The samples revealed a low level of residual porosity less than 0.5 % in both the planes (x-y and z-y). On the other hand, the average value of cracking density was slightly higher for the z-y plane than the x-y plane.

Table 42: Residual porosity and cracking density of as-built HX samples along the x-y and z-y planes.

x-y plane	Residual porosity (%)	0.28 ± 0.09
z-y plane	Residual porosity (%)	0.36 ± 0.13
x-y plane	Cracking density (mm/mm^2)	2.40 ± 0.41
z-y plane	Cracking density (mm/mm^2)	3.32 ± 0.52

5.2.2 Microstructural investigation of as-built HX samples

After etching with kalling's No.2 the OM images (Figure 100a and 100b) show the microstructure of as-built HX samples. The melt pools created by the laser beam revealed a different shape between the x-y and z-y planes as pointed out by the yellow dash line in Figure 100a and 100b, respectively. The melt pools are not alienated due to the EOS scanning strategy, in which the laser beam is rotated of 67 ° before melting the subsequent layer of loose powder in order to reduce the anisotropic of the materials [56]. Figure 100c shows randomly orientated grains along the x-y plane highlighted by the red dash line, whereas Figure 100d reveals columnar grains along the building direction for the z-y plane, as pointed out by the red dash line.

The columnar grains grow mainly along the <001> orientation due to epitaxially grown and heat flow dissipation along z-axis [55,66]. The microcracks mostly lie along the grain boundaries both along the x-y and along the z-y plane, as highlighted by yellow arrows in Figure 100e and 100f, respectively. The microcracks along the grain boundaries of LPBF-built HX alloys have been documented in other work [8,60].

These microcracks may be generated by the segregation of elements such as Si and C along the grain boundaries leading to a reduction of the grain boundary resistance. Furthermore, C and Si could also promote the formation of carbides along the grain boundaries, triggering the microcracks formation.

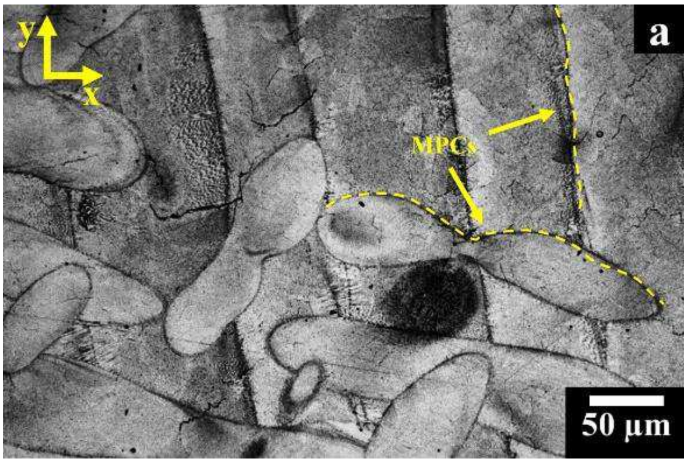

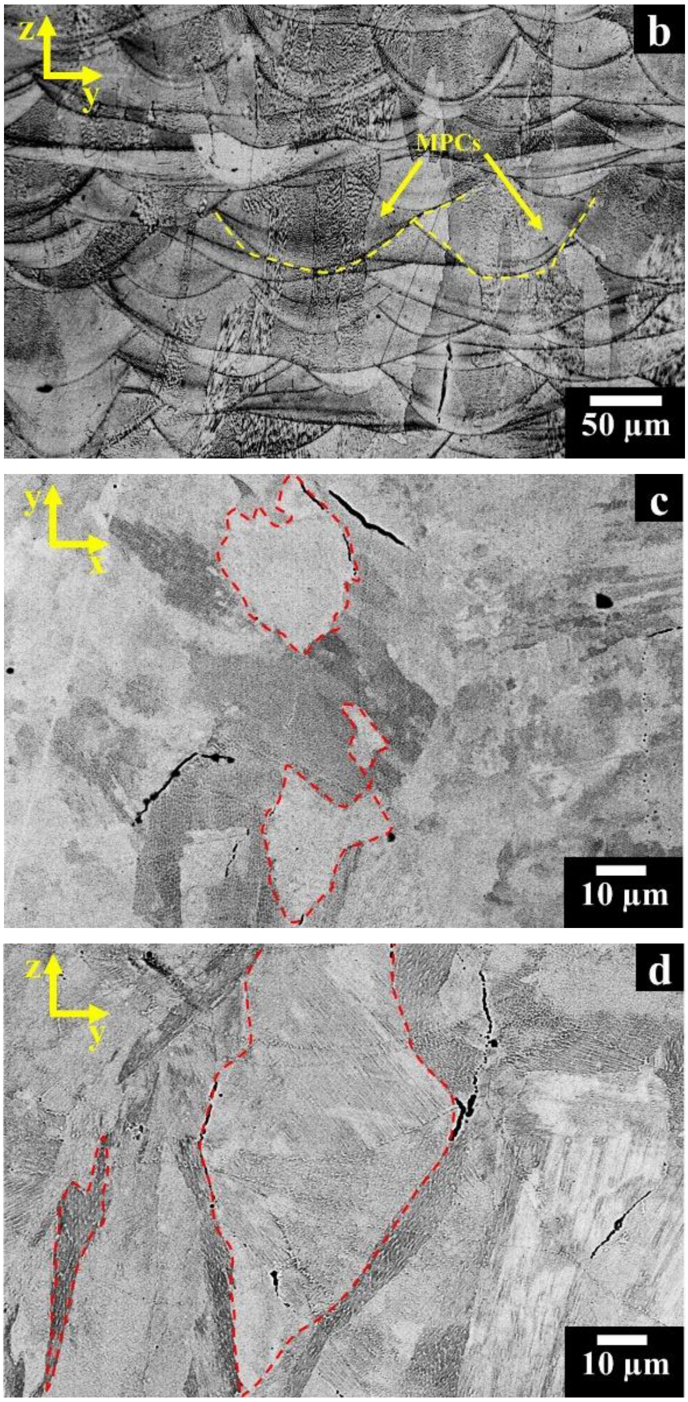
b
z
y
MPCs
50 µm
c
y
x
10 µm
d
z
y
10 µm

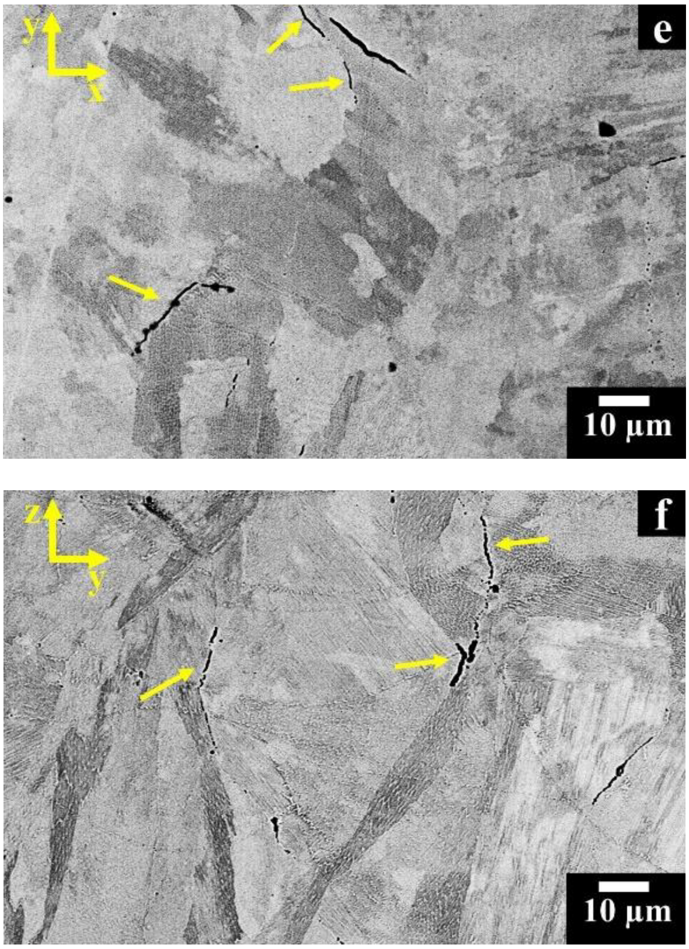

Figure 100: OM images of as-built HX samples showing: a) melt pool contours (MPCs) along the x-y plane, b) melt pools contours (MPCs) along the z-y plane; SEM images showing: c) randomly orientated grains pointed out by red dash line along the x-y plane; d) columnar grains indicated by red dash line along the z-y plane; e) microcracks mainly located along the grain boundaries indicated by yellow arrows along x-y plane; f) microcracks primarily located along the grain boundaries indicated by yellow arrows along the z-y plane; Kalling's No.2 etchant was used.

From the OM and SEM investigations can be concluded that the randomly orientated grains are the cross sectioned columnar grains along the x-y plane (perpendicular to the building direction) as graphically illustrated in Figure 101.

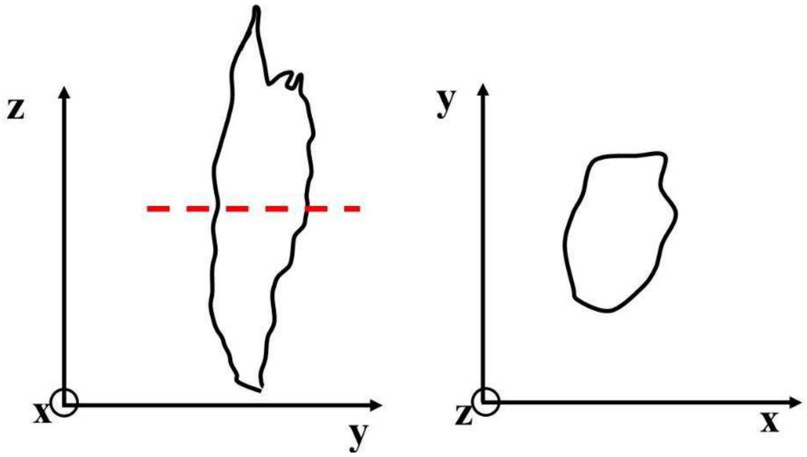

Figure 101: Graphically representation of the columnar grains along the z-y plane and the cross-sectioned columnar grain along the x-y plane.

The melt pools (Figure 102a) consist of fine dendritic architectures as can be seen in FESEM images (Figure 102b and 102c). It was not possible to detect entirely formed secondary dendrites, due to the extremely rapid cooling rates of the process. The primary dendritic cellular and columnar architectures showed sub-micrometric primary dendritic arm spacing (PDAS) of 0.60 ± 0.25 μm as shown in the magnified FESEM images in Figure 102c and 102d.

The very fine primary dendritic size was also detected by numerous investigation on LPBF-built Ni-based superalloys, including Hastelloy X alloy [55,66,140]. The dendritic structures throughout exhibited nanometric precipitates with size from 30 to 250 nm and elongated bright phases along the interdendritic regions with a length generally up to 500 nm may be segregated elements.

The smallest nanoprecipitates were generally located at the dendritic core whereas the largest ones were chiefly presented in the interdendritic regions. Due to the very fine dimensions of these precipitates, it was not possible to identify their nature through FESEM equipped with an EDS analysis and further investigation should be addressed.

However, Tomus et al.[61] found that as-built HX alloy presented similar nanometric precipitates, and TEM analysis identified these precipitates as Mo-rich carbides, suggesting that they were Mo-rich M_6C carbides.

These results are consistent with the numerous works on the study of the microstructure of HX alloys produced by conventional technologies as well as by

T-T-T diagram of HX alloy [6,20,43]. In fact, only carbides are formed during short thermal exposure, whereas other phases such as σ (sigma) and μ (mu) phases can be formed by prolonged thermal exposure [20,43].

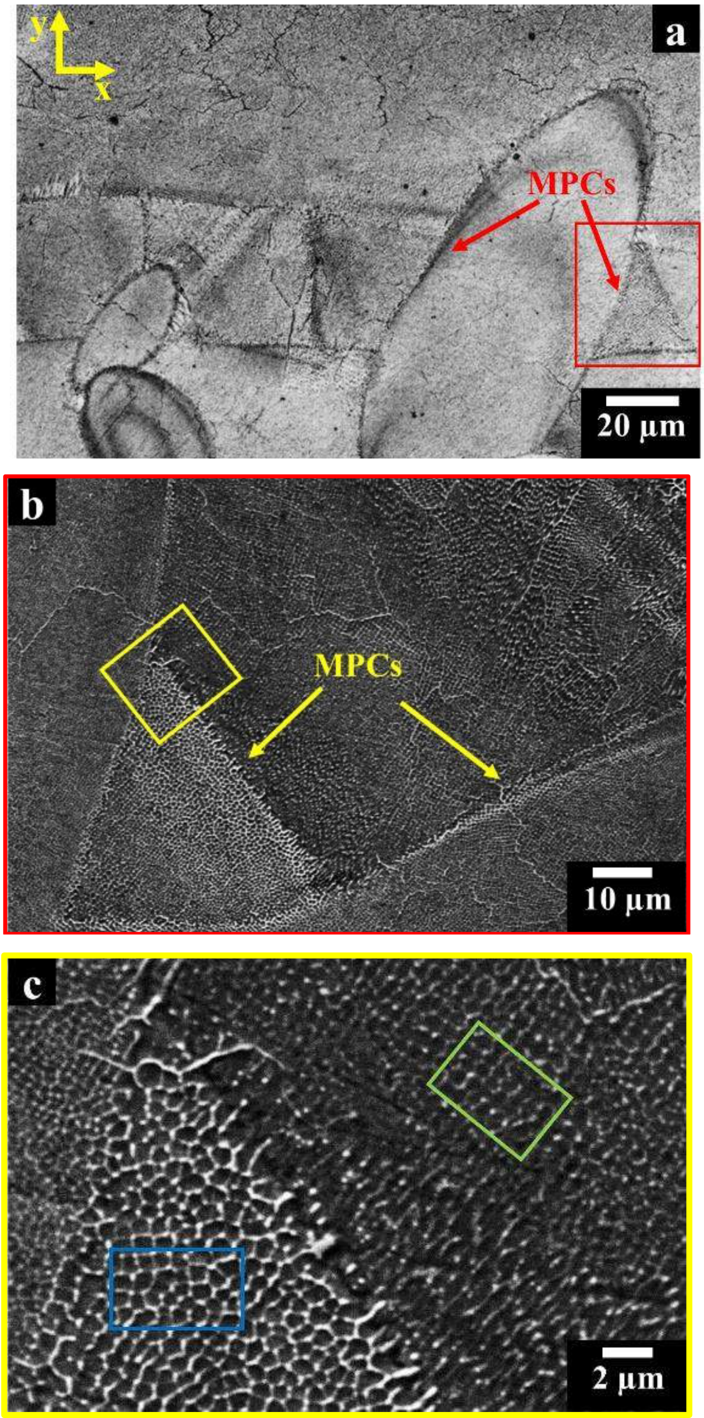
y
x
a
MPCs
20 µm
b
MPCs
10 µm
c
2 µm

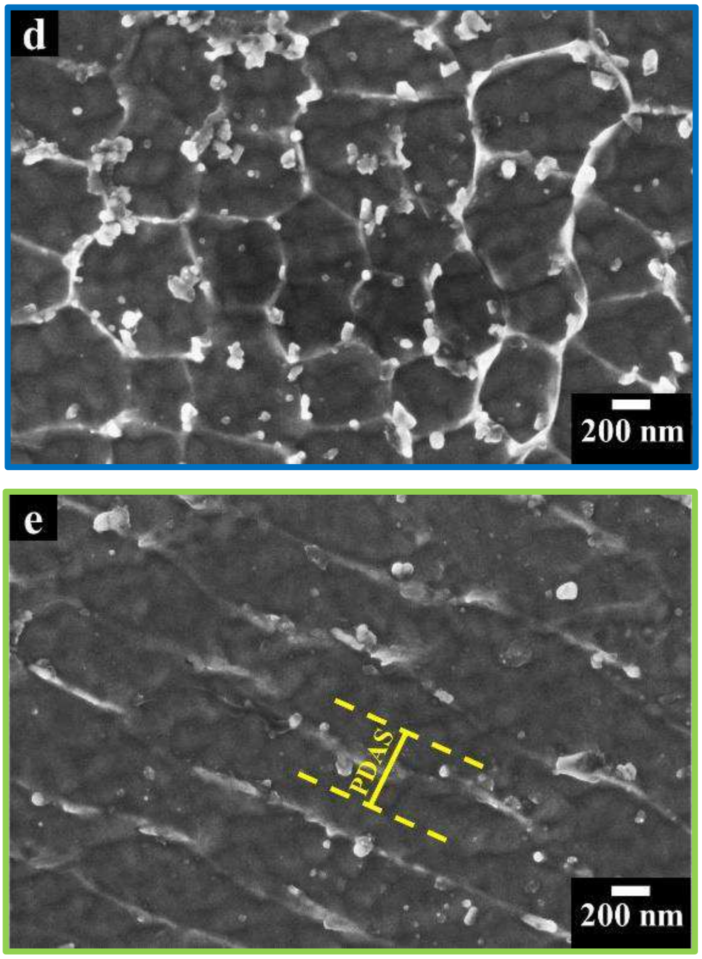

Figure 102: (a) OM image of as-built HX samples showing the melt pools created by the laser beam along the x-y plane; (b, c, d, e) FESEM images of as-built HX samples along the x-y plane at different magnifications showing: (b) melt pools contours (MPCs); (c) fine primary dendritic structure; (d) primary cellular dendritic structures with nanometric precipitates; (e) primary columnar dendritic structures with nanometric precipitates; Kalling's No.2 etchant was used.

The PDAS can be associated with the cooling rates (ε) as demonstrated in the literature, so the average values of PDAS (reported above 0.60 ± 0.25 µm) was used to estimate the cooling rates using the following equation (1): [55]

$$\text{PDAS} = a\ \varepsilon^{(-b)} \qquad (9)$$

Where *a* and *b* are constants of the material, and for nickel-based superalloys, $a \approx 50\mu m$ (K/s) and $b = 1/3$. In this way, it was estimated an average cooling rate of around 6 10^5 K/s, that is coherent with other studies on Ni-based superalloys produced by LPBF process [55,88,140]. The microstructural investigation showing extremely fine dendrite architectures explain why as-built HX samples had a very high hardness of 235 ± 5 HBW and 97 ± 0.4 HRB with respect to the standard values of 86-88 HRB for SHT HX despite a large presence of microcracks [41].

5.2.3 XRD analysis of as-built HX state

Figure 103 shows the XRD spectrum of as-built HX sample along the x-y plane exhibiting the presence of the γ-fcc phase, with a calculated lattice parameter of 3.607 ± 0.007 Å.

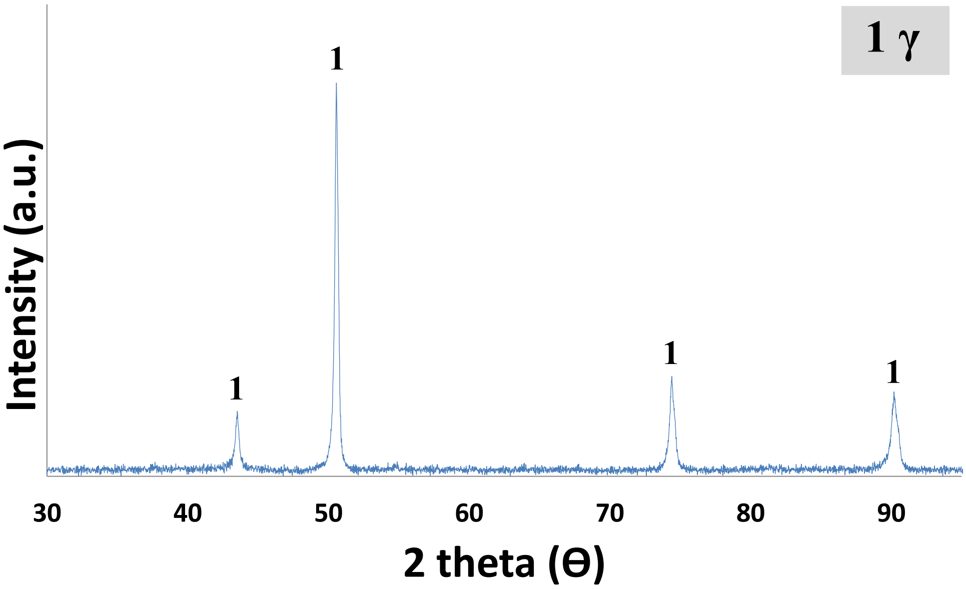

Figure 103: XRD spectrum of as-built HX sample along the x-y plane.

From the spectrum is possible to note a very pronounced γ (200) texture for as-built HX samples along the x-y plane that is congruent with other LPBF-built Ni-based superalloys such as Inconel 718 and Inconel 625 [55,64]. In fact, the process involved the growth of columnar grains with (100) orientation along the building direction (z-axis), resulting in a strong (200) texture along the x-y plane as reported in the literature [64].

For as-built HX state was not possible to reveal peaks of the Mo-rich M_6C carbides observed previously in FESEM images, probably because below the sensitivity threshold of the instrument. The table with the lattice parameters of γ austenitic phase calculated for the different peaks is available in Appendix A.

5.2.4 TMA of as-built HX state

Figure 104 reveals the CTE as function of the temperature for the as-built HX state. The CTE curve exhibited two deflections around 570 °C and 720 °C, which may be associated with the precipitation of carbides. The mean CTE of as-built HX samples was determined 14.7 10^{-6} $°C^{-1}$ (at 538 °C) and 15.8 10^{-6} $°C^{-1}$ (at 871 °C), whereas traditional sheets of HX have values of 15.1 10^{-6} $°C^{-1}$ (at 538 °C) and 16.2 10^{-6} $°C^{-1}$ (at 871 °C) [3].

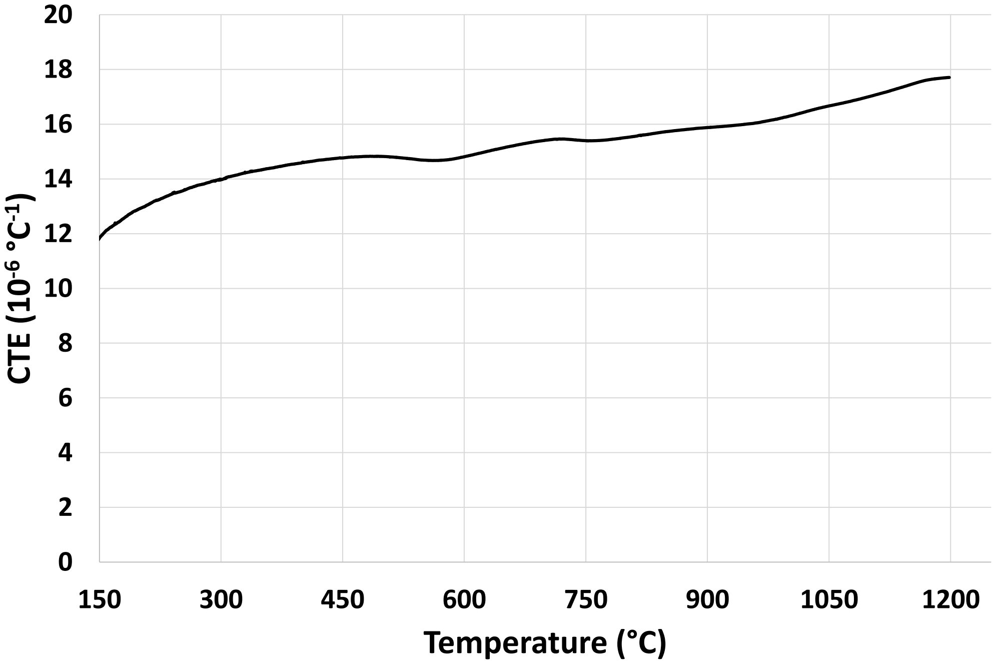

Figure 104: Coefficient of thermal expansion (CTE) vs temperature of as-built HX sample.

5.2.5 Solidification and microcracks formation discussion of as-built HX samples

As mentioned before, the as-built HX samples exhibited a significant number of nanometric Mo-rich M_6C carbides (30-250 nm), while the elongated bright phases along the interdendritic areas could be segregated elements.

The solidification of Ni-based superalloys can explain the formation of these fine carbides. During the solidification, the high susceptibility to segregation elements (i.e. Mo, W, C, Si) are rejected from dendrite to interdendritic region. This phenomenon leads to a higher concentration of these elements in the interdendritic regions promoting the carbides formation. Furthermore, the presence of fine carbides inside the dendrite core can derive from the solute trapping caused by the very high cooling rates of LPBF, in which a part of the high susceptibility to segregation elements (also included C and Mo) are captured inside the dendrite [55,140]. However, the above discussion does not take into account that the laser beam has enough power to melt more than one layer of powder and that the material is subjected to continuous heating flow dissipation from the top to the bottom of the component during its fabrication. These subsequent remelting and resolidification together with thermal dissipation can promote the formation of new carbides.

This hypothesis regarding the microstructure development triggered by subsequent thermal cycles is schematically proposed in Figure 105, and it is consisted with the literature about the rapid solidification on Ni-based superalloys by means of laser beam technologies.

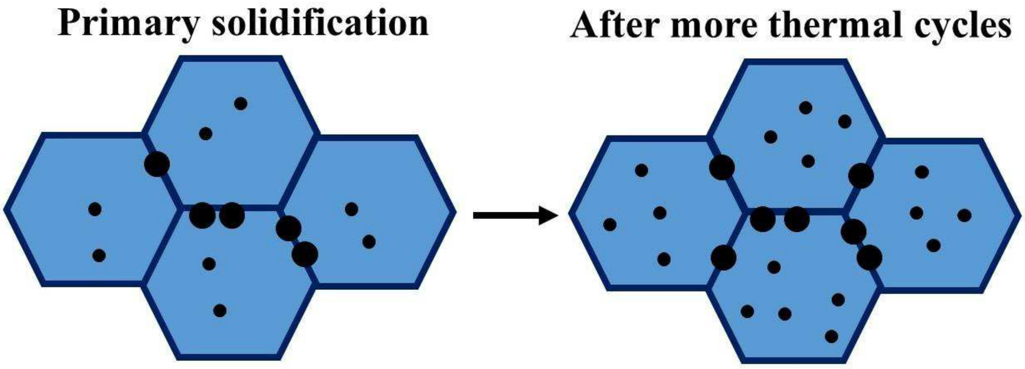

Figure 105: Schematic diagram of cellular dendritic structures of as-built HX samples. The black spherical circle represents the Mo-rich M_6C carbides whereas the blue and dark blue areas represent the dendritic and interdendritic regions, respectively. Primary solidification showed a low fraction of carbides, the largest ones in the interdendritic areas. After more thermal cycle consisted of continuous remelting and resolidification coupled with continuous thermal flows dissipation the microstructure made up of a higher number of carbides with respect to the initial solidification.

During the current investigation, it was shown that the as-built HX samples presented a large number of microcracks along the grain boundaries and a minor number of microcracks inside the grains. Both types of microcracks could be promoted by a significant number of carbides, formed along the grain boundaries or within the interdendritic areas [8].

According to the above discussion, a possible way to prevent the microcracks formation may be represented by the reduction of C and Si in the starting HX powder. Besides, the cracking density could also be reduced by increasing the concentration of solid solution elements together with the reduction of tramp elements [140]. In this way, it could be possible to develop an alloy with a higher ultimate tensile strength (UTS) with respect to the original alloy, reducing the possibility that the residual stresses surpass the UTS leading to a crack formation [140].

Finally, a process parameter optimisation can reduce the cracking density, although it was demonstrated that remain microcracks inside the material [59,140]. Besides, it should be taken into account that the variation of some parameters (e.g. scan speed) can reduce the build-up rate to an unacceptable level for the industrial processes.

5.3 Solutionizing treatments optimisation

5.3.1 SHT HX samples at 1175 °C for different times

Figure 106 reports the Brinell hardness of as-built and SHT HX samples at 1175 °C for different times.

The as-built HX samples revealed a hardness of 235 ± 5 HBW due to its very fine dendritic structures. After a solutioning performed at 1175 °C for 15 minutes the hardness decrease at 185 ± 6 HBW, essentially due to the grain growth resulting in equiaxed grains with an ASTM grain size number G mainly of 6.0-6.5 (grain diameter from 37.8 µm to 44.9).

After a solutioning at 1175 °C for 30 minutes, the hardness decreased further to 154 ± 4 HBW, exhibiting ASTM grain size number G mainly of 6.0-5.5 (grain diameter around 53.4-44.9 µm).

By contrast for prolonged solutioning performed at the same temperature for 1 hour and 2 hours, the Brinell hardness values were 148 ± 3 and 151 ± 2 HBW, respectively, showing very similar values to each other. Besides, for both the SHT HX states the ASTM grain size G was chiefly of 5.5.-4.5 (grain diameter around 53.4-75.5 µm).

The SHT HX samples for 1 and 2 hours revealed similar hardness and grain size, so the solutioning performed at 1175 °C for 1 hour was chosen as optimised condition to reduce the post-processing time, as stated in a previously published work [139]. For this optimised SHT condition it was also determined an 80.0 ± 0.5 HRB.

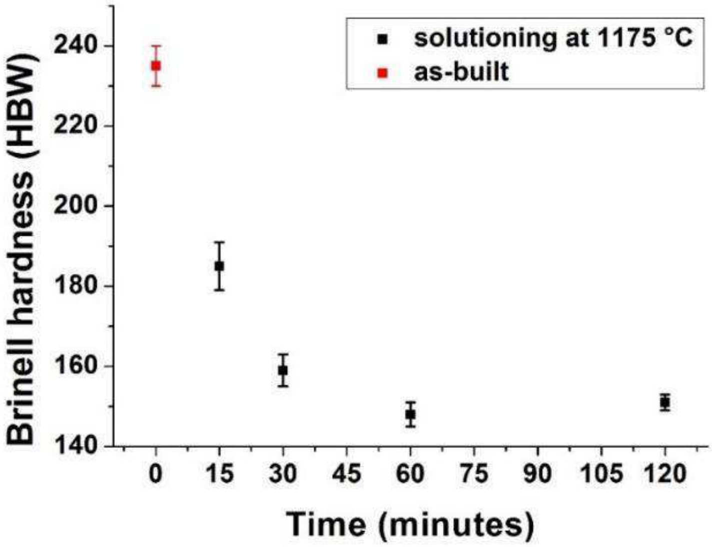

Figure 106: Brinell hardness of as-built HX samples and SHT HX samples at 1175 °C for 15, 30 ,60 and 120 minutes. *All the SHT samples were water quenched.

The solution treatments dissolved the dendritic structures, relief the residual stresses as well as led to the formation of small and large equiaxed grains. The mainly determined ASTM grain size number G and corresponding grain diameters for each SHT state are reported in Table 43.

Table 43: The ASTM grain size number G and corresponding grain size of SHT HX samples.

Heat treatment*	ASTM Grain size No (G)	grain diameters (µm)
1175 °C 15 min	6.0 - 6.5	37.8- 44.9
1175 °C 30 min	6.0-5.5	44.9- 53.4
1175 °C 60 min	5.5 - 4.5	53.4- 75.5
1175 °C 120 min	5.5- 4.5	53.4 – 75.5

**All the samples were water quenched*

The OM images of SHT HX samples heat-treated at 1175 °C for different times showing the effect of the recrystallization are displayed in Figure 107.

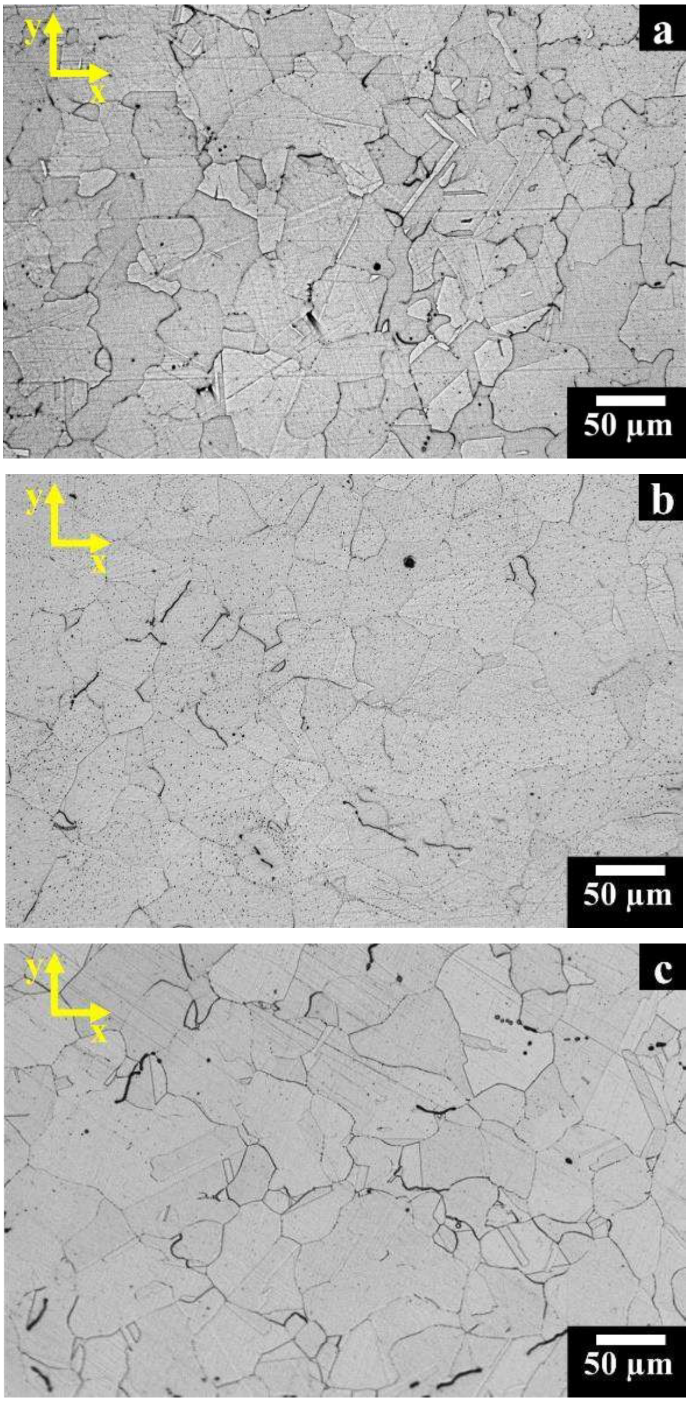
y
x
a
50 µm
y
x
b
50 µm
y
x
c
50 µm

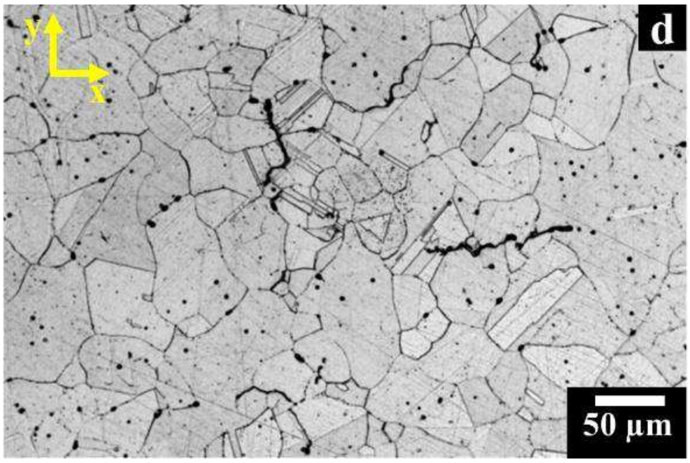

Figure 107: OM images of SHT HX samples at 1175 °C for different times: (a) 1175 °C for 15 min; (b) 1175 °C for 30 min; (c) 1175 °C for 60 min; (d) 1175 °C for 120 min; Kalling's No.2 etchant was used.

5.3.2 Microstructure investigation on optimised SHT condition

The microstructure of SHT HX samples at 1175 °C for 1 hour exhibited the same level of porosity and cracking density of as-built condition. The microcracks were randomly orientated along x-y planes (Figure 108a) and they were orientated along the building direction (z-axis) for the z-y planes, as can be observed in Figure 108b.

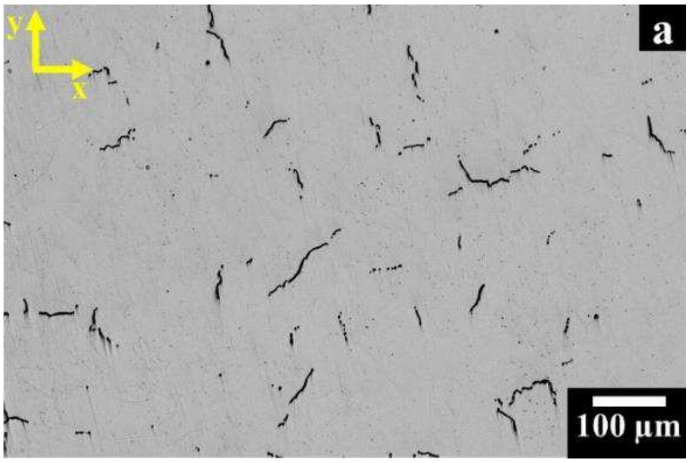

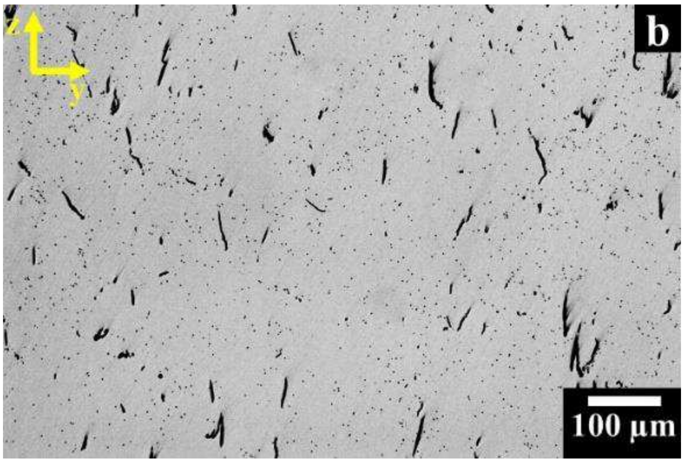

Figure 108: OM images of SHT HX samples at different magnification showing the microcracks orientation along x-y plane (a) and along the z-y plane (b).

The measument of the residual porosity and craking density revealed similar values to as-built condition as reported in Table 44, demonstrating that the solutioning did not have a significant effect on pores and microcracks.

Table 44: Residual porosity and cracking density of optimised SHT HX samples along x-y and z-y planes.

x-y plane	Residual porosity (%)	0.25 ± 0.06
z-y plane	Residual porosity (%)	0.31 ± 0.05
x-y plane	Cracking density (mm/mm^2)	2.60 ± 0.60
z-y plane	Cracking density (mm/mm^2)	3.32 ± 0.58

The solution treatments involved the recrystallization triggered by high temperature and by high residual stresses led to the formation of equiaxed grains for both the planes (x-y and z-y) with the microcracks mainly located along the grain boundaries, as can be seen in Figure 109a and 109b. In this way, it was developed a more homogenous microstructure with more isotropic properties. At higher magnification view (Figure 109c and 109d), the OM images revealed the presence of very fine inter/intragranular precipitates with a fraction of 0.35 ± 0.10 %.

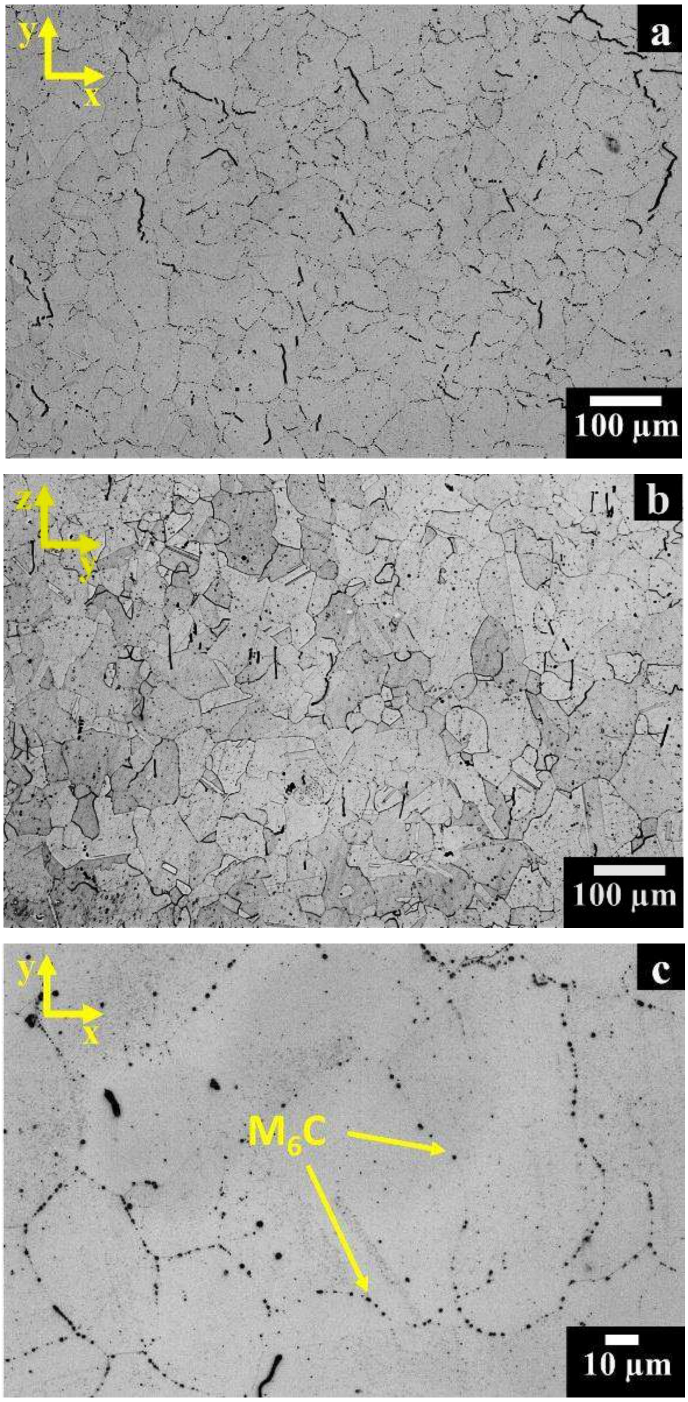
y
x
a
100 µm
z
y
b
100 µm
y
x
c
M6C
10 µm

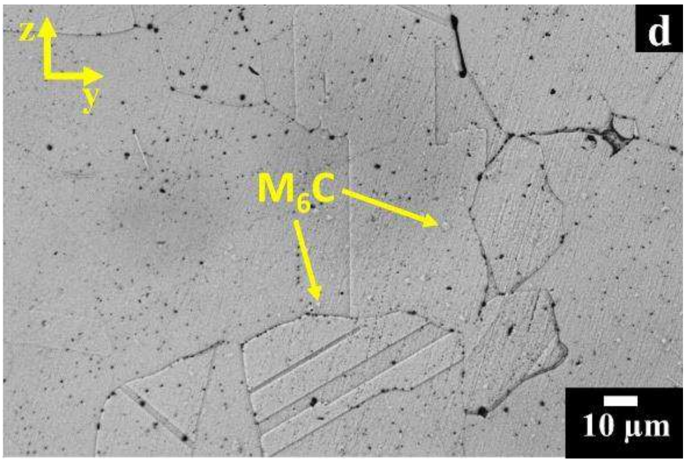

Figure 109: OM images of optimised SHT HX samples at 1175 °C for 1 hour showing: (a, b) equiaxed grains along x-y and z-y planes, respectively; (c, d) equiaxed grains and fine precipitates along x-y and z-y planes, respectively. Kalling's No.2 etchant was used.

The FESEM images (Figure 110a and 110b) of SHT HX samples exhibited very fine inter/intragranular carbides, with size from sub-micrometric up to around 1-1.5 µm. These carbides were enriched in Mo as highlighted by EDS results in Table 45, suggesting that they were Mo-rich M_6C carbides. The results are coherent with the literature, since a temperature of 1175 °C for a short time can only promote the formation of Mo-rich M_6C carbides[6,20].

It was interesting to note that these micrometric Mo-rich M_6C Carbides (1.0-1.5 µm) were not detected during the previous FESEM investigation on as-built HX samples, so that they may be originated during the heat treatment due to the formation of secondary carbides otherwise due to the grown of previously formed carbides.

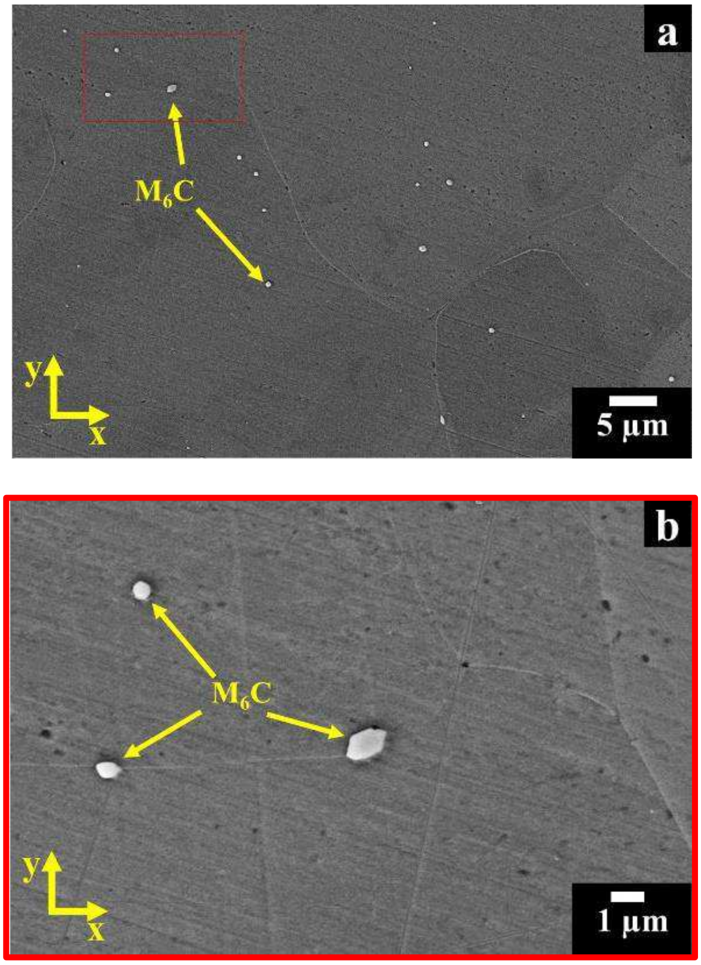

Figure 110: FESEM images of optimised SHT HX samples along x-y plane showing: (a) the grain boundaries of equiaxed grains and M_6C carbides; (b) showing fine inter/intragranular M_6C carbides; Kalling's No.2 etchant was used.

Table 45: EDS results of the γ austenitic matrix and Mo-rich M_6C carbide for optimised SHT HX sample.

Element	γ austenitic matrix		Mo-rich M_6C carbide	
	wt (%)	at (%)	wt (%)	at (%)
Ni	43.2	44.8	29.8	33.4
Cr	19.6	23.1	18.8	23.8
Fe	17.6	19.2	12.8	15.1
Mo	11.4	7.2	31.1	21.4
Co	1.9	2.0	1.8	2.0
W	5.4	1.8	4.6	1.6
Si	0.9	1.9	1.1	2.7
Total	100.0	100.0	100	100

However, the high number of large microcracks drastically reduce the mechanical properties and fatigue life of these components, so other process should be performed in order to eliminate or reduce the number of microcracks.

5.3.3 XRD analysis of optimised SHT HX state

Figure 111 reveals the XRD spectrum of the optimised SHT HX (at 1175 °C for 1 hour) exhibited the only presence of the γ phase with a calculated γ phase lattice parameter of 3.599 ± 0.004 Å. The table with the lattice parameters of γ austenitic phase calculated for the different peaks is available in Appendix A.

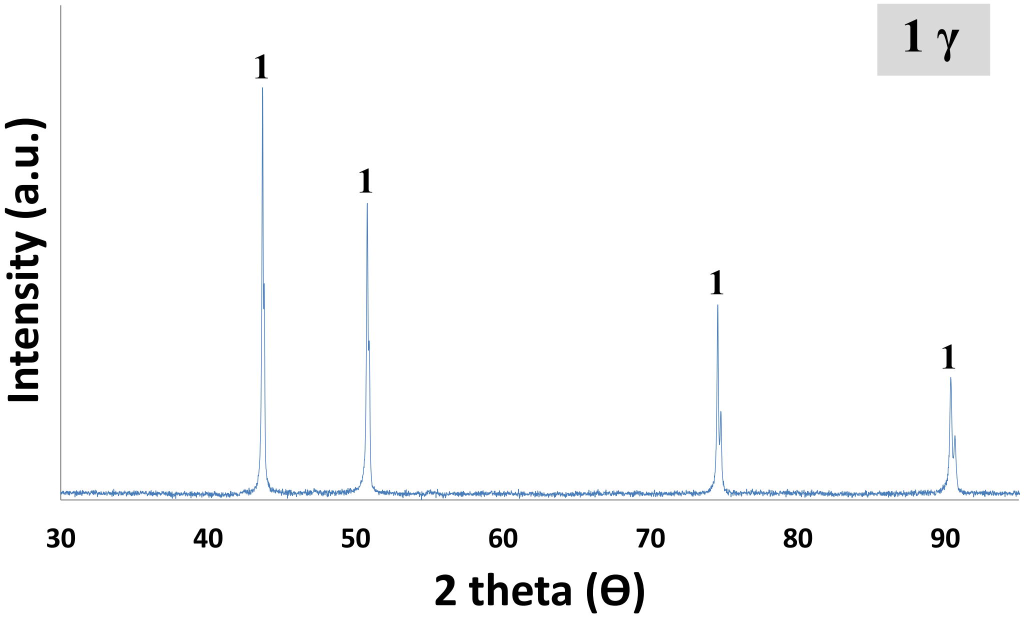

Figure 111: XRD spectrum of optimised SHT HX samples showing the peaks of γ austenitic phase.

5.3.4 TMA of optimised SHT HX state

Figure 112 displays the CTE as function of the temperature for the SHT HX state. The graph exhibited two deflections around 600 °C and 780 °C that may be correlated to the precipitation of carbides.

The CTE differences between the as-built and SHT HX samples can be associated with different microstructural features and the C available inside the matrix to form carbides. The mean CTE of SHT HX samples was determined 15.0 10^{-6} °C^{-1} (at 538 °C) and 16.4 10^{-6} °C^{-1} (at 871 °C), whereas traditional sheets of HX have a value of 15.1 10^{-6} °C^{-1} (at 538 °C) and 16.2 10^{-6} °C^{-1} (at 871 °C) [3]. The value of LPBF-SHT HX alloy is very similar to traditional SHT HX alloy, probably due to a similar grain size and microstructure.

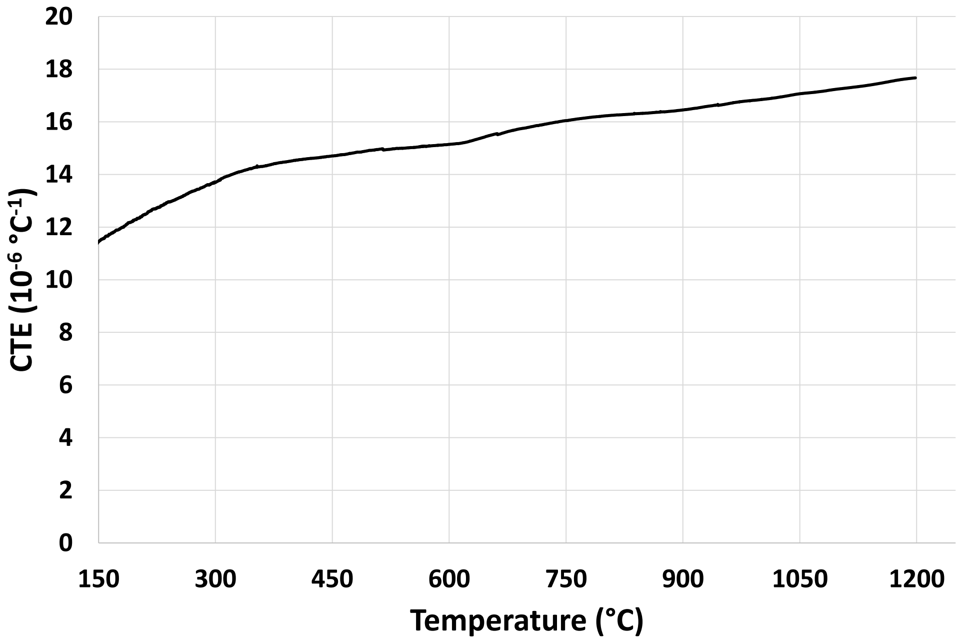

Figure 112: Coefficient of thermal expansion (CTE) vs temperature of SHT HX sample.

5.3.5 SHT HX samples at 1066 °C for 1 hour

It was also performed a preliminary study performing a solution treatment at 1066 °C for 1 hour, which promoted a recrystallization with small grains without eliminating the presence of the melt pools contours (Figure 113a and 113b).

It was not possible to attribute a precise ASTM grain size number G caused by the difficulty to identify all the grain boundaries (in contrast to the HX samples heat-treated at 1175 °C) and by the presence of melt pool contours that could be exchanged as grain boundaries. However, using the apparent grain size could be estimated a grain size mainly between 10 and 50 μm along x-y plane.

The fine inter/intracarbides formed during the heat treatment were enriched in Mo and W with respect to the γ matrix (see EDS in Table 46), suggesting the formation of Mo-rich M_6C carbides. The largest carbides (around 3 μm) were mainly located along the grain boundaries or the microcracks (Figure 113c and 113d).

The hardness was 210 ± 5 HBW slightly inferior to the as-built condition 235 ± 5 HBW due to the dissolution of the dendritic architectures and an initial recrystallization. However, a similar microstructure with small grains and large precipitates is not desirable to work at high temperature, so this heat treatment was not considered for subsequent investigation.

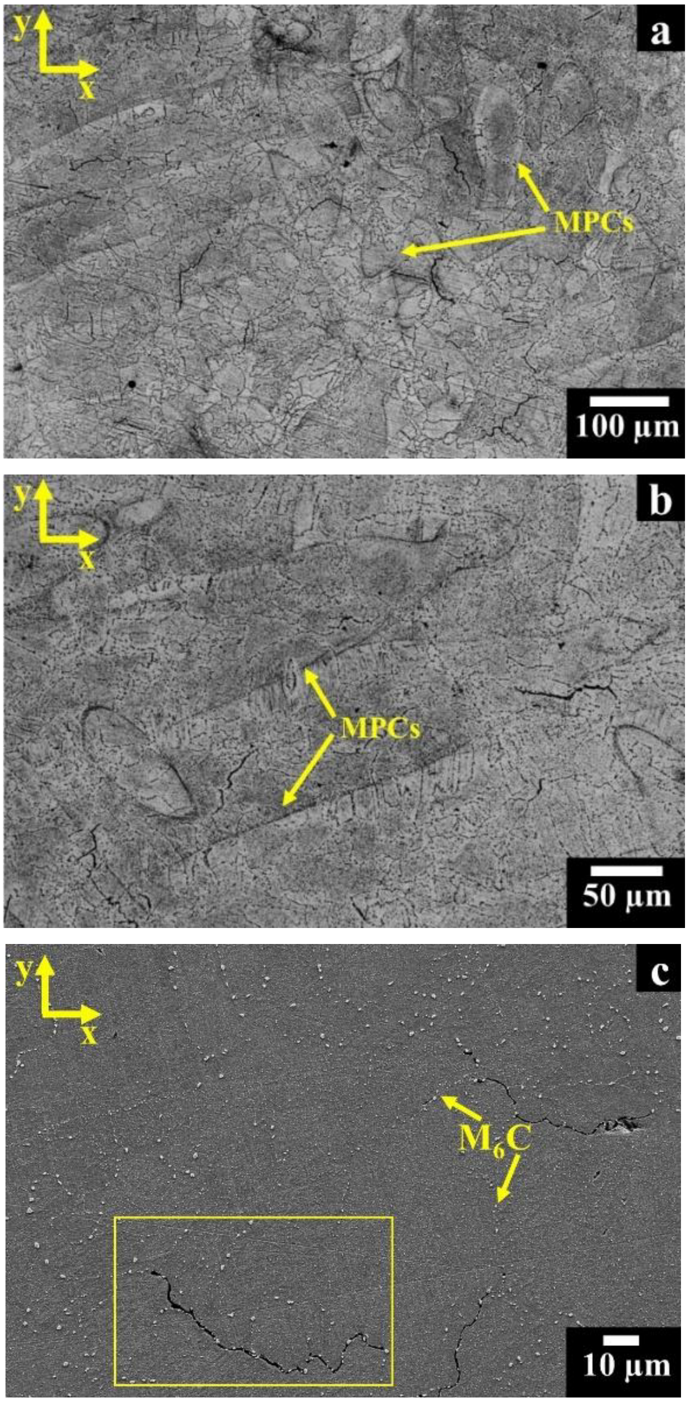
y
x
a
MPCs
100 µm
y
x
b
MPCs
50 µm
y
x
c
M6C
10 µm

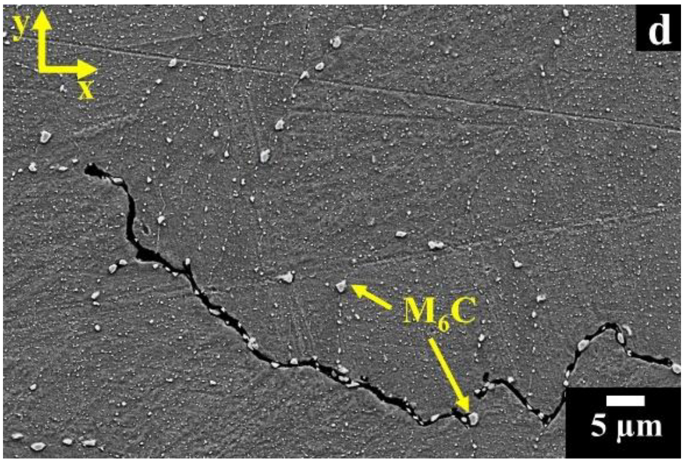

Figure 113: OM images of SHT HX samples at 1066 °C for 1 hour along x-y plane showing (a, b) melt pool countours (MPCs) and a starting recrystallization; FESEM images showing (c, d) Mo-rich M_6C carbides mainly located along the grain boundaries and cracks. Kalling's No.2 etchant was used.

Table 46: EDS results of the γ austenitic matrix and Mo-rich M_6C carbides for SHT HX samples at 1066 °C for 1 hour.

Element	γ austenitic matrix		Mo-rich M_6C carbide	
	wt (%)	at (%)	wt (%)	at (%)
Ni	42.2	44.1	31.4	35.9
Cr	20.0	23.5	16.4	21.3
Fe	17.5	19.2	13.6	16.4
Mo	11.8	7.5	24.1	16.9
Co	1.7	1.8	1.3	1.5
W	5.9	2.0	11.6	4.2
Si	0.9	1.9	1.6	3.8
Total	100.0	100.0	100.0	100.0

5.4 Microstructural evolution of SHT HX samples under thermal exposures

5.4.1 Hardness investigation of SHT HX heat-treated at 745 °C and 788 °C for different times

The Brinell hardness of optimised SHT HX samples under specific thermal exposure is reported in Figure 114. The heat-treated samples at 745 °C and 788 °C for 3 hours improved the hardness up to 177 ± 6 HBW and 171 ± 2 HBW, respectively with respect to the 148 ± 3 HBW of SHT condition. Besides for the heat-treated HX samples at 745 °C and 788 °C for 6 hours were obtained a hardness value of 185 ± 6 HBW and 182 ± 2 HBW, respectively. For prolonged thermal exposure at 745 °C and 788 °C for 200 hours, the hardness increased at 237 ± 3 HBW and at 233 ± 4 HBW, respectively.

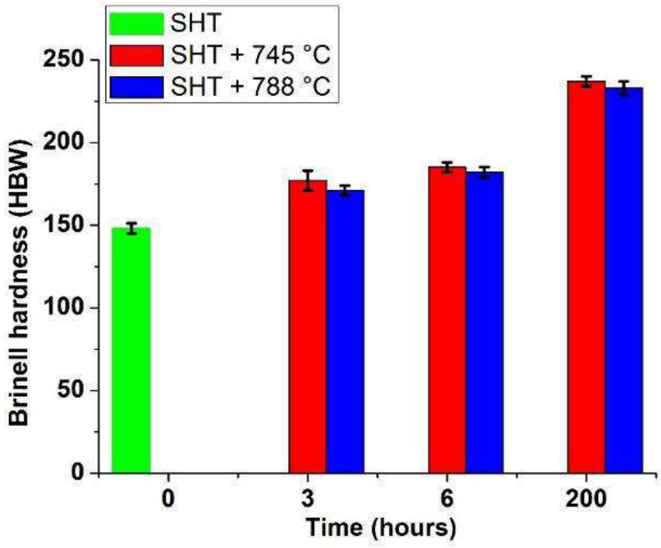

Figure 114: Brinell hardness of SHT samples and heat-treated HX samples for different times at 745 °C (SHT + 745 °C represented with red colour) and 788 °C (SHT + 788 °C associated with blue colour).

5.4.2 Microstructural investigation of SHT HX heat-treated at 745 °C for different times

A thermal exposure at 745 °C up to 200 hours did not alter the grain size with respect to SHT condition, showing an extensive phases precipitation involving a hardness increment. The heat-treated SHT HX samples at 745 °C for 3 hours exhibited the formation of intergranular Cr-rich $M_{23}C_6$ carbides at the grains boundaries as can be seen in Figure 115a.

The FESEM images (Figure 115b and 115c) show the Cr-rich $M_{23}C_6$ carbides predominantly formed along the grains boundaries creating a continuous film of carbides of 200-400 nm.

The Mo-rich M_6C carbides formed during the LPBF process or during the solutioning treatments were also presented, since the temperature was not high enough to dissolve Mo-rich M_6C carbides, although they were not detected during this investigation.

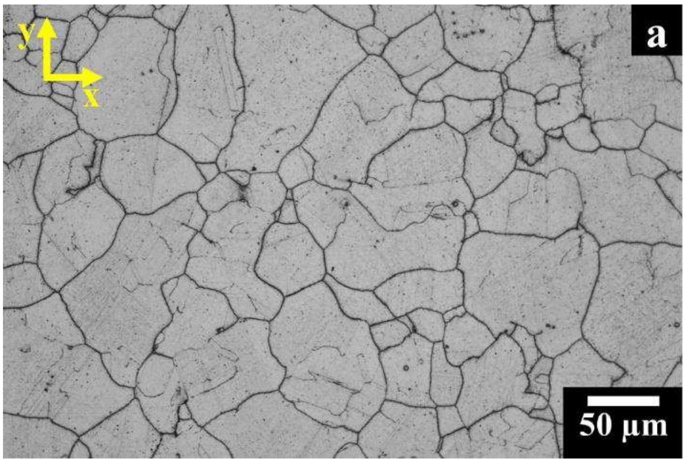

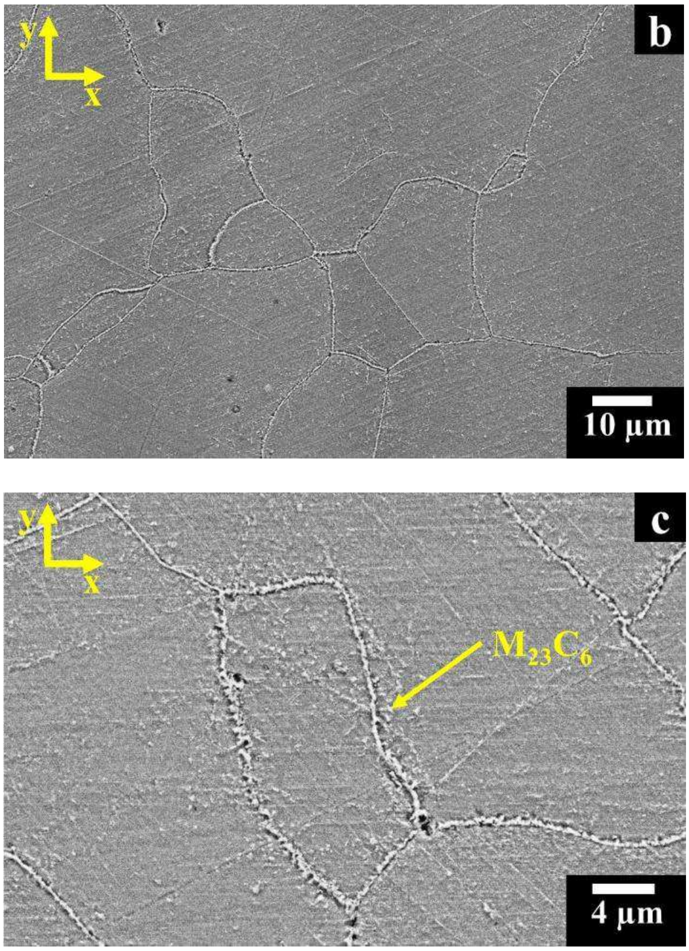

Figure 115: Microstructure of SHT +745 °C 3 h HX sample showing:(a) OM image of equiaxed grains with $M_{23}C_6$ carbides at grain boundaries; (b, c) FESEM images exhibiting $M_{23}C_6$ carbides along the grain boundaries.

The heat-treated SHT HX samples at 745 °C for 6 hours revealed a similar microstructure to the previous one as can be seen in Figure 116a, 116b and 116c. The micrographs exhibited continous films of Cr-rich $M_{23}C_6$ carbides along the grain boundaries with a thickness around 200-400 nm (the same of the previous condition).

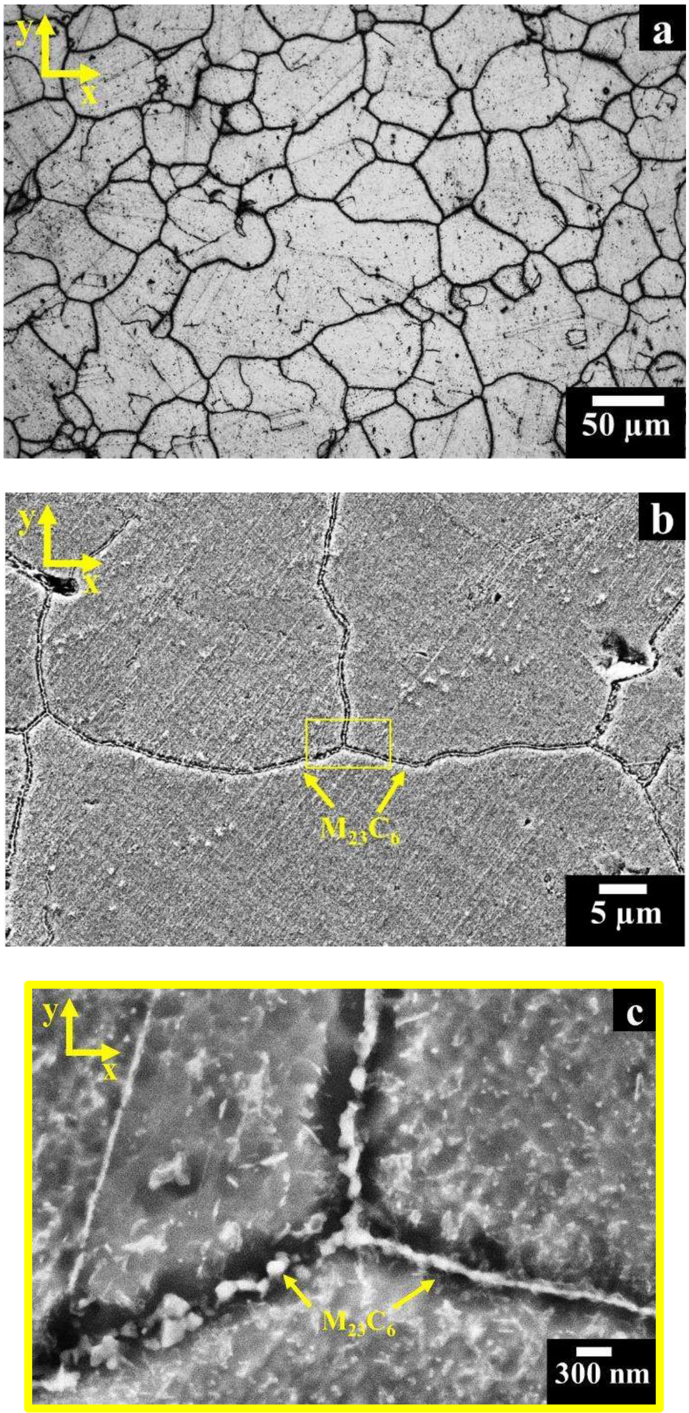
y
x
a
50 µm
y
x
b
$M_{23}C_6$
5 µm
y
x
c
$M_{23}C_6$
300 nm

Figure 116: Microstructure of SHT +745 °C 6 h HX sample showing:(a) OM image of equiaxed grains with $M_{23}C_6$ carbides at grain boundaries; (b, c) FESEM images exhibiting $M_{23}C_6$ carbides along the grain boundaries.

After a prolonged thermal exposure at 745 °C for 200 hours, the microstructure revealed a significant presence of precipitates inside the grains and along the grain boundaries as illustrated in Figure 117a.

The morphology of these precipitates can be observed in FESEM images (Figure 117b), showing micrometric size 1-2 µm and elongated particles up to 5 µm. The shape and morphology of these precipitates can be attributed both σ and µ phases that are both rich in Mo and Cr with a low level of Ni and Fe as revealed by EDS results reported in Table 47.

According to the T-T-T diagram and the literature on HX alloys, a similar thermal exposure could mainly promote the σ phase formation [6,20].

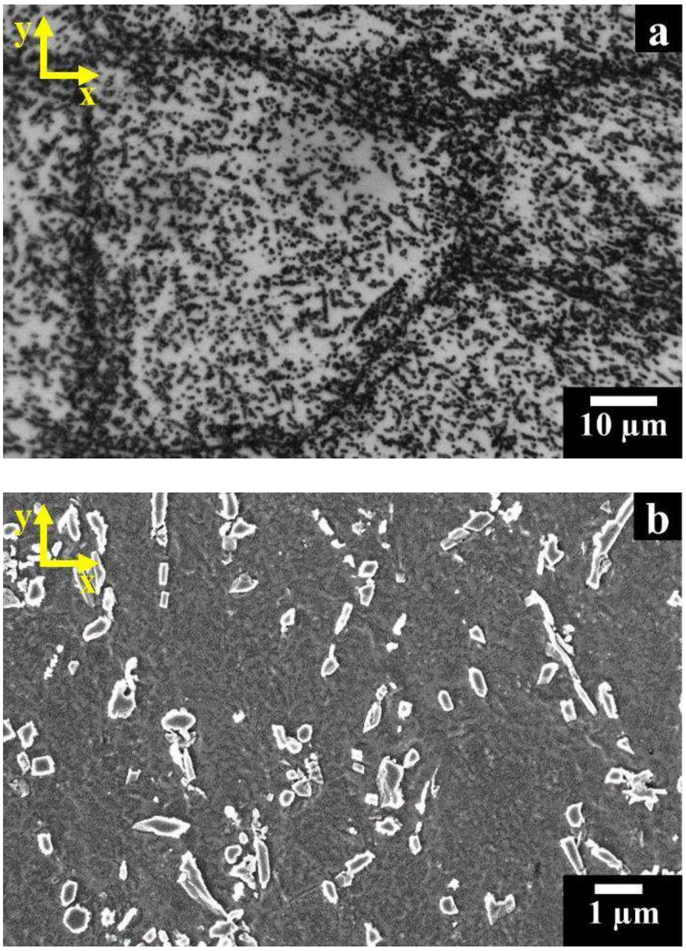

Figure 117: (a) OM image of SHT + 745 °C 200 h HX sample showing equiaxed grains with a significant fraction of precipitates; (b) FESEM image of SHT + 745 °C 200 h HX sample showing the precipitates morphology.

Table 47: EDS values of γ austenitic matrix and precipitates of prolonged heat-treated HX samples at 745 °C for 200 h.

	γ austenitic matrix		Precipitates	
Element	wt (%)	at (%)	wt (%)	at (%)
Ni	47.3	47.1	27.9	30.2
Cr	22.3	25.1	22.9	28.0
Fe	19.3	20.2	13.6	15.5
Mo	7.8	4.8	29.5	19.5
Co	2.2	2.1	1.5	1.6
W	0.9	0.3	2.6	0.9
Si	0.2	0.4	1.8	4.1
Total	100.0	100.0	100.0	100.0

5.4.3 XRD analysis of heat-treated SHT at 745 °C for different times

Figure 118 compares the XRD spectra of SHT HX sample heat-treated at 745 °C for 3, 6 and 200 hours, along the x-y plane.

The three samples revealed only the presence of γ austenitic phase with a lattice parameter of 3.600 ± 0.001 Å for SHT + 745 °C 3 h, 3.603 ± 0.002 Å for SHT + 745 °C 6 h and 3.586 ± 0.003 Å for SHT + 745 °C 200 h.

The prolonged heat-treated HX samples exhibited a lower lattice parameter than other conditions that can be attributed to a solution elements depletion due to a large formation of precipitates. For the short thermal exposures at 745 °C, the carbides could not be detected because below the sensitivity threshold of the instrument or due to the peaks overlap with the γ matrix. The table with the lattice parameters of γ austenitic phase calculated for the different peaks is available in Appendix A.

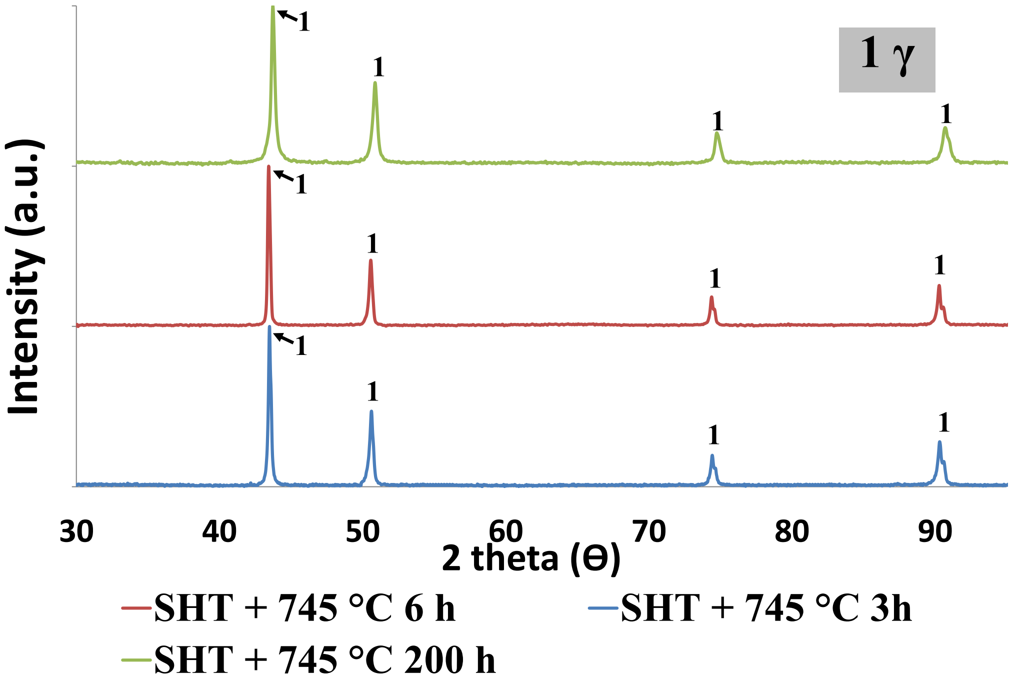

Figure 118 : XRD spectra of SHT HX samples heat-treated at 745 °C for 3,6 and 200 hours showing the peaks of γ austenitic phase.

5.4.4 Microstructural investigation of SHT HX heat-treated at 788 °C for different times

The heat treatment performed at 788 °C up to 200 hours did not alter the grain size with respect to the SHT HX state.

The heat-treated SHT HX samples at 788 °C for 3 hours exhibited a very similar microstructure to SHT HX samples heat-treated at 745 °C for 3 hours, showing the formation of intergranular Cr-rich $M_{23}C_6$ carbides at the grain boundaries, as can be seen in Figure 119a.

The FESEM images (119b, and 119c) revealed larger continuous film of Cr-rich $M_{23}C_6$ carbides with a thickness around 600-800 nm with respect to 200-400 nm of SHT heat-treated samples at 745°C for the same time. However, it should be noted that the temperature was not high enough to dissolve inter/intragranuler M_6C carbides detected in the SHT state.

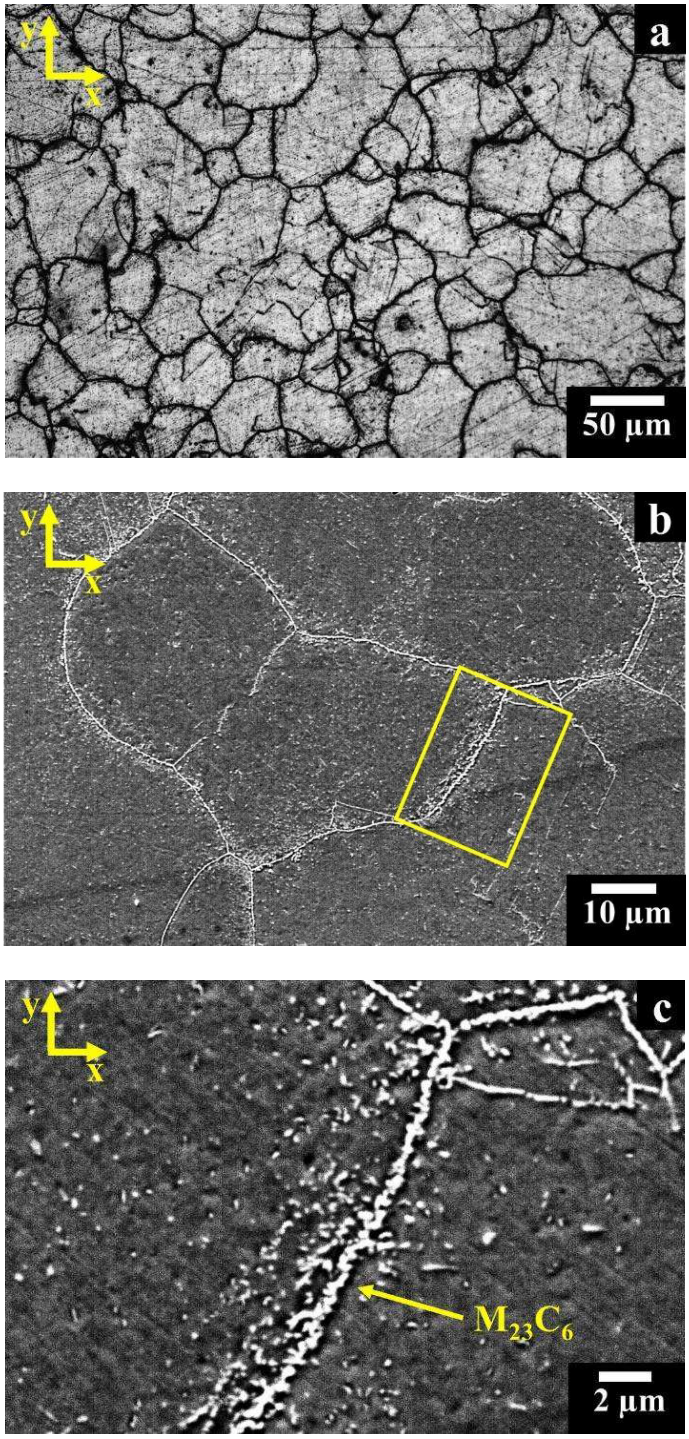

Figure 119: Microstructure of SHT +788 °C 3 h HX samples showing:(a) OM image of equiaxed grains with $M_{23}C_6$ carbides at grain boundaries; (b, c) FESEM images exhibiting $M_{23}C_6$ carbides along the grain boundaries.

From the images in Figure 120a, 120b and 120c the heat-treated SHT HX samples at 788 °C for 6 hours exhibited a similar microstructure to the previous one, showing the precipitation of countinous film of Cr-rich $M_{23}C_6$ carbides mainly located along the grain boundaries with a thickness around 600-800 nm (the same of the previous condition).

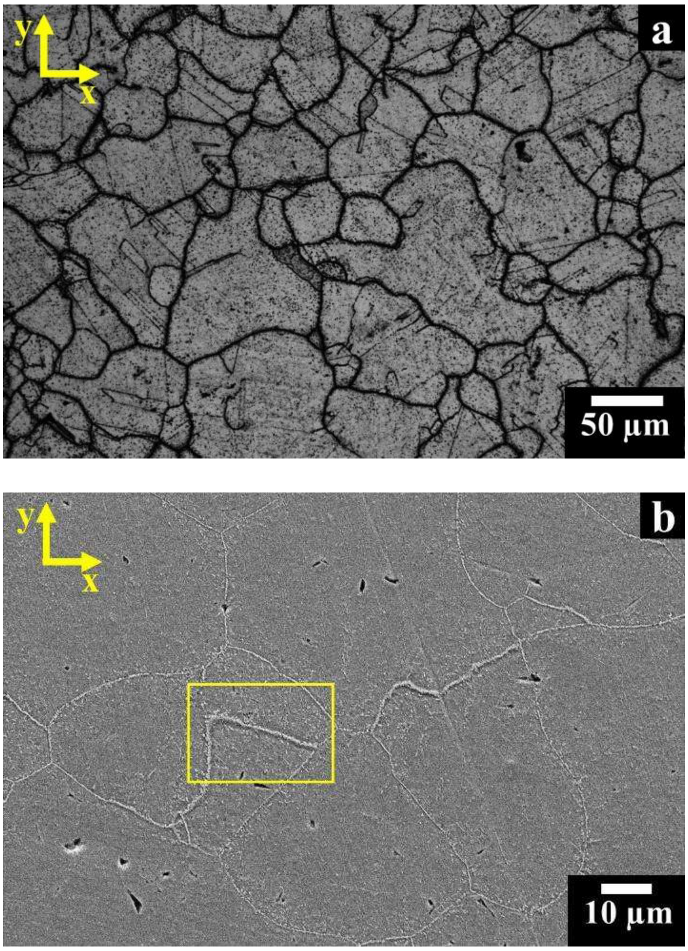

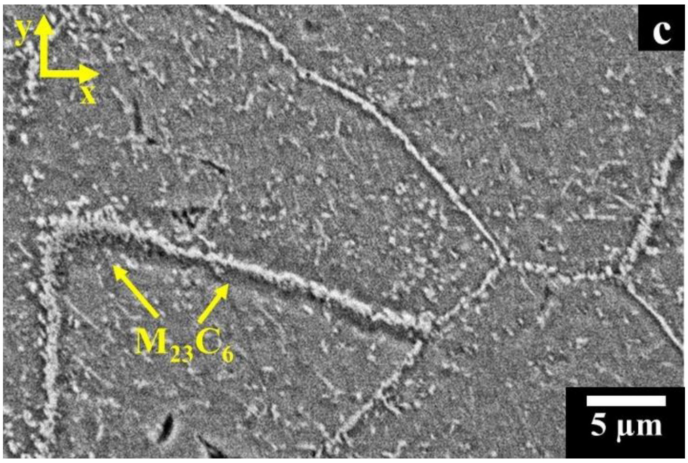

Figure 120: Microstructure of SHT +788 °C 6 h HX samples showing:(a) OM image of equiaxed grains with $M_{23}C_6$ carbides at grain boundaries; (b,c) FESEM images exhibiting $M_{23}C_6$ carbides along the grain boundaries.

The microstructure of SHT HX samples heat-treated at 788 °C for 200 hours were similar to SHT HX sample heat-treated at 745 °C for 200 hours, revealing a large presence of inter/intragranular precipitates as shown in Figure 121a. The morphology of these precipitates can be observed in FESEM image (Figure 121b), showing micrometric size 1-2 µm and elongated particles up to 5 µm (the same size of SHT + 745 °C 200 h HX samples).

Also in this case, the shape and morphology of these precipitates can be attributed both σ and µ phases that are both rich in Mo and Cr with a low level of Ni and Fe as revealed by EDS results (Table 48), suggesting the formation of σ phase [6,20].

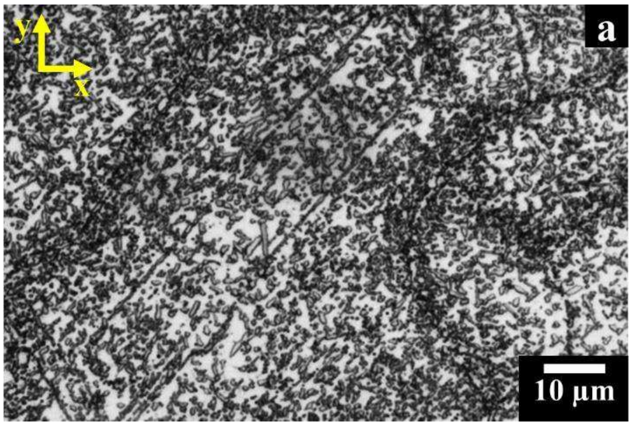

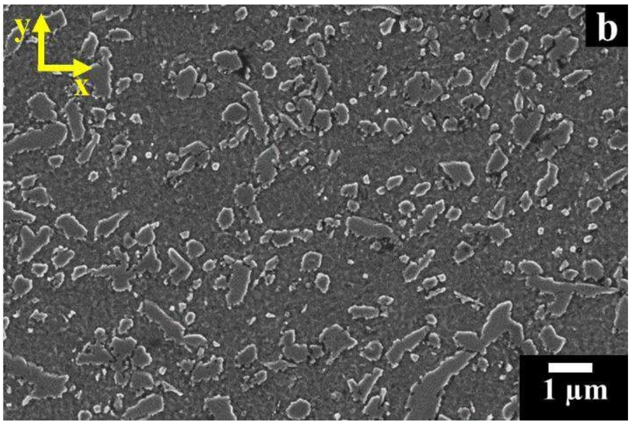

Figure 121: (a) OM image of SHT + 788 °C 200 h HX samples showing equiaxed grains with a significant fraction of precipitates; (b) FESEM image of SHT + 788 °C 200 h HX sample showing the precipitates morphology.

Table 48: EDS results of SHT heat-treated at 788 °C for 200 h HX samples.

	γ austenitic matrix		Precipitates	
Element	wt (%)	at (%)	wt (%)	at (%)
Ni	46.1	46.2	35.0	38.6
Cr	22.1	25.0	18.5	23.0
Fe	19.1	20.1	15.5	18.0
Mo	8.6	5.3	18.2	12.3
Co	1.9	2.0	1.7	1.9
W	1.8	0.6	9.9	3.5
Si	0.4	0.8	1.1	2.6
Total	100.0	100.0	100	100

5.4.5 XRD analysis of heat-treated SHT at 788 °C for different times

Figure 122 compares the XRD spectra of SHT HX sample heat-treated at 788 °C for 3, 6 and 200 hours along the x-y plane.

Also in this case, the three samples exhibited only the presence of γ phase with a lattice parameter of 3.598 ± 0.002 Å for SHT + 745 °C 3 h, 3.598 ± 0.002 Å for SHT + 745 °C 6 h and 3.593 ± 0.001 Å for SHT + 745 °C 200 h.

The microstructure of prolonged heat-treated samples showed a significant number of precipitates that could take part of the solute elements such as Cr and Mo to form σ or μ phases, resulting in a reduction of the lattice parameters with respect to the SHT HX samples.

On the contrary, the HX samples heat-treated at 788 °C for short times showed a similar lattice parameter to SHT HX samples.The presence of carbides along the grain boundaries could not be detected by means of XRD analysis, probably due to below the sensitivity threshold of the instrument, otherwise, due to the peaks overlap with the γ matrix.

The table with the lattice parameters of γ austenitic phase calculated for the different peaks is available in Appendix A.

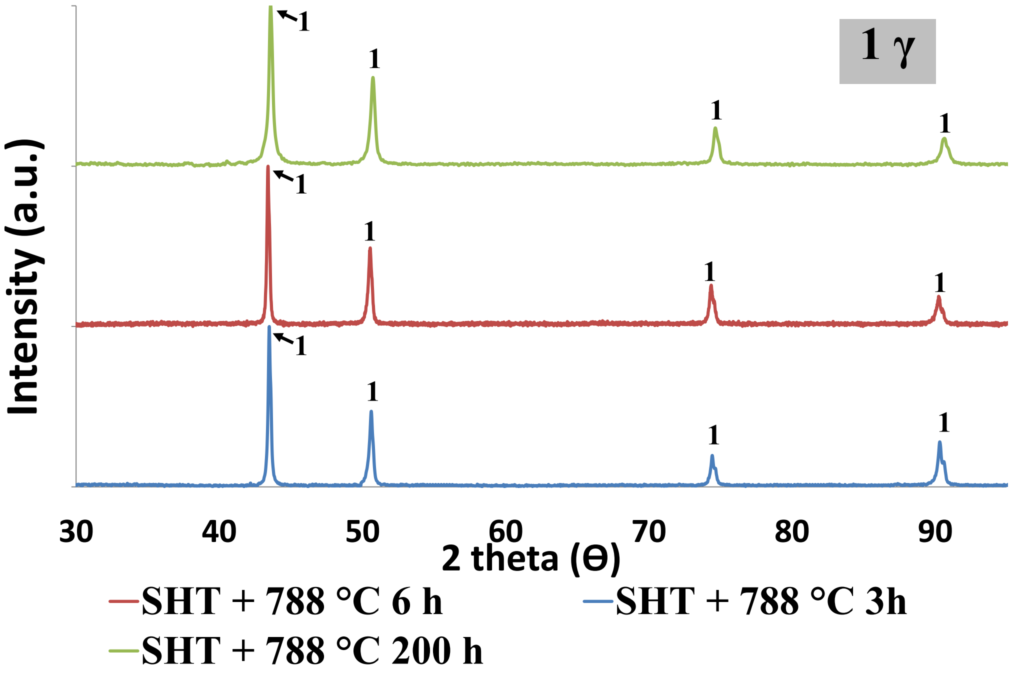

Figure 122: XRD spectra of SHT HX samples heat treated at 788 °C for 3, 6 and 200 hours showing the peaks of γ austenitic phase.

5.4.6 Characterisation of extracted carbides form SHT HX samples heat-treated at 745 °C and 788 °C

The extracted carbides of SHT samples heat-treated at 745 °C for 6 hours (SHT + 745 °C 6 h) and heat-treated samples at 788 °C for 6 hours (SHT + 788 °C 6 h) were filtered using a glass fiber filter and subsequently observed at SEM in Figure 123a and 123b, respectively.

The SEM images revealed the aggregation of extremely fine carbides and the EDS analysis determined a very high enrichment of Cr inside the carbides, indicating the formation of Cr-rich $M_{23}C_6$ carbides for both the samples. The EDS results are reported in Table 49 revealed a good correlation between the two results. It should be noted that Si was not determined since the carbides were deposited on a glass fiber filter.

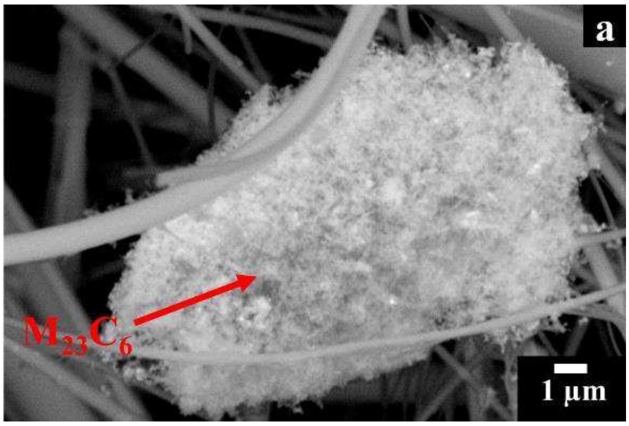

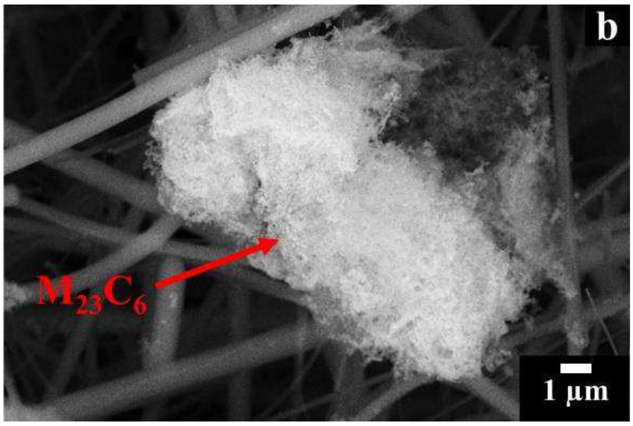

Figure 123: SEM images of extracted carbides from: (a) SHT + 745 °C 6 h HX samples and (b) SHT + 788 °C 6 h HX samples; the extracted carbides were deposited on a glass fiber filter.

Table 49: EDS results on Cr-rich $M_{23}C_6$ carbides for extracted carbides form SHT + 745 °C 6 h and SHT + 788 °C 6 h HX samples.

Element	SHT + 745 °C 6 h		SHT + 788 °C 6 h	
	Cr-rich $M_{23}C_6$ carbides		Cr-rich $M_{23}C_6$ carbides	
	wt (%)	at (%)	wt (%)	at (%)
Ni	7.5	8.1	4.9	5.4
Cr	56.2	68.4	56.0	69.8
Fe	4.1	4.6	4.2	4.8

Mo	24.8	16.3	23.3	15.8
Co	-	-	0.1	0.1
W	7.4	2.6	11.5	4.1
Si*	-	-	-	-
Total	100.0	100.0	100.0	100.0

**Si was not determined to avoid overstimation due to the glass fiber filter.*

5.4.7 XRD spectra of extracted carbides of heat-treated SHT HX samples

The XRD spectra of the extracted carbides of SHT HX samples heat-treated at 745 °C for 6 hours (SHT + 745 °C 6 h) and 788 °C for 6 hours (SHT + 788 °C 6 hours) are displayed in Figure 124. The extracted carbides exhibited peaks of Cr-rich $M_{23}C_6$ carbide, a less marked presence of Mo-rich M_6C carbides as well as peaks attributed to residual aggregates of γ matrix. All these identified phases have a fcc crystal structure.

Using the peaks of Cr-rich $M_{23}C_6$ carbides was determined a lattice parameter of 10.709 ± 0.014 Å for SHT + 745 °C 6 h state and 10.721 ± 0.013 Å for SHT + 788 °C 6 h HX state. The Cr-rich $M_{23}C_6$ carbide has a characteristic lattice parameter from 10.50 to 10.70 Å, although its lattice parameter can be modified by other elements which take part in the carbide formation such as Fe, Mo and W [3]. It was demonstrated that the $M_{23}C_6$ carbide could also have a higher lattice parameter of 10.70 Å, depending on the chemical composition of the alloy, which makes available the elements to the carbides formation. For instance, it was found that Cr-rich $M_{23}C_6$ carbide enriched in W had a lattice parameter of 10.869 Å[141]. The presence of Cr-rich $M_{23}C_6$ after ageing treatments is congruent with other studies on HX alloy [6,20].

Furthermore, the XRD spectra highlighted some peaks of Mo-rich M_6C carbides with a lattice parameter of 11.044 ± 0.027 Å (SHT + 745°C 6 h state) and a lattice parameter of 11.042 ± 0.012 Å (SHT + 788 °C 6 h state), compatible with the lattice parameter of Mo-rich M_6C carbide reported in the literature [3,43,117]. The presence of Cr-rich $M_{23}C_6$ carbides was further supported by EDS results, whereas during the SEM investigation no Mo-rich M_6C carbides were detected, probably due to the very low number of this type of carbide. These Mo-rich M_6C carbides could be carbides formed during the solution treatments or carbides formed during the subsequent thermal exposure at 745 °C and 788 °C. The table with the values of all lattice parameters determined by the peaks of Cr-rich $M_{23}C_6$ and Mo-rich M_6C carbides is available in Appendix A.

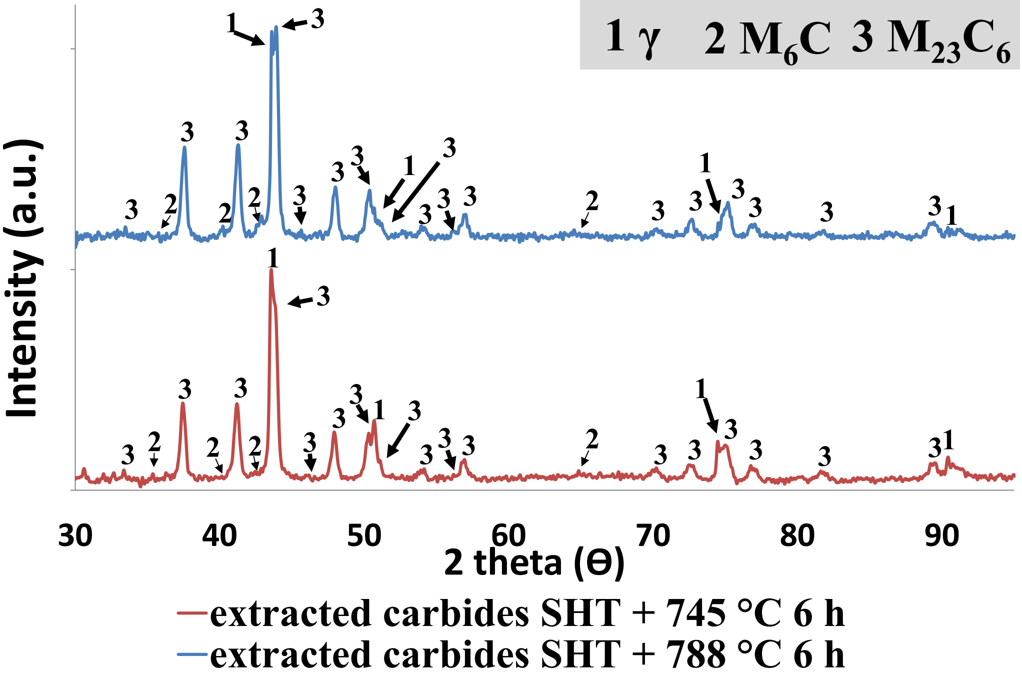

Figure 124: XRD spectra of extracted carbides from SHT HX samples + 745 °C 6 h and SHT HX samples + 788 °C for 6 h.

5.5 Characterisation of HIPed HX samples

5.5.1 Microstructural characterisation of HIPed HX samples

The HIP treatment performed at 1160 °C for 4 hours at 103 MPa eliminated all the microcracks and also reduced the porosity level with respect to the as-built and SHT conditions as visible in Figure 125a and 125b. Besides, the values of residual porosity and cracking density are reported in Table 50.

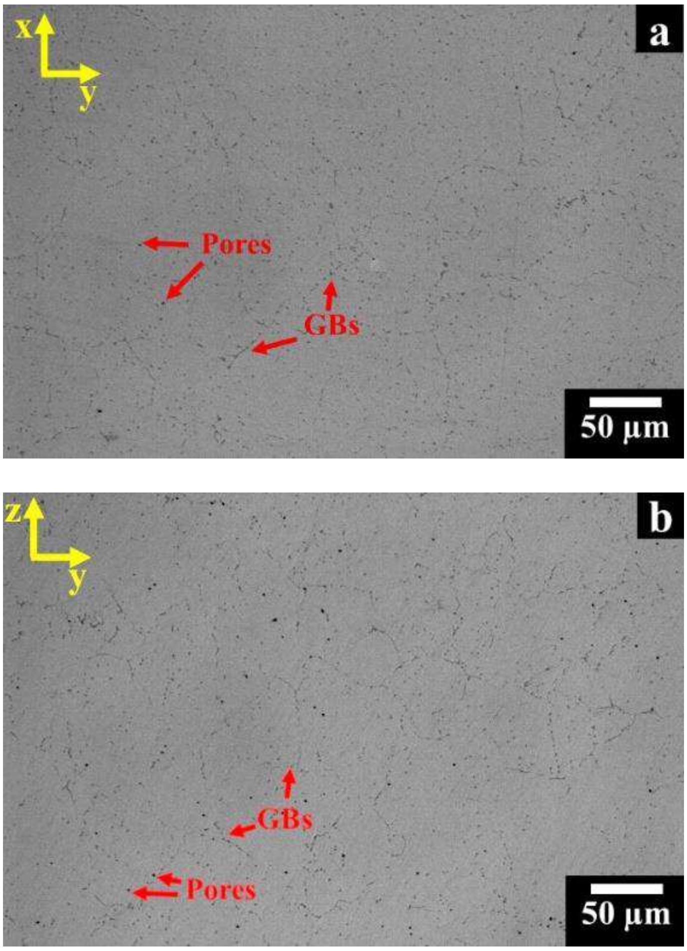

Figure 125: OM images of HIPed HX samples along x-y and z-y planes showing (a, b) grain boundaries (GBs) and very small spherical pores.

Table 50: Residual porosity and cracking density of HIPed HX samples along x-y and z-y planes.

x-y plane	Residual porosity (%)	0.05 ± 0.01
z-y plane	Residual porosity (%)	0.06 ± 0.02
x-y plane	Cracking density (mm/mm^2)	0
z-y plane	Cracking density (mm/mm^2)	0

The HIPed samples revealed a greater hardness than the SHT condition with a hardness of 159 ± 3 HBW and 84 ± 1 HRB. These hardness values derived from a microstructure consisted of equiaxed grains with a large presence of inter/intragranular carbides (Figure 126a and 126b).

The ASTM grain size number G was mainly 4.5-5.5 (grain diameters from 53.4 to 75.5 μm) for both x-y and z-y planes, leading to the formation of an isotropic material. The determined grain size of HIPed samples was similar to the optimised SHT HX samples (1175 °C 1 h). At higher magnifications (Figure 126c and 126d), it was possible to see that the globular intragranular carbides were scattered throughout the austenitic matrix with a total carbides fraction of 7.23 ± 0.80%.

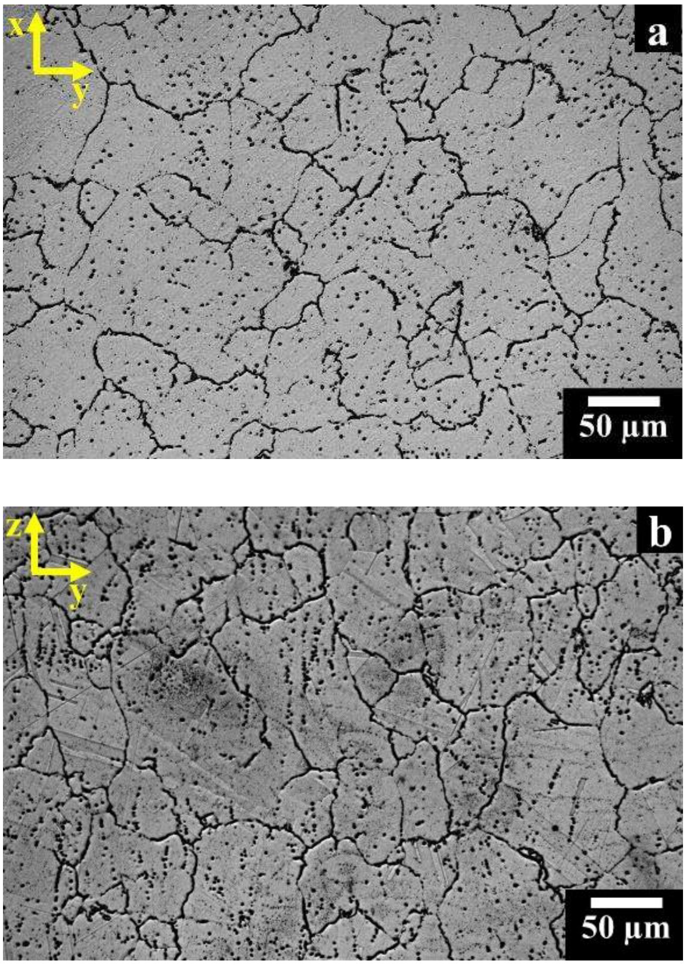

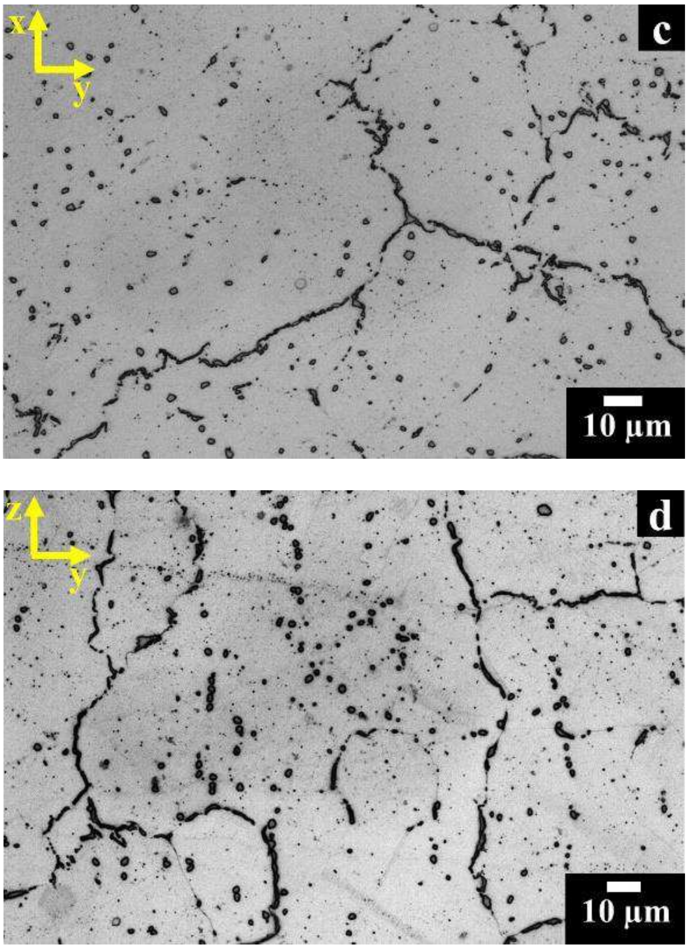

Figure 126: OM images of HIPed HX samples showing (a, b) equiaxed grains along x-y and z-y planes respectively; (c, d) the carbides along the grain boundaries and within the grains along x-y and z-y planes, respectively. Kalling's No.2 etchant was used.

The FESEM images (Figure 127a and 127b) revealed the morphology of these carbides. According to the literature, the elongated shape of the intergranular carbides (with a length up to 15 µm) could be attributed to Cr-rich $M_{23}C_6$ and Mo-rich M_6C carbides formation, whereas the intragranular globular carbides (with a size around 1.5-2.5 µm) could be associated with the formation of Mo-rich M_6C carbides [6,141]. In fact, the slow HIP cooling rate could initially promote the formation of M_6C carbides and then at a lower temperature the formation of $M_{23}C_6$ carbides, as can be deducted by the T-T-T diagram of Hastelloy X [20].

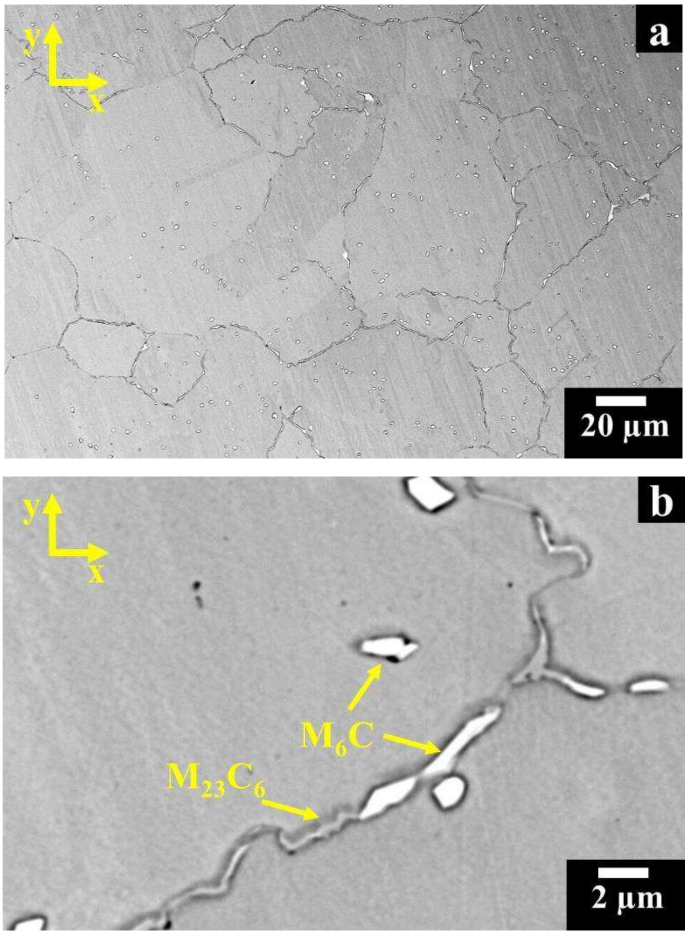

Figure 127: FESEM images of HIPed HX samples showing: (a) equiaxed grains with carbides along the grain boundaries and inside the grains; (b) the morphology of the Mo-rich M_6C and Cr-rich $M_{23}C_6$ carbides; Kalling's No.2 etchant was used.

5.5.2 Characterisation of extracted carbides from HIPed HX samples

In order to confirm the formation of these carbides, the extracted carbides of the HIPed samples were analysed by means of SEM+EDS and XRD analyses. The SEM images (Figure 128a and 128b) exhibited residual aggregate particles of austenitic matrix, together with Mo-rich M_6C carbides and elongated Cr-rich $M_{23}C_6$ carbides, as also supported by EDS results in Table 51. The EDS results revealed no trace of Si and W inside the austenitic matrix due to these elements were consumed to form the carbides.

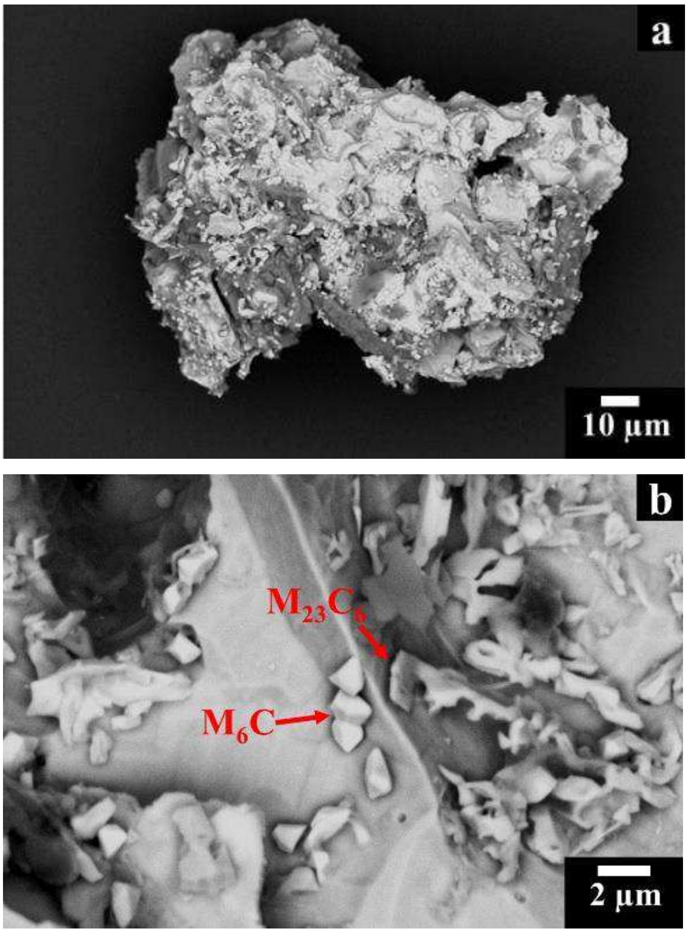
a
10 µm
b
$M_{23}C_6$
M_6C
2 µm

Figure 128: SEM images showing: (a) residual of austenitic matrix; (b) Mo-rich M_6C carbides and Cr-rich $M_{23}C_6$ carbides.

Table 51: EDS results of austenitic matrix, a Mo-rich M_6C carbide and a Cr-rich $M_{23}C_6$ carbide.

	Aggregate of γ austenitic matrix		Mo-rich M_6C carbide		Cr-rich $M_{23}C_6$ carbide	
Element	wt (%)	at (%)	wt (%)	at (%)	wt (%)	at (%)
Ni	46.9	37.9	14.8	19.6	9.2	9.3
Cr	23.2	21.1	11.6	17.4	56.1	64.6
Fe	18.9	16.0	5.0	6.9	6.3	6.7
Mo	3.1	1.5	50.0	40.4	21.8	13.7
Co	2.4	1.9	0.7	0.9	0.3	0.4
W	-	-	14.7	0.9	4.4	1.4
Si	-	-	3.1	8.5	1.9	4.0
Total	100.0	100.0	100.0	100.0	100.0	100.0

5.5.3 XRD spectra of HIPed HX samples and extracted carbides

The XRD spectra of HIPed HX sample (along the x-y plane) and extracted carbides are displayed in Figure 129. The XRD spectrum of the HIPed sample revealed the γ phase with a lattice parameter of 3.608 ± 0.003 Å and a peak of Mo-rich M_6C carbide.

The XRD spectrum of extracted carbides showed the presence of Mo-rich M_6C carbides with a lattice parameter of 11.049 ± 0.011 Å and Cr-rich $M_{23}C_6$ carbides with a lattice parameter of 10.748 ± 0.025 Å, revealing a good correlation with the literature [3,43,117,141]. The table with the values of lattice parameters of $M_{23}C_6$ is available in Appendix A.

As observed before, the extracted carbides were attacked to aggregated particles of γ phase, so some peaks could be associated with the presence both of carbides and γ phase, as indicated in the spectrum. The XRD analysis confirmed the presence of both Mo-rich M_6C and Cr-rich $M_{23}C_6$ carbides found during the SEM investigation of extracted carbides.

The table with the values of all lattice parameters determined by the peaks of Cr-rich $M_{23}C_6$ and Mo-rich M_6C carbides is available in Appendix A.

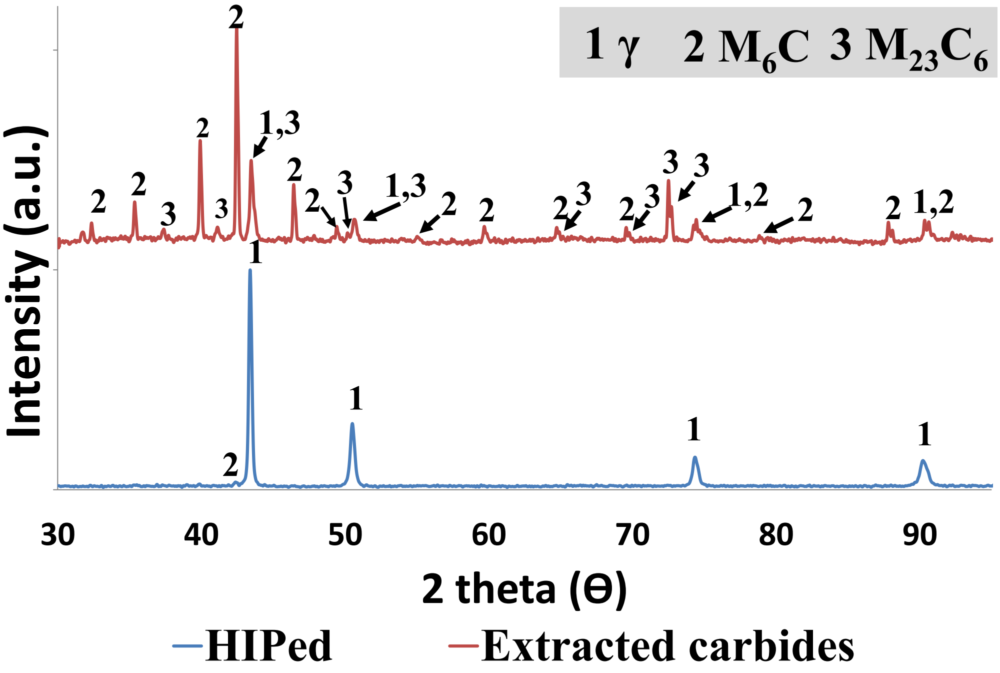

Figure 129: XRD diffraction patterns of HIPed HX sample (along x-y plane) and extracted carbides from HIPed samples.

5.5.4 TMA of HIPed HX state

Figure 130 shows the CTE as function of the temperature for the HIPed HX state. The CTE did not exhibit relevant deflections as previously observed for as-built and SHT HX samples.

A possible explanation for this phenomenon is that the HIPed samples showing a large number of carbides have lower C inside the matrix and along the grain boundaries with respect to the as-built and SHT condition, avoiding the formation of a large number of carbides during thermal exposure at high temperature.

The average CTE of HIPed HX sample was determined 15.8 10^{-6} °C^{-1} (at 538 °C) and 17.6 10^{-6} °C^{-1} (at 871 °C), whereas traditional sheets of HX have a value of 15.1 10^{-6} °C^{-1} (at 538 °C) and 16.2 10^{-6} °C^{-1} (at 871 °C) [3].

The higher mean CTE of HIPed HX samples with respect to all the other conditions and traditional sheets of HX alloy may be explained by means of the microstructure of HIPed samples. In fact, these samples exhibited a large presence of Mo-rich M_6C and Cr-rich $M_{23}C_6$ carbides, involved a depletion of Mo, W, Cr in the austenitic matrix, leading to a CTE improvement. This hypothesis is supported by other work that studied the effect of Mo and W in solid solution on CTE [142].

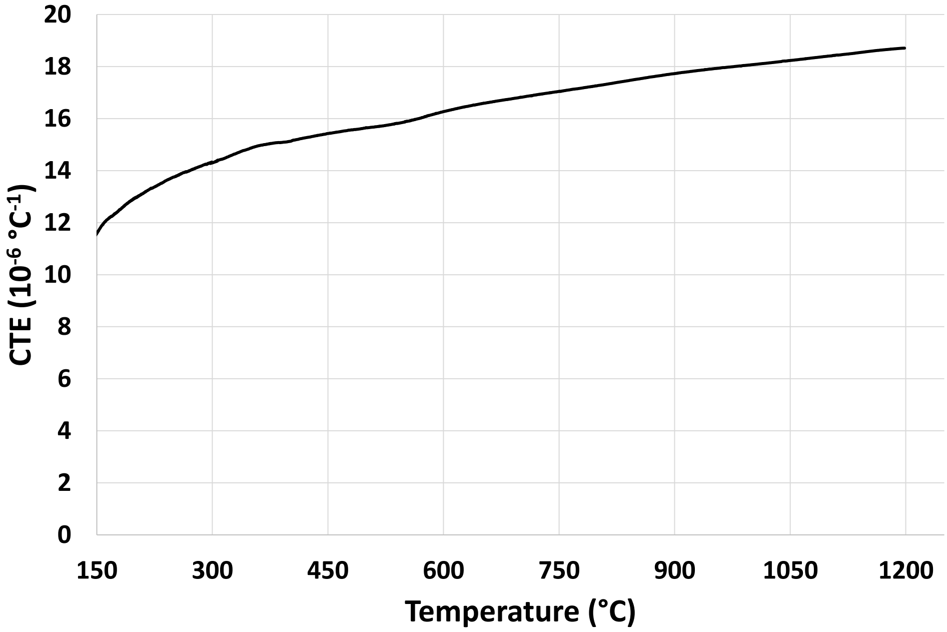

Figure 130: Coefficient of thermal expansion (CTE) vs temperature of HIPed HX sample.

5.6 HIPed+SHT HX samples

5.6.1 Solutionizing treatment optimisation on HIPed HX samples

In order to reduce the number of carbides, it was performed a solution treatment at 1175 °C for different times obtaining a hardness reduction as can be seen in Figure 131.

The HIPed HX samples revealed a hardness of 159 ± 3 HBW, whereas after a solutioning performed at 1175 °C for 15 minutes the hardness slightly decreased at 155 ± 4 HBW, essentially due to the carbides dissolution.

For prolonged solutioning at 1175 °C for 30, 60 and 120 minutes the hardness remained almost unchanged with a value of 154 ± 4 HBW, 154 ± 3 HBW and 153 ± 3 HBW, respectively.

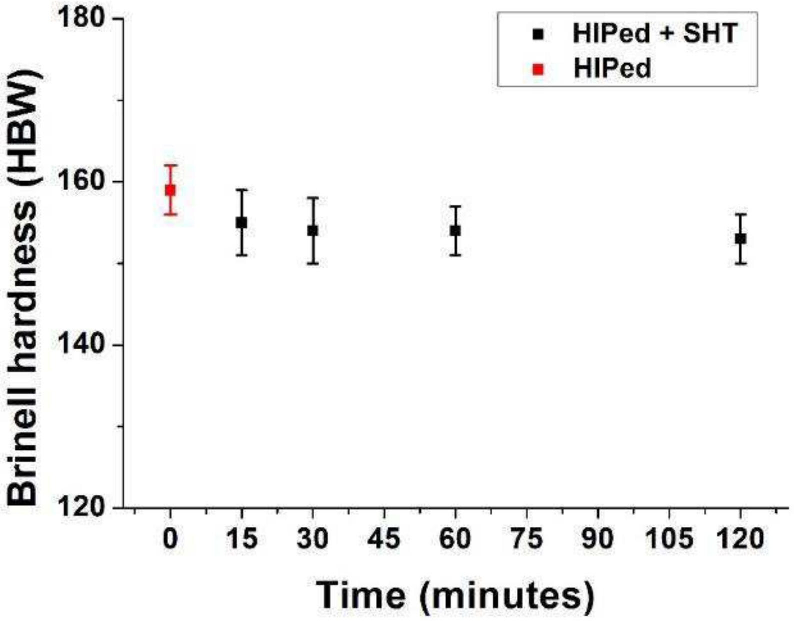

Figure 131: Brinell hardness values of HIPed and HIPed+SHT samples at 1175 °C for 15, 30, 60 and 120 minutes.

From the hardness measurements, it was chosen as optimised condition the HIPed samples followed by solutioning at 1175 °C for 30 minutes. This optimised HIPed+SHT condition revealed a HRB of 81 ± 1.

5.6.2 Microstructural investigation of optimised HIPed+SHT HX samples

The HIPed+SHT HX samples are crack-free as can be seen in Figure 132a and 132b. The values of residual porosity and cracking density for different planes are reported in Table 52, showing values similar to the HIPed HX state.

After etching with kalling's No.2 the microstructure exhibited equiaxed grains with ASTM grain size G mainly between 4.5 and 5.5 (corresponding to a grain diameter from 53.4 to 75.5 µm) for both x-y and z-y planes as can be observed in Figure 132c and 132d.

Besides, the OM images (Figure 132e and 132f) exhibited the presence of small inter/intragranular Mo-rich M_6C carbides, whereas the solution treatment would seem almost completely to dissolve the elongated Cr-rich $M_{23}C_6$ carbides. A carbides fraction of 0.65 ± 0.15 % was determined.

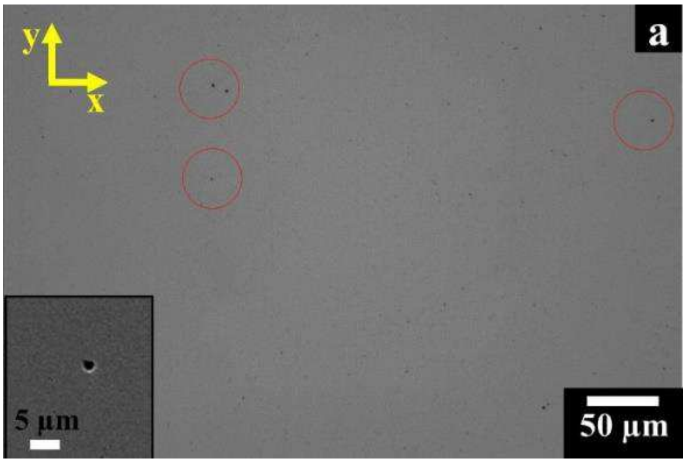

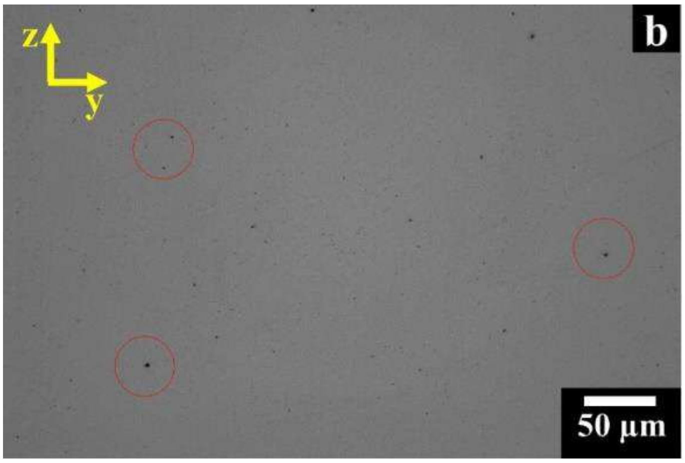

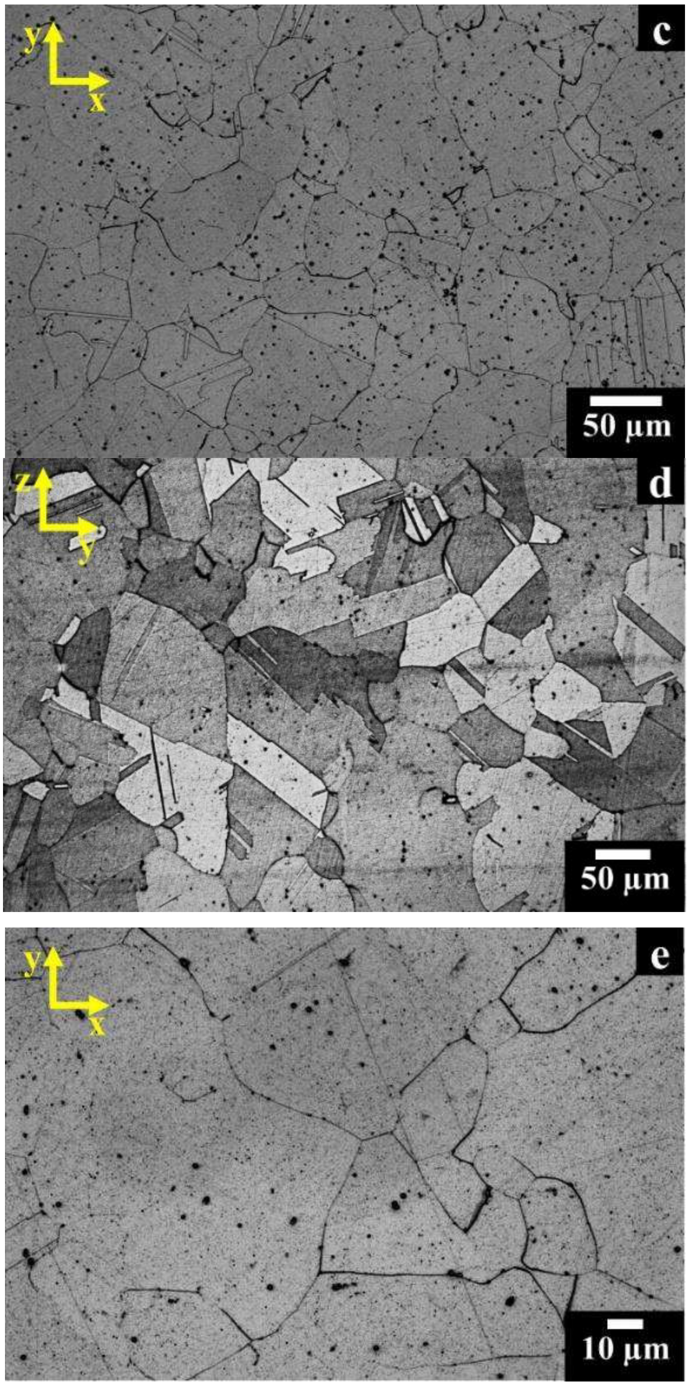
c
y
x
50 µm
d
z
y
50 µm
e
y
x
10 µm

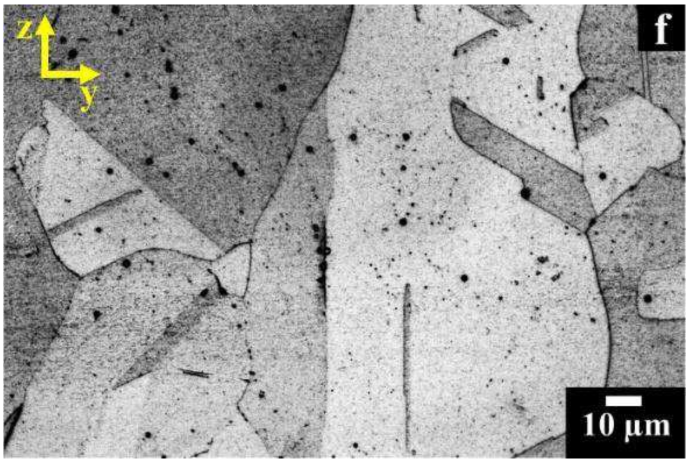

Figure 132: OM images of HIPed+SHT samples (at 1175 °C for 30 minutes) at different magnifications showing (a, b) the very few pores along x-y and z-y planes, with inset of a spherical pore; (c,d) the equiaxed grains and carbides along x-y and z-y planes; (e, f) the formation of carbides inside the materials; the samples was etched with Kalling'n No.2 reagent.

Table 52: Residual porosity and cracking density of HIPed+SHT HX samples along x-y and z-y planes.

x-y plane	Residual porosity (%)	0.04 ± 0.01
z-y plane	Residual porosity (%)	0.06 ± 0.02
x-y plane	Cracking density (mm/mm^2)	0
z-y plane	Cracking density (mm/mm^2)	0

The size of the inter/intragranuler Mo-rich M_6C carbides was generally around 1.0 with the largest ones around 2.0-2.5 µm, as can be observed in Figure 133a and 133b. The results of EDS analysis performed on the austenitic matrix and on the Mo-rich M_6C carbides are reported in Table 53.

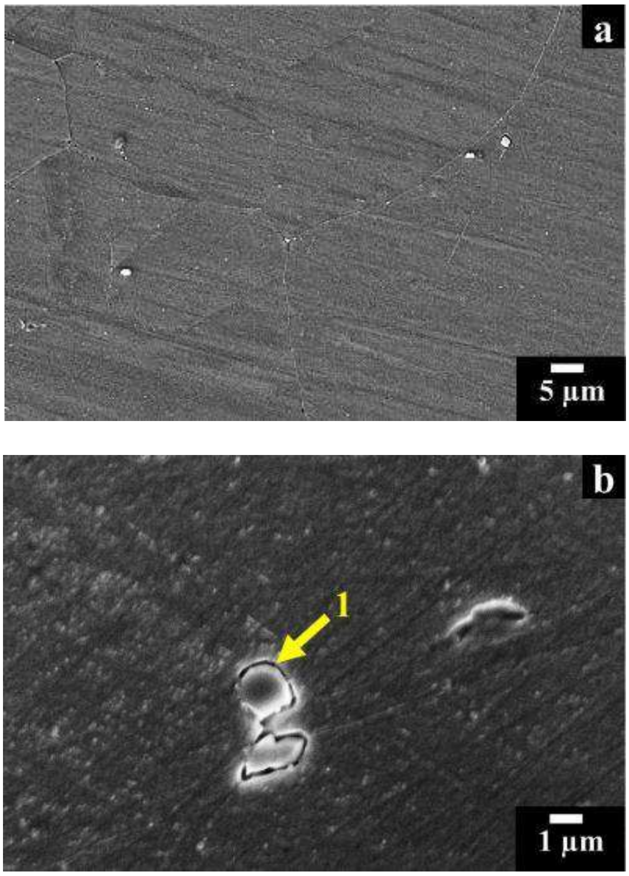

Figure 133: FESEM images of optimised HIPed+SHT samples at (1175 °C for 30 min) showing (a, b) very fine inter/intragranular Mo-rich M_6C carbides, where a intragranular Mo-rich M_6C carbides is indicated by the yellow arrow 1; Kalling's No.2 reagent was used.

Table 53: EDS results of γ austenitic matrix and Mo-rich M_{6C} carbide for optimised HIPed+SHT HX sample.

Element	γ austenitic matrix		Mo-rich M_6C carbide	
	wt (%)	at (%)	wt (%)	at (%)
Ni	45.6	45.8	28.0	32.1
Cr	22.3	25.2	19.6	25.3
Fe	19.2	20.2	11.4	13.7
Mo	9.2	5.6	32.6	22.8

Co	2.1	2.1	1.4	1.6
W	1.3	0.4	6.0	2.2
Si	0.3	0.7	1.0	2.3
Total	100.0	100.0	100	100

This microstructure has a less supersaturation of C with respect to the as-built and SHT samples as can be assumed by a higher fraction of micrometric (1.0-2.5 µm) M_6C carbides. Therefore, the microstructural evolution of these heat-treated samples is expected to be similar to traditional SHT HX alloys [6,20,43,44]

5.6.3 XRD spectrum of optimised HIPed+SHT HX state

Figure 134 reveals the XRD spectrum of optimised HIPed+SHT HX samples exhibited the peaks of γ phase with a lattice parameter of 3.608 ± 0.005 Å together with a peak associated with the presence of Cr-rich $M_{23}C_6$ carbides, suggesting that after the solution treatment a small fraction of this type of carbide remained along the grain boundaries.

However, the microstructure of HIPed+SHT samples did not reveal elongated or film of Cr-rich $M_{23}C_6$ carbides, so only a discrete number of fine Cr-rich $M_{23}C_6$ did not degenerate the ductility. The table with the lattice parameters of γ austenitic phase and Cr-rich $M_{23}C_6$ carbides calculated for the different peaks is available in Appendix A.

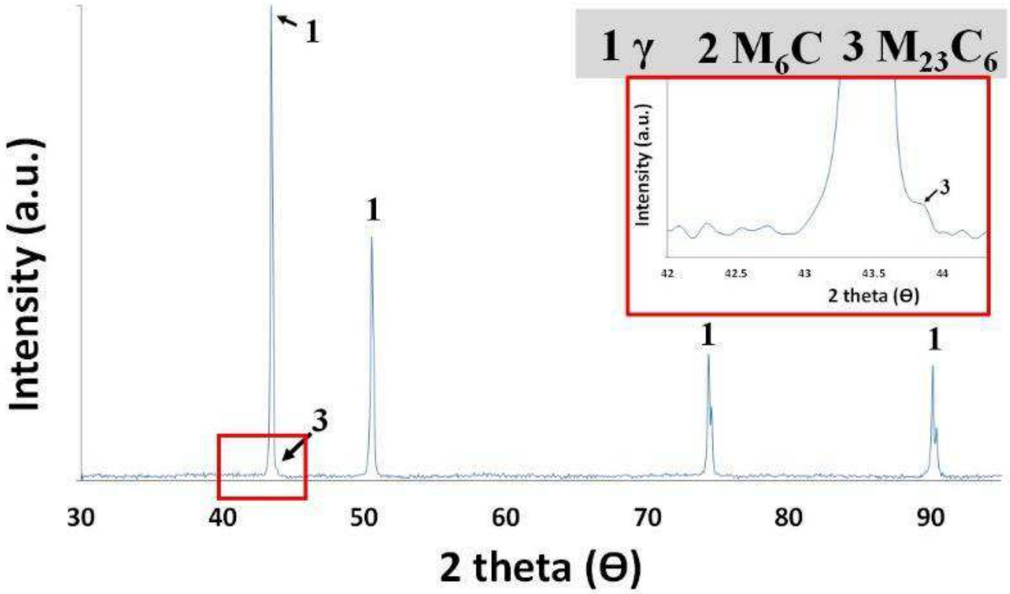

Figure 134: XRD spectrum of optimised HIPed+SHT HX samples.

5.6.4 TMA of optimised HIPed+SHT HX state

Figure 135 shows the CTE as function of the temperature for the HIPed+SHT HX state. The CTE curve presented two deflections around 600 °C and 780 °C as previously observed for the SHT HX samples.

These deflections may be associated with the precipitation of carbides. The average CTE of HIPed+SHT HX samples was determined 15.1 10^{-6} $°C^{-1}$ (at 538 °C) and 16.1 10^{-6} $°C^{-1}$ (at 871 °C), whereas traditional sheets of HX have a value of 15.1 10^{-6} $°C^{-1}$ (at 538 °C) and 16.2 10^{-6} $°C^{-1}$ (at 871 °C) [3]. The average CTE of HIPed+SHT HX and traditional SHT HX alloy are similar to each other since they have a similar grain size and microstructure.

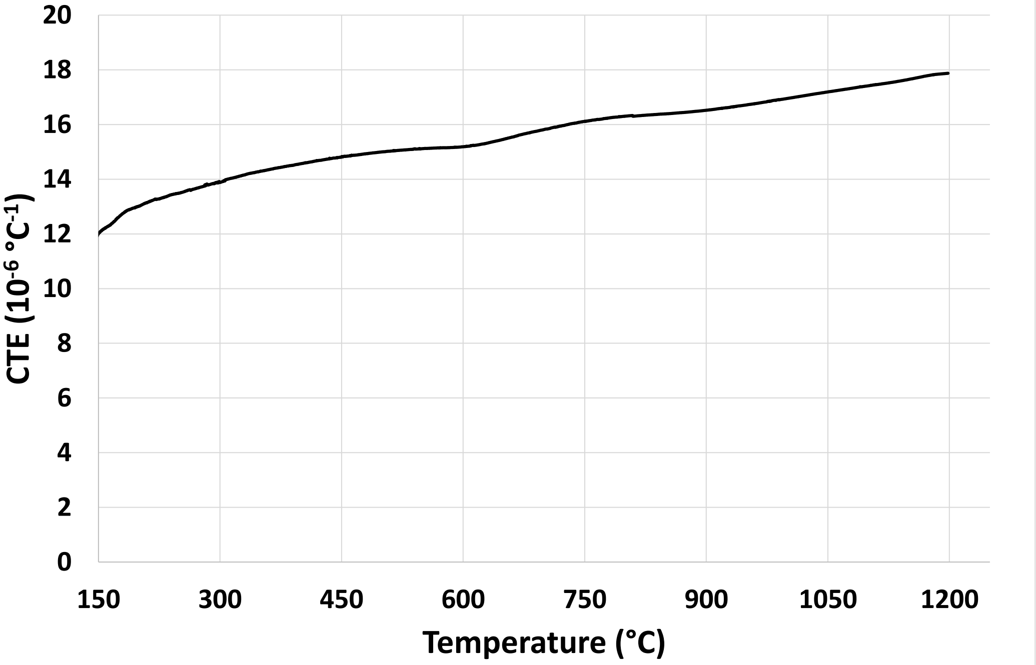

Figure 135: Coefficient of thermal expansion (CTE) vs temperature of HIPed+SHT HX sample.

5.6.5 HIPed and subsequent solutionizing treatment at 1066 °C for 1 hour

The HIPed samples were solutionized at 1066 °C for 1 hour in order to study the microstructure for a lower solution temperature with respect to 1175 °C (temperature recommended for HX alloy), resulting in a microstructure similar to HIPed samples, as can be seen in Figure 136a and 136b. The size of intragranular Mo-rich M_6C carbides was around 1.5 µm with elongated intergranular Cr-rich $M_{23}C_6$ carbides up to 15 µm (Figure 136c and 136d).

It could be concluded that a heat treatment performed at 1066 °C for 1 hour was not sufficient to dissolve the Cr-rich $M_{23}C_6$ carbides, although this type of carbides exhibited a starting size reduction. Furthermore, the negligible impact of this solution treatment was also proved by hardness test that revealed Brinell hardness value of 160 ± 3 HBW, very similar to HIPed samples with a value of 159 ± 3 HBW.

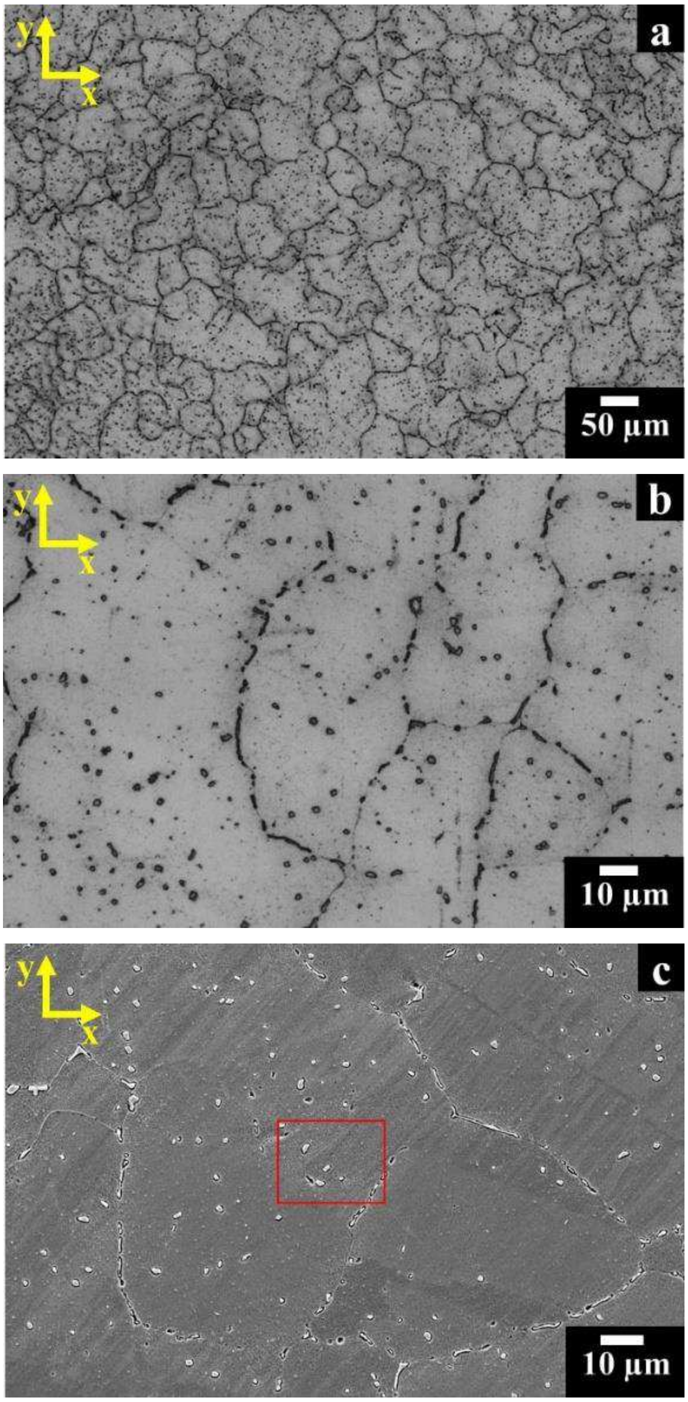
y
x
a
50 µm
y
x
b
10 µm
y
x
c
10 µm

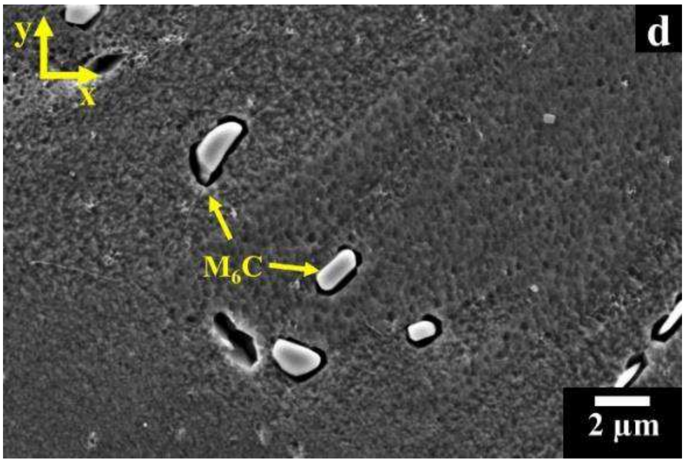

Figure 136: (a, b) OM images of HIPed+SHT samples at 1066 °C for 1 hour exhibiting equiaxed grains and carbides along x-y plane; (c, d) FESEM images of HIPed+SHT samples at 1066 °C for 1 hour showing the morphology and size of Mo-rich M_6C carbides. Kalling's No.2 etchant was used.

The Table 54 reported the EDS values of austenitic matrix and Mo-rich M_6C carbides.

Table 54: EDS results of γ austenitic matrix and Mo-rich M_6C carbides for HIPed+SHT HX sample at 1066 °C for 1 hour.

Element	γ austenitic matrix		Mo-rich M_6C carbide	
	wt (%)	at (%)	wt (%)	at (%)
Ni	46.1	46.5	26.8	31.0
Cr	21.8	24.8	16.9	22.2
Fe	18.5	19.5	11.6	14.2
Mo	9.8	6.1	37.2	26.4
Co	2.4	2.4	1.6	1.8
W	1.3	0.4	4.8	1.7
Si	0.1	0.3	1.1	2.7
Total	100.0	100.0	100	100

5.7 Conclusions

Overall, at the beginning, the HX powder was characterised to identify its shape, morphology, chemical composition as well as the flowability.

Afterward, the study of as-built HX samples revealed a microstructure made up of columnar grains along the building direction and randomly orientated grains perpendicular to the building direction, exhibiting throughout all the material a significant number of microcracks mainly located along the grain boundaries.

A theory has been proposed to explain the solidification of the as-built HX samples and the formation of the microcracks. Besides, some hypotheses to reduce the cracking density were given.

In order to obtain a microstructure with equiaxed grains different solution treatments were performed, leading to a microstructure with equiaxed grains and small Mo-rich M_6C carbides. In this way, it was possible to choose a tailored temperature and time as optimised SHT condition.

Afterward, the microstructure evolution of SHT HX samples was studied under thermal exposures at 745 °C and 788 °C for short and prolonged times, using temperature, in which HX components may be subjected as the cross ducts in the high-temperature gas-cooled reactor (HTGR).

The thermal exposures promoted the formation of Cr-rich $M_{23}C_6$ carbide films along the grain boundaries of the equiaxed grains due to a high supersaturation of C. These Cr-rich $M_{23}C_6$ carbide films have a harmful effect on the ductility and creep resistance. Besides, prolonged aged HX samples revealed micrometric phases that may be identified as σ and μ phases.

The second part of this work instead was focused on reducing the cracking density of as-built HX samples using the HIP treatment. The microstructure of the HIPed HX samples was studied demonstrating the presence both of Mo-rich M_6C carbides and Cr-rich $M_{23}C_6$.

Finally, different solution treatments were carried out on the HIPed HX samples, allowing the determination of an optimised solution treatment (HIPed+SHT condition), resulting in a microstructure without microcracks similar to the traditional SHT HX alloys.

These results proved that LPBF-built HX alloy after a HIP treatment combined with a solution treatment could generate crack-free components with grain size and inter/intracarbides similar to traditional commercially available SHT HX alloys.

Chapter 6

Overall Conclusions and future works

In this thesis, two Ni-based superalloys were built by LAM processes. IN625 alloy fabricated by LPBF and DED and HX alloy produced by LPBF.

The results showed that IN625 had wide process window parameters to obtain dense IN625 samples for both processes. Therefore, it was possible to select appropriate process parameters in order to have a high build-up rate.

Afterwards, it was shown the microstructural evolution of the LPBF IN625 alloy under different heat treatments, showing the tensile properties of as-built and selected heat-treated IN625 conditions. All the tensile properties resulted to be superior to the minimum required values in the ASTM standard for wrought IN625 alloy, indicating their possible application for industrial production.

However, the only exception was the direct aged state revealed slightly lower ductility but also remarkable higher tensile strengths than data reported in the ASTM standard, due to the presence of γ'' phases and carbides, coupled with very fine dendritic microstructures.

Finally, for LPBF HX alloys, both the chemical composition and process parameters must be carefully designed, in order to avoid the formation of microcracks during the LPBF process. However, the work presented in this thesis demonstrated that whether microcracks occur during the process, a HIP treatment could be used to close them. Besides, a subsequent tailored solutioning treatment could generate a microstructure similar to SHT wrought HX alloys used for high-temperature applications. In this way, it is possible to recover the components reducing the number of defective parts for industrial applications.

The results showed that LAM techniques can be widely used to produce Ni-based superalloys, after appropriate post-processing. Therefore, the research should investigate more in details new post-processing tailored for LPBF materials.

Finally, future works should also focus on the mechanical properties at high temperature as well as study fatigue properties of Ni-based superalloys produced by LAM techniques.

Appendix A

Table A1. As-built HX sample (γ phase)

2theta	d (Å)	h	k	l	a (Å)
43.480	2.079	1	1	1	3.596
50.494	1.808	2	0	0	3.611
74.334	1.275	2	2	0	3.607
90.083	1.088	3	1	1	3.613
		Average a (Å)			**3.607 ± 0.007**

Table A2. Optimised SHT (1175 °C 1 h) HX sample (γ phase)

2theta	d (Å)	h	k	l	a (Å)
43.592	2.075	1	1	1	3.593
50.708	1.799	2	0	0	3.598
74.467	1.273	2	2	0	3.601
90.339	1.086	3	1	1	3.602
		Average a (Å)			**3.599 ± 0.004**

Table A3. SHT + 745 °C 3 h HX sample (γ phase)

2theta	d (Å)	h	k	l	a (Å)
43.486	2.079	1	1	1	3.600
50.622	1.801	2	0	0	3.602
74.491	1.272	2	2	0	3.598
90.355	1.086	3	1	1	3.600
		Average a (Å)			**3.600 ± 0.001**

Table A4. SHT + 745 °C 6 h HX sample (γ phase)

2theta	d (Å)	h	k	l	a (Å)
43.442	2.075	1	1	1	3.604
50.572	1.798	2	0	0	3.605
74.388	1.271	2	2	0	3.603
90.300	1.085	3	1	1	3.602
		Average a (Å)			**3.603 ± 0.002**

Table A5. SHT + 745 °C 200 h sample (γ phase)

2theta	d (Å)	h	k	l	a (Å)
43.715	2.068	1	1	1	3.582
50.872	1.793	2	0	0	3.586
74.745	1.269	2	2	0	3.588
90.696	1.082	3	1	1	3.590
		Average a (Å)			**3.586 ± 0.003**

Table A6. SHT + 788 °C 3 h sample (γ phase)

2theta	d (Å)	h	k	l	a (Å)
43.548	2.076	1	1	1	3.595
50.680	1.799	2	0	0	3.598
74.484	1.272	2	2	0	3.599
90.384	1.085	3	1	1	3.600
		Average a (Å)			**3.598 ± 0.002**

Table A7. SHT + 788 °C 6 h sample (γ phase)

2theta	d (Å)	h	k	l	a (Å)
43.546	2.076	1	1	1	3.595
50.683	1.799	2	0	0	3.598
74.503	1.272	2	2	0	3.598
90.382	1.085	3	1	1	3.600
		Average a (Å)			**3.598 ± 0.002**

Table A8. SHT + 788 °C 200 h sample (γ phase)

2theta	d (Å)	h	k	l	a (Å)
43.573	2.075	1	1	1	3.593
50.736	1.797	2	0	0	3.595
74.640	1.270	2	2	0	3.592
90.605	1.083	3	1	1	3.593
		Average a (Å)			**3.593 ± 0.001**

Table A9. Extracted M_6C carbides (in blue) and $M_{23}C_6$ carbides (in red) of SHT + 745 °C 6 h HX sample

2theta	d (A)	h	k	l	a (Å)
33.371	2.682	4	0	0	10.727
37.556	2.392	4	2	0	10.697
39.909	2.256	4	2	2	11.053
41.199	2.189	4	2	2	10.721
42.400	2.129	5	1	1	11.064
43.956	2.057	5	1	1	10.691
46.537	1.949	4	4	0	11.026
48.085	1.890	4	4	0	10.691
50.358	1.810	5	3	1	10.707
54.059	1.694	6	2	0	10.716
56.183	1.615	5	3	3	10.711
64.559	1.442	7	3	1	11.075
70.250	1.338	8	0	0	10.706
72.704	1.299	8	2	0	10.712
75.214	1.262	6	6	0	10.707
76.830	1.239	7	5	1	10.732
81.670	1.178	9	1	1	10.728
88.300	1.105	7	7	1	10.999
	$M_{23}C_6$ average value (Å)				**10.709 ± 0.014**
	M_6C average value (Å)				**11.044 ± 0.027**

Table A10. Extracted M_6C carbides (in blue) and $M_{23}C_6$ carbides (in red) of SHT +788 °C 6 h HX sample

2theta	d (A)	h	k	l	a (Å)
33.371	2.682	4	0	0	10.727
37.414	2.401	4	2	0	10.737
39.980	2.252	4	2	2	11.035
41.199	2.189	4	2	2	10.721
42.400	2.121	5	1	1	11.064
43.790	2.065	5	1	1	10.729
46.430	1.953	4	4	0	11.050
47.925	1.896	4	4	0	10.725
50.331	1.811	5	3	1	10.713

51.191	1.782	6	0	0	10.694
54.137	1.692	6	2	0	10.702
56.214	1.634	5	3	3	10.718
57.000	1.614	6	2	2	10.704
64.859	1.436	7	3	1	11.029
70.044	1.342	8	0	0	10.734
72.565	1.301	8	2	0	10.730
75.052	1.264	6	6	0	10.726
76.770	1.240	7	5	1	10.739
81.828	1.176	9	1	1	10.711
87.806	1.110	7	7	1	11.048
$M_{23}C_6$ average value (Å)					**10.721 ± 0.013**
M_6C average value (Å)					**11.042 ± 0.015**

Table A11. HIPed HX samples, γ phase in black and M_6C carbides in blue

2theta	d (Å)	h	k	l	a (Å)
42.434	2.127	5	1	1	11.054
43.366	2.084	1	1	1	3.610
50.471	1.806	2	0	0	3.612
74.311	1.275	2	2	0	3.606
90.183	1.087	3	1	1	3.606
Average a (Å) for γ phase					**3.608 ± 0.003**

Table A12 Extracted M_6C carbides (in blue) and $M_{23}C_6$ carbides (in red) of HIPed HX sample

2theta	d (Å)	h	k	l	a (Å)
32.347	2.764	4	0	0	11.057
35.346	2.536	3	3	1	11.056
37.363	2.404	4	2	0	10.751
39.903	2.257	4	2	2	11.055
41.128	2.192	4	2	2	10.739
42.4340	2.127	5	1	1	11.054
43.516	2.077	5	1	1	10.794

46.410	1.954	4	4	0	11.055
49.454	1.841	6	0	0	11.045
50.175	1.816	5	3	1	10.744
54.939	1.669	6	2	2	11.073
59.699	1.547	7	1	1	11.048
64.731	1.438	7	3	1	11.049
64.901	1.435	6	4	2	10.739
69.569	1.350	7	3	3	11.048
69.763	1.346	8	0	0	10.771
72.505	1.302	8	2	0	10.738
72.705	1.299	8	2	0	10.712
74.287	1.275	7	5	1	11.044
78.837	1.213	9	1	1	11.048
87.806	1.110	7	7	1	11.048
88.117	1.107	9	3	3	11.017
90.680	1.083	8	6	2	11.040
M_6C average value (Å)					**11.049 ± 0.011**
$M_{23}C_6$ average value (Å)					**10.748 ± 0.025**

Table A13. Optimised HIPed+SHT (1175 °C 30 min) condition, γ phase in black and $M_{23}C_6$ carbides in red.

2theta	d (Å)	h	k	l	a (Å)
43.424	2.081	1	1	1	3.615
43.800	2.064	5	1	1	10.727
50.531	1.804	2	0	0	3.608
74.335	1.275	2	2	0	3.605
90.180	1.087	3	1	1	3.606
Average a (Å)					**3.608 ± 0.005**

References

[1] I.A. Choudhury, M.A. El-Baradie, Machinability of nickel-base super alloys: a general review, J. Mater. Process. Technol. 77 (1998) 278–284. doi:10.1016/S0924-0136(97)00429-9.

[2] B. Geddes, H. Leon, X. Huang, Superalloys - Alloying and Performance, 1° edition, ASM International, Materials Park, OH, 2010.

[3] M.J. Donachie, S.J. Donachie, Superalloys A Technical Guide, 2° edition, ASTM Insternational, Materials Park, OH, 2002.

[4] T.M. Pollock, S. Tin, Nickel-Based Superalloys for Advanced Turbine Engines: Chemistry, Microstructure and Properties, J. Propuls. Power. 22 (2006) 361–374. doi:10.2514/1.18239.

[5] S. Floreen, G.E. Fuchs, W.J. Yang, The Metallurgy of Alloy 625, in: E.A. Loria (Ed.), Superalloys 718, 625, 706 Var. Deriv. Miner. Met. Mater. Socity, 1994: pp. 13–37. doi:10.7449/1994/Superalloys_1994_13_37.

[6] H.M. Tawancy, Long-term ageing characteristics of Hastelloy alloy X, J. Mater. Sci. 18 (1983) 2976–2986. doi:10.1007/BF00700780.

[7] R.C. Reed, The superalloys Foundamentals and applications, Cambridge University Press, 2006. doi:doi.org/10.1017/CBO9780511541285.

[8] D. Tomus, P.A. Rometsch, M. Heilmaier, X. Wu, Effect of minor alloying elements on crack-formation characteristics of Hastelloy-X manufactured by selective laser melting, Addit. Manuf. 16 (2017) 65–72. doi:10.1016/j.addma.2017.05.006.

[9] R.A. Ricks, A.J. Porter, R.C. Ecob, The growth of γ' precipitates in nickel-base superalloys, Acta Metall. 31 (1983) 43–53. doi:10.1016/0001-6160(83)90062-7.

[10] R.A. MacKay, M. V. Nathal, D.D. Pearson, Influence of molybdenum on the creep properties of nickel-base superalloy single crystals, Metall. Trans. A. 21 (1990) 381–388. doi:10.1007/BF02782418.

[11] K. Löhnert, F. Pyczak, Microstructure evolution in the nickel base superalloy Allvac®718PlusTM, 7th Int. Symp. Superalloy 718 Deriv. (2010) 877–891.

[12] W.T. Loomis, J.W. Freeman, D.L. Sponseller, The influence of molybdenum on the γ'phase in experimental nickel-base superalloys, Metall. Trans. 3 (1972) 989–1000. doi:10.1007/BF02647677.

[13] M. Doi, T. Miyazaki, The effect of elastic interaction energy on the shape, J. Chem. Inf. Model. 53 (2013) 1689–1699. doi:10.1017/CBO9781107415324.004.

[14] a. S. Wilson, Formation and effect of topologically close-packed phases in nickel-base superalloys, Mater. Sci. Technol. 836 (2016) 1–11. doi:10.1080/02670836.2016.1187335.

[15] L.M. Suave, J. Cormier, P. Villechaise, A. Soula, Z. Hervier, D. Bertheau, et al., Microstructural Evolutions during Thermal Aging of Alloy 625: Impact of Temperature and Forming Process, Metall. Mater. Trans. A Phys. Metall. Mater. Sci. 45 (2014) 2963–2982. doi:10.1007/s11661-014-2256-7.

[16] H.C. Pai, M. Sundararaman, A Comparison of the Precipitation Kinetics of y" Particles in Virgin and Re-Solutioned Alloy 625, Superalloys 718, 625, 706 Var. Deriv. 3 (2005) 487–495. doi:10.7449/2005/Superalloys_2005_487_495.

[17] F.T. Furillo, J.M. Davidson, J.K. Tien, L.A. Jackman, The effects of grain boundary carbides on the creep and back stress of a nickel-base superalloy, Mater. Sci. Eng. 39 (1979) 267–273. doi:10.1016/0025-5416(79)90065-X.

[18] M. Sundararaman, P. Mukhopadhyay, S. Banerjee, Carbide precipitation in nickel base superalloys 718 and 625 and their effect on mechanical properties, TMS Superalloys 718. (1997) 625–706. doi:10.7449/1997/Superalloys_1997_367_378.

[19] W.H. Jiang, X.D. YAO, H.R. GUAN, H. Z.Q., Secondary M 6 C precipitation in a cobalt-base superalloy, J. Mater. Sci. Lett. 18 (1999) 303–305.

[20] J.C. Zhao, M. Larsen, V. Ravikumar, Phase precipitation and time-temperature-transformation diagram of Hastelloy X, Mater. Sci. Eng. A. 293 (2000) 112–119. doi:10.1016/S0921-5093(00)01049-2.

[21] G. Lvov, V.I. Levit, M.J. Kaufman, Mechanism of primary MC carbide decomposition in Ni-base superalloys, Metall. Mater. Trans. A. 35 (2004) 1669–1679. doi:10.1007/s11661-004-0076-x.

[22] C. Wang, Y. Guo, J. Guo, L. Zhou, Investigation and improvement on structural stability and stress rupture properties of a Ni-Fe based alloy, Mater. Des. 88 (2015) 790–798. doi:10.1016/j.matdes.2015.09.098.

[23] M.R. Abedi, H. Sabet, H. Razavi, The Effect of Repair Welding Number on Microstructure of Hastelloy X Fabricated via TIG Process, Int. J. Mater. Sci. Appl. 5 (2016) 43–48. doi:10.11648/j.ijmsa.20160502.12.

[24] G. Bai, J. Li, R. Hu, T. Zhang, H. Kou, H. Fu, Effect of thermal exposure on the stability of carbides in Ni-Cr-W based superalloy, Mater. Sci. Eng. A. 528 (2011) 2339–2344. doi:10.1016/j.msea.2010.11.088.

[25] J.X. Dong, X.S. Xie, R.G. Thompson, The influence of sulfur on stress-rupture fracture in inconel 718 superalloys, Metall. Mater. Trans. A. 31 (2000) 2135–2144. doi:10.1007/s11661-000-0131-1.

[26] R.T. Holt, W. Wallace, Impurities and trace elements in nickel-base superalloys, Int. Mater. Rev. 21 (1976) 1–24. doi:10.1179/095066076790136762.

[27] O.P. Sinha, M. Chatterjee, V.V.R.S. Sarma, S.N. Jha, Effect of residual elements on high performance nickel base superalloys for gas turbines and strategies for manufacture, Bull. Mater. Sci. 28 (2005) 379–382. doi:10.1007/BF02704253.

[28] A. Mitchell, A.J. Schmalz, C. Schvezov, S.L. Cockcroft, The Precipitation of Primary Carbides in Alloy 718, Superalloys 718, 625, 706 Var. Deriv. (1994) 65–78. doi:10.7449/1994/Superalloys_1994_65_78.

[29] C.C. Silva, H.C. de Miranda, M.F. Motta, J.P. Farias, C.R.M. Afonso, A.J. Ramirez, New insight on the solidification path of an alloy 625 weld overlay, J. Mater. Res. Technol. 2 (2013) 228–237. doi:10.1016/j.jmrt.2013.02.008.

[30] S. Petroni, Heat Treatment Effect on Multicomponent Nickel Alloys Structure, Fme Trans. 35 (2007) 189–193.

[31] J.N. DuPont, Solidification of an alloy 625 weld overlay, Metall. Mater. Trans. A. 27 (1996) 3612–3620. doi:10.1007/BF02595452.

[32] J.N. DuPont, C.V. Robino, A.R. Marder, M.R. Notis, Solidification of Nb-bearing superalloys: Part II. Pseudoternary solidification surfaces, Metall. Mater. Trans. A. 29 (1998) 2797–2806. doi:10.1007/s11661-998-0320-x.

[33] H. Bernstein, Materials issues for users of gas turbines, in: Proc. 27th Texas A&M, 2006: pp. 1–16.

http://turbolab.tamu.edu/proc/turboproc/T27/Vol27017.pdf.

[34] P. Pizzi, P.L. Tarditi, S. Tosto, E. Ramous, P. Matteazzi, Microstructural stability of nickel superalloy coatings, Mater. Sci. Eng. 54 (1982) 1–7. doi:10.1016/0025-5416(82)90023-4.

[35] M.J. Cieslak, The Solidification Behavior of an Alloy 625/718 Variant, in: E.A. Loria (Ed.), Superalloys 718, 625 Var. Deriv., 1991: pp. 71–80. doi:10.7449/1991/Superalloys_1991_71_80.

[36] H. Chandler, Heat Treater's Guide Practices and Procedures for Nonferrous Alloys, ASM International, Materials Park, OH, 1996.

[37] INCONEL® alloy 625, www.Specialmetals.com. (2013) 1–18. http://www.specialmetals.com/assets/documents/alloys/inconel/inconel-alloy-625.pdf (accessed February 10, 2017).

[38] M. Kohler, Effect of the elevated-temperature-precipitation in alloy 625 on properties and microstructure, in: L.E. A. (Ed.), Superalloys 781, 625 Var. Deriv., The Mineral, Metal and Meterials Society, 1991: pp. 363–374.

[39] L.E. Shoemaker, Alloys 625 and 725: Trends in properties and applications, in: E.A. Loria (Ed.), 6th Int. Symp. Superalloys 718, 625, 706 Deriv., 2005: pp. 409–418. doi:10.7449/2005/Superalloys_2005_409_418.

[40] H. Eiselstein, D. Tillack, The Invention and Definition of Alloy 625, Superalloys 718, 625 Var. Deriv. (1991) 1–14. doi:10.7449/1991/Superalloys_1991_1_14.

[41] Haynes-International, Hastelloy X Alloy, High-Temperature Alloy. (1997) 16. http://www.haynesintl.com/alloys/alloy-portfolio_/High-temperature-Alloys/HASTELLOY-X-alloy/HASTELLOY-X-principal-features.aspx (accessed June 9, 2017).

[42] C. Brinkman, P. Rittenhouse, W. Corwin, J. Strizak, Application of Hastelloy X in gas-cooled reactor systems, Road Springfield, Virginia, 1976. doi:10.2172/7347624.

[43] G.Y. Lai, An investigation of the thermal stability of a commercial Ni-Cr-Fe-Mo alloy (hastelloy alloy X), Metall. Trans. A. 9 (1978) 827–833. doi:10.1007/BF02649792.

[44] R. V. Miner, M.G. Castelli, Hardening mechanisms in a dynamic strain aging alloy, HASTELLOY X, during isothermal and thermomechanical cyclic deformation, Metall. Trans. A. 23 (1992) 551–561.

doi:10.1007/BF02801173.

[45] D.D. Gu, W. Meiners, K. Wissenbach, R. Poprawe, Laser additive manufacturing of metallic components: materials, processes and mechanisms, Int. Mater. Rev. 57 (2012) 133–164. doi:10.1179/1743280411Y.0000000014.

[46] I. Gibson, D.W. Rosen, B.Stucker, Additve Manufacturing Technologies - Rapid Prototyping to Direct Digital Manufacturing, 2nd ed., Springer US, 2010. doi:10.1017/CBO9781107415324.004.

[47] S.M. Thompson, L. Bian, N. Shamsaei, A. Yadollahi, An overview of Direct Laser Deposition for additive manufacturing; Part I: Transport phenomena, modeling and diagnostics, Addit. Manuf. 8 (2015) 36–62. doi:10.1016/j.addma.2015.07.001.

[48] L.N. Carter, X. Wang, N. Read, R. Khan, M. Aristizabal, K. Essa, et al., Process optimisation of selective laser melting using energy density model for nickel based superalloys, Mater. Sci. Technol. 32 (2016) 657–661. doi:10.1179/1743284715Y.0000000108.

[49] L.N. Carter, M.M. Attallah, R.C. Reed, Laser Powder Bed Fabrication of Nickel-Base Superalloys: Influence of Parameters; Characterisation, Quantification and Mitigation of Cracking, Superalloys 2012. (2012) 577–586. doi:10.1002/9781118516430.ch64.

[50] E.O. Ezugwu, Key improvements in the machining of difficult-to-cut aerospace superalloys, Int. J. Mach. Tools Manuf. 45 (2005) 1353–1367. doi:10.1016/j.ijmachtools.2005.02.003.

[51] G.P. Dinda, A.K. Dasgupta, J. Mazumder, Laser aided direct metal deposition of Inconel 625 superalloy: Microstructural evolution and thermal stability, Mater. Sci. Eng. A. 509 (2009) 98–104. doi:10.1016/j.msea.2009.01.009.

[52] S.H. Huang, P. Liu, A. Mokasdar, L. Hou, Additive manufacturing and its societal impact: A literature review, Int. J. Adv. Manuf. Technol. 67 (2013) 1191–1203. doi:10.1007/s00170-012-4558-5.

[53] D. Herzog, V. Seyda, E. Wycisk, C. Emmelmann, Additive manufacturing of metals, Acta Mater. 117 (2016) 371–392. doi:10.1016/j.actamat.2016.07.019.

[54] D. Manfredi, F. Calignano, M. Krishnan, R. Canali, E.P. Ambrosio, S. Biamino, et al., Additive Manufacturing of Al Alloys and Aluminium Matrix

Composites (AMCs), in: Monteirio A. Waldemar (Ed.), Light Met. Alloy. Appl., 1st ed., InTech, Rijeka, Croatia, 2014: pp. 3–34. doi:10.5772/57069.

[55] S. Li, Q. Wei, Y. Shi, Z. Zhu, D. Zhang, Microstructure Characteristics of Inconel 625 Superalloy Manufactured by Selective Laser Melting, J. Mater. Sci. Technol. 31 (2015) 946–952. doi:10.1016/j.jmst.2014.09.020.

[56] G. Marchese, X. Garmendia Colera, F. Calignano, M. Lorusso, S. Biamino, P. Minetola, et al., Characterization and Comparison of Inconel 625 Processed by Selective Laser Melting and Laser Metal Deposition, Adv. Eng. Mater. 19 (2017) 1–9. doi:10.1002/adem.201600635.

[57] G. Marchese, E. Bassini, M. Calandri, E.P. Ambrosio, F. Calignano, M. Lorusso, et al., Microstructural investigation of as-fabricated and heat-treated Inconel 625 and Inconel 718 fabricated by direct metal laser sintering : contribution of Politecnico di Torino and Istituto Italiano di Tecnologia (IIT) di Torino, Met. Powder Rep. 0 (2016) 2–7.

[58] M. Rombouts, G. Maes, M. Mertens, W. Hendrix, Laser metal deposition of Inconel 625: Microstructure and mechanical properties, J. Laser Appl. 24 (2012) 363–374. doi:10.2351/1.4757717.

[59] F. Wang, X.H. Wu, D. Clark, On direct laser deposited Hastelloy X: dimension, surface finish, microstructure and mechanical properties, Mater. Sci. Technol. 27 (2011) 344–356. doi:10.1179/026708309X12578491814591.

[60] N.J. Harrison, I. Todd, K. Mumtaz, Reduction of micro-cracking in nickel superalloys processed by Selective Laser Melting: A fundamental alloy design approach, Acta Mater. 94 (2015) 59–68. doi:10.1016/j.actamat.2015.04.035.

[61] D. Tomus, Y. Tian, P.A. Rometsch, M. Heilmaier, X. Wu, Influence of post heat treatments on anisotropy of mechanical behaviour and microstructure of Hastelloy-X parts produced by selective laser melting, Mater. Sci. Eng. A. 667 (2016) 42–53. doi:10.1016/j.msea.2016.04.086.

[62] Q. Jia, D. Gu, Selective laser melting additive manufacturing of Inconel 718 superalloy parts: Densification, microstructure and properties, J. Alloys Compd. 585 (2014) 713–721. doi:10.1016/j.jallcom.2013.09.171.

[63] Z. Wang, K. Guan, M. Gao, X. Li, X. Chen, X. Zeng, The microstructure and mechanical properties of deposited-IN718 by selective laser melting, J. Alloys Compd. 513 (2012) 518–523. doi:10.1016/j.jallcom.2011.10.107.

[64] K.N. Amato, S.M. Gaytan, L.E. Murr, E. Martinez, P.W. Shindo, J. Hernandez, et al., Microstructures and mechanical behavior of Inconel 718 fabricated by selective laser melting, Acta Mater. 60 (2012) 2229–2239. doi:10.1016/j.actamat.2011.12.032.

[65] V.A. Popovich, E.V. Borisov, A.A. Popovich, V.S. Sufiiarov, D.V. Masaylo, L. Alzine, Functionally graded Inconel 718 processed by additive manufacturing: Crystallographic texture, anisotropy of microstructure and mechanical properties, Mater. Des. 114 (2017) 441–449. doi:10.1016/j.matdes.2016.10.075.

[66] E. Chlebus, K. Gruber, B. Kuźnicka, J. Kurzac, T. Kurzynowski, Effect of heat treatment on microstructure and mechanical properties of Inconel 718 processed by selective laser melting, Mater. Sci. Eng. A. 639 (2015) 647–655. doi:10.1016/j.msea.2015.05.035.

[67] L. Zhu, Z.F. Xu, P. Liu, Y.F. Gu, Effect of processing parameters on microstructure of laser solid forming Inconel 718 superalloy, (2017). doi:10.1016/j.optlastec.2017.08.027.

[68] C. Zhong, A. Gasser, J. Kittel, K. Wissenbach, R. Poprawe, Improvement of material performance of Inconel 718 formed by high deposition-rate laser metal deposition, Mater. Des. 98 (2016) 128–134. doi:10.1016/j.matdes.2016.03.006.

[69] P. Kanagarajah, F. Brenne, T. Niendorf, H.J. Maier, Inconel 939 processed by selective laser melting: Effect of microstructure and temperature on the mechanical properties under static and cyclic loading, Mater. Sci. Eng. A. 588 (2013) 188–195. doi:10.1016/j.msea.2013.09.025.

[70] L. Rickenbacher, T. Etter, S. Hövel, K. Wegener, High temperature material properties of IN738LC processed by selective laser melting (SLM) technology, Rapid Prototyp. J. 19 (2013) 282–290. doi:10.1108/13552541311323281.

[71] M. Zhong, H. Sun, W. Liu, X. Zhu, J. He, Boundary liquation and interface cracking characterization in laser deposition of Inconel 738 on directionally solidified Ni-based superalloy, Scr. Mater. 53 (2005) 159–164. doi:10.1016/j.scriptamat.2005.03.047.

[72] L.N. Carter, C. Martin, P.J. Withers, M.M. Attallah, The influence of the laser scan strategy on grain structure and cracking behaviour in SLM powder-bed fabricated nickel superalloy, J. Alloys Compd. 615 (2014) 338–347. doi:10.1016/j.jallcom.2014.06.172.

[73] V.D. Divya, R. Mu??oz-Moreno, O.M.D.M. Mess??, J.S. Barnard, S. Baker, T. Illston, et al., Microstructure of selective laser melted CM247LC nickel-based superalloy and its evolution through heat treatment, Mater. Charact. 114 (2016) 62–74. doi:10.1016/j.matchar.2016.02.004.

[74] M.M. Attallah, R. Jennings, X. Wang, L.N. Carter, Additive manufacturing of Ni-based superalloys: The outstanding issues, MRS Bull. 41 (2016) 758–764. doi:10.1557/mrs.2016.211.

[75] J.P. Kruth, G. Levy, F. Klocke, T.H.C. Childs, Consolidation phenomena in laser and powder-bed based layered manufacturing, CIRP Ann. - Manuf. Technol. 56 (2007) 730–759. doi:10.1016/j.cirp.2007.10.004.

[76] F. Calignano, D. Manfredi, E.P. Ambrosio, L. Iuliano, P. Fino, Influence of process parameters on surface roughness of aluminum parts produced by DMLS, Int. J. Adv. Manuf. Technol. 67 (2013) 2743–2751. doi:10.1007/s00170-012-4688-9.

[77] D. Manfredi, F. Calignano, M. Krishnan, R. Canali, E.P. Ambrosio, E. Atzeni, From powders to dense metal parts: Characterization of a Commercial AlSiMg Alloy Processed through Direct Metal Laser Sintering, Materials (Basel). 6 (2013) 856–869. doi:10.3390/ma6030856.

[78] Y. Lu, S. Wu, Y. Gan, T. Huang, C. Yang, L. Junjie, et al., Study on the microstructure, mechanical property and residual stress of SLM Inconel-718 alloy manufactured by differing island scanning strategy, Opt. Laser Technol. 75 (2015) 197–206. doi:10.1016/j.optlastec.2015.07.009.

[79] G. Kasperovich, J. Haubrich, J. Gussone, G. Requena, Correlation between porosity and processing parameters in TiAl6V4 produced by selective laser melting, Mater. Des. 105 (2016) 160–170. doi:10.1016/j.matdes.2016.05.070.

[80] N. Shamsaei, A. Yadollahi, L. Bian, S.M. Thompson, An overview of Direct Laser Deposition for additive manufacturing; Part II: Mechanical behavior, process parameter optimization and control, Addit. Manuf. 8 (2015) 12–35. doi:10.1016/j.addma.2015.07.002.

[81] J. Mazumder, A. Schifferer, J. Choi, Direct materials deposition: designed macro and microstructure, Mater. Res. Innov. 3 (1999) 118–131. doi:10.1007/s100190050137.

[82] J. Yu, X. Lin, L. Ma, J. Wang, X. Fu, J. Chen, et al., Influence of laser deposition patterns on part distortion, interior quality and mechanical properties by laser solid forming (LSF), Mater. Sci. Eng. A. 528 (2011)

1094–1104. doi:10.1016/j.msea.2010.09.078.

[83] A.H. Nickel, D.M. Barnett, F.B. Prinz, Thermal stresses and deposition patterns in layered manufacturing, Mater. Sci. Eng. A. 317 (2001) 59–64. doi:10.1016/S0921-5093(01)01179-0.

[84] A.K. Windeck, Günther Schuh, Marek Behr, Christian Brecher, Andreas Bührig-Polaczek, Walter Michaeli , Robert Schmitt, Jens Arnoscht , Arne Bohl , Damien Buchbinder, Jan Bültmann, Andrei Diatlov, Stefanie Elgeti , Werner Herfs , Christian Hinke, INTEGRATIVE PRODUCTION TECHNOLOGY FOR HIGH-WAGE COUNTRIES, in: Christian Brecher (Ed.), Integr. Prod. Technol. HIGH-WAGE Ctries., 1st ed., Springer Berlin Heidelberg, 2012: pp. 77–142. doi:10.1007/978-3-642-21067-9_3.

[85] Anatoliy Popovich, V.S. Additional, Metal Powder Additive Manufacturing, in: Intech, InTech, 2016: pp. 111–133. doi:10.5772/63337.

[86] A.B. Spierings, M. Voegtlin, T. Bauer, K. Wegener, Powder flowability characterisation methodology for powder-bed-based metal additive manufacturing, Prog. Addit. Manuf. 1 (2016) 9–20. doi:10.1007/s40964-015-0001-4.

[87] A. Kreitcberg, V. Brailovski, S. Turenne, Elevated temperature mechanical behavior of IN625 alloy processed by laser powder-bed fusion, Mater. Sci. Eng. A. 700 (2017) 540–553. doi:10.1016/j.msea.2017.06.045.

[88] D. Zhan, W. Niu, X. Cao, Z. Liu, Effect of standard heat treatment on the microstructure and mechanical properties of selective laser melting manufactured Inconel 718 superalloy, Mater. Sci. Eng. A. 644 (2015) 32–40. doi:10.1016/j.msea.2015.06.021.

[89] B. Song, X. Zhao, S. Li, C. Han, Q. Wei, S. Wen, et al., Differences in microstructure and properties between selective laser melting and traditional manufacturing for fabrication of metal parts: A review, Front. Mech. Eng. 10 (2015) 111–125. doi:10.1007/s11465-015-0341-2.

[90] G.K.L. Ng, A.E.W. Jarfors, G. Bi, H.Y. Zheng, Porosity formation and gas bubble retention in laser metal deposition, Appl. Phys. A Mater. Sci. Process. 97 (2009) 641–649. doi:10.1007/s00339-009-5266-3.

[91] M. Rombouts, J.P. Kruth, L. Froyen, P. Mercelis, Fundamentals of selective laser melting of alloyed steel powders, CIRP Ann. - Manuf. Technol. 55 (2006) 187–192. doi:10.1016/S0007-8506(07)60395-3.

[92] I. Yadroitsev, A. Gusarov, I. Yadroitsava, I. Smurov, Single track formation

in selective laser melting of metal powders, J. Mater. Process. Technol. 210 (2010) 1624–1631. doi:10.1016/j.jmatprotec.2010.05.010.

[93] C.Y. Yap, C.K. Chua, Z.L. Dong, Z.H. Liu, D.Q. Zhang, L.E. Loh, et al., Review of selective laser melting: Materials and applications, Appl. Phys. Rev. 2 (2015). doi:10.1063/1.4935926.

[94] Y. Chen, F. Lu, K. Zhang, P. Nie, S.R. Elmi Hosseini, K. Feng, et al., Dendritic microstructure and hot cracking of laser additive manufactured Inconel 718 under improved base cooling, J. Alloys Compd. 670 (2016) 312–321. doi:10.1016/j.jallcom.2016.01.250.

[95] B. Radhakrishnan, R.G. Thompson, Liquid film migration (LFM) in the weld heat affected zone (HAZ) of a ni-base superalloy, Scr. Metall. Mater. 24 (1990) 537–542. doi:10.1016/0956-716X(90)90197-O.

[96] B. Radhakrishnan, R.G. Thompson, A quantitative microstructural study of intergranular liquation and its relationship to hot cracking, Metallography. 21 (1988) 453–471. doi:10.1016/0026-0800(88)90006-7.

[97] M.G. Collins, A.J. Ramirez, J.C. Lippold, An investigation of ductility-dip cracking in nickel-based weld metals - Part III, Weld. J. 83 (2004) 39S–49S.

[98] G. a. Young, T.E. Capobianco, M. a. Penik, B.W. Morris, J.J. McGee, The mechanism of ductility dip cracking in nickel-chromium alloys, Weld. J. 87 (2008) 31S–43S. http://www.aws.org/wj/supplement/WJ_2008_02_s31.pdf.

[99] X. Wang, N. Read, L.N. Carter, R.M. Ward, M.M. Attallah, Defect Formation and its Mitigation in Selective Laser Melting of High γ′ Ni-Base Superalloys, Superalloys 2016. (2016) 351–358. doi:10.1002/9781119075646.ch38.

[100] R.J. Moat, A.J. Pinkerton, L. Li, P.J. Withers, M. Preuss, Residual stresses in laser direct metal deposited Waspaloy, Mater. Sci. Eng. A. 528 (2011) 2288–2298. doi:10.1016/j.msea.2010.12.010.

[101] Z. Wang, E. Denlinger, P. Michaleris, A.D. Stoica, D. Ma, A.M. Beese, Residual stress mapping in Inconel 625 fabricated through additive manufacturing: Method for neutron diffraction measurements to validate thermomechanical model predictions, Mater. Des. 113 (2017) 169–177. doi:10.1016/j.matdes.2016.10.003.

[102] S. Bontha, N.W. Klingbeil, P.A. Kobryn, H.L. Fraser, Thermal process maps for predicting solidification microstructure in laser fabrication of thin-wall structures, J. Mater. Process. Technol. 178 (2006) 135–142.

doi:10.1016/j.jmatprotec.2006.03.155.

[103] S. Bontha, N.W. Klingbeil, P.A. Kobryn, H.L. Fraser, Effects of process variables and size-scale on solidification microstructure in beam-based fabrication of bulky 3D structures, Mater. Sci. Eng. A. 513–514 (2009) 311–318. doi:10.1016/j.msea.2009.02.019.

[104] J.P. Kruth, L. Froyen, J. Van Vaerenbergh, P. Mercelis, M. Rombouts, B. Lauwers, Selective laser melting of iron-based powder, J. Mater. Process. Technol. 149 (2004) 616–622. doi:10.1016/j.jmatprotec.2003.11.051.

[105] F. Abe, K. Osakada, M. Shiomi, K. Uematsu, M. Matsumoto, The manufacturing of hard tools from metallic powders by selective laser melting, J. Mater. Process. Technol. 111 (2001) 210–213. doi:10.1016/S0924-0136(01)00522-2.

[106] EOS GmbH Electro Optical Systems, EOSINT M 270 data sheet, (2015) 1–21. http://www.nobilium.com/skin/frontend/ultimo/default/pdf/TD_M270_Dental-Package_10-15_en.pdf (accessed September 3, 2017).

[107] EOS GmbH Electro Optical Systems, Eosint M280, (2013) 4. https://cdn2.scrvt.com/eos/public/e1dc925774b24d9f/55e7f647441dc9e8fdaf944d18416bdb/systemdatasheet_M280_n.pdf (accessed September 3, 2017).

[108] EOS GmbH Electro Optical Systems, EOSINT M 270 data sheet, (2005) 2. https://dmlstechnology.com/images/pdf/EOSINT_M_270.pdf (accessed September 3, 2017).

[109] EOS GmbH Electro Optical Systems, Technical Description EOSINT M 280, (2013) 40. http://webbuilder5.asiannet.com/ftp/2684/TD_M280_en_2011-03-29.pdf (accessed September 3, 2017).

[110] EOS GmbH - Material data sheet, Material data sheet - EOS Nickel Alloy IN625, (2011) 1–5. http://ip-saas-eos-cms.s3.amazonaws.com/public/d1327facdca0e32a/373a60ec4f5c891b7dbcdf572e37d3b0/EOS_NickelAlloy_IN625_en.pdf (accessed June 8, 2016).

[111] Thermal Surfacing Marine & Offshore Industry Solutions, Hoganas AB. (2013) 1–12. https://www.hoganas.com/globalassets/media/sharepoint-documents/BrochuresanddatasheetsAllDocuments/MarineandOffshoreIndustrySolutions.pdf (accessed May 23, 2016).

[112] LPW Technology, PowderRange Metal powders from LPW, (2017) 7. http://www.lpwtechnology.com/wp-content/uploads/2016/11/LPW-Powders-Brochure-2017.pdf (accessed September 3, 2017).

[113] G.F. Vander Voort, Metallography Of Superalloys, Ind. Heat. (2003) 40–43. doi:10.1017/S1431927604883442.

[114] K.B. Small, D.A. Englehart, T.A. Christman, Guide to etching specialty alloys, Adv. Mater. Process. 166 (2008) 32–37.

[115] G. Vander Voort, E. Manilova, Metallographic Techniques for Superalloys, Microsc. Microanal. 10 (2004) 690–691. doi:10.1017/S1431927604883442.

[116] B. Fultz, J.M. Howe, Transmission electron microscopy and diffractometry of materials, 2008. doi:10.1007/978-3-540-73886-2.

[117] Z. Xu, L. Jiang, J. Dong, Z. Li, X. Zhou, The effect of silicon on precipitation and decomposition behaviors of M6C carbide in a Ni-Mo-Cr superalloy, J. Alloys Compd. 620 (2015) 197–203. doi:10.1016/j.jallcom.2014.09.112.

[118] K. Shinzato, T. Baba, A laser flash apparatus for thermal diffusivity and specific heat capacity measurements, J. Therm. Anal. 64 (2001) 413–422. doi:10.1023/A:1011594609521.

[119] L. Avala, M. Bheema, P.K. Singh, R.K. Rai, S. Srivastava, Measurement of Thermo Physical Properties of Nickel Based Superalloys, Int. J. Mech. Eng. Robot. 1 (2013) 108–112.

[120] J.C. La Salle, B.C. Sherman, Net shape Hastelloy X made by metal injection molding using an aqueous binder, 5,989,493, 1999. https://www.google.ch/patents/US5989493.

[121] T. Vilaro, C. Colin, J.D. Bartout, As-fabricated and heat-treated microstructures of the Ti-6Al-4V alloy processed by selective laser melting, Metall. Mater. Trans. A Phys. Metall. Mater. Sci. 42 (2011) 3190–3199. doi:10.1007/s11661-011-0731-y.

[122] S. Biamino, A. Penna, U. Ackelid, S. Sabbadini, O. Tassa, P. Fino, et al., Electron beam melting of Ti-48Al-2Cr-2Nb alloy: Microstructure and mechanical properties investigation, Intermetallics. 19 (2011) 776–781. doi:10.1016/j.intermet.2010.11.017.

[123] A. Kreitcberg, V. Brailovski, S. Turenne, Effect of heat treatment and hot isostatic pressing on the microstructure and mechanical properties of Inconel 625 alloy processed by laser powder bed fusion, Mater. Sci. Eng. A. 689

(2017) 1–10. doi:10.1016/j.msea.2017.02.038.

[124] T. Antonsson, H. Fredriksson, The effect of cooling rate on the solidification of INCONEL 718, Metall. Mater. Trans. B-Process Metall. Mater. Process. Sci. 36 (2005) 85–96. doi:10.1007/s11663-005-0009-0.

[125] J.N. DuPont, A.R. Marder, M.R. Notis, C. V Robino, Solidification of Nb-bearing superalloys: Part II. Pseudoternary solidification surfaces, Metall. Mater. Trans. A. 29 (1998) 2797–2806. doi:10.1007/s11661-998-0320-x.

[126] F.J. Xu, Y.H. Lv, B.S. Xu, Y.X. Liu, F.Y. Shu, P. He, Effect of deposition strategy on the microstructure and mechanical properties of Inconel 625 superalloy fabricated by pulsed plasma arc deposition, Mater. Des. 45 (2013) 446–455. doi:10.1016/j.matdes.2012.07.013.

[127] I. Yadroitsev, L. Thivillon, P. Bertrand, I. Smurov, Strategy of manufacturing components with designed internal structure by selective laser melting of metallic powder, Appl. Surf. Sci. 254 (2007) 980–983. doi:10.1016/j.apsusc.2007.08.046.

[128] P. Wang, B. Zhang, C.C. Tan, S. Raghavan, Y.-F. Lim, C.-N. Sun, et al., Microstructural characteristics and mechanical properties of carbon nanotube reinforced Inconel 625 parts fabricated by selective laser melting, Mater. Des. 112 (2016) 290–299. doi:10.1016/j.matdes.2016.09.080.

[129] C.U. Brown, G. Jacob, M. Stoudt, S. Moylan, J. Slotwinski, A. Donmez, Interlaboratory Study for Nickel Alloy 625 Made by Laser Powder Bed Fusion to Quantify Mechanical Property Variability, J. Mater. Eng. Perform. 25 (2016) 3390–3397. doi:10.1007/s11665-016-2169-2.

[130] M. Kohler, Effect of the elevated-temperature-precpitation in Alloy 625 on properties and microstructure, in: E.A. Loria (Ed.), Superalloys 718, 625, 706 Var. Deriv., TMS (The Minerals, Metals & Materials Society), Pennsylvania, 1991: pp. 363–374.

[131] L. Ferrer, B. Pieraggi, J.F. Uginet, Microstructural Evolution During Thermomechanical Processing of Alloy 625, in: E.A. Loria (Ed.), Superalloys 718,625 Var. Deriv., 1991: pp. 217–228.

[132] C. Vernot-Loier, F. Cortial, Influence of Heat Treatments on Microstructure, Mechanical Properties and Corrosion Behaviour of Alloy 625 Forged Rod, in: E.A. Loria (Ed.), Superalloys 718, 625 Var. Deriv., 1991: pp. 409–422.

[133] A. Kumar, T. Jayakumar, B. Raj, Influence of precipitation of intermetallics on Young's modulus in nickel and zirconium base alloys, Philos. Mag. Lett.

86 (2006) 579–587. doi:10.1080/09500830600936401.

[134] J. Mittra, S. Banerjee, R. Tewari, G.K. Dey, Fracture behavior of Alloy 625 with different precipitate microstructures, Mater. Sci. Eng. A. 574 (2013) 86–93. doi:10.1016/j.msea.2013.03.021.

[135] H. Qi, M. Azer, a. Ritter, Studies of Standard Heat Treatment Effects on Microstructure and Mechanical Properties of Laser Net Shape Manufactured INCONEL 718, Metall. Mater. Trans. A. 40 (2009) 2410–2422. doi:10.1007/s11661-009-9949-3.

[136] G.P. Dinda, A.K. Dasgupta, J. Mazumder, Laser aided direct metal deposition of Inconel 625 superalloy: Microstructural evolution and thermal stability, Mater. Sci. Eng. A. 509 (2009) 98–104. doi:10.1016/j.msea.2009.01.009.

[137] F. Xu, Y. Lv, Y. Liu, B. Xu, P. He, Effect of heat treatment on microstructure and mechanical properties of inconel 625 alloy fabricated by pulsed plasma arc deposition, Phys. Procedia. 50 (2013) 48–54. doi:10.1016/j.phpro.2013.11.010.

[138] F. Xu, Y. Lv, Y. Liu, F. Shu, P. He, B. Xu, Microstructural Evolution and Mechanical Properties of Inconel 625 Alloy during Pulsed Plasma Arc Deposition Process, J. Mater. Sci. Technol. 29 (2013) 480–488. doi:10.1016/j.jmst.2013.02.010.

[139] G. Marchese, S. Biamino, M. Pavese, D. Ugues, M. Lombardi, G. Villillo, et al., Heat treatment optimization of Hastelloy X superalloy produced by Direct Metal Laser Sintering, in: Proc. Euro PM 2015 Int. Powder Metall. Congr. Exhib., European Powder Metallurgy Association, Reims, France, 2015: pp. 1–6. https://www.epma.com/publications/euro-pm-abstracts-proceedings/cd-and-usb-proceedings/product/euro-pm2015-proceedings-usb.

[140] N.J. Harrison, I. Todd, K. Mumtaz, Reduction of micro-cracking in nickel superalloys processed by Selective Laser Melting: A fundamental alloy design approach, Acta Mater. 94 (2015) 59–68. doi:10.1016/j.actamat.2015.04.035.

[141] G. Bai, J. Li, R. Hu, Z. Tang, X. Xue, H. Fu, Effect of temperature on tensile behavior of Ni-Cr-W based superalloy, Mater. Sci. Eng. A. 528 (2011) 1974–1978. doi:10.1016/j.msea.2010.11.053.

[142] F.C. Hull, S.K. Hwang, J.M. Wells, R.I. Jaffee, Effect of composition on thermal expansion of alloys used in power generation, J. Mater. Eng. 9

(1987) 81–92. doi:10.1007/BF02833790.